# FINITE ELEMENT MODELING OF OPTIC NERVE HEAD BIOMECHANICS IN A RAT MODEL OF GLAUCOMA

A Dissertation
Presented to
The Academic Faculty

by

Stephen A. Schwaner

In Partial Fulfillment
of the Requirements for the Degree
Doctor of Philosophy in Bioengineering in the
George W. Woodruff School of Mechanical Engineering

Georgia Institute of Technology
December 2019

# FINITE ELEMENT MODELING OF OPTIC NERVE HEAD BIOMECHANICS IN A RAT MODEL OF GLAUCOMA

Approved by:


Dr. C. Ross Ethier, Advisor
Department of Biomedical Engineering
*Georgia Institute of Technology*

Dr. J. Brandon Dixon
School of Mechanical Engineering
*Georgia Institute of Technology*

Dr. Andrés J. García
School of Mechanical Engineering
*Georgia Institute of Technology*

Dr. Ian A. Sigal
Department of Opthalmology
*University of Pittsburgh*

Dr. Rudolph L. Gleason
School of Mechanical Engineering
*Georgia Institute of Technology*



Date Approved: 08/05/2019

To my wife, Sarah, and my two daughters, Lily and Anna.

# ACKNOWLEDGEMENTS

First, I would like to acknowledge the training and support that I received from my advisor, Dr. Ross Ethier. The lessons that he has given to me will serve me well in my career and my family life. In particular, Dr. Ethier always pushed me to put forth my best work and has greatly elevated my oral and written communications skills. He has also been especially supportive during times of stress in my family and encouraged me to be the best husband and father that I can be. I will always be grateful for that.

I would also like to thank several postdoctoral fellows and research scientists who provided training, advice, and mentorship, including Dr. Ian Campbell, Dr. Andrew Feola, Dr. Julia Raykin, and Dr. John Mulvihill.

Two extremely capable and willing administrators also deserve my thanks: Laura Paige and Tracie Dinkins. Both women have helped me to navigate incredibly stressful situations. My time at Georgia Tech would have been much more difficult without them.

Finally, I would like to acknowledge my wife, Sarah. I think that completing the work in this dissertation has put almost as much pressure on her as it has on me. Throughout the last six years, she has provided a steady stream of support and encouragement, and she has stepped up to take care of our family on many occasions when I was overburdened with work. The last six years would have been filled with more stress and would have been lacking in happiness without her.

# TABLE OF CONTENTS

# LIST OF TABLES

# LIST OF FIGURES

39. The undeformed configuration is shown in all images to ensure viewing of consistent cut planes.

# LIST OF SYMBOLS AND ABBREVIATIONS

| | |
|---|---|
| 05_3P | 5$^{th}$ percentile third principal strain |
| 95_1P | 95$^{th}$ percentile first principal strain |
| AFM | atomic force microscopy |
| ASCO | anterior scleral canal |
| BM | Bruch's membrane |
| $c_1$ | first Mooney-Rivlin coefficient |
| $c_3$ | exponential fiber stress coefficient |
| $c_4$ | fiber uncrimping coefficient |
| CEI | controlled elevation of intraocular pressure |
| CSFp | cerebrospinal fluid pressure |
| CRA | central retinal artery |
| CRV | central retinal vein |
| DIC | digital image correlation |
| $E$ | elastic modulus |
| ESPI | electronic speckle pattern interferometry |
| ECM | extra cellular matrix |
| EG | experimental glaucoma |
| FE | finite element |
| FEM | finite element modeling |
| GFAP | glial fibrillary acidic protein |
| IAC | inferior arterial canal |
| IOP | intraocular pressure |
| $k_f$ | fiber concentration factor |

| | |
|---|---|
| LC | lamina cribrosa |
| micro-CT | micro-computed tomography |
| nerve-ASCO | optic nerve opening in the anterior scleral canal |
| nerve-PSCO | optic nerve opening in the posterior scleral canal |
| OCT | optical coherence tomography |
| ONH | optic nerve head |
| PNVP | perineural vascular plexus |
| PSCO | posterior scleral canal |
| RGC | retinal ganglion cell |
| RLTP | retrolaminar tissue pressure |
| RNFL | retinal nerve fiber layer |
| ROS | reactive oxygen species |
| SCO | scleral canal opening |
| SD-OCT | scanning domain-optical coherence tomography |
| $\theta_p$ | preferred fiber direction |
| $\nu$ | Poisson's ratio |

# SUMMARY

Glaucoma is the leading cause of irreversible blindness and is characterized by the dysfunction of retinal ganglion cells (RGC), the cells that send vision information from the retina to the brain. All current therapies focus on lowering intraocular pressure (IOP), a causative risk factor in the disease. However, they are not always effective. Although it is well-accepted that elevated IOP-induced biomechanical insult to the optic nerve head (ONH), the region in the posterior eye where RGC axons exit, is key to glaucoma pathophysiology, the mechanisms by which biomechanical insult leads to RGC death are unknown. Rat glaucoma models present an opportunity for understanding glaucoma biomechanics and are widely used in the field. However, rat ONH biomechanics have not been characterized and rat ONH anatomy differs substantially from the human.

Therefore, the purpose of this thesis was to provide the first characterization of rat ONH biomechanics to the glaucoma field. To this end, we completed three specific aims. First, we used inverse modeling combined with whole-eye inflation testing to extract material properties from the rat sclera. Second, we conducted a sensitivity study to investigate the effects of anatomical and material property variation on rat ONH strains using a parameterized finite element model of the rat ONH. Lastly, we developed a methodology for building rat ONH FE models with individual-specific geometry and simulated the effects of elevated IOP. Key results include the finding that the patterns of strain in the rat ONH are less symmetric than those in the human, and the highest strains occur in the inferior nerve. In all three aims, the results emphasized the importance of collagen fiber organization on optic nerve strains. Lastly, the patterns and magnitude of optic nerve strain in the parameterized model showed good concordance with those observed in the individual-specific models, suggesting that the higher throughput

parameterized models may be able to replace individual-specific models of the rat ONH moving forward. The results from this work can serve to inform future modeling studies on rat ONH biomechanics, and provide context for interpreting rat glaucoma studies with the goal of learning more about the link between biomechanical insult and RGC pathophysiology in glaucoma.

.

# CHAPTER 1. INTRODUCTION

The purpose of this this thesis is to explain the importance of modeling rat optic nerve head biomechanics in glaucoma research, what results I have obtained after five and a half years of work, and how this information should be utilized in the field going forward. In this introduction, I will first give the reader an overview of glaucoma, explain the relevance of intraocular pressure in the disease process and as a therapeutic target, and give a brief introduction to glaucoma biomechanics. I will then explain the motivation for characterizing rat ONH biomechanics. Finally, I will give an overview of the three specific aims of this thesis.

## 1.1 Glaucoma

### 1.1.1 Overview

In a 2015 poll that asked Americans about their greatest health fears, blindness was ranked as one of the most feared disabilities, ranked even ahead of ailments such as loss of a limb, loss of memory, and loss of speech (Scott, 2015). Unfortunately, glaucoma, the second leading cause of blindness and the *leading* cause of irreversible blindness, is not well understood. It is projected to affect 76 million people throughout the world by the year 2020 (Tham et al., 2014), and although several different modes of therapy exist, they are not always effective.

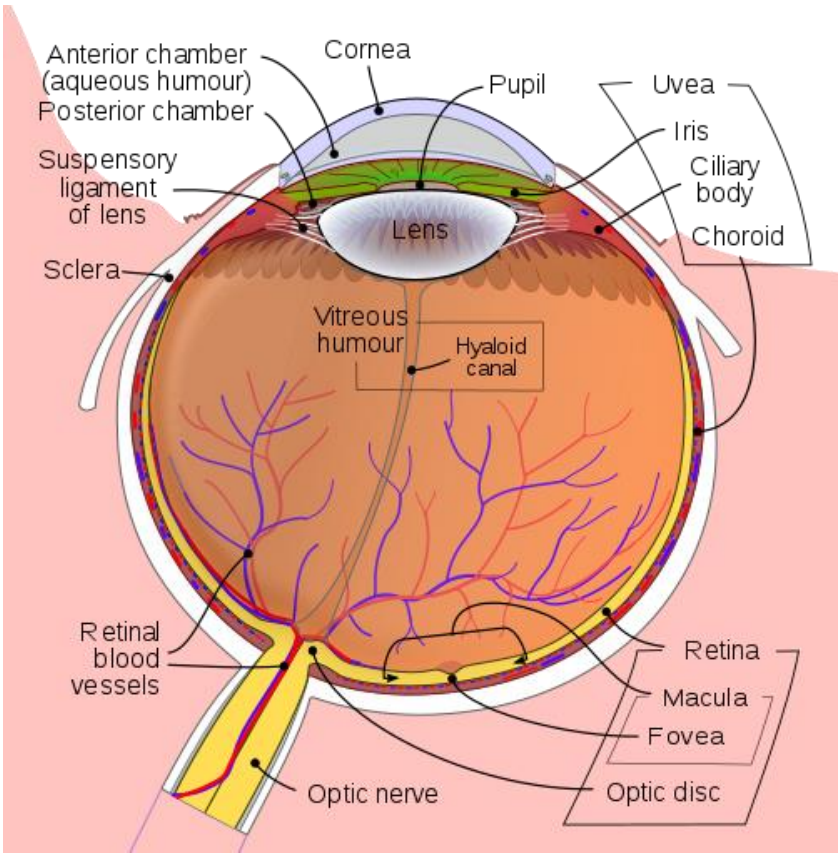


**Figure 1. Overview of human eye anatomy. Created by Jordi Noguè, distributed under a CC BY-SA 3.0 license (Source: https://commons.wikimedia.org/wiki/File: Schematic_ diagram_of_the_human_eye_en.svg)**

Part of the difficulty in understanding this disease is that the term “glaucoma” refers to a spectrum of disease states with different characteristics and causes (Quigley, 1999). They all share a common pathology, which is the loss of function of retinal ganglion cell (RGC) axons and structural changes to the optic nerve head described as “cupping” (Burgoyne, 2015). RGCs are the neurons that relay vision information from the retina to the brain via axons that exit the eye through a canal in the posterior globe. The region at which they exit the eye is called the optic nerve head (ONH), which is known to be an early and primary site of damage in glaucoma (Minckler et al., 1977; Quigley & Addicks, 1980; Quigley et al., 1981). The ONH is not the only site of pathology in glaucoma, but it will be the focus in this thesis.

The most common type of glaucoma in the west is called “primary open-angle glaucoma”, which is estimated to make up more than 80% of cases in the United States (Friedman, 2004; Weinreb et al., 2014). In this form of glaucoma, damage progression and onset of blindness are slow, taking place over several years. This means that a patient can remain undiagnosed and untreated until later stages in the disease when they finally notice symptoms. At that point, it is likely that significant vision loss has already occurred (Varma et al., 2011).

### 1.1.2 Elevated Intraocular Pressure: Risk Factor and Therapeutic Target

Principal risk factors for glaucoma include elevated intraocular pressure (IOP), age, family history of the disease, and African American descent, among others (Weinreb et al., 2014). Elevated IOP is considered to be a causative risk factor, which indicates the importance of biomechanics in the disease. In fact, it is generally agreed that the increased mechanical stress and strain in the ONH due to elevated IOP are important drivers leading to RGC dysfunction (Burgoyne, 2011). Further, IOP lowering remains the only clinically-validated therapeutic intervention in glaucoma. Even in cases of normal tension glaucoma, in which the patient experiences glaucomatous vision loss at normal levels of IOP, lowering IOP is still the standard treatment (Anderson, 2003).

Clinicians treat glaucoma using several types of IOP-lowering drugs with different modes of action. Surgical treatments, including devices that provide an extra path of fluid drainage from the eye, are second-line options. Unfortunately, in many cases these methods are ineffective at preventing further vision loss (Anderson, 2003). In addition, the administration of IOP-lowering drugs must be carried out in a strict regimen by the patient. As a result, lack of patient compliance frequently allows the disease to progress (Okeke

et al., 2009). Thus, novel therapies with new modes of action other than lowering IOP are needed and will likely require a better understanding of the pathophysiology of RGC loss.

### 1.1.3 Glaucoma Biomechanics

Even though it is widely accepted that biomechanics play a fundamental role in the disease, the mechanisms by which biomechanical insult lead to and/or influence the progression of RGC dysfunction are not well understood. As is evident by the information above, this is due in part to the fact that glaucoma has multiple layers of complexity. The first layer, the actual disease process leading up to RGC death, is not well understood because a variety of factors are likely at play. Even though biomechanical insult has been identified as a likely driver of glaucomatous damage, there are several “triggers” at which biomechanical insult could be initiating damage progression (Alqawlaq et al., 2018; Burgoyne, 2011). Some of these may be primarily responsible for RGC apoptosis, but it is likely that they interact. In addition, the biomechanical environment of the ONH is extremely complex. Researchers are just now beginning to develop capabilities to answer questions such as “What is a common magnitude and mode of strain experienced by an RGC axonal bundle after IOP is elevated”, even though these questions have been asked for decades.

## 1.2 Motivation for the Characterization of Rat ONH Biomechanics

In this context, rodent glaucoma models, particularly rat models of ocular hypertension, are highly valuable research tools. As will be discussed, they closely mimic glaucoma pathophysiology and their low cost and ease of use allow for the high subject numbers necessary for mechanistic studies (Morrison et al., 2011). However, they cannot yet be used to make connections between biomechanical insult and RGC death because rat ONH biomechanics data is missing from the field. Unfortunately, it cannot simply be

inferred from the studies on large mammals because rat ONH anatomy is markedly different from that of humans and other large mammals. Fortunately, recent histomorphometry work has provided a data set describing detailed, 3D rat ONH anatomy that can be used to build finite element (FE) models (Pazos et al., 2015, 2016). The purpose of this thesis is to use FE modeling to provide the biomechanical characterization of the rat ONH under glaucomatous conditions that is currently missing from the field. The results from this work will enable connections to be made between the patterns of biomechanical insult they provide with cellular response patterns from current and future rat glaucoma studies to learn more about RGC pathogenesis.

### 1.3 Specific Aims

**Specific Aim1:** Determine the biomechanical properties of the rat sclera using inverse finite element modeling

No studies to date have determined the biomechanical properties of rat ONH tissues necessary for FE modeling. Ideally, we would have tested each mechanically-relevant tissue in and adjacent to the ONH. However, we here chose to focus on the sclera, as previous studies suggest that the sclera is most influential in determining human ONH mechanical response; further, other ONH-relevant tissues are extremely difficult to isolate and test. The sclera was subjected to a combination of inflation testing with digital image correlation and inverse FE analysis to determine parameters describing tissue stiffness and regional fiber directions. These material properties will inform future attempts to model and understand biomechanical behavior in the rat ONH, including FE models in Aims 2 and 3.

**Specific Aim 2:** Determine the factors that most influence rat optic nerve head biomechanics in a sensitivity analysis using a parameterized finite element model

We developed a generic, parameterized rat ONH FE model based on image data sets provided by a collaborating lab, and material properties from Specific Aim 1. The geometry and material parameters of this model were parametrically-variable, and FE analysis was used to simulate ONH stress and strain patterns. We performed a sensitivity analysis using Latin hypercube sampling, a computationally efficient statistical sampling technique, to explore the influence of model parameters on biomechanical outcome measures. As a result, we determined which anatomical features and material parameters most impact rat ONH biomechanics.

**Specific Aim 3:** Determine strain patterns in rat ONHs under elevated IOP using individual-specific FE modeling

Although generic FE models such as developed in Aim 2 are ideal for performing sensitivity analyses, they come with the necessary drawback of using simplified geometries. Therefore, we used complex, individual-specific geometries in this Aim, creating models with higher geometric fidelity than Aim 2. We simulated the effects of IOP elevation using seven rat-specific geometries (based on image data as in Aim 2) and material properties (Aim 1). The data acquired from these FE models provides a framework for interpreting previous and future results from rat glaucoma studies. Specifically, regional patterns of stress and strain predicted by our models can be compared to regional patterns of biological outcomes, such as ONH astrocyte realignment and RGC degeneration, currently being measured in our lab and others. These comparisons can be used to draw conclusions about how biomechanics influences cellular behavior in glaucoma, ultimately driving development of non-IOP lowering glaucoma therapies.

# CHAPTER 2. BACKGROUND

In this chapter, I will first explain how the balance of fluid flow in the eye affects IOP. I will then proceed to describe the anatomy of the ONH and the pathophysiological events that occur there in glaucoma. Next, I will give a description of ONH biomechanics, including relevant experimental and modeling studies to date. Finally, I will describe the strengths and weaknesses of rat models of ocular hypertension and any biomechanically-relevant rodent glaucoma studies.

## 2.1 Flow of Aqueous Humor

A key element of primary open-angle glaucoma is the production and outflow of a clear fluid called aqueous humor, which can be thought of as the body's solution to nutrition delivery in the eye while maintaining ocular transparency to allow the passage of light. Aqueous humor is produced by processes on the surface of the ciliary body, which lies posterior to the iris. This fluid exits the eye through a series of tissues with varying fluid resistance in the angle between the cornea and the iris. The interaction between aqueous production and outflow resistance determines the level of IOP in the eye, with high resistance and/or high production causing elevated IOP. The tissues through which aqueous flows have highly sensitive outflow/IOP control functions (Ashpole et al., 2014; Johnson et al., 1989; Stumpff & Wiederholt, 2000), but as one can imagine, if this control is hindered or dysfunctional, as is the case in a significant set of glaucoma subtypes, IOP can be chronically elevated. Thus, an important aim of the glaucoma field is to understand and manipulate the mechanisms that control aqueous humor flow and regulate IOP. However, damage to the ONH is what directly causes blindness in glaucoma and will be the focus of this thesis.

## 2.2 Anatomy of the Optic Nerve Head and Surrounding Tissues

To understand glaucoma pathophysiology, one must first have a grasp of ONH anatomy. In this section, I will first define the directional terms that will be used throughout this thesis to describe relative positions within the eye. I will then describe the tissues in and around the human ONH region and their functions. Anatomy of the rat ONH will be dealt with in Section 2.5.3. Finally, I will give a description of the resident cells in the ONH and their respective roles.

### 2.2.1 Explanation of Directional Terms

Before describing the tissues of the ONH, it is helpful to define a set of directions, namely “superior”, “inferior”, “anterior”, “posterior”, “temporal”, and “nasal”. The superior and inferior directions point toward the forehead and chin, respectively; the anterior and posterior directions point out of the face and back into the skull, respectively; and the temporal and nasal directions point toward the temple and nose, respectively. Note that the temporal and nasal directions are flipped for two eyes from the same subject (contralateral eyes).

### 2.2.2 Main Tissues and Their Primary Functions

As mentioned above, the ONH is the region in the posterior eye where RGC axons converge before exiting the globe. The axons form the optic nerve as they pass through the scleral canal. The sclera, the white part of the eye, together with the cornea, forms the main connective tissue shell of the eye. Like most load-bearing soft tissues, the sclera is primarily composed of a proteoglycan matrix reinforced by layers of organized collagen and elastin fibers (Young, 1985). The thickness of the sclera varies but is in the range of 0.5–1 mm in humans (Norman et al., 2010). Directly interior to the sclera is a bed of

vascular tissue called the choroid, which serves as a blood supply for the retina (Hirata et al., 2011; Lee et al., 2016). Separating the choroid and retina is a thin (c. 3 µm), but tough connective tissue membrane called Bruch's membrane (BM) that is primarily made up of collagen and elastin (Curcio & Johnson, 2012).

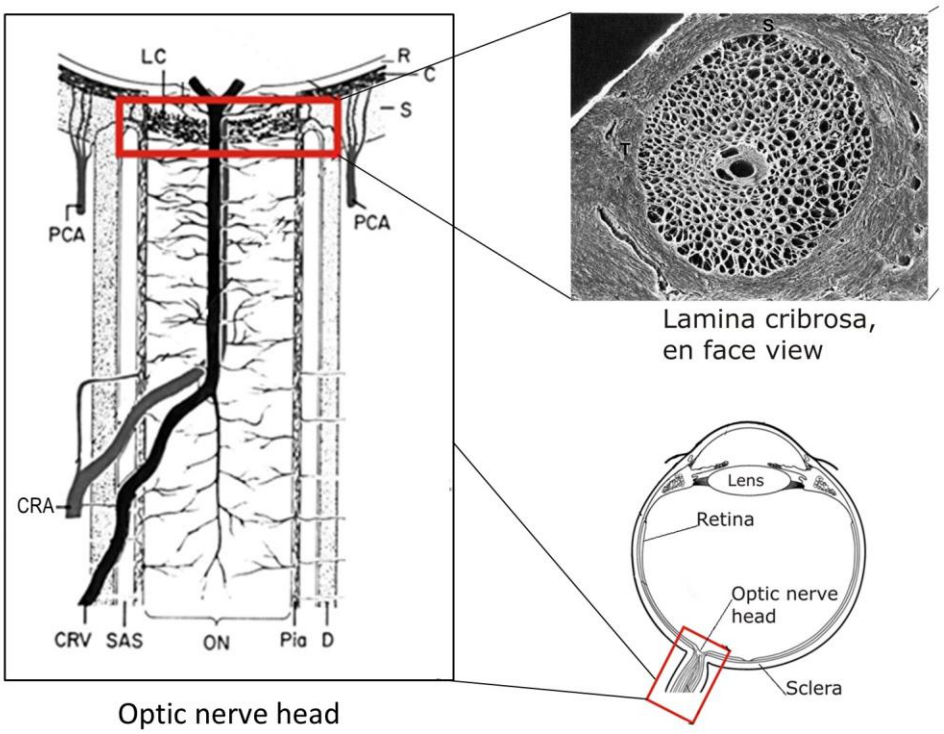


**Figure 2. Left: Schematic of the human ONH. Abbreviations: R (retina), C (choroid), S (sclera), PCA (posterior ciliary artery), SAS (subarachnoid space), ON (optic nerve), D (dura mater). Top right: Electron microscopic image of the LC. Bottom right: Schematic of the eye anatomy. All three represent human anatomy. Adapted from (Ethier & Simmons, 2007).**

The retina is organized into layers of neurons, with glial cells throughout, that have different roles in sensing and processing light information. Processed vision information is transmitted to the visual cortex via the RGC axons, which form the "retinal nerve fiber layer" (RNFL), the innermost layer of the retina. The elegant process of sensing, processing, and transmitting light information requires the retina to maintain a high metabolic rate, making it necessary to have an efficient retinal circulatory system. The

choroid is positioned adjacent to the retina in order to perform this role for the exterior retinal layers, and a series of vessels laid across the inner retina supply the inner layers (Yu et al., 2019).

Spanning the scleral canal in human eyes is a web-like connective tissue called the lamina cribrosa (LC), which separates the optic nerve tissue into three regions: the prelaminar region (anterior to the LC), the laminar region, and the retrolaminar region (posterior to the LC). The beams of the LC connect in a complex pattern, resulting in pores of different shapes, sizes, and tortuosities through which bundles of RGC axons pass. The LC beams are composed primarily of collagen and elastin (Goldbaum, 1989; Hernandez et al., 1987) and are thought to provide mechanical support to the RGC axon bundles as they pass through the scleral canal, a weak point in the otherwise tough corneoscleral shell (Downs et al., 2008). The LC also serves as a scaffold for capillaries running through the LC beams that provide blood to the axon bundles (Anderson, 1969). As seen in Figure 2, the capillaries are supplied with blood by the posterior ciliary arteries that pass through and out of the sclera near the ONH (Hayreh, 2001).

The LC provides mechanical stability to individual axon bundles, but the optic nerve sheath provides mechanical support to the nerve as a whole. It is composed of two main layers: the pia mater and dura mater, both connective tissues with high collagen content (Taban et al., 2001). The pia mater originates from the posterior scleral surface, directly encases the optic nerve, and has a thickness of approximately 50 μm (Jonas et al., 2014). The dura mater is thicker than the pia at about 300 μm (Hasenfratz, 1987). It also arises from the posterior sclera but does not directly encase the pia and nerve, instead surrounding the subarachnoid space that contains cerebrospinal fluid (CSF).

### 2.2.3 The Cellular Environment of the ONH

As mentioned, the RGC axons form the vast majority of the optic nerve. Within the prelaminar neural tissue and LC, these axons have no myelin sheath. Posterior to the LC, the axons are myelinated, and the optic nerve becomes thicker as a result. Other cell types in the ONH region which are important in optic nerve homeostasis include oligodendrocytes, microglia, scleral fibroblasts, LC cells, and astrocytes.

Oligodendrocytes and microglia are both types of glial cells. Oligodendrocytes maintain the myelin sheaths of the RGC axons posterior to the LC, and microglia primarily act as immune surveillance cells by performing phagocytosis of unwanted materials. Scleral fibroblasts are important for maintaining the ECM of the peripapillary sclera, and LC cells are cells unique to the ONH that maintain the ECM of the LC beams (Hernandez, 2000; Kang & Yu, 2015).

Astrocytes line the beams of the LC and are distributed throughout the optic nerve, providing a number of support functions for the RGC axons (Hernandez et al., 2008). These important glial cells have a distinct morphology, consisting of many long processes protruding from the cell body that end in foot plates usually either adjacent to an LC beam or RGC axon bundle. Astrocytes are thought to be responsible for providing nutritional support to the axon bundles by facilitating diffusion of nutrients from the LC beam capillaries to the axons (Anderson, 1969). As ONH astrocyte footplates have only been observed attaching to LC beams, it is thought that nutrients have to first diffuse through the LC beam ECM before reaching astrocyte foot plates (Anderson, 1969; Yang et al., 2017). Astrocytes also provide neurotrophic support, regulate ionic and neurochemical homeostasis, and assist in remodeling the ECM (Alqawlaq et al., 2018; Hernandez et al., 2008). Lastly, they have a unique phagocytic role in which they phagocytose discarded

RGC mitochondria in a process called transmitophagy, which is critical for healthy RGC functioning (Bihlmeyer et al., 2014; Nguyen et al., 2011).

In summary, the eye is a highly sophisticated organ for sensing and processing visual information. Particularly at the ONH, many tissues of varying functions, sizes, and compositions intimately interact, making it a difficult but fascinating region to study. Also intricate is the homeostatic environment of the ONH, which is maintained by the complementary actions of several different cell types, and the main purpose of which is to provide optimal conditions for the RGC axons. As will be discussed in the next section, this has implications for glaucoma pathophysiology.

### 2.3 Pathophysiology of the Optic Nerve Head in Glaucoma

It is well-accepted that biomechanics are important in glaucoma and that biomechanical insult, namely increased mechanical stress and strain, to the ONH is a risk factor for RGC death in glaucoma (Burgoyne, 2011). It is known that RGC death in glaucoma occurs through apoptosis and that this pathway is likely initiated due to the disruption of several aspects of RGC homeostasis (Alqawlaq et al., 2018; Quigley, 1999; Quigley et al., 1995; Stowell et al., 2017; Yang et al., 2017). However, the precise ways in which homeostasis is disrupted, the order of and relationships between different damaging events, and exactly how biomechanical factors influence some or all glaucomatous events are not known.

In this section, I will first describe the clinical signs of glaucoma. I will then move on to describe the remodeling changes that occur in the ONH followed by changes in cellular behavior. Finally, I will give a summary of the factors that likely lead to RGC death.

### 2.3.1 Clinical Markers

Glaucoma is difficult to define and sometimes difficult to diagnose. Although abnormal characteristics, such as higher-than-normal IOP, can flag a patient as being at risk for glaucoma, the disease cannot be truly diagnosed without observing ONH changes over time (Weinreb et al., 2014). A primary marker of glaucoma is the posterior bowing and thinning of the LC and thinning of the prelaminar neural tissue and RNFL. This is manifested clinically as “cupping” or “excavation” of the ONH, which can be quantified by the “cup to disc ratio”. The cup can be seen as a light-colored oval at the ONH while the disc is a dark oval-shaped ring surrounding it. As cupping occurs, the cup diameter increases, and the disc thins. The posterior bulging of the LC is intuitive when thinking about what might happen to ONH tissues due to IOP elevation, but interestingly, this same effect is seen in normal tension glaucoma (Burgoyne, 2015; Li et al., 2016). This reveals that different combinations of ONH structural factors and material properties can lead to an ONH that is vulnerable to mechanical insult even at relatively low levels of IOP. The converse is also true: some individuals live with relatively high IOP, but do not develop glaucoma (Quigley, 2005).

The most telling marker of glaucoma besides cupping is progressive vision loss. As glaucoma progresses, RGC axons are lost to apoptosis (Quigley et al., 1982, 1995; Quigley & Addicks, 1980), an energy-dependent form of cell death, resulting in a “progressing” visual field that typically shrinks towards a central island of vision before complete blindness occurs. As noted, vision loss, and even signs like cupping, do not manifest until damage is well underway. This is extremely unfortunate because vision loss in glaucoma is essentially irreversible, and it is possible that the changes occurring build on each other, making the eye more susceptible to further damage the longer they remain unchecked (Alqawlaq et al., 2018; Yang et al., 2017). A better understanding of glaucoma

biomechanics could allow identification of at-risk or glaucomatous patients before these other signs occur. In addition, therapies that aim to alter biomechanical properties could be used in tandem with the current IOP-lowering methods to produce an additive, or possibly synergistic, effect on disease progression.

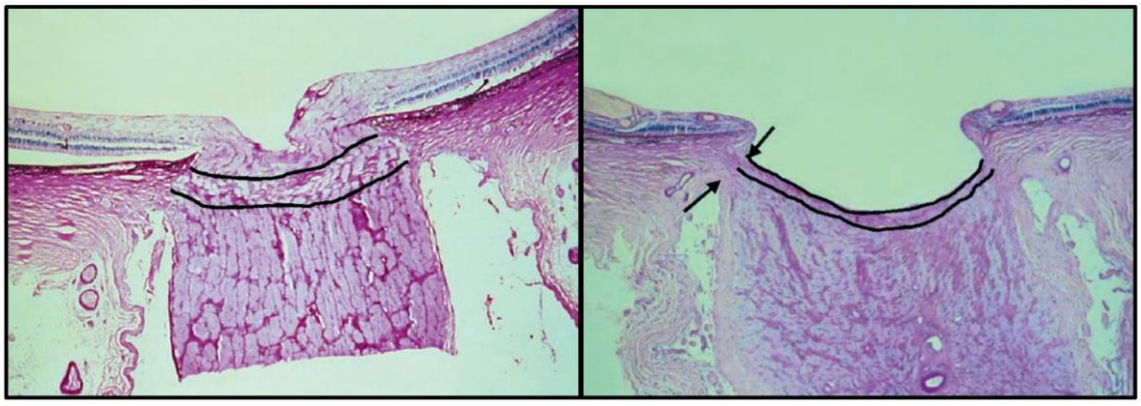

**Figure 3. Histologic sections through a normal (left) and glaucomatous (right) human ONH from (Jonas, 2003). The interior of the eye is shown in the upper part of the figure, and the boundaries of the LC are outlined in black. Cupping, thinning of the prelaminar neural tissue, and bowing of the LC is observed in the glaucomatous ONH.**

### 2.3.2 Remodeling

Since remodeling of structural tissues in the body is usually the result of mechanical stimuli, the remodeling changes that occur in glaucoma are consistent with the involvement of biomechanics in the disease. It is well-known that changes to the ECM occur in the LC and peripapillary sclera (sclera immediately surrounding the optic nerve) (Hernandez et al., 1990; Pena et al., 2001; Quigley et al., 1991, 1991), and for some time, morphological changes in human and monkey glaucoma have been documented (Bellezza et al., 2003; Jonas, 2003; Quigley et al., 1983). However, over the last decade, a technique called 3D histomorphometry developed by Drs. Claude Burgoyne and Crawford Downs has made more in-depth characterization of ONH anatomy possible

(Burgoyne et al., 2004). Combined with optical coherence tomography (OCT) imaging, this technique was used in a series of studies on the monkey experimental glaucoma model to precisely characterize ONH structural changes from early to end stage glaucoma (Burgoyne et al., 2004; Cull et al., 2012; Downs et al., 2007; Fortune et al., 2016, 2016; Gardiner et al., 2012; Ing et al., 2016; Ivers et al., 2016; Lockwood et al., 2015; Reynaud et al., 2016; Roberts et al., 2009, 2010; Strouthidis et al., 2011, 2011, 2010; Yang et al., 2007, 2009, 2007, 2009, 2017, 2011, 2011). They described five major changes: posterior deformation and bowing of the LC, scleral canal expansion, posterior migration of the LC, a thickening of the LC in early disease stages followed by a late thinning of the LC, and posterior bowing of the peripapillary sclera. With regards to the LC migration, Roberts et al. postulated that the LC recruits retrolaminar septa, connective tissue strands that run through the optic nerve, as the LC migrates (Roberts et al., 2009).

### 2.3.3 Cellular Responses in Glaucoma

#### 2.3.3.1 Retinal Ganglion Cells

Past research indicates that axonal transport of neurotrophic factors, especially BDNF, is a key RGC function that is disrupted in glaucoma and results in apoptosis (Moons et al., 2015; Pease et al., 2000; Quigley et al., 2000). This blockage of transport occurs at the level of the ONH, which, along with the ONH remodeling changes, indicates that the ONH is a primary site of damage (Quigley & Addicks, 1981; Quigley & Anderson, 1976). It is a common hypothesis in the field that regardless of the causes preceding it, failure to accomplish retrograde transport is a common step before RGC apoptosis occurs (Morrison et al., 2011).

#### 2.3.3.2 Astrocytes

Astrocytes play a major role in glaucoma, and in fact, they begin to display "activated" behavior characteristic of glaucomatous damage before the death of RGCs occurs (Sun et al., 2013). One such behavior is the formation of a "glial scar", in which astrocytes, along with microglia, oligodendrocytes, and scleral fibroblasts, increase ECM production, forming connective tissue in place of the damaged axons (Hernandez, 2000). In addition to changes in protein expression (Hernandez et al., 2008), activated astrocytes will withdraw and reorient their processes. In rodent models, they reorient their processes from perpendicular to parallel to the nerve axis in response to IOP elevation (Sun et al., 2013; Tehrani et al., 2016, 2014). Interestingly, astrocytes will revert to normal organization if IOP is returned to normal after a short elevation period.

It is important to note that astrocytes are mechanosensitive, and the behavior astrocytes exhibit in glaucoma is consistent with observations of cultured astrocytes activated by mechanical stimuli. Specifically, when exposed to dynamic strain in 3D culture, astrocytes have been shown to reorient their processes perpendicular to the direction of stretch and upregulate MMP activity (Mulvihill et al., 2018).

#### 2.3.3.3 Microglia, Oligodendrocytes, and Invading Monocytes/Macrophages

Microglia also play a role in RGC damage (Bosco et al., 2015). Like astrocytes, these cells become activated in a glaucomatous ONH. When activated, they increase production of proinflammatory chemokines, reactive oxygen species (ROS), matrix metalloproteinases, and a variety of neurotrophic factors (Yuan & Neufeld, 2000). They also increase phagocytic activity and, along with oligodendrocytes, contribute to glial scar formation (Hernandez, 2000).

In severely damaged ONHs of experimental glaucoma models, invading monocytes/macrophages have been observed in the optic nerve. Their specific role in the disease is yet to be discovered, and it is not understood whether they add to the likelihood of RGC apoptosis or if their presence is simply indicative of inflammatory conditions (Alqawlaq et al., 2018; Howell et al., 2012; Johnson et al., 2014, 2011).

### 2.3.4 Underlying Causes of RGC Death

Although the precise etiology of RGC apoptosis in glaucoma is not yet understood, the field has described an array of mechanisms that are likely involved (Alqawlaq et al., 2018; Burgoyne, 2011; Yang et al., 2017).

#### 2.3.4.1 Direct Mechanical Insult

Direct mechanical insult in the form of shearing or compression of RGC axons may cause the blockage in axonal transport seen at the ONH (Balaratnasingam et al., 2008). In this scenario, particularly weak areas of a given LC or a peripapillary sclera would put nearby RGC axons at high risk of damage after elevated IOP. An increase in IOP also results in an increase in the translaminar pressure difference, and thus a steeper translaminar pressure gradient. This likely requires the RGCs to expend more energy for retrograde transport and may cause or contribute to the ONH axonal transport blockage (Band et al., 2009; Yang et al., 2014, 2017).

#### 2.3.4.2 Inhibition of Blood Supply

Vascular changes in the ONH are associated with glaucoma, and many in the field have hypothesized that they are the primary cause of RGC death (Cull et al., 2013; Leske, 2009; Liang et al., 2009; Wang et al., 2014). For example, increased strain experienced by the LC and peripapillary sclera may compress capillaries in those tissues, slowing the

supply of blood to RGC bundles (Burgoyne, 2011). There is also evidence that the lack of blood flow is a secondary effect of decreased autoregulation capacity in the ONH, the cause of which is debated (Schmidl et al., 2011; Werkmeister et al., 2012).

#### 2.3.4.3 Direct Effects of Remodeling

In addition to biomechanical effects, the remodeling changes to the LC may have a direct impact on RGC homeostasis. Early thickening of the LC may make it more difficult for diffusion to occur across LC beams, leaving the RGCs vulnerable to nutritional deficits. Also, the support activities of oligodendrocytes and microglia may become more difficult due to the posterior migration and septal recruitment of the LC (Yang et al., 2017). A lack of myelin upkeep could result in higher energy demands on RGCs, and hindrance of microglia activity may leave them more vulnerable to pro-apoptotic factors such as reactive oxygen species (Alqawlaq et al., 2018).

#### 2.3.4.4 Activation of Glial Support Cells

The previously discussed behavior of an activated astrocyte may make it less able to perform critical support functions for the RGC axons (Alqawlaq et al., 2018). Notably, retraction and reorientation of their processes likely prevents them from facilitating diffusion from capillaries to RGCs. In addition, their increase in ECM production may leave less energy for essential phagocytic roles like transmitophagy, again leaving the RGCs exposed to energy deficits and mitochondrial stress. Activated astrocytes may also push RGCs toward apoptosis by changing their usual buffering behavior of neurochemicals and producing proinflammatory cytokines.

Activated microglia are also involved in the events leading to RGC death. Recently it has been shown that microglia contribute to RGC death in a mouse model of glaucoma,

(Howell et al., 2012). This is likely due to the increase in production of proinflammatory chemokines and reactive oxygen species.

In summary, glaucoma is a debilitating disease that can be diagnosed and treated by physicians, but the state of clinical care is imperfect. Earlier diagnosis and more effective or complementary treatment options are both needed. However, the glaucomatous process is difficult to understand. A series of remodeling changes and cellular responses have been documented, but it is still not perfectly clear how the two influence each other. It is a prevalent hypothesis in the field that biomechanics are involved, directly or indirectly, in all of the events and processes that promote glaucomatous damage (Burgoyne, 2011). However, although many processes, particularly at the cellular level, have been suggested, the relationships between them are not well understood, and some of them have not yet been confirmed. A more sophisticated understanding of ONH biomechanics is a necessary step for answering open questions about glaucoma pathophysiology.

## 2.4 Optic Nerve Head Biomechanics

Since an overwhelming body of evidence strongly indicates that mechanical stress and/or strain in the ONH influence glaucoma, there is strong motivation to characterize ONH biomechanical behavior, including the precise patterns of stress and strain that the ONH experiences at different levels of IOP. This is difficult because individual-to-individual variations in anatomy and material properties are enough to produce substantially different stress and strain patterns. Even without this variation, the ONH is a very complicated system, since many different tissues with complicated morphologies all interact in the same compact and difficult-to-access area. In addition, all these tissues respond to

mechanical stress in a nonlinear fashion, and the connective tissues like the sclera and LC are anisotropic.

In this section, I will give a review of what we know about the material properties of each tissue relevant to ONH biomechanics, focusing on the sclera and LC, and the studies that brought us that information. I will then summarize previous ONH modeling studies and state-of-the-art techniques that have surfaced in the last several years.

### 2.4.1 The Loading Environment of the ONH

The eye can be thought of as a pressure vessel, with the ONH being the weak point in an otherwise tough corneoscleral shell. As IOP increases, loads are transferred from the sclera to the lamina cribrosa, and the laminar beams further transfer stress and strain to RGC axon bundles and other resident cells in complex patterns. The prelaminar neural tissue and lamina also directly resist IOP acting on their anterior surfaces. From the posterior side, cerebrospinal fluid pressure (CSFp) is experienced by the pia mater and transferred to the optic nerve and to the LC in the form of retrolaminar tissue pressure (RLTP), which closely follows CSFp (Morgan et al., 1998). The difference between IOP and RLTP can result in increased LC bowing (García-Montesinos et al., 2017; Yan et al., 1994). However, the effect of hoop stress transferred to the LC from the sclera, pulling the LC taut, can be much greater than effects of IOP acting directly on the prelaminar neural tissues. Finally, blood pressure exists within the central retinal vessels, but a recent modeling study showed that its effect on the ONH is minimal compared to that of IOP and CSFp (Hua et al., 2018).

2.4.1.1 IOP

IOP is important to the functioning of the eye as maintaining a precise shape is crucial for the eye's optical properties. The mean value of IOP over a time course of minutes is approximately 15 mmHg for a human eye during the day (Mosaed et al., 2005). The mean IOP value follows a circadian rhythm throughout the day, with highest values at night and lowest values at midday. It is important to note that this fluctuation might have implications for glaucoma. In rats it has been shown that eyes with a seemingly normal IOP reading during the day can experience higher than normal pressures at night, resulting in RGC loss (Jia et al., 2000).

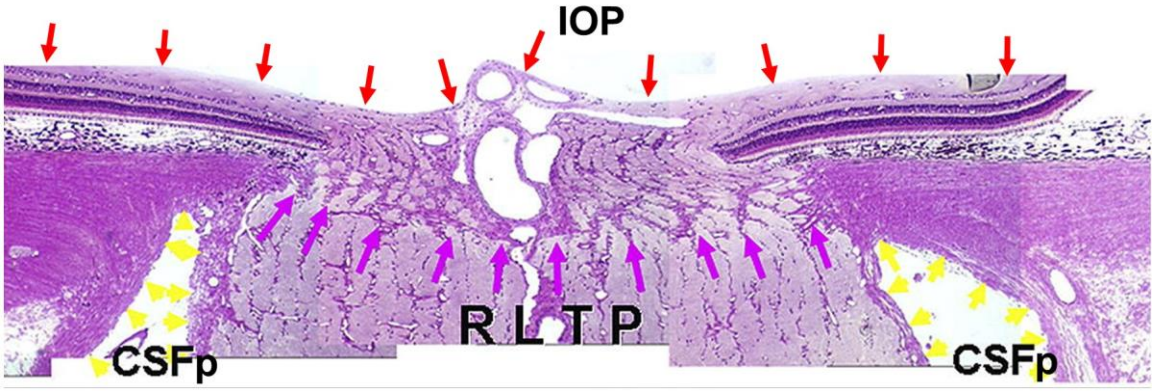


**Figure 4. Histologic section through a monkey ONH with the main pressure loads indicated. Abbreviations: intraocular pressure (IOP), cerebrospinal fluid pressure (CSFp), retrolaminar tissue pressure (RLTP). Modified from (Burgoyne, 2011).**

However, the instantaneous value of IOP varies constantly and can undergo dramatic increases due to events such as blinking (~ 10 mmHg), looking sideways (~ 10 mmHg), and lid squeezing/eye rubbing (~ 80 mmHg) (Campbell et al., 2014; Coleman & Trokel, 1969). In addition, there is a period fluctuation of 2-4 mmHg called the ocular pulse, due to cardiac cycle-induced blood volume changes in the choroid. Although they may play a role in glaucoma progression (Dastiridou et al., 2009; Vulsteke et al., 2008), it is still

not well known how these second-to-second fluctuations and spikes in IOP affect a person's risk. However, the recent development of real time IOP telemetry monitoring in monkeys and rats has provided a way to study how these transient fluctuations affect glaucoma risk and progression (Bello & Passaglia, 2017; Crawford Downs et al., 2011).

#### 2.4.1.2 CSFp and RLTP

As mentioned, the pia mater is surrounded by CSF and is thus directly acted upon by CSFp. The magnitude of CSFp at the posterior eye is determined by the balance of production and outflow of CSFp and is influenced by the person's posture. When standing, CSFp at the ONH will be lower than when the person is lying down, with typical values of 0 mmHg and 10 mmHg, respectively (Feola et al., 2016). RLTP results from CSFp acting on the pia mater and optic nerve. As shown by a study on dogs, it closely follows CSFp (Morgan et al., 1998). As discussed, the difference between IOP and RLTP has implications for LC bowing and RGC axonal transport. In fact, there is evidence to support the idea that low CSFp contributes to glaucoma damage or risk (Berdahl et al., 2008, 2008; Ren et al., 2010; Yang et al., 2014).

### 2.4.2 Biomechanics of Relevant Tissues and Implications for Glaucoma

Although stress and strain in the ONH involves interactions of several tissues, evidence suggests that the LC and sclera are the most influential. Specifically, in several previous modeling studies, the material properties of the sclera and LC were shown to be very important, with scleral stiffness actually being the most influential in some studies. (Hua et al., 2018; Sigal et al., 2009, 2005). Therefore, the focus of this section will be on these two tissues.

Specifically, here we focus on relevant macro and microstructural features, experimental evaluation of deformation/strain, and experimental characterization of tissue properties (including the use of inverse FE modeling). Although it may be alluded to here, most of the ONH modeling work will be discussed in Section 2.4.3.

#### 2.4.2.1 The Lamina Cribrosa

##### *2.4.2.1.1 Macrostructure*

As mentioned, the LC is a connective tissue structure that spans the scleral canal. The thickness of the LC in the human eye is usually on the order of 450 μm but can vary significantly (Jonas, 2003; Kotecha et al., 2006), and its bowed shape can take a variety of forms, ranging from trough-like to saddle-like (Thakku et al., 2015). Since cupping is a primary sign of glaucoma but depends on subjective assessment by clinicians, significant research effort has gone into defining LC morphology metrics that can be objectively assessed (Tan et al., 2018). Important characteristics that have been associated with glaucoma include lower LC thickness (Chung et al., 2016; Hao et al., 2019; Kim et al., 2016), larger LC depth (Hao et al., 2019; Kim et al., 2018, 2015; Lee et al., 2017), higher LC curvature (Kim et al., 2016; Lee et al., 2017), and particular characteristics of the 3D shape of the anterior LC surface (Thakku et al., 2015). Some of these measures have serious flaws for clinical application. For example, it is not clear if LC thickness can be reliably assessed because the current standard imaging technique, OCT, usually cannot resolve the posterior lamina surface. LCD is flawed because it requires a reference plane such as BM opening, which is affected by changing factors such as choroidal thickness. However, LC curvature and shape have high potential for getting around these issues, as both are assessed at the anterior LC surface and neither require a reference plane. For example, Thakku et al. developed the LC global shape index (LC-GSI), which can describe

a variety of surface shapes with a single number ranging from -1 (spherical cup) to +1 (spherical cap), and showed that it is correlated with two factors related to glaucoma.

*2.4.2.1.2 Constituents and Microstructure*

The main components of the LC extracellular matrix beams are collagen fibers, elastin fibers, basement membranes, and proteoglycans (Hernandez et al., 1987). Collagen types I and III form fibers throughout the LC beams (Albon et al., 1995; Hernandez et al., 1987), and as shown by scanning electron microscopy, elastin fibers are numerous in the beams. At the interface where the LC beams insert into the peripapillary sclera, there is a beautiful organization of elastin in which a densely populated ring of elastin fibers surrounds the scleral canal with fibers extending from this ring and into the LC beams at a nearly perpendicular angle (Quigley et al., 1991).

The microstructural characteristics of collagen fibers in the LC have been quantified in recent studies utilizing polarized light microscopy (Jan et al., 2015). Collagen fibers have varying levels of crimp throughout the LC, and when the LC is stretched, the fibers are recruited (bear load), proceeding from those that are less crimped to more crimped (Jan & Sigal, 2018). In addition, thick beams tend to have more highly crimped fibers than thin beams (Brazile et al., 2018), meaning that the thin beams will appear stiffer than thick beams at lower levels of stretch.

The LC's organization of beams and pores also has an important impact on its mechanical behavior. It is highly complex, and can be thought of as a web-like or sponge-like structure in which pores are interconnected and have tortuous paths (Lockwood et al., 2015; Wang et al., 2018). Early methods for characterizing LC organization included imaging modalities such as electron microscopy or confocal scanning laser ophthalmoscopy that could view the surface of or projection through the LC (Akagi et al.,

2012; Chauhan et al., 2013; Quigley et al., 1983). More promising 3D methods have used registered stacks of histological or OCT slices to build 3D renderings of the LC beams and pores (Girkin et al., 2017; Reynaud et al., 2016; Wang et al., 2013).

Throughout these studies, researchers have searched for relevant patterns of beam and pore architecture in monkey and human eyes. The main points of agreement are that there tends to be a larger pore diameter and smaller beam width in the peripheral compared to central LC, and in the superior and inferior quadrants compared to the temporal and nasal quadrants (Jonas et al., 1991; Lockwood et al., 2015; Nadler et al., 2014; Quigley & Addicks, 1981; Wang et al., 2016). Interestingly, a preferential pattern of damage in the superior and inferior poles of the LC has been reported in both monkey and human glaucoma, suggesting a link between the larger pore size and higher vulnerability to axonal damage (Dandona, 1990; Quigley, 1999; Quigley & Addicks, 1981; Quigley et al., 1982). However, a recent, ongoing study on monkeys has yet to confirm this pattern (Yang et al., 2017).

*2.4.2.1.3 Mechanical Behavior*

The LC is a tissue that is difficult to access and handle. Uniaxial testing of scleral strips containing the LC has been used to estimate the LC elastic modulus to be 2–3 MPa (Spoerl et al., 2005). Recently, an application of the virtual fields method paired with OCT has shown promise for evaluating stiffness of the LC complex in vivo, but so far, it has only been applied to a single eye in a validation study (Zhang et al., 2017).

Although material property characterization has been difficult, a great deal has been learned about LC deformation and strain due to elevated IOP. Before high quality in situ imaging was available, early studies utilized histology after perfusion fixation of contralateral eyes at different levels of pressure to determine how the LC deforms in

human and monkey eyes (Bellezza et al., 2003; Yan et al., 1994; Yang et al., 2009, 2011). Surprisingly, they found that the lamina displaced posteriorly in some subjects and anteriorly in others. In addition, there was evidence of high shearing at the periphery of the LC, where most of the posterior displacement took place. They also often saw expansion of the scleral canal, and posited that the cases of anterior LC displacement were due to the sclera pulling the LC taut. Modeling studies have also looked into this relationship and will be discussed in Section 2.4.3.

Later studies used non-invasive imaging techniques including OCT, second harmonic-generation imaging, and micro-computed tomography (micro-CT) (Agoumi et al., 2011; Beotra et al., 2018; Coudrillier et al., 2016; Midgett et al., 2017; Quigley et al., 2017; Sigal et al., 2014). Sigal et al. observed that the local patterns of strain were highly complicated and regions of highest stretch, compression, and shear did not colocalize (Sigal et al., 2014). Two later studies using digital volume correlation found that compressive strain was the strain mode with highest magnitude, LCs from older eyes have lower strains, and shearing is largest in the periphery (Coudrillier et al., 2016; Midgett et al., 2017). Finally, in an exciting development, Boetra et al. were able to use OCT scans to calculate in vivo 3D strains in human LCs due to IOP elevation which has implications for mapping strain and LC properties of human eyes in vivo moving forward (Beotra et al., 2018).

These experimental studies on the LC emphasized the complexity of deformation and strain fields at the beam and pore level. Although assessing deformation and strain of the LC as a whole or as a continuum is useful, assessing strains at the level of RGC axons is likely the level of specificity needed to fully understand biomechanically-mediated mechanisms of RGC damage. The combination of highly specific strain mapping with

microscale LC models will be an especially powerful research tool. Development of these models has begun and will be discussed below.

#### 2.4.2.2 The Sclera

##### *2.4.2.2.1 Constituents and Structure*

Although seemingly simple at first glance, the sclera is a surprisingly complex and heterogeneous tissue, even across its thickness. The thickness of the sclera varies along the meridional direction from approximately 600 µm at the limbus (connection point with the cornea), to 450 µm at the equator, to 1000 µm at the posterior pole (Norman et al., 2010; Vurgese et al., 2012). Near the ONH, just nasal to the posterior pole, the peripapillary sclera has a thickness of about 400 µm.

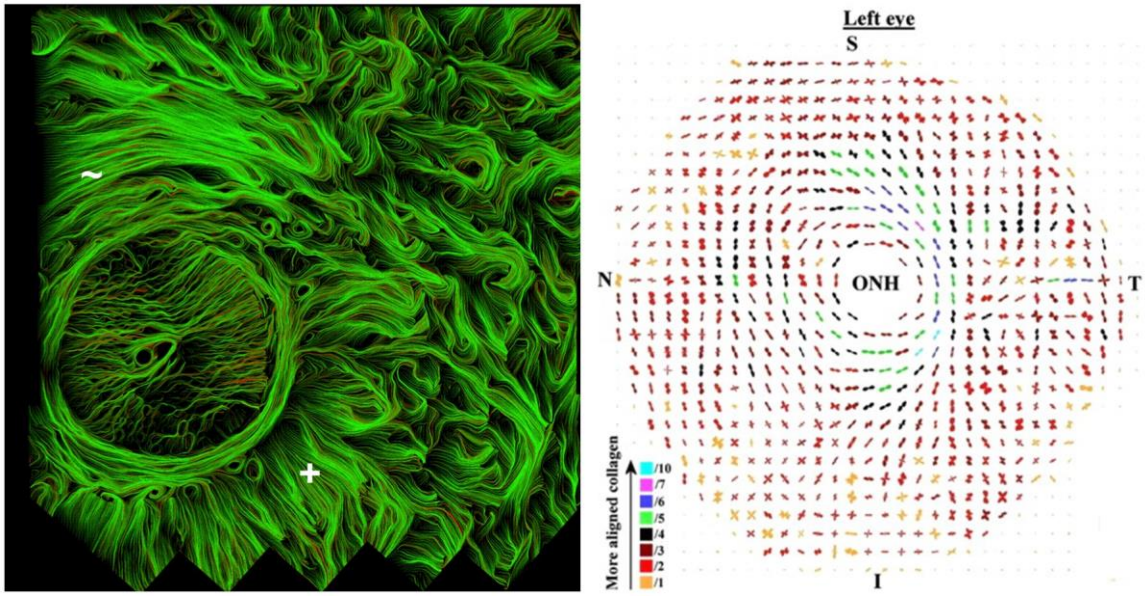


**Figure 5. Left: Collagen fiber traces in and near the ONH of a human eye from (Gogola et al., 2018). Traces were produced from polarized light microscopy images. Fibers within the LC beams as well as circumferential (~) and meridional (+) fibers within the peripapillary sclera are visible. Interweaving fibers with low alignment are visible in the right side of the image. Note that the plane of view crosses multiple layers through the thickness of the sclera. Right: Fiber alignment map produced from wide angle X-ray scattering from (Pijanka et al., 2012). Map shows highly aligned circumferential fibers near the ONH but more randomly aligned fibers elsewhere. Colors indicate degree of alignment and small arrows indicate the two primary axes of alignment.**

The sclera is quite robust, being made up of an ECM of proteoglycans reinforced by elastin and collagen fibers, and containing about 50% collagen by weight (Keeley et al., 1984). Around 90% of the collagen fibers are type I (Summers Rada et al., 2006), but types I, III, V, and VI are all present in smaller quantities (Watson & Young, 2004). Like its thickness, sclera microstructure is also heterogeneous, causing it to have anisotropic properties that vary from location to location due to the arrangement of collagen fibers. These fibers are organized in several layers throughout the thickness of the sclera, with each layer having its own preferred fiber direction that lies within a plane locally tangent to the scleral surface (Komai & Ushiki, 1991; Summers Rada et al., 2006; Young, 1985).

Over the years, the primary fiber direction and degree of fiber alignment have been mapped in the sclera of several animal species and in humans using wide-angle X-ray scattering, small-angle light scattering, and inverse modeling (Coudrillier et al., 2013, 2015, 2015, 2015; Danford et al., 2013; Girard et al., 2011, 2009, 2011, 2009; Grytz & Meschke, 2010; Grytz et al., 2011; Grytz & Siegwart, 2015; Oxlund & Andreassen, 1980; Pijanka et al., 2012, 2014, 2015). These studies consistently found that in the peripapillary sclera, collagen fibers are highly aligned in the circumferential direction, forming a ring around the scleral canal. However, both direction and degree of alignment are highly variable in most other locations throughout the sclera, and few studies have comprehensively described how these parameters vary across the scleral thickness (Pijanka et al., 2015). In addition, Coudrillier et al. found that aged eyes have lower scleral anisotropy than younger eyes.

As with the LC, the recent application of polarized light microscopy has provided more detailed information about regional and through-thickness scleral fiber organization, as well as information on fiber crimping (Gogola et al., 2018; Jan et al., 2015, 2017, 2017; Jan & Sigal, 2018; Sigal et al., 2018). These studies confirmed the consistent existence of the ring of collagen fibers around the scleral canal, found that meridional fibers extend from the circumferential ring into the peripheral sclera in the inner most layers of scleral thickness, and observed collections of interweaving fibers with low alignment throughout the scleral thickness in many regions. Quantifying collagen crimp, Jan et al. showed that groupings of fibers with varying levels of crimp reside throughout the sclera. As pressure increases and the sclera stretches, more and more groups of fibers are “uncrimped” or “activated”, contributing to the highly nonlinear response of the sclera to load (Jan & Sigal, 2018).

Lastly, after performing polarized light microscopy in several studies, Voorhees et al. proposed that collagen fibers in the sclera, rather than being organized in groups of relatively short, interconnecting fibers, pass all the way from one side of the limbus to the other, with many passing directly adjacent and tangential to the scleral canal (2018). With analytical models, they showed that this could be more effective at reducing strain in the ONH than the more traditional understanding of fiber organization.

*2.4.2.2.2 Mechanical Behavior*

There are several ways in which the sclera has been tested for mechanical properties. As expected, uniaxial testing was the first method utilized and has been repeated several times over the years (Avetisov et al., 1983; Chen et al., 2014; Downs et al., 2003; Elsheikh et al., 2010; Friberg & Lace, 1988; Geraghty et al., 2012; Spoerl et al., 2005). There are several key findings from these tests. First, they measured the scleral elastic modulus to be anywhere between 1 MPa and 60 MPa. Second, they showed that the sclera stiffens nonlinearly as it is stretched and that it is viscoelastic. Third, by taking strips of sclera from different regions, they showed that its stiffness properties are heterogeneous throughout, but this is dependent on species. Lastly, they showed that the sclera stiffens with age.

Biaxial testing performed by Elaghi et al. was an improvement on previous studies as it is more similar than uniaxial testing to the mode of loading that the sclera experiences in vivo (Eilaghi et al., 2010). Stiffness constants for an anisotropic Fung model were obtained, showing that there was high variability between subjects. The anisotropy of the tissue was also assessed, and the authors were surprised to find that the overall trend was close to isotropic behavior. However, in this study, scleral samples were taken from regions outside the peripapillary sclera, which were shown to have mainly low degree of

fiber alignment in the imaging studies discussed above, and inflation testing studies discussed below.

Inflation testing with surface tracking methods, namely electronic speckle pattern interferometry (ESPI) or digital image correlation (DIC), allowed the entire sclera to be tested under nearly in vivo conditions, rather than interrogating dissected samples of scleral tissue. These studies showed that the strain and displacement fields at the surface of the sclera are complex, as expected. Coupled with inverse FE modeling, each research group fit displacement data with several different material models that all incorporated proteoglycan matrix stiffness, fiber stiffness, fiber direction, and degree of fiber alignment. Girard et al. performed a series of these tests on monkey eyes (Girard et al., 2009, 2009, 2011, 2009), and Coudrillier et al. studied human eyes (Coudrillier et al., 2013, 2016, 2015, 2015, 2015, 2012). In addition to fiber alignment data, both groups found that aged and glaucomatous eyes are stiffer than young or normal eyes. Coudrillier et al. also used forward modeling simulations to show that anisotropy in the peripapillary sclera has a high influence on ONH deformation.

A third fiber-reinforced model that accounted for collagen crimp was used by Grytz et al. in inverse FEM on human eyes (Grytz et al., 2014, 2014). Their unique model allowed them to estimate strains at the fiber level, the collagen network level, and the macroscopic level. They found that the collagen strains were the same in the peripapillary and peripheral sclera even though the macroscopic plane strains were different. This interesting finding suggests that scleral remodeling of collagen fibers is driven by the goal of maintaining similar levels of stress and strain at the fiber level.

Interestingly, many studies have shown that the sclera stiffens with age and as a result of changes in glaucoma. However, it is not understood whether scleral stiffening in

glaucoma is an attempt by cells to remodel the sclera to be more resistant to effects of elevated IOP, or if it is an “undesired” effect of the disease process that ultimately results in increased damage to the ONH. In addition, more study is required to better understand how changes in the intricate network of scleral fibers influence the biomechanical response of the ONH.

#### 2.4.2.3 The Pia Mater and Dura Mater

Like the sclera, the pia mater and dura mater are composed of a proteoglycan matrix and have a high density of collagen fibers (Taban et al., 2001). Most studies have looked at sections of tissue around the brain or spinal cord, not near the ONH. However, evidence suggests that these tissues are anisotropic, undergo nonlinear stiffening behavior, and that they are relatively stiff, albeit less stiff than the sclera (Jin et al., 2014; Raykin et al., 2017; Shetye et al., 2014; Wang et al., 2016). The mechanics of these tissues have not been extensively studied, but a sensitivity analysis by Sigal et al. ranked their influence as relatively low on the list of considered factors (Sigal et al., 2005). However, an updated study that included the effects of cerebrospinal fluid pressure ranked the dura as highly influential (Hua et al., 2018). In addition, other modeling work has shown that large eye movements can induce high strains in the ONH (Wang et al., 2017, 2016). The pia and dura mater are more directly involved in the transfer of load to the ONH in this scenario than in that of elevated IOP.

#### 2.4.2.4 The CRA and CRV

Although the CRA and CRV pass directly through the center of the LC and nerve at and near the level of the ONH in humans, not much is known about their properties or how their position and/or mechanical properties influence ONH strains. To our knowledge, there have been no studies directly investigating the properties of the central retinal

vessels. Modeling studies to date have treated them as isotropic tissues that behave in a linear fashion and assumed stiffness values that were found for vessels of similar size in other parts of the body (Feola et al., 2017; Sigal et al., 2004). However, it should be noted that a recent modeling study showed that although central retinal vessel properties do influence ONH response to elevated IOP, the ONH is not highly sensitive to changes in their values (Hua et al., 2018).

#### 2.4.2.5 The Choroid and BM

As mentioned, the choroid is a bed of vascular tissue and BM is a thin membrane with high collagen and elastin content. Although difficult to isolate, there have been some studies investigating the properties of the choroid and BM. When tested as a choroid-BM complex without separating the two, stiffness values were approximately an order of magnitude lower than the sclera (Chen et al., 2014; Friberg & Lace, 1988; Ugarte et al., 2006). Others have tested the tensile modulus of a BM-choroid complex with most of the choroid removed and found values that were similar to the sclera or greater (Chan et al., 2007; Wang et al., 2018).

#### 2.4.2.6 The Retina and Optic Nerve

The neural tissues of the eye, the retina and optic nerve, are the weakest tissues involved in ONH biomechanics. These tissues have much less ECM than others in the eye, with little to no elastin or collagen content (Burgoyne et al., 2004; Jonas, 2003). Difficult to isolate and test due to their fragility, there is not much information available on their mechanical properties. In a few instances, labs have managed to test uniaxial strips of retina and found moduli values approximately two orders of magnitude lower than the sclera (Chen et al., 2010, 2014). As one would expect, sensitivity analyses have ranked optic nerve stiffness as highly influential on optic nerve strains (Sigal et al., 2005), but the

exact material properties of the ONH neural tissue will not be of utmost importance until knowledge in the glaucoma biomechanics field becomes sophisticated enough to predict what strain levels are pathogenic for RGCs. As will be discussed, models are getting more and more sophisticated, so the importance of understanding this tissue's precise biomechanical behavior is growing.

In summary, a number of tissues with varying mechanical properties in the ONH have impacts on its biomechanical environment. The LC is particularly important and difficult to understand. Both the macro and microstructural characteristics of the LC influence its mechanical behavior and have implications for glaucoma susceptibility. Although difficult, accurately taking into account the organization of LC beams and of collagen and elastin fibers within the beams is important for improving understanding of ONH biomechanics. As evidenced by the experimental studies on LC deformation, the localized patterns of stress and strain are highly variable, so this microstructural information will be necessary to understand the levels and modes of stress and strain that different cell types and micro-structures (such as capillaries) in the ONH are exposed to. The sclera is also important but complex. Although much has been learned about the networks of fibers through the multilayered sclera and how their organization influences scleral behavior, more work is required to develop a complete understanding, especially if therapies targeting scleral biomechanics are to be developed. This is made more evident by the fact that new theories about the overarching pattern of scleral fibers are still being put forth (Voorhees et al., 2018). Lastly, other tissues within the ONH region will also require more careful characterization moving forward as ONH modeling efforts become more sophisticated (see Section 2.4.3).

### 2.4.3 ONH Modeling Studies

There have been a range of ONH modeling studies to date, some focusing on LC or sclera and others incorporating as many aspects of the ONH as possible. Although there had been previous work on mathematical modeling of the biomechanics in the ONH, the first study to use finite element modeling to compute stress and strain in the LC was Bellezza et al. in 2000. They began with a simple model of the sclera and LC, with linear elastic behavior assigned to both, and showed that even at low levels of IOP, stress in the lamina is significant and is dependent on scleral canal shape and size and peripapillary scleral thickness (Bellezza et al., 2000). Since this initial study, several other labs have utilized finite element models with increasing levels of complexity to describe and learn about the biomechanical environment of the ONH. The purpose of this section is to provide a review of different techniques and levels of complexity used in FE models of the ONH over the years, as well as some of the main conclusions drawn from these studies.

#### 2.4.3.1 Parameterized Models of the ONH Response to IOP

One of the most useful implementations of ONH modeling has been a series of studies that used parameterized ONH models to investigate the ONH response to elevated IOP, the first of which was developed by Sigal et al. (2004). They made improvements to Bellezza's initial modeling attempts by including the retina, prelaminar and post-laminar neural tissues, the pia mater, and a more realistic peripapillary scleral geometry in an idealized, axisymmetric model of the ONH and posterior eye (Sigal et al., 2004). All tissues were considered incompressible and linearly elastic. This was an extremely powerful model because it used a parameterized geometry to explore a large parameter space and required relatively low computational power while maintaining fidelity to true ONH geometry. The authors showed that mean tensile strains in the LC, 4% to 7.7%, were high

even when representing the LC as a continuum without complex beam architecture, and that strains in the LC were more dependent on scleral properties than LC properties. This second assertion was strengthened in a study which made use of the parameterized ONH model in an extensive sensitivity analysis on variations in anatomical features and material properties that included 505 model variations. Results showed that the most influential factor on ONH biomechanics was scleral stiffness, followed by eye radius, LC stiffness, IOP, and scleral thickness (Sigal et al., 2005). This motivated Norman et al. to more closely investigate the effect of scleral thickness on ONH strains by embedding the generic ONH model into parameterized corneoscleral shells informed by shape and thickness measurements made on human donor eyes (Norman et al., 2011). They found that varying the peripapillary scleral thickness greatly affected peak tensile strains in the LC.

Later, Sigal expanded on these findings by investigating the interactions between parameters, showing again that scleral and LC properties and their interactions were the most influential on ONH biomechanics, but also adding that no one factor had the highest influence on all outcome measures or singlehandedly produced large strains (Sigal, 2009). Along this same vein of thought, two later studies made use of the parameterized ONH model to run hundreds of thousands of model iterations to investigate how ONH response patterns might be distributed in large populations (Sigal et al., 2012; Voorhees et al., 2016). The results were surprising. The first study showed that the majority of ONH responses were confined to a small percentage of the entire response region, meaning that parameters in the ONH interact to deform under IOP in a consistent way (Sigal et al., 2012). The later study showed that atypical ONH features do not usually lead to atypical ONH response and that ONHs with typical response patterns often have one or multiple atypical features. The implication of these interaction studies is that the ONH reacts to IOP in difficult-to-understand and even non-intuitive ways, i.e. that a “weak” ONH is likely not

recognizable based on analysis of a few characteristics. Instead, to truly be able to identify vulnerable ONHs with high certainty, a comprehensive analysis of anatomic features and material properties is required.

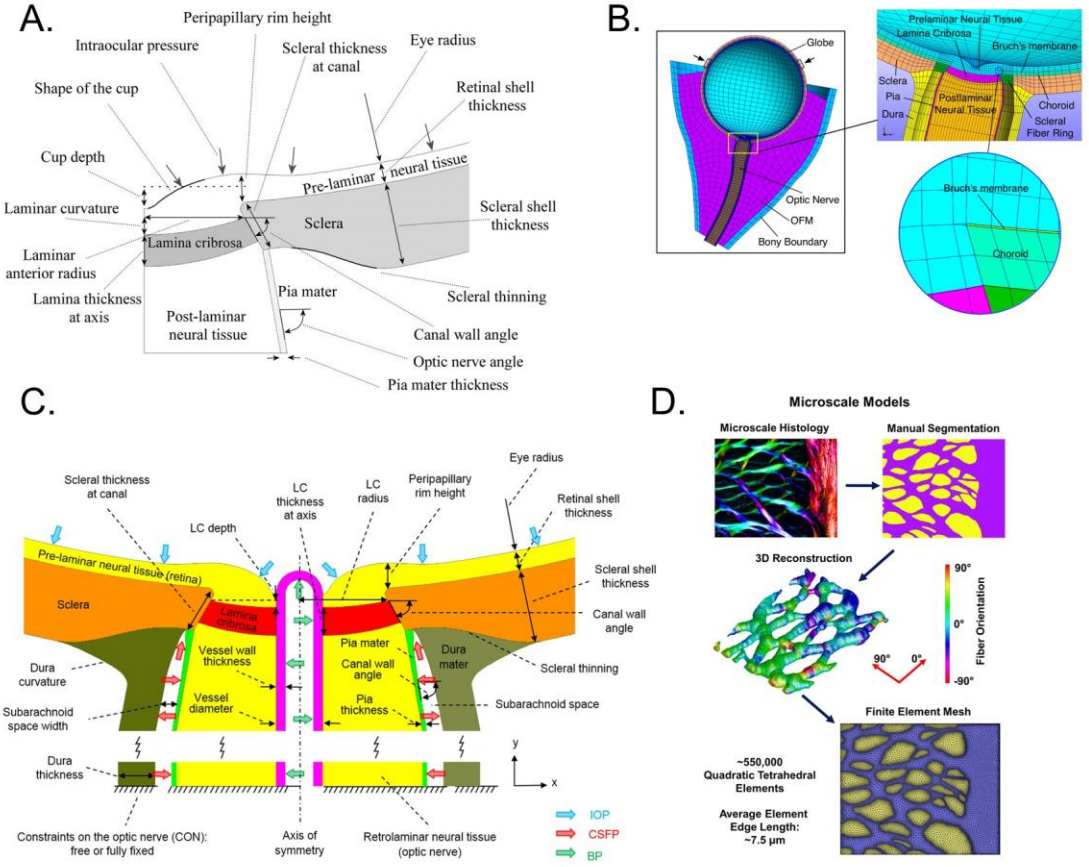


**Figure 6. Examples of ONH finite element models. A.: The first parameterized model of the human ONH from (Sigal et al., 2005) with geometric parameters indicated. B.: Human eye model used for eye movement studies from (Wang et al., 2017). C.: Updated version of the parameterized ONH model from (Hua et al., 2018) with geometric parameters, loads, and optic nerve boundary conditions indicated. D.: The process for building subject-specific microscale models of the LC beams and neural tissue from (Voorhees et al., 2017).**

One other recent effort is of note. Recently, Hua et al. published a follow up study to the 2005 sensitivity analysis (Hua et al., 2018). The model geometry was updated to include the dura mater and central retinal vessels, and a longer optic nerve and sheath,

and model conditions were updated to include blood pressure, CSFp, and constraints on the posterior end of the optic nerve. The authors found an updated list of the six most influential factors on ONH biomechanical response, placing IOP and nerve constraints as the top two factors, followed by the sclera modulus, LC modulus, dura mater modulus, and CSFp. The study also found that changes in IOP and CSFp produced very different effects on the system (not simply opposite effects), meaning that the translaminar pressure difference may not be a good metric for inferring ONH biomechanical response in vivo. Note that this assessment excludes direct effects on RGC axonal transport.

#### 2.4.3.2 Individual-Specific Models of the ONH Response to IOP

Individual-specific modeling is a valuable complement to parametric studies. Specifically, it can identify ONH responses that only manifest when a highly specific combination of parameters exists, including anatomical features than cannot be represented in generic models. Most individual-specific modeling to date has focused on matching model geometry with true anatomy, since accurate and localized material properties are much more difficult to obtain.

In addition to the generic model, Sigal and colleagues built ONH models with fully individual-specific geometry and added the quantification of compressive and shear strain to their analysis (Sigal et al., 2009, 2007, 2009). The new geometry resulted in less symmetric patterns of strain than the generic model, but differences in strain magnitudes and patterns were similar between different eyes. However, changes in material properties produced large variations in strain magnitudes, showing that material properties may be more important than anatomical differences for explaining susceptibility to elevated IOP. In addition, the authors found that the most common mode of strain was compressive, with median values around 7% to 9% in the LC. No other studies to date have built fully

individual-specific model geometries of human ONHs with the full list of tissues seen in the generic models, and no studies have incorporated individual-specific material properties in these models.

#### 2.4.3.3 Modeling the Effect of IOP on the Sclera and LC

Motivated by the results of the sensitivity analyses, some studies focused on modelling the sclera and/or LC when exposed to elevated IOP. In one such study which modelled the sclera and LC as linear elastic solids, Sigal et al. used morphing methods to generate an array of models with different LC geometries and scleral thicknesses (Sigal et al., 2010, 2011). They found that in most cases, the scleral canal expanded and pulled the LC taught as expected, but in other cases, especially with a stiff sclera or shallow LC, LC deepening occurred.

Other modeling efforts focused on representing the contribution of the LC's connective tissue beam structure to its mechanical response. Downs et al. used an elegant multiscale modeling approach to compute stress and strains in individual LC beams (Downs et al., 2009). They generated several individual-specific scleral shells and LC models from monkey eyes, assigning orthotropic linear elastic properties to each element in the LC based on connective tissue volume fraction and beam direction data. They projected deformation results to individual-specific sections of LC beam structures, and showed that stress and strain in individual beams were much higher than those predicted in continuum models, an expected but important finding. Roberts et al. continued this work in two follow up studies on normal and EG monkey eyes (Roberts et al., 2010, 2010). They abandoned the multiscale modeling but showed with the microstructure-informed continuum models that strain inversely correlated with connective tissue volume

fraction, strain tended to be highest in the temporal region of the monkey LCs, and the remodeling effects in EG eyes resulted in reduced scleral canal expansion and LC strains.

Recently a similar and more advanced pair of studies was conducted by Voorhees et al. The authors used polarized light microscopy to obtain highly localized fiber density and direction data of sheep eyes and used this data to inform a “meso-scale” continuum model of the peripapillary sclera and LC, and to build microscale models of sections in the LC that precisely adhered to beam and pore geometry (Voorhees et al., 2017). After applying deformation data to the microscale models as boundary conditions, they showed that neural tissue in the pores experienced high strains (7 % to 12 %), pores near the boundary had the highest strains, and material property variations scaled strains up or down but did not change their pattern. In the second study, the authors demonstrated that pore shape and size was predictive of neural tissue strains within them (Voorhees et al., 2017).

Lastly, Coudrillier et al. focused on the effects of scleral anisotropy on LC strains (Coudrillier et al., 2013). First, the authors obtained fiber alignment data from wide-angle X-ray scattering, fiber and matrix stiffness data from inverse finite element modeling, and scleral geometry data, and incorporated this information into fiber-reinforced scleral shell models each with a generic LC represented as a continuum with neo-Hookean properties. By progressively decreasing the level of anisotropy of the sclera in their models, they showed that lowering anisotropy in the mid-posterior sclera had little effect on LC deformation, but changing the peripapillary sclera to be isotropic resulted in large increases in scleral canal expansion and LC stress and strain.

#### 2.4.3.4 Modeling the Effect of non-IOP Loads on the ONH

At least two other groups have added tissues to the original generic model developed by Sigal et al. to study how factors other than IOP affect stress and strain in the ONH. Wang et al. published two studies examining the effects of eye movements using a sophisticated generic eye model. They added the dura mater, extra-orbital fat, and adjacent bony margins to model geometry, and they improved material properties by modeling the sclera and LC as Mooney-Rivlin solids reinforced by collagen fibers and modeling the dura and pia mater as strain-stiffening, isotropic solids. (Wang et al., 2016). Interestingly, they found that common eye movements produced strains in the ONH that were larger than those produced by an IOP of 50 mmHg, and that these strains were reduced with a stiff sclera but increased with a stiff dura mater. Next, the authors added the choroid and BM, represented as linear elastic solids, and added the scleral fiber ring. They found that eye turn movements produced large stress concentrations in the peripapillary sclera (Wang et al., 2017).

Jin et al. further added to this model, including the effects of pulsating blood pressure in arteries and veins that pass through the sclera and choroid, and modelled the choroid as a biphasic solid (Jin et al., 2018). The showed that pulsations expanded the choroid and induced shearing in the ONH neural tissues, and that increasing scleral stiffness resulted in more shear.

Lastly, Feola et al. developed an axisymmetric ONH model to investigate the effects of elevated CSFp during space flight (Feola et al., 2016) and repurposed it to examine the effects of choroidal swelling (Feola et al., 2018). They included the central retinal vessels, dura mater, BM, and choroid, and they also modelled the scleral, pia mater, and dura

mater as fiber-reinforced solids. The study showed that choroidal swelling alone could result in ONH strains at levels experienced by an IOP of 30 mmHg.

In summary, the collection of ONH models produced to date has been an invaluable source of information for the glaucoma field. The sensitivity and interaction studies especially are useful for identifying important ONH characteristics and their effects in ways that would be impossible or impractical to do experimentally. The evolution of model fidelity and resulting development (and even changing of conclusions over the years) shows that it is valuable for researchers to continue adding details and improvements to the current models. A major point of development that needs to occur is the integration of individual-specific material properties and anatomy. As demonstrated by the interaction and individual-specific studies to date, differences in ONH morphology are not enough to explain the range in susceptibility to elevated IOP seen clinically. Lastly, recent additions to the ONH modeling library, such as the eye rotation models, are pushing the field to explore how loads other than IOP could affect ONH biomechanics and the glaucomatous process. It is important for future studies and clinical practice to keep in mind how these other modes of insult might interact with more commonly considered glaucoma risk factors to contribute to the disease process. Taken as a group, these studies demonstrate the importance of modeling in glaucoma biomechanics and show how models can help researchers to gain a better understanding of the ONH biomechanical environment.

## 2.5 The Rat Model of Glaucoma

Rodent models of glaucoma are widely used because they provide several advantages over large animal models (Morrison et al., 2011). They are relatively inexpensive and easy to house and handle, inbred strains provide study subjects with very low genetic variability, a wide array of cell-biology techniques can be utilized on rodents,

and mice can be genetically manipulated and the ability to do so is becoming easier in rats (Meek et al., 2017). Comparing rats vs. mice for usefulness in glaucoma studies, the rat eye is much easier to handle and to perform certain biomechanical tests on due to its larger size. Although several rat glaucoma models have been used in the past that do not focus on the elevation of IOP, only the ocular hypertensive models will be considered here.

### 2.5.1 Methods for Inducing Ocular Hypertension

The goal of ocular hypertensive models is to produce a mild to moderate (to avoid non-glaucomatous injury such as ischemia) IOP elevation in the experimental eye that is sustained over weeks, resulting in glaucomatous damage to the ONH. For example, average IOP in an awake Brown Norway rat is approximately 20 mmHg, and a sustained pressure elevation of 5 mmHg to 10 mmHg is sufficient to produce damage (Jia et al., 2000). There are five main methods for inducing ocular hypertension in rats to mimic primary open angle glaucoma: microbead injection into the anterior chamber, episcleral vein cauterization, laser-induced scarring of aqueous outflow passages, injection of hypertonic saline into episcleral veins, and the relatively new controlled elevation of IOP (CEI) model (Morrison et al., 2016, 2011). However, the cautery model has been shown to be less appropriate than the others because it does not actually obstruct aqueous humor outflow passages as originally thought (Nissirios et al., 2008). Note that the other models except for the CEI model involve obstructing outflow of aqueous humor. The microbead model obstructs flow through the trabecular meshwork by either using aqueous flow or a magnet to deliver injected microbeads into the trabecular meshwork region (Morgan & Tribble, 2015). The laser model involves irradiating the limbal vasculature (vasculature at the transition between sclera and cornea near the trabecular meshwork) to induce scarring, thus blocking aqueous outflow (Morrison et al., 2008). Injecting hypertonic saline into episcleral veins also results in scarring of aqueous outflow passages

(Morrison et al., 1997). Finally, the CEI model involves inserting a needle attached to a fluid reservoir into the anterior chamber of an anesthetized rat and using it to hold IOP at an elevated pressure for 8 hours. Unlike the other methods, the CEI model has close control over IOP and always induces a low amount of damage to the ONH, making it useful for studying the earliest stages in the glaucomatous process.

### 2.5.2 Advantages and Pathophysiology of Rat Glaucoma Models

The rat is a widely-used animal model for glaucoma for several reasons. First, ocular hypertensive rat models of glaucoma present with similar damage patterns as occur in human glaucoma, including RGC apoptosis (Guo et al., 2005; Hanninen et al., 2002; Johnson et al., 2000), ECM deposits in the ONH indicative of remodeling (Johnson et al., 1996, 2000), astrocyte activation and migration (Dai et al., 2012; Li et al., 2015; Tehrani et al., 2016, 2014), and blockage of axonal transport (Zhang et al., 2015). Further, the ONH is a main and early site of damage (Morrison et al., 1997; Pease et al., 2000; Quigley et al., 2000). Second, consistent regional patterns of cellular response that occur in rat EG offer unique opportunities for the study of RGC pathogenesis. Namely, RGC axons tend to degenerate in the superior nerve first before the damage spreads (Dai et al., 2012; Morrison et al., 2015), and the mechanosensitive ONH astrocytes reorient their processes from perpendicular to parallel to the nerve axis in the inferior nerve first (Tehrani et al., 2016, 2014). The regionally-specific and seemingly contradictory patterns of these responses provide useful biological outcomes with which to compare regional biomechanical outcomes. Third, as mentioned, rodent models like the rat are much less expensive and much easier to manage than monkey models, making them more useful for mechanistic studies that require a high number of subjects.

### 2.5.3 Rat Optic Nerve Head Anatomy Compared to the Human

However, there are substantial differences between rat and human ONH anatomy (Morrison et al., 2011; Pazos et al., 2015), including 5 differences that are of particular interest as seen in Figure 7. 1) The rat lacks a connective tissue lamina cribrosa spanning the neurovascular scleral canal, although a few collagenous septa exist along with capillaries that traverse the canal. In addition, at the level of the sclera, a dense network of astrocytes is arrayed perpendicular to the nerve axis in a pattern similar to that of the human LC beams. 2) The central retinal vein (CRV) and artery (CRA) pass through the sclera on the inferior side of the nerve, rather than along the center of the optic nerve. At the level of the sclera, they divide, with the CRA passing into a separate canal in the sclera and the CRV travelling along the pia mater. 3) There is a vascular plexus between the optic nerve and the sclera on the nerve's superior side. It is referred to as the perineural vascular plexus (PNVP) and seems to be continuous with and similar in nature to the choroid. The existence of the PNVP is the reason why the main scleral canal in the rat is sometimes called the neurovascular canal. 4) There is a separate canal in the sclera inferior to the neurovascular canal through which a series of arteries, including the CRA, pass. It will be referred to as the inferior arterial canal (IAC). A "sling" of scleral tissue separates the two scleral openings. 5) BM has an "overhang" region on the superior side of the nerve tissue which forces RGC axons to pass around it as they enter the neurovascular canal.

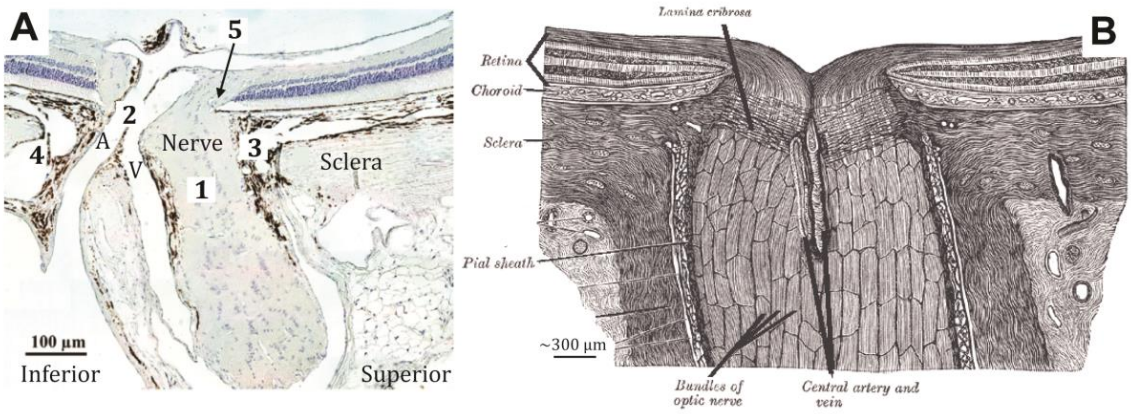


**Figure 7. Histologic section of the rat (A) and schematic drawing of the human (B) ONH illustrating their anatomical differences, including 5 key differences of particular interest 1)-5) as described in the text. Abbreviations: central retinal artery (A) and central retinal vein (V). From (Schwaner et al., 2018).**

These anatomical features are likely to influence rat ONH biomechanics, and the lack of connective tissue LC is especially concerning for correctly interpreting results from rat EG studies. However, these anatomical differences present both a challenge and an opportunity. It can be challenging to interpret what rat EG results mean for human glaucoma, especially from studies in which biomechanics are a main focus. However, understanding how biomechanical insult leads to RGC apoptosis even in the absence of an LC could provide a unique perspective that sheds light on RGC pathogenesis in human glaucoma.

### 2.5.4 Previous Studies on Rodent ONH Biomechanics

To date, rat ONH biomechanics have not been characterized, but there are a few related studies of note. Two different groups quantified scleral fiber orientation in rat eyes. Girard et al. used small-angle light scattering to map fiber orientation and degree of alignment throughout the entire eye (Girard et al., 2011), and Baumann et al. used polarization-sensitive OCT to determine fiber direction in the peripapillary sclera

(Baumann et al., 2014). Fibers were most highly aligned at the equator but also showed alignment at the peripapillary sclera and anterior sclera. The primary fiber direction was circumferential at the peripapillary sclera and limbus and close to meridional everywhere else.

Fortune and colleagues used OCT to visualize the rat ONH and retina while undergoing controlled IOP elevation at levels ranging from 40 mmHg to 70 mmHg (Fortune et al., 2011). They observed retinal thinning, posterior displacement of the ONH as a whole, and outward bowing of the peripapillary sclera and attached tissues, but they did not see any changes to BM opening size. Due to limitations with OCT at the time, they were not able to quantify any other deformation measures. Notably, IOP elevation to 70 mmHg interfered with retinal blood flow.

Finally, since the anatomy is similar to that of a rat, three biomechanics related studies on the mouse eye are of note. Myers et al. and Nguyen et al. used inflation testing and DIC to quantify the expansion of the globe at IOP up to 45 mmHg (Myers et al., 2010; Nguyen et al., 2013). They were able to make eye-to-eye stiffness comparisons, first showing that younger eyes are stiffer than older ones, and then showing that the CD1 strain which has higher susceptibility to RGC damage also experiences higher scleral strain than B6 mice. However, they were not able to provide true material property values. In an impressive study, Ngyuen et al. used multiphoton microscopy and DVC to quantify in vitro deformation in mouse eye explants that were genetically modified to have their astrocytes express GFP (Nguyen et al., 2017). They found that strains were greatest in the temporal-nasal direction, the peripapillary sclera opening expanded over the course of several days, and that astrocytes reoriented their processes to be parallel to the nerve axis. Lastly, Kimball et al. showed that cross-linking of the sclera induced by glyceraldehyde injection resulted in increased RGC death in a mouse glaucoma model

(Kimball et al., 2014). This was surprising, since previous modeling and experimental studies have indicated that a stiffer sclera results in reduced ONH strains.

In summary, rat models of ocular hypertension are well established and have advantages that make them a valuable and necessary complement to monkey glaucoma models. Specifically, they provide an opportunity for detailed mechanistic studies that can answer many of the open questions in glaucoma pathophysiology. However, since the link between biomechanical insult and cellular responses in glaucoma represents a primary gap in knowledge of the field, this opportunity will be missed if rat ONH biomechanics are not characterized. This thesis aims to provide this characterization to the glaucoma research community, with the ultimate goal of learning more about the effects of biomechanics on RGC pathogenesis.

## 2.6 Organization of this Thesis

The following chapters were written as journal articles. Thus, when I refer to "previous work", I am referring to other chapters in the thesis. In addition, when I cite other chapters in this thesis, as (Schwaner, Submitted), the citation may refer to work that has not actually been submitted as of the date of this thesis but whose submission is imminent. The "Submission Details" section at the beginning of each chapter provides more information on this point, including the author list and abstract. Lastly, I note that the last two Chapters in this thesis were completed "out of order", i.e. Chapter 6 was completed before Chapter 5. Chapters 5 and 6 were originally being done in parallel, but rather than wait for Chapter 5 to be completed, I completely finished Chapter 6, as it was unclear how long the final troubleshooting steps in Chapter 5 would take. Finally, when citing work that has not yet been published, (Schwaner, Submitted-a) will refer to Chapter 4, (Schwaner, Submitted-b) will refer to Chapter 6, and (Schwaner, Submitted-c) will refer to Chapter 5.

# CHAPTER 3. A METHODOLOGY FOR INDIVIDUAL-SPECIFIC MODELING OF RAT OPTIC NERVE HEAD BIOMECHANICS IN GLAUCOMA

## 3.1 Submission Details

Authors: Stephen A. Schwaner, Alison M. Kight, Robert N. Perry, Marta Pazos, Hongli Yang, Elaine C. Johnson, John C. Morrison, Claude F. Burgoyne, C. Ross Ethier

Status: Published in *The Journal of Biomechanical Engineering*., **140**(8), pp. 084501-1 – 084501-10

### Abstract

Glaucoma is the leading cause of irreversible blindness and involves the death of retinal ganglion cells (RGCs). Although biomechanics likely contributes to axonal injury within the optic nerve head (ONH), leading to RGC death, the pathways by which this occurs are not well understood. While rat models of glaucoma are well-suited for mechanistic studies, the anatomy of the rat ONH is different from the human, and the resulting differences in biomechanics have not been characterized. The aim of this study is to describe a methodology for building individual-specific finite element (FE) models of rat optic nerve heads. This method was used to build three rat ONH FE models and compute the biomechanical environment within these ONHs. Initial results show that rat ONH strains are larger and more asymmetric than those seen in human ONH modeling studies. This method provides a framework for building additional models of normotensive and glaucomatous rat ONHs. Comparing model strain patterns with patterns of cellular response seen in studies using rat glaucoma models will help us to learn more about the

link between biomechanics and glaucomatous cell death, which in turn may drive development of novel therapies for glaucoma.

## 3.2 Introduction

Glaucoma is the leading cause of irreversible blindness, affecting an estimated 70 million people worldwide (Tham et al., 2014). Blindness in glaucoma patients is initiated by loss of retinal ganglion cell (RGC) axons, which transmit visual information from the retina to the brain. Elevated intraocular pressure (IOP) is a main and causative risk factor (AGIS7, 2010; Morrison et al., 1990), leading to the hypothesis that biomechanical insult is a key driver leading to RGC axon degeneration (Burgoyne, 2011). Current therapies all focus on lowering IOP, although this is not always effective at preventing further vision loss.

The optic nerve head (ONH) is the location where RGC axon bundles exit the eye. In the human eye, axons pass through pores in a connective tissue web called the lamina cribrosa, which spans the scleral canal. The ONH has been identified as an early and primary region of glaucomatous damage for several reasons, including posterior bowing and remodeling of the lamina cribrosa (Downs et al., 2007; Roberts et al., 2009; Yang et al., 2007), remodeling of the surrounding sclera (Agapova et al., 2003; Bellezza et al., 2003; Burgoyne et al., 1995; Girard et al., 2011; Hernandez, 2000; Hernandez et al., 2008; Morrison et al., 1990; Pena et al., 2001; Quigley et al., 1991, 1991), sectoral RGC axonal injury corresponding to the ONH (Quigley et al., 1981; Schlamp et al., 2006), and disruption of RGC axonal transport at the level of the lamina cribrosa (Gaasterland et al., 1978; Quigley & Addicks, 1980). However, the pathways by which biomechanical insult results in RGC death are not well understood. Commonly proposed possibilities include direct mechanical insult to RGC axons, nutrition scarcity due to IOP-induced remodeling

or obstructed capillaries (Langham, 1980; Roberts et al., 2009), and decreased support from ONH resident cells (i.e. astrocytes) to RGCs due to mechanical activation (Morgan, 2000, 2004; Quigley, 1999; Tehrani et al., 2016, 2014). This lack of understanding has prompted many studies on ONH biomechanics in several species, particularly in humans and monkeys (Chen et al., 2014; Coudrillier et al., 2013, 2015, 2015, 2012; Eilaghi et al., 2010, 2010; Grytz et al., 2014, 2011; Norman et al., 2011; Sigal et al., 2009, 2011, 2005, 2004, 2009). As IOP is elevated, stress and strain are increased in the ONH in complex patterns due to the intricate anatomy and mechanical behavior of ONH tissues. Although constantly improving imaging technologies are making it more possible to measure strain *in vivo* (Nguyen et al., 2017; Sigal et al., 2014), computational modeling remains a key tool for understanding the complex biomechanics of the ONH. Previous modeling studies on the human have identified scleral stiffness as the most important factor in glaucoma-related ONH biomechanics (Sigal et al., 2009, 2005), and more recent studies have begun to explore the impact of lamina cribrosa and peripapillary scleral microstructure (Jan et al., 2017; Sigal et al., 2014).

In distinction to biomechanical studies, much of what we know about cellular behavior and degeneration in glaucoma has come from rodent model studies (Morrison et al., 2011). The rat is a particularly useful animal model for mechanistic glaucoma studies for several reasons. 1) Acute and chronic ocular hypertensive experimental glaucoma models exist for the rat and present with similar ONH pathophysiology as that seen clinically (Dai et al., 2012; Johnson et al., 1996; Morrison et al., 1997, 2016; Tehrani et al., 2016). 2) Regional patterns of rat RGC loss and astrocyte activation offer unique opportunities for study. In experimental glaucoma rat studies, the RGC axons in the superior optic nerve tend to die first (Morrison et al., 2011). In addition, it was recently shown that mechanosensitive ONH astrocytes activate and reorient their processes in the

inferior nerve before those in the superior nerve (Tehrani et al., 2016). 3) Rodent experimental glaucoma models are necessary for high subject-number studies because they are less expensive and easier to manage than monkey models. 4) Rodent experimental glaucoma studies allow for better control of factors that may influence RGC death (vs. human).

However, there are substantial differences between rat and human ONH anatomy (Morrison et al., 2011; Pazos et al., 2015) (Figure 8). 1) The rat lacks a connective tissue lamina cribrosa spanning the neurovascular scleral canal. 2) The central retinal vein (CRV) and artery (CRA) pass through the sclera on the inferior side of the nerve, rather than within the center of the optic nerve. 3) There is a vascular plexus between the optic nerve and the sclera of the neurovascular canal, referred to as the perineural vascular plexus (PNVP). 4) There is an additional canal in the sclera, the inferior arterial canal (IAC), which is separated from the neurovascular canal by a scleral sling. 5) BM extends into the nerve tissue on its superior side creating a BM overhang. These differences are likely to affect rat ONH biomechanics, and although several studies on rodent ONH biomechanics have been conducted (Campbell et al., 2017; Girard et al., 2011; Myers et al., 2010; Nguyen et al., 2017), no computational modeling study has been done to date.

Therefore, there is a need for an in-depth characterization of the IOP-induced biomechanical environment in the rat ONH that will allow us to better interpret results from rat glaucoma studies. For example, comparing strain patterns in the ONH with patterns of biological response from rat experimental glaucoma studies could help us to determine the pathway between biomechanical insult and RGC death. This knowledge would assist in novel therapy development and early identification of at-risk patients. Our goal is to fill this need by using recently available data sets describing normal and glaucomatous rat ONH tissue anatomy (Pazos et al., 2015, 2016) to build individual-specific finite element

models of rat ONHs. We here present a method for building these models as well as initial results on strain patterns in the rat ONH.

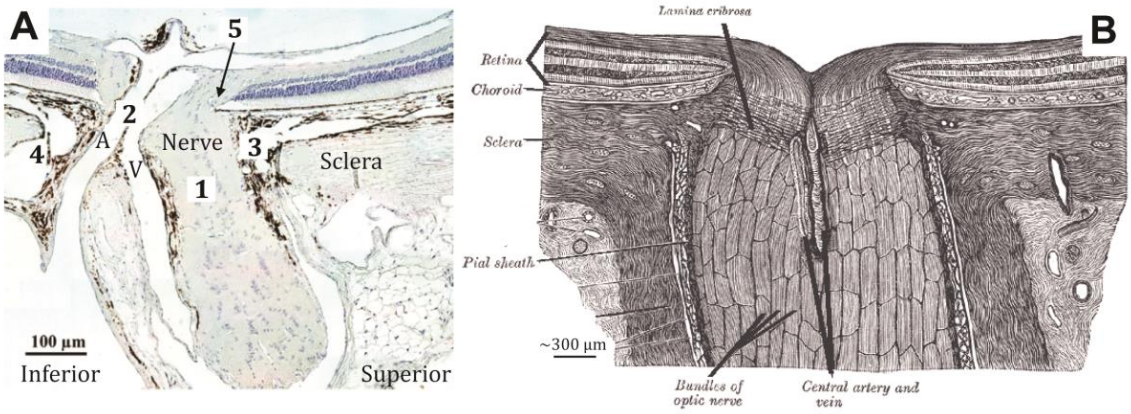


**Figure 8. Histologic section of the rat (A) (modified from (Morrison et al., 2011)) and schematic drawing of the human (B) ONH (modified from (Henry Vandyke Carter, 1918))illustrating their anatomical differences, including 5 key differences of particular interest 1)-5) as described in the text. Abbreviations: central retinal artery (A) and central retinal vein (V).**

## 3.3 Methods

### 3.3.1 Building Model Geometry

3D digital reconstructions of optic nerve heads (ONHs) from normotensive, ostensibly normal rat eyes were built from histomorphometric data sets, collected as previously described (Pazos et al., 2015, 2016). Animals were male Brown Norway rats between 9.5 and 10.5 months of age. After animals were sacrificed via $CO_2$ euthanasia, eyes were perfusion-fixed *in situ* while experiencing an estimated IOP of 10 mmHg and an estimated arterial pressure in the range of 40 – 100 mmHg. The justification for these values is given below. Eyes were enucleated and each ONH was removed using a 3 mm trephine and embedded in paraffin. The resulting block was serial sectioned at 1.5 µm thickness using an automated microtome starting at the vitreoretinal interface and

proceeding through the ONH. After each section was cut, the block surface was stained with a 1:1 (v/v) mixture of Ponceau S and acid fuchsin stains, then imaged at a resolution of 1.5 x 1.5 µm per pixel using a custom device. The images were then aligned and stacked into a digital 3D reconstruction of the ONH. In this work, we provide information on three reconstructions of three separate rat eyes (MR04OD, MR05OD, and MR10OS) from three separate rats.

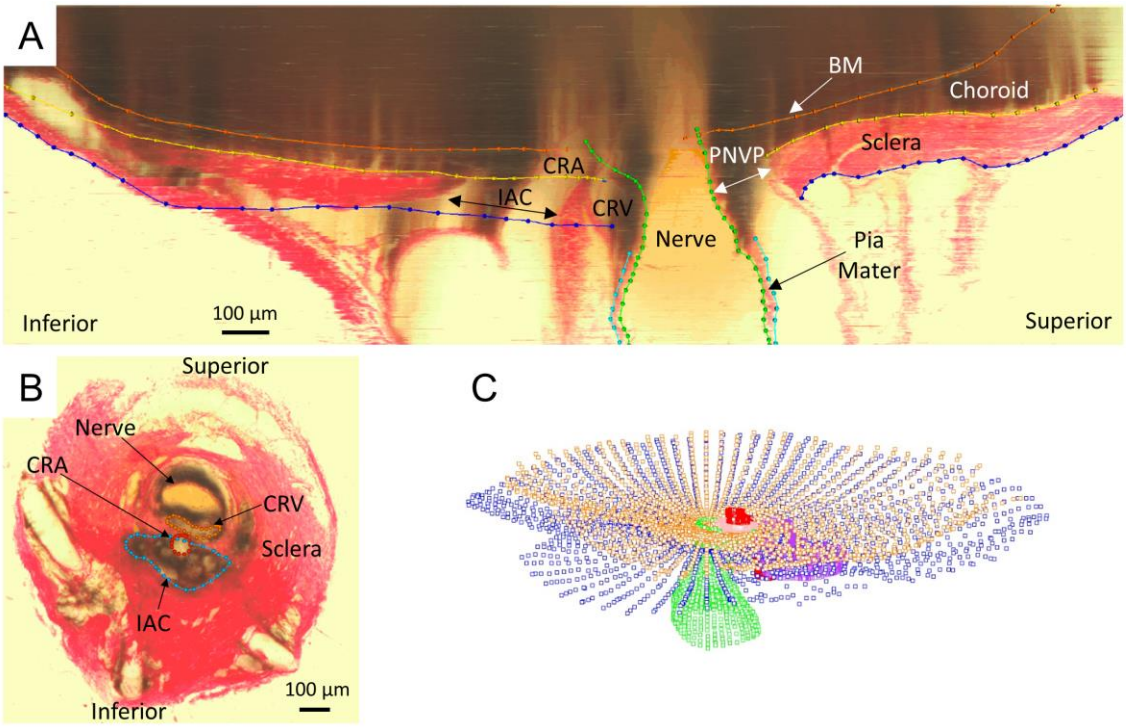


**Figure 9. Manual delineation of tissue boundaries. A.) Radial section through rat ONH with tissue boundaries delineated: BM (orange), anterior scleral boundary (yellow), posterior scleral boundary (blue), neural boundary (green), posterior pia mater outer boundary (cyan). B) Cross section normal to nerve axis with tissue boundaries delineated: CRV (orange), CRA (red), IAC (blue). C) Point clouds produced from delineation of radial sections and cross sections.**

Using custom software (Multiview (Downs et al., 2007)), tissue boundaries were manually delineated (Figure 9). Bruch's membrane (BM), the anterior scleral surface, the posterior scleral surface, neural boundary, outer posterior pia mater surface, and the side branches of the central retinal vein (CRV) were delineated by viewing radial sections

through the ONH. The anterior scleral canal opening, posterior scleral canal opening, and BM opening were also delineated in this view. The central retinal artery (CRA), main CRV lumen, and inferior arterial canal (IAC) were delineated by viewing transverse sections through the ONH. We chose to disregard the long posterior ciliary arteries which feed into the CRA just posterior to the globe. Depending on their placement within or just outside the sclera, different sections along their lengths were either considered part of the sclera, or were not included in delineation. We also did not include delineations of the dura mater because we decided to focus on tissues primarily influenced by IOP. The dura mater will be included in future studies that focus on changes in cerebrospinal fluid pressure. The resulting 3D point clouds describing tissue geometry were imported into Rhino 5 SR 14 (Robert McNeel & Associates).

Non-uniform rational basis spline (NURBS) surfaces were fit to the point clouds and were joined to create volumes representing each tissue (Figure 10) using Rhino. NURBS curves and surfaces are useful for representing complex geometries, such as those of biological tissues, because they offer a high degree of accuracy for representing free form geometry with lower memory requirements than faceted approximations of geometry. The Rhino T-Splines plugin (Autodesk Inc.) was used to build tissue geometries that were particularly difficult to represent, i.e. the three connecting branches of the CRV. Curves and surfaces were smoothed to make them more amenable to meshing. Smoothing of the original point cloud data occurred at several steps in the geometry building process. The chosen settings within Rhino fitting functions affected the smoothness of the resulting curve or surface. For example, forcing a curve to pass directly through every point in a given set often produced a jagged curve, so this requirement was usually relaxed. In addition, after the initial fitting of original point cloud data, sometimes curves and surfaces were smoothed using the built-in Rhino function “Smooth” and T-Splines function “Flatten”.

In addition to the outer surfaces of the IAC, CRA, and CRV which required smoothing in all three eyes, smoothing was done as needed to remove features such as small “wrinkles” or “sharp” sections within curves and surfaces, while taking care not to edit more prominent features of tissue morphology. The outer surfaces of the IAC, CRA, and CRV required smoothing in every model. Also, since tissues near the edges of the histomorphometric reconstructions were more prone to artifacts (tissue curling, bending, etc.) than those in the center, geometry outside of a 1.5 mm diameter cylinder centered at the center of BM opening was removed from the model. Boolean operations were used in areas where tissues intersected each other. For example, since the CRA passes through the BM, choroid, sclera, and IAC, the CRA geometry was subtracted from each of those tissues. This ensured that adjacent tissues shared common surfaces and helped to produce conforming meshes between tissues. In cases where the thickness of the tissue could not be determined from the reconstructions, a constant thickness was assumed. Specifically, we made thickness measurements of the CRV wall (3 μm), CRA wall (10 μm), and anterior pia mater (20 μm) from previously gathered histology slides of the rat ONH. The anterior pia mater was defined as being anterior to the posterior scleral surface. For model MR05OD only, which was the first model built before the above procedure had been refined, the posterior pia mater was also given a constant thickness of 20 μm; revising this model to make the small corrections to posterior pia mater thickness would have been labor intensive and would have likely had very small effects on model results. The BM was given a thickness of 3 μm based on published data on the human BM (Bailey et al., 2001; Candiello et al., 2007; Curcio & Johnson, 2012). After each model geometry was completed, a custom RhinoPython script was used to project the volume boundaries back onto the original reconstruction sections to ensure that ONH anatomy was accurately represented (Figure 12). In addition, a custom script was written to calculate the minimum distance between each delineation point and its respective tissue surface, representing

the error between the manual delineations and the resulting model geometries. Tissue volumes were then exported to Trelis 16.3.6 (Computation Simulation Software, LLC) for meshing.

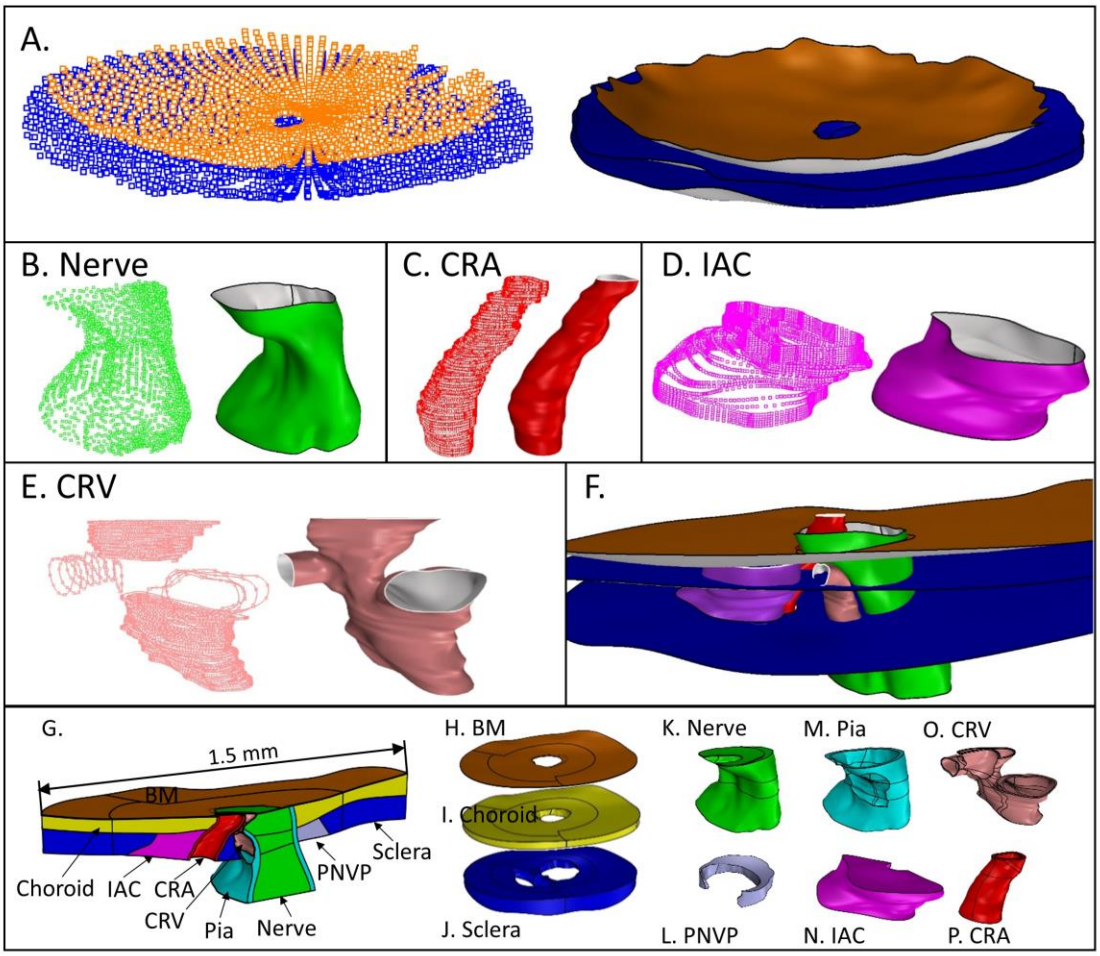


**Figure 10. Overview of geometry building process. See text for abbreviations. A-E) Point cloud and surface fit of A) BM and sclera, B) optic nerve, C) CRA, D) IAC, E) CRV. F) Intersecting tissue surfaces before Boolean operations were performed. G) Superior-Inferior cut view of MR05OD model geometry. H)-P) Individual tissue volumes (not to scale): H) BM, I) choroid, J) sclera, K) optic nerve, L) PNVP, M) pia mater, N) IAC, O) CRV, P) CRA.**

### 3.3.2 Meshing and Constraints

Because the model geometry was so complex, most of the model was meshed using tetrahedral elements. However, due to the thinness of BM, it could not be meshed using

tetrahedral elements without either using an unreasonably high mesh density or producing skewed element shapes. Meshing the entire volume of the choroid and sclera with tetrahedra also produced too many elements. To overcome these problems, we divided each ONH model into an inner region containing tissues with complex geometry (nerve, pia mater, CRV, CRA, PNVP, IAC) and an outer region containing only tissues with simpler geometry (sclera, choroid, BM) (Figure 11). The outer region was meshed with 8-node hexahedral elements. The inner region was meshed with a combination of 6-node wedge elements and 4-node tetrahedral elements. Since this meshing scheme created a nonconforming mesh between the simple region and complex region, tied constraints were implemented at these boundaries. A general contact without friction was also implemented between inner surfaces of the CRV vessel wall in the model of MR05OD because its CRV geometry resulted in contact between opposite sides of the CRV wall.

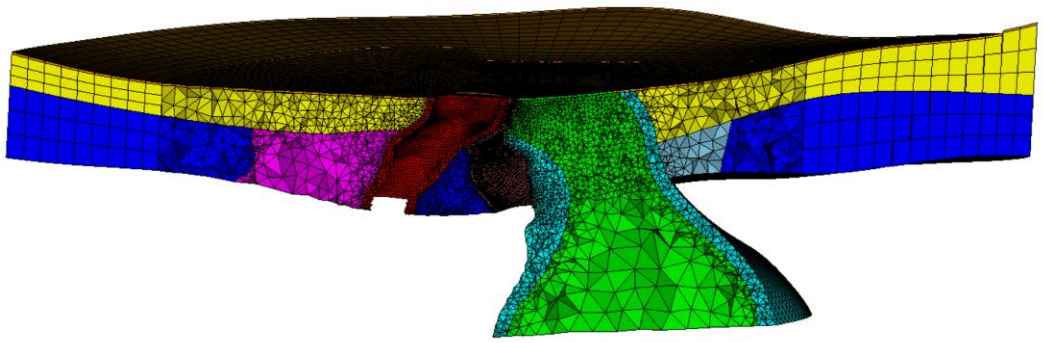

**Figure 11. Mixed meshing scheme. Tied constraints connect hexahedral elements along the model outside with tetrahedral and prism elements within the complex model center.**

### 3.3.3 Material Properties

Since it has been established that connective tissues in the eye, especially the sclera, contain organized layers of collagen (Jan et al., 2017, 2017), nonlinear, anisotropic material models are appropriate for modeling their mechanical behavior. However, to our

knowledge, the mechanical behavior of rat ONH tissues has not been characterized. Therefore, as a first-pass effort, we modeled all tissues as isotropic, neo-Hookean solids. All tissues were assumed to be nearly incompressible and were thus given a Poisson's ratio value of 0.49. We used tissue stiffness values (Table 1) from previous modeling studies on the human ONH for the sclera, pia mater, optic nerve, and central retinal vessels (Sigal et al., 2007, 2005, 2004, 2009). For BM and the choroid, we assumed values from the literature (Candiello et al., 2007; Chen et al., 2010, 2014; Curcio & Johnson, 2012). We assumed that the PNVP and IAC had the same material properties as the choroid, all highly vascularized tissues.

**Table 1. Tissue elastic modulus values.**

| Tissue | Elastic Modulus (MPa) | Tissue | Elastic Modulus (MPa) |
|---|---|---|---|
| BM | 7 | Choroid | 0.1 |
| Sclera | 3 | PNVP | 0.1 |
| Pia Mater | 3 | IAC | 0.1 |
| CRA Wall | 0.3 | Optic Nerve | 0.03 |
| CRV Wall | 0.3 | | |

### 3.3.4 Loads

Our 3D point cloud data represents the ONH geometry at perfusion fixation pressures. We used a "relative displacement" approach to account for the preexisting stress and strain in the ONH at perfusion fixation. This approach provides a more accurate solution than neglecting the effects of prestress without having to implement more involved, iterative methods (Grytz & Downs, 2013). As prescribed by this approach, we

treated the model geometry as created from 3D point cloud data as the unloaded ONH geometry. We applied loads (IOP, CRA blood pressure (BP), and CRV BP) equal to those experienced by the ONH during perfusion fixation, and assumed that the resulting model state represented the pre-loaded reference configuration, i.e. was under the stress and strain experienced by the ONH at perfusion fixation. Next, we applied additional loads to bring the model to a glaucomatous loading state, and we calculated the change in strain relative to the pre-loaded reference configuration.

#### 3.3.4.1 Pre-Loaded Reference State

IOP at fixation was estimated to be 10 mmHg based on previous experience with the IOP of anesthetized rats (Jia et al., 2000), and CRA BP at fixation was in the range of 40 mmHg – 100 mmHg as measured by a pressure transducer connected to the perfusion line. We assumed the lower end of the CRA fixation BP range, and thus applied a large CRA BP in the second step of our model simulation to reach glaucomatous conditions. This corresponds to a “worst case scenario” in our model because applying a larger CRA BP is more likely to cause high strains within adjacent sections of the optic nerve. For example, in the cases of MR04OD and MR05OD, a small portion of anterior optic nerve tissue was in contact with the CRA and experienced strain due to expansion of the CRA. Finally, we assumed that CRV BP closely followed IOP (Flammer & Konieczka, 2015). In summary, we took the pressures experienced by the eye during perfusion fixation to be 10 mmHg IOP, 10 mmHg CRV BP, and 40 mmHg CRA BP. IOP was applied to the anterior surfaces of BM, the optic nerve, the CRA, and the CRV, while CRA BP and CRV BP were applied to each vessel lumen.

#### 3.3.4.2 Glaucomatous Loading State

A daytime (light phase) IOP of approximately 30 mmHg and above will usually produce glaucomatous damage in a rat, depending on duration of exposure (Jia et al., 2000, 2000; Morrison et al., 2005). We estimated that blood pressure in the CRA of an awake rat is likely around 110 mmHg (Heuven & Kiel, 2009; Jiang et al., 2018). It is difficult to determine CRV pressure, but we assumed that it closely follows IOP. Therefore, the pressure loads applied in the second step of our model simulation were 20 mmHg IOP, 20 mmHg CRV BP, and 70 mmHg CRA BP, representing the increases in respective pressures over the pre-loaded reference state. All strains reported herein thus represent a change in strain from the pre-loaded reference configuration.

### 3.3.5 Boundary Conditions

We utilized a submodeling approach to apply realistic boundary conditions to the edges of each ONH FE model (Norman et al., 2011; Sigal et al., 2009, 2009, 2005). Submodeling involves solving a less detailed “full model” (in our case, the entire posterior half of the eye), that encompasses the true region of interest or “submodel” (in our case, the ONH). Displacements from the full model were mapped to nodes on the edges of the submodel and applied as boundary conditions using the Abaqus submodeling feature. We built a posterior eye model with simplified ONH geometry that included a choroid, sclera, optic nerve, PNVP, and IAC (Figure 12). We did not include the CRA and CRV because that level of detail would have required a much denser mesh. Since the long axis and diameter of the rat eye only differ by about 2% (Pazos et al., 2015), we modeled the posterior eye as a half sphere with a diameter of 6.41 mm (Pazos et al., 2015). The choroid and sclera had constant thicknesses of 100 µm and 60 µm, respectively (Pazos et al., 2015). To generate a simplified ONH geometry, we measured the cross section of the

optic nerve, PNVP and IAC at the level of the anterior choroid, anterior sclera, and posterior sclera in 5 ONH geometries: 3 that were used in this study and 2 additional geometries. The nerve and PNVP cross sections were represented as ellipses, and the IAC cross sections were represented as half ellipses. To measure the dimensions of each tissue cross section, points were laid on the cross section boundary, a plane was fit through the points, and the points were projected to the plane using Rhino. A Matlab script was used to fit an ellipse through those points, and the major and minor axes were recorded as well as their center locations relative to BM opening. Each of these measures were averaged and used to create generalized tissue cross sections for the posterior eye model. Tissue volumes were generated by lofting a surface through the generalized cross sections. We applied boundary conditions to nodes on the flat, anterior surface of the posterior eye model. Nodes were allowed to move in the r direction, but were fixed in the z and θ directions. The z axis was coincident with the central axis of the half sphere (Figure 12). As in the submodels, we applied IOP in two loading steps: 10 mmHg and an additional 20 mmHg. IOP was applied to the anterior surface of the choroid and optic nerve. The material properties for each tissue were the same as for the submodel.

#### 3.3.5.1 Submodel/Posterior Eye Model Registration

Matching between the submodel and posterior eye model was done via a combination of manual and automatic adjustments. First, the submodel geometry was manually translated and rotated until it closely matched the posterior eye geometry. We focused on matching the anterior scleral surfaces of the two models, especially at the edges of the submodel, and then tried to line up the nerve, PNVP, and IAC. Next, we overlaid points on the outer, anterior surface of the sclera, the PNVP cross section boundary at the level of the sclera, and the IAC cross section boundary at the level of the sclera for the submodel and posterior eye model. These points were imported into Matlab

and an automatic surface registration algorithm (Zhang, 1994) was used to make small adjustments. We then inspected the fit, and manually made fine adjustments as necessary. Since there were differences in scleral and choroidal thickness and surface contour between ONH models, it was impossible to produce matches which resulted in the entire submodel edge being contained within the posterior eye model geometry. For this reason, we added blocks of very soft material (elastic modulus of 0.01 MPa) to the anterior choroidal surface and posterior scleral surface of the posterior eye model where submodel boundaries sometimes protruded as a way to interpolate displacement values to the nodes at these protruding edges.

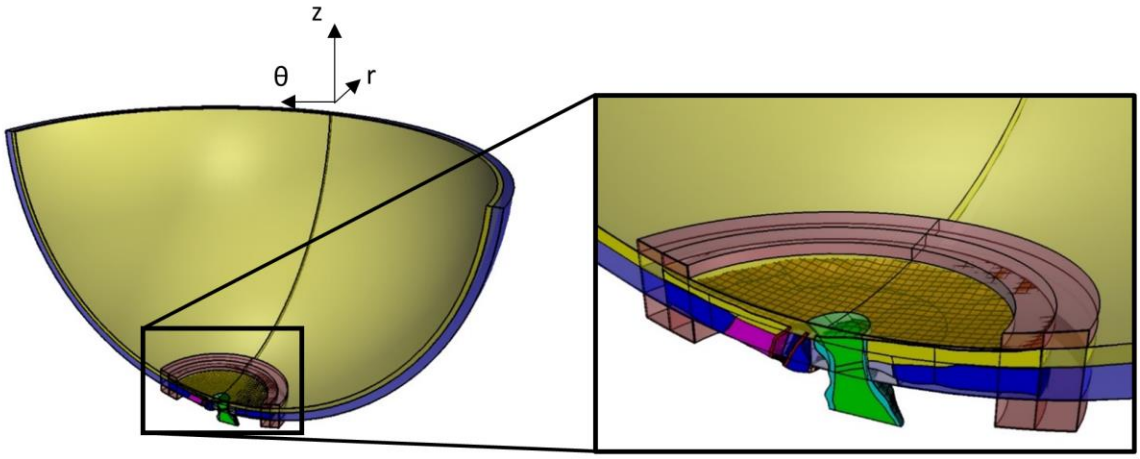


**Figure 12. Superior-Inferior cut plane view illustrating a match between individual-specific model geometry (opaque) with generic posterior eye geometry (semi-transparent). Tissue colors are the same as in Fig. 3. Transparent red blocks on anterior choroid and posterior sclera are the very soft material used to interpolate displacement values to any protruding individual-specific model edges.**

All simulations were run using Abaqus 2016 (Dassault Systèmes) on a virtual machine with an Intel Xeon CPU E5-26900 v3 @ 2.60GHz with 50 GB of RAM. Results were post-processed using the abaqus2matlab toolbox (Papazafeiropoulos et al., 2017), a custom Matlab script, and Paraview (Kitware, Inc.).

## 3.4 Results

### 3.4.1 Model Geometry

Average errors between the manual delineations and resulting model geometries for MR04OD, MR05OD, and MR10OS were 5.8 µm, 5.5 µm, and 5.0 µm, indicating that the model geometries closely matched the original delineations. Figure 13 shows an example of the good agreement between the MR05OD model geometry and the true ONH anatomy as illustrated by projecting points from the model edges back onto the original reconstruction sections.

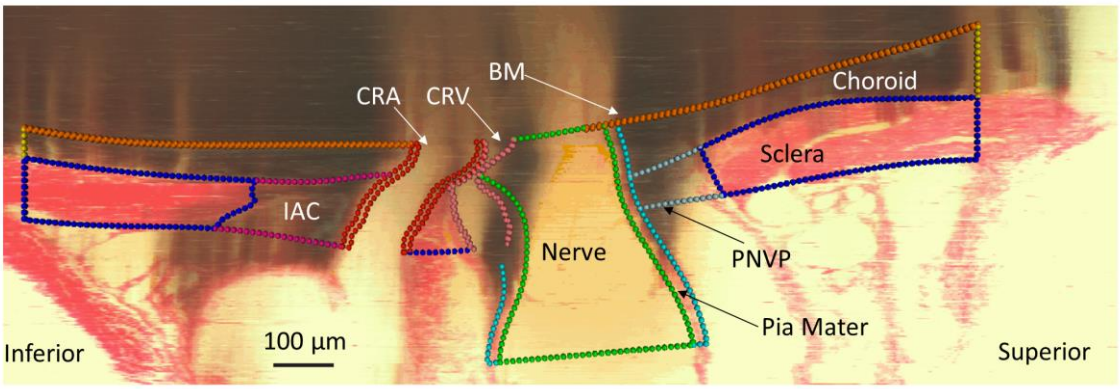


**Figure 13. Projection of model tissue outlines onto digital section to ensure accurate representation of individual-specific tissue geometry. Note that the "shadow-like" appearance in parts of the section is an artifact of the reconstruction process. It occurs because highly pigmented tissue within the semi-transparent paraffin block can be seen even before it is cut by the microtome.**

### 3.4.2 Mesh Sensitivity

We evaluated model sensitivity to mesh density by solving the MR05OD model with low, medium, and high-density meshes which had node counts of 87,429, 175,941, and 340,016. In three out of the four quantified strain measures (listed below), the error between the high and medium-density meshes was substantially lower than the error

between the medium and low-density meshes (Table 2). In these three cases, error decreased to at most 1/5 of the original value. The exception was the relative error for average third principal strain, which increased from 0.56% to 1.17%. However, the relative error in all quantified strain measures between the medium-density mesh and high-density mesh was less than 2% of the medium density mesh strain values. For these reasons, we decided that the medium-density mesh was sufficient, and we ensured that the mesh density of each model was approximately at that of the medium-density mesh or greater. The resulting node counts for each model were 221,937 for MR04OD, 175,941 for MR05OD, and 412,175 for MR10OS.

**Table 2. Mesh density study results.**

| | Low Density Mesh | Medium Density Mesh | High Density Mesh |
|---|---|---|---|
| **First Principal Strain Mean** | 3.81% | 3.96% | 3.98% |
| **First Principal Strain 95$^{th}$ Percentile** | 5.78% | 5.85% | 5.86% |
| **Third Principal Strain Mean** | -4.21% | -4.24% | -4.29% |
| **Third Principal Strain 5$^{th}$ Percentile** | -6.80% | -6.83% | -6.84% |

### 3.4.3 Optic Nerve Strain Patterns

For the most part, patterns of strain were consistent between models, with first and third principal strain concentrations occurring in the inferior side of the anterior half of the

nerve (Figure 14). In two of the models, the nerve tissue came into contact with the CRA and strain concentrations were observed at this interface. The level of strain that occurred around the BM overhang on the superior side of the nerve varied between models. MR04OD experienced the most consistent elevation of strain along the BM overhang edge, while MR05OD presented with less strain near the BM overhang.

We quantified the average and 95$^{th}$ percentile first principal strain and average and 5$^{th}$ percentile third principal strain in the anterior nerve, defined as nerve tissue from the level of the BM to the level of the posterior scleral surface (about 150 µm posterior to BM) (Table 3). The 95$^{th}$ and 5$^{th}$ percentile values were chosen for quantification because they are a measure of the most extreme strains in the tissue, which are most likely to invoke a cellular response, while avoiding potential numerical errors associated with the 100$^{th}$ and 1$^{st}$ percentile values, e.g. due to badly shaped elements. The second principal strain magnitudes were much lower than first or third principal strain values, so we focused on reporting the first and third principal strains. MR04OD and MR05OD had similar strain values but the values of MR04OD and MR10OS differed by as much as 27%.

**Table 3. Computed 1$^{st}$ and 3$^{rd}$ principal strains in the anterior optic nerve.**

| | **First Principal Strain** | | **Third Principal Strain** | |
|---|---|---|---|---|
| Model | Mean | 95$^{th}$ Percentile | Mean | 5$^{th}$ Percentile |
| MR04OD | 3.65% | 5.74% | -4.23% | -6.61% |
| MR05OD | 3.96% | 5.85% | -4.24% | -6.83% |
| MR10OS | 4.38% | 7.11% | -5.70% | -8.40% |

In earlier stages of methods development, we ran model simulations that did not include a preloading step, and therefore did not account for the effects of prestress (data not shown). However, adding in a preloading step did not significantly alter the overall strain patterns calculated by each model. Including the effects of prestress will likely be more important for future versions of the models that account for the nonlinear stiffening behavior of the sclera (see below).

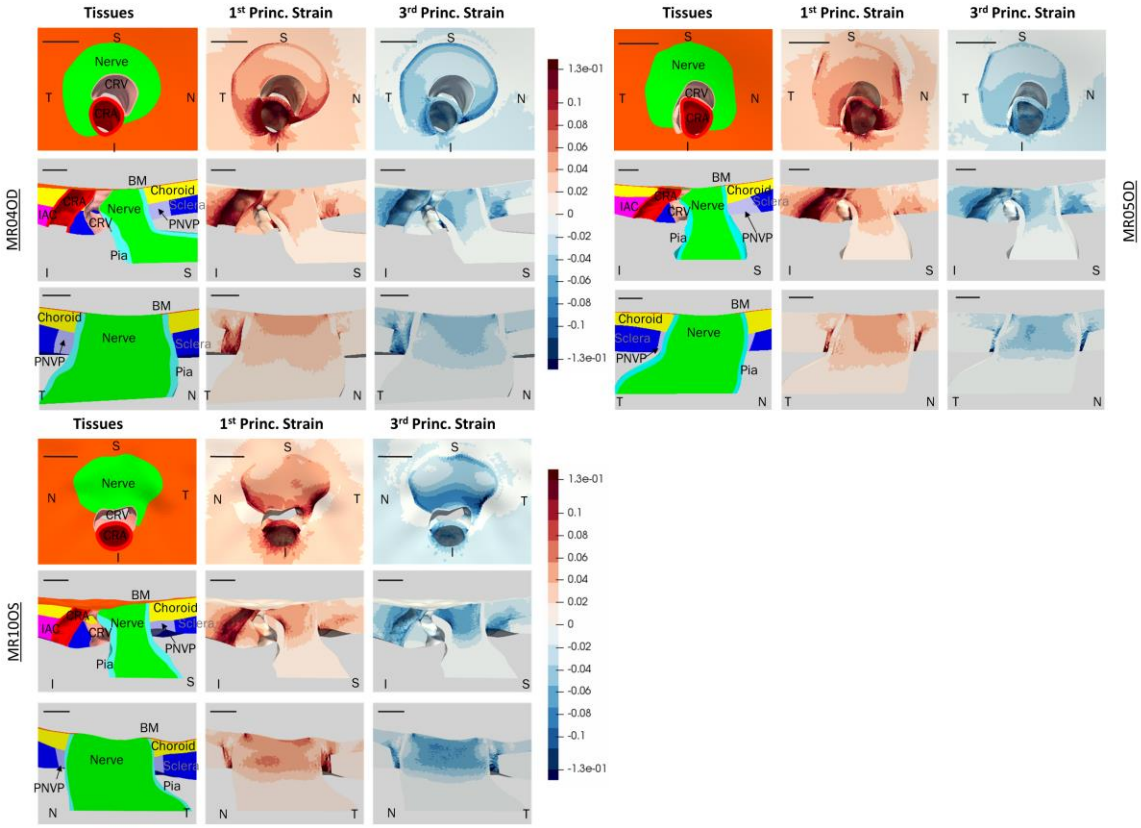


**Figure 14. Computed 1st and 3rd principal strain patterns for 3 different rat ONH models: MR04OD (top left), MR05OD (top right), and MR10OS (bottom left). Superior (S), inferior (I), nasal (N), and temporal (T) directions are indicated. Top rows show en face view, middle rows show S-I cut view, and bottom rows show T-N cut view. Tissue colors are the same as in Figure 10. All scale bars are 100 µm. All three models have primary strain concentrations along the inferior side of the anterior nerve. MR10OS and MR04OD have more prominent strain concentrations around the BM overhang edge than MR05OD. MR10OS has particularly high strain concentrations in the inferior nerve as seen from the en face view.**

## 3.5 Discussion

Our methodology is capable of producing rat ONH finite element models which closely adhere to the true, complex rat ONH anatomy. This is made evident when the tissue boundaries of our models are overlaid on the original digital rat ONH reconstructions Figure 13). This was consistent with our finding that the highest average error between model geometry and the tissue delineations was only 5.8 µm.

As expected, our initial results predict different strain patterns and higher strain magnitudes than those previously reported in human ONH modeling studies. The human ONH has a higher degree of anatomical symmetry, with ONH tissues being arranged in an approximately axisymmetric pattern around the central retinal vessels. The rat ONH is somewhat symmetric about the sagittal plane, but is not axisymmetric like the human ONH. This affected strain patterns in the rat ONH models, with main strain concentrations occurring in the inferior nerve and, in the case of MR04OD and MR10OS, in the nerve tissue in contact with the BM overhang. We also expected that rat ONH strains would be higher than in the human, since the rat ONH lacks the biomechanical support of a collagenous lamina cribrosa as in the human ONH. Our models confirmed this expectation, with predicted strains at an IOP load of 20 mmHg (10 mmHg to 30 mmHg) similar to those seen in the human ONH at an IOP load of 45 mmHg (Sigal et al., 2009) (5 mmHg to 50 mmHg). For example, in the prelaminar neural tissue of the human ONH models, first principal strain median and 95$^{th}$ percentile values ranged from approximately 2% to 4% and 5% to 9%, respectively, while third principal strain median and 5$^{th}$ percentile values ranged from approximately -4% to -5% and -9% to -13%. In all cases except for the third principal 5$^{th}$ percentile strains, the human values were about the same as those of the rat despite the human ONH being subjected to approximately double the IOP load that our rat ONH models were.

This difference is likely due to the existence of a collagenous lamina cribrosa in the human ONH. It is also possible that other anatomical differences contributed to the generally higher strain levels in the rat. For example, scleral stiffness and thickness have previously been shown to strongly influence ONH strain in the human eye. Although the rat eye is only about 4 times smaller in diameter than the human eye, the rat sclera is 5 to 10 times thinner than the human sclera (Pazos et al., 2015). In addition, the IAC creates

an additional “weak point” in the rat sclera that does not exist in the human sclera. The strains we predicted were also similar to those determined by a recent experimental study on strains in the mouse astrocytic lamina under an IOP elevation from 10 to 30 mmHg (Nguyen et al., 2017), which estimated mean strains in the nasal-temporal and superior-inferior direction to be 5.21% and 3.74%, respectively.

Although we expected our models to produce asymmetric stress and strain patterns in the optic nerve, we were surprised by the predominantly inferior localization of the strain concentrations. Since the BM was modelled with a large modulus (7 MPa) compared to the optic nerve (0.03 MPa), we expected to see the highest strain concentrations where the BM overhang contacted the nerve. In addition, previous rat glaucoma studies have reported a preferential superior pattern of RGC axonal degeneration (Tehrani et al., 2016, 2014), leading us to predict that we would also see the highest levels of strain in the superior nerve. However, it was recently shown that astrocytes, known to be mechanosensitive, will reorient their processes in response to a chronic IOP elevation (Tehrani et al., 2014). A follow-up study, which exposed rats to an acute IOP elevation, demonstrated that astrocytes in the inferior optic nerve tended to reorient their processes before those in the superior optic nerve (Tehrani et al., 2016). This does seem to match with the prediction of our models that the most prominent strain concentrations occurred in the inferior nerve. As mentioned above, it is possible that these large strains primarily occur in the inferior nerve due in part to the inferior placement of the CRA, CRV, and IAC causing a weak region of the sclera just inferior to the scleral canal. At this point, we have only qualitatively compared patterns of strain between models, but plan to perform in-depth quantification of regional nerve strain levels in future work.

### 3.5.1 Limitations

The models presented here have several limitations, primarily due to simplifications made in the assumed tissue constitutive relations. First, the stiffnesses that we used in our model were either derived from measurements from other species or were educated estimates. It is likely that the values we chose are at least within the correct ranges for each tissue, but in the future, it will be important to determine properties that are specific to the rat ONH. In addition, the assumption that the tissues behave as isotropic neo-Hookean solids falls short from modelling true soft tissue behavior in several ways. Notably, it does not capture the nonlinear stiffening behavior that soft tissues are known to exhibit as they experience increased strain. However, it is still useful to compare our model results to previous studies on the human ONH which also utilized linear elastic material models. Second, modelling tissues as isotropic gives them an unrealistically high bending stiffness, since connective tissues generally have a higher tensile strength than compressive strength. Third, the isotropic assumption also fails to account for differences in in-plane stiffness which likely exist due to organization of collagen fibers. The isotropic assumption is especially likely to cause error in the modelled scleral and pia mater behavior. We have plans to include the effects of collagen fibers in the sclera in future modeling attempts, and are interested to see if this will change the strain patterns we currently observe. Note that a representation of the pia mater with a lower compressive modulus could potentially decrease the strain concentration we currently see in the inferior nerve.

In this study, we have only presented results from three models. Previous studies have shown that eye-to-eye variations in geometry can have noticeable effects on ONH strain values (Sigal et al., 2009), and we already saw differences in the models reported

here. Modeling efforts are ongoing and we plan to model eight normal rat ONH geometries in total.

Although the histomorphometric method used to build the rat ONH digital reconstructions accurately preserves important anatomic and morphologic relationships, it is known that tissue fixation and tissue embedding cause differential shrinkage of tissue constituents which may distort ONH tissues prior to digital reconstruction and modeling (Yang et al., 2007). Currently, there is no strategy to identify, quantify, and correct for these effects in our reconstructions. Their effects on the predicted stress and strain levels and patterns in our models are therefore unknown.

The computed results have not been experimentally validated. Although extremely challenging, it is possible that optical coherence tomography could be used to track the deformation of tissue landmarks during in vivo inflation testing of a rat eye and such displacements compared with computed values in the future.

## 3.6 Conclusion

We developed a method for creating individual-specific models of rat ONHs utilizing 3D point cloud data sets, and presented initial strain results from three ONH models utilizing tissue properties similar to those previously used in earlier modeling studies on the human ONH (Sigal et al., 2004, 2009). Our models predicted more asymmetric strain patterns than in the human, higher strain magnitudes than in the human, and strain concentrations that align with recently reported patterns of astrocyte activation and reorientation. Applying this method to additional normotensive and glaucomatous rat ONHs and comparing their strain results to patterns of cell response from rat experimental glaucoma studies will help us to learn more about how biomechanics affects glaucoma pathophysiology.

# CHAPTER 4. BIOMECHANICAL PROPERTIES OF THE RAT SCLERA OBTAINED WITH INVERSE FINITE ELEMENT MODELING

## 4.1 Submission Details

Authors: Stephen A. Schwaner, Bailey G. Hannon, Andrew J. Feola, C. Ross Ethier

Submission Status: In preparation for *Biomechanics and Modeling in Mechanobiology*

### Abstract

It is widely accepted that biomechanics plays an important role in glaucoma pathophysiology, but the mechanisms involved are largely unknown. Rats are a common animal model of glaucoma, and finite element models are being developed to provide much-needed insight into the biomechanical environment of the posterior rat eye. However, material properties of rat ocular tissues, including the sclera, are currently unknown. Since the sclera plays a major role in posterior segment ocular biomechanics, our goal was to use inverse finite element modeling to extract rat scleral material properties from experimental data. We first used digital image correlation to measure scleral surface displacement during whole-globe inflation testing. We modeled the sclera as a nonlinear material with embedded collagen fibers, then fit modeled displacements to experimental data using a differential evolution algorithm. Subject-specific models were constructed in which 3 parameters described the stiffness of the ground substance and collagen fibers in the posterior eye, and 16 parameters defined the primary orientation and alignment of fibers within eight scleral sub-regions. We successfully extracted scleral material properties for eight rat eyes. Model displacements recreated general patterns of

the experimental displacements but did not always match local patterns. The fiber directions and fiber concentration parameters were highly variable, but on average, fibers were aligned circumferentially and were more aligned in the peripapillary sclera than in the peripheral sclera. The material properties determined here will be used to inform future finite element models of the rat posterior eye with the goal of elucidating the role of biomechanics in glaucoma pathophysiology.

## 4.2 Introduction

Glaucoma is the second most prevalent cause of blindness worldwide (Tham et al., 2014). Although it is widely accepted that biomechanics plays an important role in glaucoma, the specifics of this role are not well understood (Campbell et al., 2014). Elevated intraocular pressure (IOP) is a key risk factor in glaucoma, and computational modeling studies have shown that high IOP results in increased mechanical stress and strain in ocular tissues, particularly in the optic nerve head (ONH) region, a main and early site of glaucomatous damage (Hua et al., 2018; Quigley et al., 1981; Sigal et al., 2007, 2004). However, it is not known exactly how biomechanical insult leads to axonal degeneration in the ONH, which is the cause of glaucomatous vision loss (Alqawlaq et al., 2018; Quigley, 1999).

Rodent models of glaucomatous optic neuropathy, such as the rat, have proven useful for mechanistic studies and also have certain advantages over monkey models because of their lower cost, ease of animal husbandry, and low genetic variability between individuals. However, rat ocular biomechanics have not been well characterized; in fact, our previous study is the only attempt to-date to perform computational modeling of rat ONH biomechanics (Schwaner et al., 2018). Computational modeling has the potential to provide the detailed biomechanical information necessary to investigate the relationships

between biomechanical insult and ONH pathophysiology, but to be accurate, this approach requires ONH tissue material property information. This information is not currently available for the rat. Previous work has shown that scleral stiffness is the most influential material property on ONH biomechanics in human modeling studies (Hua et al., 2018; Sigal et al., 2005), and our preliminary studies have supported a similar finding in the rat (not published). Therefore, the purpose of this study was to determine material properties of the rat sclera. To do so, we carried out mechanical testing of rat sclera followed by inverse finite element modeling (FEM) to extract material parameter values from experimental data.

The sclera is a tough connective tissue with a complex organization of collagen fibers (Gogola et al., 2018). Although it has been represented in some modeling studies as an isotropic solid (Hua et al., 2018; Sigal et al., 2004), in an effort to be true to the physiology, other studies have implemented material models that consist of an isotropic matrix reinforced by collagen fibers (Coudrillier et al., 2013; Feola et al., 2018; Wang et al., 2016). Previous studies characterizing scleral biomechanics have utilized a variety of methods including uniaxial strip testing (Chen et al., 2014), biaxial testing of scleral samples (Eilaghi et al., 2010), and whole globe inflation testing (Coudrillier et al., 2015; Girard et al., 2009; Myers et al., 2010). Whole globe inflation testing was used in the present study because it is the most physiologically relevant form of loading, because it allowed us to interrogate an intact sclera rather than excised samples, and because it is the most feasible method to perform on the small rat eye. We utilized inverse FEM to extract material properties from experimental scleral deformation data because it allowed us to assess regional scleral properties, account for local scleral thickness variation, and employ a fiber-reinforced material model. The properties reported by this study will inform future efforts to model rat ONH biomechanics.

## 4.3 Methods

### 4.3.1 Experimental Method

#### 4.3.1.1 Animals

Twenty male Brown Norway rats (10-13 months old; Charles River Laboratories, Inc., Wilmington, MA) were used for this study. All procedures were approved by the Institutional Animal Care and Use Committee at the Georgia Institute of Technology. Some rats were removed from this study according to exclusion criteria discussed below.

#### 4.3.1.2 Optical Coherence Tomography Scanning

The thickness of the sclera varies with position, and thus it was necessary to determine scleral thickness for inverse FEM (Norman et al., 2010); we accomplished this by performing in vivo spatial-domain optical coherence tomography (SD-OCT; Envisu R4300; Leica Microsystems, Buffalo Grove, IL) volume scans (Figure 15). Before SD-OCT, animals were anesthetized with ketamine (60 mg) and xylazine (7.5 mg/kg) and a drop of topical tetracaine (1%) was applied to the eye. After induction of anesthesia, eyes were dilated with a topical drop of tropicamide (1%). We used SD-OCT to obtain five image volumes of the posterior region of each eye near the ONH. The first volume was centered on the ONH and then subsequent images were taken of the superior, inferior, temporal, and nasal regions adjacent to the ONH. All volumes included the ONH to aid in later image registration. Each image volume was a 2.7 mm by 2.7 mm rectangular scan consisting of 100 b-scans with 1000 a-scans per b-scan. Note that the scans shown in Figure 15 do not appear rectangular because the rays outside of a 2.7 mm diameter circle are blocked by the edges of the imaging lens holder. Before each scan, the reference arm of the SD-OCT system was adjusted until the image of the sclera appeared “flat” on the screen, as is

standard practice. This corresponds to the situation in which all rays emitted by the SD-OCT probe pass through a convergence point in the eye, ensuring that each ray travels the same distance before reaching the sclera. This in turn, allows accurate thickness measurements to be made. After SD-OCT, IOP was measured in each eye using a Tonolab tonometer (Icare, Raleigh, NC) previously calibrated in-house by elevating IOP between 5-50 mmHg using a hydrostatic column (data not shown). An average of six IOP measurements was taken to be the anesthetized IOP of the rat.

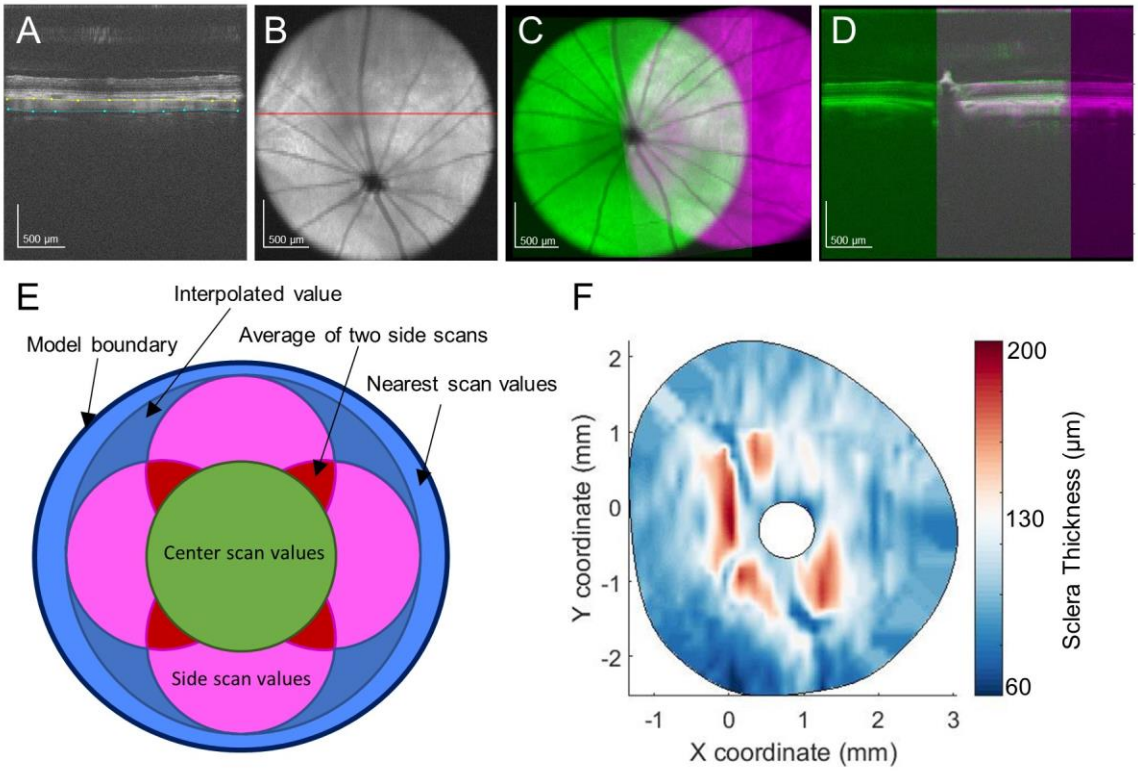


**Figure 15 Measuring scleral thickness from SD-OCT scans. A. SD-OCT B-scan with the anterior (yellow) and posterior (cyan) scleral surfaces delineated. B. Average intensity projection through the sclera, choroid, and retina. Red line indicates b-scan in panel A. C. Registration of two SD-OCT volume scans, obtained by aligning the ONH and retinal vessels as seen in two average intensity projection images. D. Registration of the same two SD-OCT volume scans in the axial direction by aligning the anterior scleral surface as seen in two b-scans passing through the ONH. The colors in this panel are identical to those in panel C. E. Schematic detailing how thickness data from five SD-OCT volumes was combined into a single thickness map. F. Typical final thickness map for a rat sclera.**

#### 4.3.1.3 Whole-Globe Inflation Testing

We implemented an established inflation testing method described elsewhere (Hannon et al., 2019. Submitted). Briefly, after animals were euthanized by $CO_2$ asphyxiation, their eyes were removed and cleaned of extra-orbital tissue. It was necessary to leave a small amount of tissue surrounding the ONH to prevent leaking during inflation testing. After cutting a hole in the cornea, the eye was secured, cornea

side down, to a testing apparatus using superglue, and a speckle pattern was applied to the posterior scleral surface using graphite powder (#970 PG, General Pencil Company, Inc., Redwood City, CA). The rig was filled with baby oil to prevent drying of the eye and attached to an inflation testing setup via Luer connections (Figure 16). IOP was controlled by changing the height of a reservoir containing 1X phosphate buffered saline (PBS) in series with the eye.

All measurement equipment was calibrated regularly before testing. The pressure transducer was calibrated by raising the reservoir through a series of pressure steps to correlate sensor voltage with known pressures. Weekly intrinsic and daily extrinsic calibrations of two stereo cameras (Dantec Dynamics, Holtsville, NY) were performed with a calibration target according to manufacturer protocols. During extrinsic calibration, the calibration target was submerged in mineral oil at the level of the eye to ensure compensation for the refractive index of mineral oil. The eye was imaged during the inflation test with a 100 ms exposure time.

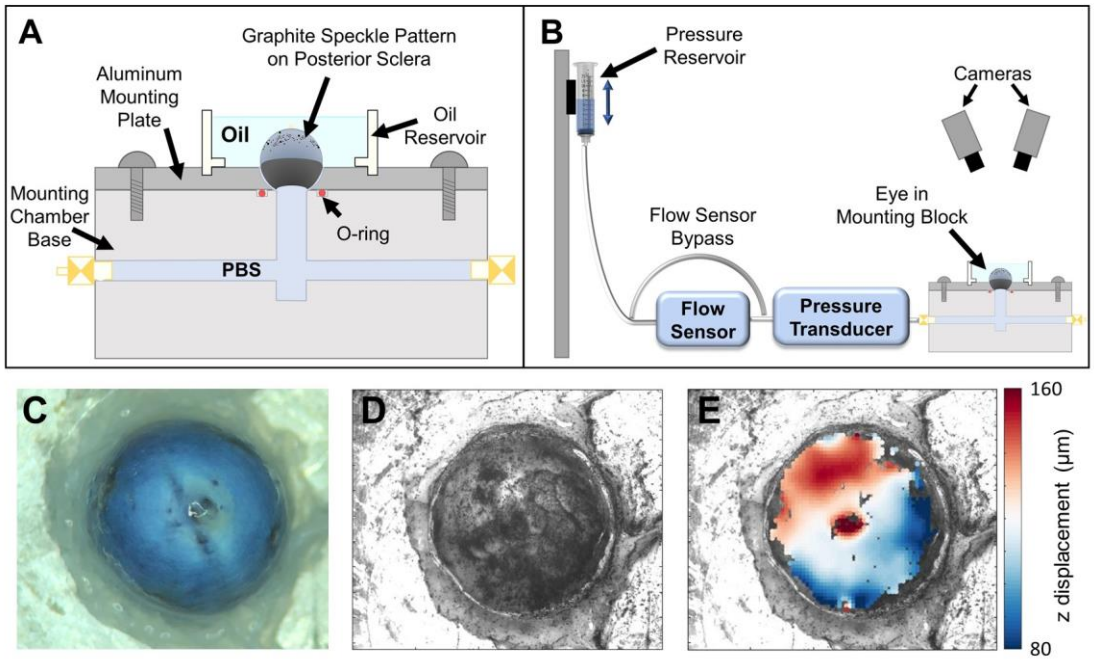


**Figure 16. Whole-globe inflation testing setup. A. Schematic of the testing rig. B. Schematic of the whole globe inflation testing apparatus. C. Overhead view of the sclera before graphite speckle pattern was applied. D. DIC camera view of the sclera after application of graphite speckle pattern. E. Facet overlay displaying z displacement (toward the camera) of the scleral surface at the end of an inflation test. A. and B. from (Hannon et al. 2019. Submitted).**

Preconditioning was carried out by first ramping IOP to 15 mmHg and holding for 5 minutes, and then performing 10 load-unload cycles from 3 to 15 mmHg at a rate of 0.5 mmHg/second. The eye was allowed to reach a steady state at 3 mmHg (see below), and then subjected to a series of pressure steps: 3 – 6 mmHg, 6 – 9 mmHg, 9 – 12 mmHg, 12 – 20 mmHg, and 20 – 30 mmHg. IOP and flow rate of PBS into the eye were monitored using a gage pressure transducer (142PC01G; Honeywell, Charlotte, NC) and an in-line flow sensor (SLG64-0075; Sensiron, Stafa, Switzerland). Before each pressure step, the eye was allowed to creep until it reached a steady state, as determined by monitoring the flow rate into the eye over time. Note that since the flow sensor acted as a resistor in series between the fluid reservoir and the eye, IOP at steady state was always slightly below the pressure applied to the system. iPerfusion software was used to record IOP and

flow data and to control the fluid reservoir (Sherwood et al., 2016). During the test, the two stereo cameras captured images of the scleral surface at a frame rate of one image every 30 seconds. In some eyes, PBS leakage occurred either through the ONH region, through vessels in the sclera, or through the glue securing the eye to the testing rig. These eyes (32 of 40) were excluded from the study. The remaining eight eyes were from eight rats.

#### 4.3.1.4 Digital Image Correlation

Istra 4D digital image correlation (DIC) software (v2.5.1, Dantec Dynamics, Holtsville, NY), was used to calculate the shape and deformation of the surface of the sclera from images taken during testing. The algorithm produced a 3D facet map overlaying the surface of the eye. The correlation parameters used were as follows: facet size of 45 pixels, grid spacing of 28 pixels, maximum permissible start point accuracy of 0.2 pixels, residuum of 30 grey values, and 3D residuum of 1.1 pixels. In 3D space, the resulting facet grid spacing was approximately 150 µm.

Displacement data was smoothed using parameters recommended by Dantec Dynamics: a grid reduction factor (minimizing the difference between the data point and the spline function) of 2 for displacement and contours, and a smoothness factor (straightens filtered data) of -0.5 for displacement and 0 for contours. Further postprocessing was accomplished using custom MATLAB (2017a; MathWorks, Natick, MA) scripts, as follows. The image taken one minute before the first pressure step, during which the eye was at an IOP of approximately 3 mmHg, was selected as the reference state. The x, y, and z displacements of each correlated facet were averaged over the last five images after reaching equilibrium at each pressure step. This average displacement was taken as the displacement of each facet at the given pressure. Only facets that were correlated in all of the last five images at the end of each of the five pressure steps were

used for analysis. Facets that were obvious outliers, e.g. had displacement values that far exceeded those of immediately neighboring facets, were removed by manual inspection.

The displacement “noise floor” of the DIC system was estimated by applying a speckle pattern to a glass bead that was approximately the size of a rat eye and imaging the eye with the stereo cameras over the course of six hours. From this test, the estimated noise floor was 0.3 μm.

#### 4.3.1.5 Scleral Thickness Measurements

We measured sclera thickness from the SD-OCT volume scans using a custom MATLAB script to view and make delineations on b-scans throughout the volumes. In brief, we delineated the boundaries of the sclera, the optic nerve, and the long posterior ciliary arteries (LPCAs) throughout each of the five SD-OCT scan volumes for each eye. Since the SD-OCT system did not track the relative locations of scan volumes from the same eye, the five volume scans had to be co-registered, as follows. An average intensity projection that clearly showed the retinal vessels and a b-scan passing through the ONH center were exported for each volume. The image slices for the intensity projections were selected such that each resulting image clearly showed the retinal vessels. We used a custom MATLAB script to register adjacent volumes (images of the superior, inferior, temporal, and nasal regions) with the central volume (image of the ONH) by aligning the ONH and retinal vessels in the intensity projection images, and by aligning the anterior scleral boundary at the ONH in the b-scans. A separate custom MATLAB script was used to measure scleral thickness by fitting splines to the delineation points on the anterior and posterior scleral surfaces, and by then extracting the axial distance (distance along an a-scan) between them at 0.1 mm intervals.

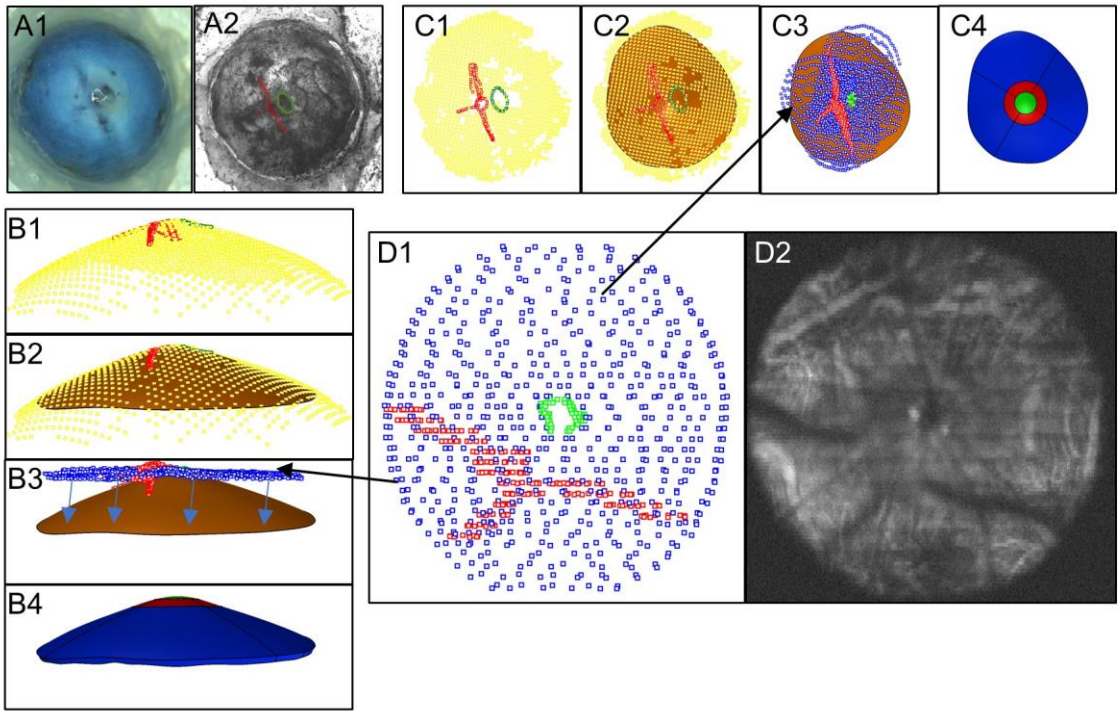


**Figure 17. Registration of thickness data with DIC data. A1. Image of eye without speckle pattern applied. A2. Eye with speckle pattern applied and LPCAs (red) and optic nerve (green) delineated. Panel C (top view) and panel B (side view) show the same steps from different viewpoints. B1. and C1. Optic nerve (green) and LPCA (red) delineations from DIC image mapped to 3D coordinates using DIC facet map (yellow). B2. and C2. Surface (orange) fit through the DIC facets forming the posterior surface of the sclera model. B3. and C3. SD-OCT delineations of the sclera (blue), LPCAs (red), and optic nerve (green) manually registered to DIC data. Arrows in B3 indicate how the thickness map was projected to the posterior model surface. B4. and C4. Model after thickness data was applied and the model was split up into eight regions. The ONH region is shown in green, the peripapillary regions are shown in red, and the peripheral regions are in blue. D1. SD-OCT delineations of the sclera (blue), LPCAs (red), and optic nerve (green). D2. Average intensity projection of slices from an SD-OCT volume in which the LPCAs and optic nerve are visible.**

Since the five SD-OCT volumes overlapped and did not usually fully encompass the region visualized by DIC imaging, the following approach was used to generate a thickness map (Figure 15E). All locations within the central SD-OCT volume were given a thickness value directly from that SD-OCT scan, while locations within overlapping regions between two peripheral (i.e. non-central) SD-

OCT volumes were given an average of the thickness values from those scans. For locations that were not contained within an SD-OCT volume scan but were contained within the convex hull of SD-OCT volume scans, an interpolated thickness value was assigned. Locations that were outside of the SD-OCT volumes' convex hull were assigned the thickness value of the nearest SD-OCT measurement or interpolated value.

### 4.3.2 Finite Element Modeling

#### 4.3.2.1 Building the Model Geometry

The 3D facet coordinates from the reference image were imported into Rhino (v5 SR14; Robert McNeel and Associates, Seattle, WA) where the model geometry was created. Note that in the following, all described surfaces are non-uniform rational basis spline surfaces, and all curves are Bezier curves. The DIC facets were fit with a surface using the Rhino "Patch" command to represent the posterior scleral surface. The outer boundary edge (farthest from the ONH) of the model anterior surface was then defined by fitting a curve through facets near the outer edges of the facet map. This approach allowed us to exclude artifacts that often existed at the facet map edges due to factors such as glare. We next imported thickness data into the model, which required registering the SD-OCT volumes with the DIC images (Figure 17). The LPCAs and the optic nerve were used as landmarks for this registration because they were visible in the DIC images and in the SD-OCT scans. In more detail, the outlines of the LPCAs and the optic nerve were manually traced in the DIC reference image, and their pixel coordinates were mapped onto the 3D facet map using a custom MATLAB script. After the sclera, LPCA, and optic nerve point clouds from SD-OCT delineations were imported into Rhino, the SD-OCT thickness data was manually registered with the DIC data by aligning the optic nerve and

LPCA point clouds from the SD-OCT scans with the tracings of the optic nerve and LPCAs from the DIC images.

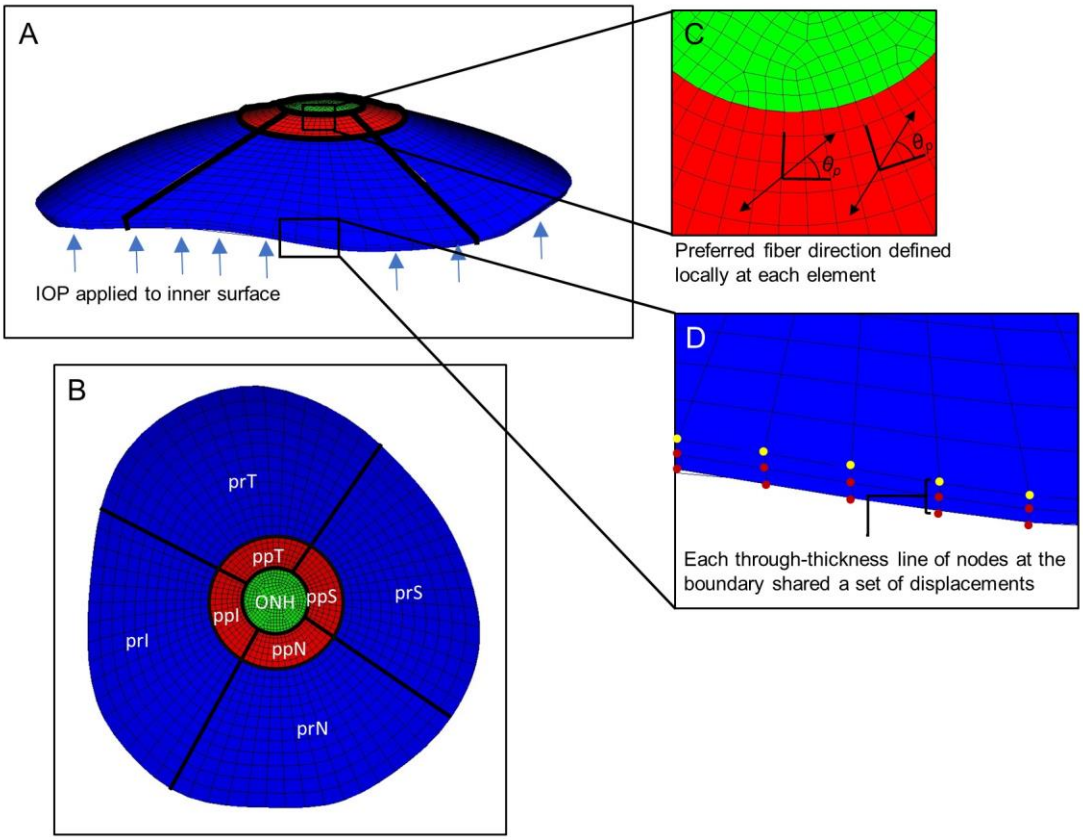


**Figure 18. FEM details. A. Side view of a finite element model mesh. IOP was applied to the anterior surface as indicated by the blue arrows. B. Top view of the meshed model with regions labelled. Orientation is the same as in the top view from Figure 17. C. Zoomed in view of the mesh in the peripapillary and ONH regions. The preferred fiber direction was defined locally at each element. D. Zoomed in view of the model outer edges (furthest from the ONH). Displacements from the DIC facet map were interpolated and applied as boundary conditions to nodes on the posterior boundary edge (yellow dots). Each through-thickness line of nodes (red dots) on the boundary surface shared displacements with the closest posterior boundary edge node, i.e. with the nearest yellow dot. Abbreviations: optic nerve head (ONH); peripapillary superior, temporal, inferior, and nasal regions (ppS, ppT, ppI, ppN); and peripheral superior, temporal, inferior, and nasal regions (prS, prT, prI, prN).**

A custom Rhino.Python script was used to apply the thickness data to the existing scleral surface. First, the thickness map was projected onto the scleral surface, and at each map location, a point was offset in the direction of the local scleral surface normal

by its associated thickness value. The resulting point cloud was then fit with a surface that represented the anterior scleral surface. The anterior surface was connected to the posterior surface by generating a third surface connecting their outer (farthest from the ONH) edges, to create the scleral model geometry. The model was then divided into nine regions so that regional fiber organization parameters could be calculated by the inverse method. First, the model was divided into an ONH region, a peripapillary sclera region, and a peripheral sclera region. The ONH region was a disc of diameter 0.75 mm centered on the ONH, the peripapillary region was an annulus of internal diameter 0.75 mm and external diameter of 1.5 mm, and the peripheral scleral region was the remainder of the model. We chose these diameters from observations of rat ONH histomorphometric reconstructions (Pazos et al., 2015; Schwaner et al., 2018) and a polarized light microscopy image of the rat sclera (kindly provided by Dr. Ian Sigal). The ONH region contained a combination of sclera, vascular, and nerve tissues (among others), but it was considered to be one homogeneous solid in the model because it was not feasible to model individual structures in the ONH region, and each individual structure alone likely did not have large effects on the deformation of the sclera. The peripapillary (pp) and peripheral (pr) sclera regions were further divided into superior (ppS and prS), inferior (ppI and prI), nasal (ppN and prN), and temporal (ppT and prT) sectors.

#### 4.3.2.2 Modeling Details: Mesh, Boundary Conditions, and Material Model

The model geometry was imported into Trelis (Computational Simulation Software, LLC; American Fork, UT) and meshed with 8-node hexahedral elements. Measured displacements (from DIC imaging) were interpolated from the facet map to the nodes on the outer boundary edge of the posterior scleral surface and applied as boundary conditions. It was assumed that nodes lying on the boundary surface

(connecting the anterior and posterior surfaces) shared the same displacements as the nearest posterior boundary edge node (Figure 18). Pressure was applied to the anterior scleral surface in a series of steps that matched the recorded IOP levels during the inflation test. For simplicity, it was assumed that a zero-stress state existed at the reference pressure; thus, all pressure increases applied to the model were relative to the reference pressure value.

The ONH was modelled as a nearly incompressible neo-Hookean solid, for which the strain energy density function takes the form:

$$W_{ONH} = \frac{\mu}{2}(I_1 - 3) - \mu \ln J + \frac{\lambda}{2}(\ln J)^2 \quad (1)$$

where $\mu$ is the shear modulus, $I_1$ is the first invariant of the right Cauchy-Green deformation tensor, $J$ is the determinant of the deformation gradient tensor, and $\lambda$ is Lame's first parameter. Since neo-Hookean materials reduce to the linear elastic model at small strains, it is common to present their material parameter values in the form of a Young's modulus, $E$, and Poisson's ratio $\nu$ using the conversion:

$$E = \frac{\mu(3\lambda + 2\mu)}{\lambda + \mu} \quad (2)$$

$$\nu = \frac{\lambda}{2(\lambda + \mu)} \quad (3)$$

The material model chosen to represent the sclera was a Mooney-Rivlin ground substance reinforced by fibers lying within the plane tangent to the posterior scleral

surface and with orientations following a Von Mises distribution (Girard et al., 2009). The strain energy density function for sclera was thus given by:

$$W_{sclera} = W_{gs} + W_{fiber} \tag{4}$$

where $W_{gs}$ is the contribution of the ground substance and $W_{fiber}$ represents the contribution of the collagen fibers. Further,

$$W_{gs} = c_1(I_1 - 3) + c_2(I_2 - 3) + \frac{K}{2}(\ln J)^2 \tag{5}$$

$$W_{fiber} = \int_{\theta_p - \pi/2}^{\theta_p + \pi/2} P(\theta)\, F_2(\lambda[\theta])\mathrm{d}\theta \tag{6}$$

where $c_1$ is the first Mooney-Rivlin coefficient, $c_2$ is the second Mooney-Rivlin coefficient, $I_2$ is the second invariant of the right Cauchy-Green deformation tensor, and $K$ is the bulk modulus. The sclera was assumed to be incompressible and thus $K$ was set as $K = 1$ GPa (Girard et al., 2009). $P(\theta)$ is the distribution function of the fibers, $\theta_p$ is the preferred fiber orientation relative to a local material coordinate system, and $F_2(\lambda[\theta])$ represents the response of the collagen fibers. The semi-circular von Mises distribution is given by:

$$P(\theta) = \frac{1}{\pi I_0(k_f)} \exp\left[k_f \cos\left(2(\theta - \theta_p)\right)\right] \tag{7}$$

where $I_0$ is the modified Bessel function of the first kind of order 0 and $k_f$ is the fiber concentration factor. The fiber response is given by:

$$F_2(\lambda) = \begin{cases} 0 & \lambda \leq 1 \\ c_3\left(e^{c_4(\lambda-1)}\left(Ei(c_4\lambda) - Ei(c_4)\right) - ln\,\lambda\right) & 1 < \lambda < \lambda_m \\ c_5(\lambda - 1) + c_6 \ln \lambda & \lambda \geq \lambda_m \end{cases} \quad (8)$$

where $c_3$ is the exponential fiber stress coefficient, $c_4$ is the fiber uncrimping coefficient, $\mathrm{Ei}(\cdot)$ is the exponential integral function, $\lambda_m$ is the fiber stretch for straightened fibers, and $c_5$ is the modulus of straightened fibers. In all simulations, we took $c_2 = 0$ MPa, causing the ground substance to behave as a neo-Hookean solid. Based on previous data demonstrating that the rat sclera behaves nonlinearly in the IOP range of 3 mmHg to 30 mmHg (Hannon et al., 2019. Submitted), we assumed that the collagen fibers never fully straightened ($\lambda > \lambda_m$ ), eliminating the need for the coefficients $c_5$ and $c_6$.

The anisotropic behavior of the sclera was determined by the values of $k_f$ and $\theta_p$. The term $k_f$ dictates the degree of anisotropy; specifically, $k_f = 0$ results in an isotropic distribution of fibers within the material plane, while $k_f = \infty$ results in all the fibers lying aligned along a preferred direction dictated by $\theta_p$. The material coordinate system of each element was defined as follows: the plane of fibers was locally tangent to the posterior scleral surface, while a value of $\theta_p = 0°$ corresponded to a fiber axis in the circumferential direction, and $\theta_p = 90°$ corresponded to a fiber axis in the meridional direction. It was assumed that the entire sclera shared common values for the coefficients $c_1$, $c_3$, and $c_4$ (Girard et al., 2009), but each region was described by its own values of $k_f$ ($k_{f\_ppS}$, $k_{f\_ppI}$, etc.) and $\theta_p$ ($\theta_{p\_ppS}$, $\theta_{p\_ppI}$, etc.), resulting in a set of 19 unknown parameters for inverse FEM calculations, namely: $c_1$, $c_3$, $c_4$, $k_{f\_prS}$, $k_{f\_prI}$, $k_{f\_prT}$, $k_{f_{prN}}$, $k_{f\_ppS}$, $k_{f\_ppI}$, $k_{f\_ppT}$, $k_{f\_ppN}$, $\theta_{p\_prS}$, $\theta_{p\_prI}$, $\theta_{p\_prT}$, $\theta_{p\_prN}$, $\theta_{p\_ppS}$, $\theta_{p\_ppI}$, $\theta_{p\_ppT}$, $\theta_{p\_ppN}$. The process of defining the model was accomplished using a combination of custom MATLAB and Rhino.Python scripts. All were solved using FEBio (v. 2.8.2; Salt Lake City, UT) (Maas et al., 2012).

### 4.3.3 Inverse Modeling and Differential Evolution

To describe the material behavior of the rat sclera, we adjusted the values of the 19 unknown material parameters to minimize the error between computed and experimental (DIC) displacements. Experimental displacement values were interpolated from the facet map at node locations on the scleral surface using a custom MATLAB script and the error was calculated using the following cost function (Girard et al., 2009):

$$\varepsilon = \frac{1}{N \cdot P} \sum_{n=1}^{N} \sqrt{\sum_{p=1}^{P} \left[ \left( x_{n,p}^{e} - x_{n,p}^{m} \right)^2 + \left( y_{n,p}^{e} - y_{n,p}^{m} \right)^2 + \left( z_{n,p}^{e} - z_{n,p}^{m} \right)^2 \right]} \qquad (9)$$

where $\left( x_{n,p}^{e}, y_{n,p}^{e}, z_{n,p}^{e} \right)$ are the components of the experimental ($e$) displacements and $\left( x_{n,p}^{m}, y_{n,p}^{m}, z_{n,p}^{m} \right)$ are the three components of the model ($m$) displacements at node $n$ and IOP level $p$. The total number of interrogated scleral surface nodes is $N$, and $P$ is the total number of IOP levels. Since there were gaps in the facet map where some facets did not correlate, only the closest node to each correlated facet was used in the cost function calculation.

We used a differential evolution (DE) optimization algorithm to minimize the cost function, which was implemented by making modifications to a MATLAB package obtained from the MATLAB file exchange (Buehren, 2017). DE has been used in inverse FEM studies on the monkey eye and has several advantages for this type of problem (Girard et al., 2009, 2011, 2009): it does not require the optimized problem to be differentiable, it can accommodate but does not require a starting guess, and it can be effective in avoiding local minima. To understand how the DE algorithm works, one can think of each trial set

of parameter values as the member of a “population”. Each algorithm iteration consists of a series of steps that includes mating between population members to produce offspring, mutation of offspring, and competition between parents and offspring. The winning member of each contest is the parameter set that produces the lowest cost function value, and the winners comprise the population for the next iteration. The particular DE package that we used allows the user to select different strategies or variations on the DE algorithm, set bounds on each parameter, and set the resolution of each parameter. There are a few important settings associated with the algorithm, including strategy, population size ($NP$), weighting factor ($F$), and crossover constant ($CR$). A more in-depth discussion can be found at (Price et al., 2005).

### 4.3.4 Two-Step Optimization Strategy

Determining material parameters, as we seek to do here, is a challenging computational problem. After empirical testing, it was determined that a two-step optimization strategy worked well for this problem. In step one, the set of optimized parameters was “compressed” to reduce the dimensionality of the parameter space. Specifically, in this step we sought parameter values for $c_1$, $c_3$, $c_4$, and a “bin” parameter for each scleral region that mapped to both a $k_f$ value and $\theta_p$ value, resulting in a total of 11 parameters to be optimized. We found that using 72 “bins” worked well, with each bin representing a $k_f$ and $\theta_p$ value as illustrated in Table 4. The search ranges for the $c$ terms were set as $0.001 \leq c_1 \leq 1$ MPa, $0.0001 \leq c_3 \leq 0.1$ MPa, and $1 \leq c_4 \leq 1000$. The algorithm settings were strategy = rand/bin/1, $NP = 50$, $F = 0.5$, and $CR = 0.9$, and the algorithm was allowed to run for 250 iterations, a total of 12,500 model simulations. The goal of this step was to accomplish a broad and conservative sampling of the parameter

space to prevent convergence on local minima while identifying the area that contained the global minimum cost function value.

**Table 4. $\theta_p$ and $k_f$ value associated with each bin value.**

| Bin Number | $\theta_p$ (°) | $k_f$ |
|---|---|---|
| 1 | 15 | 0.5 |
| 2 | 15 | 1.5 |
| 3 | 15 | 2.5 |
| 4 | 15 | 3.5 |
| 5 | 15 | 4.5 |
| 6 | 15 | 5.5 |
| 7 | 30 | 0.5 |
| 8 | 30 | 1.5 |
| : | : | : |
| 71 | 180 | 4.5 |
| 72 | 180 | 5.5 |

In step two, the full set of 19 parameters was optimized, with settings as follows: strategy = best/bin/1, $NP = 90$, $F = 0.5$, and $CR = 0.5$. The search ranges remained the same for the $c$ terms, but $k_f$ and $\theta_p$ search ranges were set to $0 \leq k_f \leq 10$ and $0 \leq \theta_p \leq 179$ degrees. The best parameter set from step one was provided as a starting guess, and the algorithm was allowed to run for 450 iterations, at total of 40,500 model simulations. Selecting the "best/bin/1" strategy resulted in a more aggressive sampling of the parameter space in which the current best population member was involved in all 90 "mating" interactions during a given iteration (Price et al., 2005).

The optimization process was parallelized by running models on 38 cores spread out over eight different computers. The process was directed by a MATLAB package

obtained from the MATLAB file exchange (Buehren, 2017). A typical model took about 50 seconds to solve and the entire optimization process took about 3.5 days per eye to complete all iterations.

### 4.3.5 Proof-of-Concept Testing

Proof-of-concept testing was performed to assess the efficacy of the optimization strategy. A set of arbitrary material properties were input into a rat sclera model and a forward calculation was performed to generate a test set of “pseudo-experimental” displacement data. The optimization protocol was tested against this data set to determine whether it could retrieve the known set of arbitrary properties. This was repeated for two different sets of material properties to ensure we could accurately determine the material properties.

### 4.3.6 Mesh Convergence

A numerical mesh convergence study was performed by systematically increasing the number of elements in the circumferential, meridional, and thickness directions and evaluating the z displacement at eight nodes located on the ONH and peripapillary region boundaries. However, we found that using the mesh that produced mesh-independent results (“the converged mesh”) in the optimization protocol described above would have resulted in computation times that were too long (on the order of a week or more per eye). To justify using a lower density mesh, a variation of the proof-of-concept test was repeated. Specifically, an arbitrary material parameter set was input into the converged mesh and used to generate a set of “pseudo-experimental” displacement data. A lower density mesh was then used in the optimization protocol to retrieve the known material parameters.

### 4.3.7 Sensitivity to ONH Stiffness

It was necessary to specify a value for ONH stiffness in the calculations, which was unknown and could not be determined by optimization due to inconsistent facet correlation (i.e. poor experimental data) in this region. Therefore, we assumed an ONH stiffness (see below) and assessed the sensitivity of model displacements to ONH stiffness by performing forward calculations with a sclera model. Because the ONH regions in the rat sclera models encompassed an area of the rat eye that contains a combination of neural, scleral, and vascular tissue, it was estimated that the Young's modulus of the ONH region lies within a range of 0.03 MPa to 1 MPa (Sigal et al., 2004). The ONH modulus was varied within this range, and the average total displacement for nodes in the peripapillary region was calculated for each modulus value.

## 4.4 Results

### 4.4.1 Proof-of-Concept Testing

We performed proof-of-concept testing to determine whether the optimization strategy provided acceptable solutions to the inverse problem. In testing, the cost function reached values of 0.021 μm and 0.005 μm for the two sets of specified material parameters, which is very small compared to the DIC "noise floor". In set one, the values for $c_1$ and $c_3$ were retrieved exactly and the value for $c_4$ had an error of only 0.2%. All but two $\theta_p$ values were retrieved exactly, and those two had errors of only 7° and 2°. All $k_f$ values but one had errors of less than 5%, and the last had an error of 10.1%. In set two, the $c_i$ values all had errors of less than 5%. All $\theta_p$ values but one were retrieved exactly, and that value had an error of only 1°. All $k_f$ values but one had errors lower than 10%, and that one had an error of 10.1%. We conclude that the optimization strategy converges

and provides an answer of sufficiently low error after the selected number of iterations (250 in step 1 and 450 in step 2).

### 4.4.2 Mesh Convergence

The mesh convergence study showed that mesh independence was reached with a mesh consisting of 10,707 nodes and 6900 elements (Figure 19). As mentioned, this mesh density would have been infeasible for use in the inverse method due to overly long computation times, so further testing was performed to determine whether a lower density mesh would be acceptable for use. The converged mesh was used to generate a set of "pseudo-experimental" data with an arbitrary parameter set, and a mesh containing 4626 nodes and 3018 elements was used to retrieve the known parameters. We judged that numerical accuracy would be considered as acceptable if the error in the retrieved parameter values was comparable to that seen in proof-of-concept testing. Using the 4626-node mesh, the cost function value was 0.218 μm. The retrieved value for $c_1$ had an error of 4%, $c_3$ had an error of 10%, and $c_4$ had an error of 2.5%. All $\theta_p$ values had errors of 1°, except for one which had an error of 6°. All $k_f$ values had errors of 8% or less. Although the cost function value was an order of magnitude higher than that seen in proof-of-concept testing, all the other parameters had comparable relative error. Thus, we considered the mesh with 4626 nodes to have sufficient numerical accuracy for the inverse FEM work, and used this as the production mesh going forward.

It should be noted that in this test, the arbitrary set of $k_f$ values were randomly generated, but forced to lie between 1 and 6, based on previous inverse FEM studies on the monkey eye (Girard et al., 2009). In an earlier proof-of-concept test, a large proportion (4 out of 8) of the randomly generated $k_f$ values were less than 1. That test was not successful, as the error of the retrieved $\theta_p$ and $k_f$ values was too high, although the

retrieved $c$ values all had errors less than 5%. This showed that if the overall degree of fiber alignment is too low, the method is not sensitive enough to resolve fiber directions accurately. This result is intuitive, because as $k_f$, decreases, the effect of $\theta_p$ on model behavior also decreases.

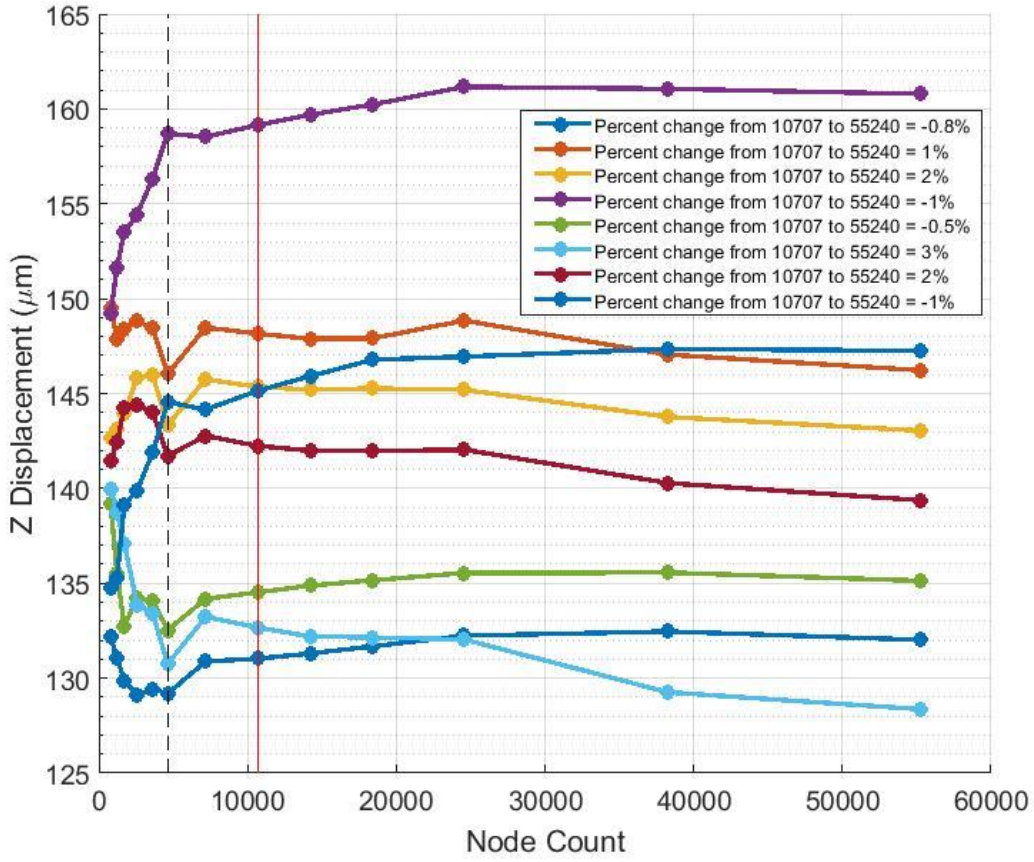


**Figure 19. Mesh convergence study. Each colored line indicates the total z displacement of a particular node. The legend details the relative error between the mesh considered to be converged (10,707 nodes, indicated by the vertical red line) and the most dense mesh with 55,240 nodes. The production mesh (4626 nodes) that was determined to have sufficient numerical accuracy is indicated by the dashed black line.**

### 4.4.3 Sensitivity to ONH Young's Modulus

To help select a suitable value for ONH Young's modulus, we investigated the sensitivity of peripapillary sclera displacement to changes in ONH stiffness. Varying the assumed ONH Young's modulus value from 0.03 to 1 MPa resulted in a 1.72 µm difference in mean peripapillary scleral nodal displacement (Figure 20). This shows that the model had a low sensitivity to ONH stiffness, since 1.72 µm is far below the experimental peripapillary sclera displacements, which were on the order of 140 µm. We estimated that

the ONH modulus was near 0.1 MPa and used this as the ONH modulus value in all simulations.

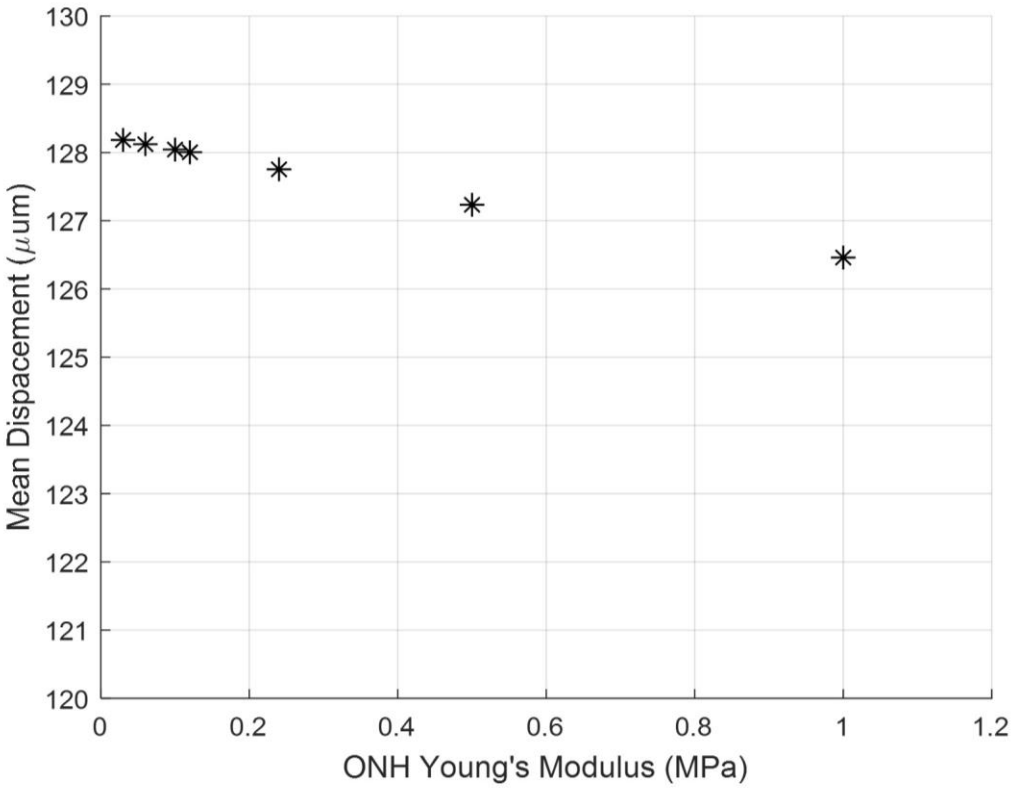


**Figure 20. Model sensitivity to assumed ONH Young's modulus. As the modulus of the ONH was increased, the mean nodal displacement of the peripapillary sclera decreased. The difference in displacement between the ONH Young's modulus values of 0.03 MPa and 1 MPa was 1.72 μm.**

### 4.4.4 Inverse Finite Element Modeling

Using the inverse method, scleral material parameter values were successfully calculated for a total of eight eyes. The average cost function value for all eyes was 5.8 μm (Table 5), which is much lower than the experimental displacement values ranging from approximately 50 μm to 230 μm. Although the models failed to match highly localized details of the experimentally-measured displacements in most eyes, they did exhibit good

agreement with the overall experimentally-measured displacement patterns (Figure 21). This was also true when comparing the model and experimental displacements at different pressure steps (not shown). The spread of $c_1$ and $c_4$ values was small, but there was high variability in $c_3$, with three of the values being an order of magnitude higher than the other five (Table 5). Note that three of the low $c_3$ values reached the specified lower boundary limit of 0.0001 MPa, and 7 $k_f$ values reached the specified upper boundary limit of 10. The $\theta_p$ and $k_f$ values were also highly variable (Figure 21–Figure 25). However, a few patterns did emerge. Specifically, the peripapillary $k_f$ values were significantly higher than those in the peripheral sclera (Wilcoxon; $p < 0.0001$) (Figure 22). The mean fiber direction was calculated for all eight scleral regions (Figure 25) as well as the peripheral and peripapillary sclera (Figure 24) according to circular statistics methods implemented in a MATLAB package obtained from the MATLAB file exchange (Berens, 2009). The fiber orientation was circumferential on average in the peripheral sclera, and to a lesser degree in the peripapillary sclera (Figure 24). Interestingly, the prI, prT, and prS regions displayed less variability in $\theta_p$ than did other regions (Figure 25). The prI and prT regions trended toward circumferential alignment (mean fiber directions of 3.2° and 176.5°), and the prS region trended toward near meridional alignment (mean fiber direction of 65.9°).

**Table 5. $c$, $k_f$, and cost function values obtained from inverse FEM. Also shown are age of animal and IOP reading at SD-OCT scan. OD indicates right eye and OS indicates left eye. IOP readings were not taken for rats 1 and 3.**

| | 1 OD | 3 OD | 7 OD | 8 OS | 12 OD | 14 OD | 18 OS | 20 OS | Mean (SD) |
|---|---|---|---|---|---|---|---|---|---|
| $c_1$ (MPa) | 0.04 | 0.03 | 0.043 | 0.051 | 0.043 | 0.045 | 0.031 | 0.019 | 0.0378 (0.0097) |
| $c_3$ (MPa) | 0.0022 | 0.0002 | 0.0054 | 0.0044 | 0.0004 | 0.0001 | 0.0001 | 0.0001 | 0.0016 (0.002) |
| $c_4$ | 243 | 342 | 312 | 274 | 312 | 433 | 349 | 363 | 329 (54) |
| $k_{f\_prS}$ | 2.76 | 0.60 | 5.11 | 0.60 | 3.17 | 1.85 | 1.26 | 1.22 | 2.07 (1.44) |
| $k_{f\_prI}$ | 2.70 | 4.10 | 1.87 | 9.84 | 5.15 | 3.95 | 1.67 | 4.54 | 4.23 (2.42) |
| $k_{f\_prT}$ | 2.86 | 1.68 | 7.03 | 6.12 | 2.75 | 0.13 | 2.04 | 1.41 | 3.00 (2.22) |
| $k_{f\_prN}$ | 5.16 | 2.28 | 3.14 | 3.96 | 3.82 | 2.73 | 0.97 | 0.51 | 2.82 (1.45) |
| $k_{f\_ppS}$ | 4.40 | 8.37 | 10.00 | 9.98 | 1.75 | 1.61 | 9.60 | 10.00 | 6.96 (3.52) |
| $k_{f\_ppI}$ | 2.88 | 1.48 | 3.96 | 2.91 | 2.10 | 4.94 | 7.70 | 9.73 | 4.46 (2.69) |
| $k_{f\_ppT}$ | 10.00 | 9.27 | 10.00 | 10.00 | 4.65 | 8.45 | 2.30 | 10.00 | 8.08 (2.77) |
| $k_{f\_ppN}$ | 5.45 | 5.39 | 7.41 | 10.00 | 6.04 | 4.48 | 0.86 | 6.13 | 5.72 (2.42) |
| *Cost (μm)* | 6.3 | 4.6 | 6.5 | 7.1 | 7.2 | 3.4 | 4.4 | 6.6 | 5.8 (1.3) |
| *Age (months)* | 13 | 13 | 11 | 11 | 11 | 11 | 10 | 10 | 11.3 (1.2) |
| *IOP at OCT (mmHg)* | NA | NA | 15.0 | 13.3 | 10 | 9.8 | 10.8 | 10 | 11.5 (2.2) |

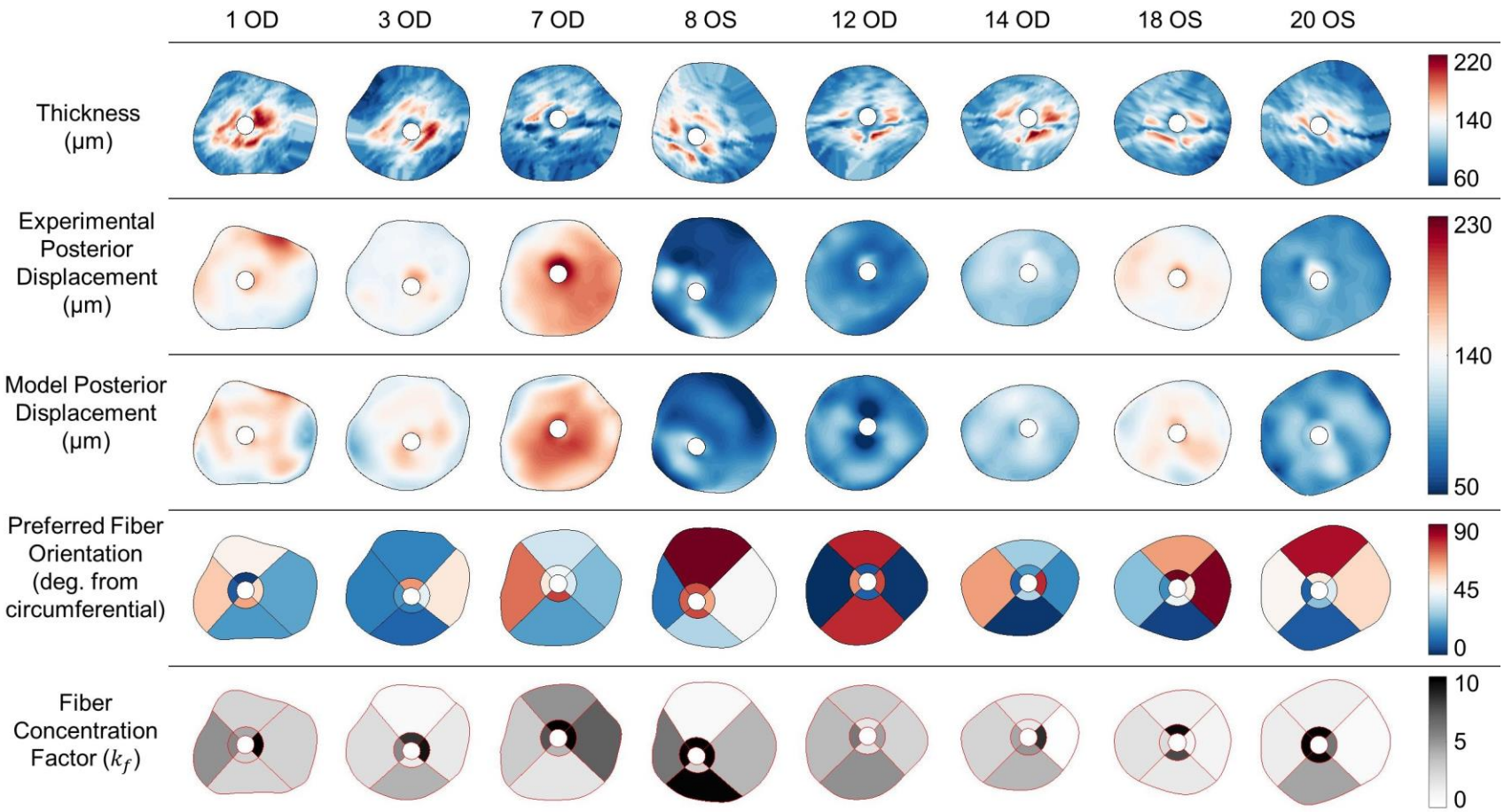
1 OD
3 OD
7 OD
8 OS
12 OD
14 OD
18 OS
20 OS
Thickness (μm)
220
140
60
Experimental Posterior Displacement (μm)
230
140
50
Model Posterior Displacement (μm)
Preferred Fiber Orientation (deg. from circumferential)
90
45
0
Fiber Concentration Factor ($k_f$)
10
5
0

**Figure 21. Comparison of scleral thickness (top row), experimental posterior displacement at the last pressure step as measured by DIC (second row), posterior displacement at the last pressure step of the finite element model (third row), preferred fiber orientation (fourth row), and fiber concentration factor (fifth row) for 8 rat eyes. In all cases, the superior direction is up and inferior direction is down. For OD eyes, the temporal direction is to the right and nasal is to the left. These directions are reversed in OS eyes. The preferred fiber orientation is displayed as the angle from a circumferential orientation. Note that a $\theta_p$ of either 45° or 135° is displayed as white. Scleral thickness was highest within and near the peripapillary region. Model displacements matched the overall pattern of experimental displacements but failed to match all local displacement patterns. The preferred fiber orientation was highly variable, but exhibited a general trend toward circumferential alignment. Fiber concentration factor was generally higher in the peripapillary sclera than the peripheral sclera.**

## 4.5 Discussion

This study provides the first quantification of rat scleral biomechanical material properties. Inverse FEM was used to fit experimentally measured displacement data obtained from whole globe inflation testing paired with DIC. The inverse method determined three parameters that dictated the nonlinear stiffening behavior of the entire posterior rat sclera ($c_1$, $c_3$, and $c_4$) and 16 parameters that dictated the anisotropy of eight scleral regions ($k_f$ and $\theta_p$). The parameter $c_1$ describes the mechanical behavior of the ground substance in the sclera, while $c_3$ and $c_4$ describe the behavior of a collagen bundle.

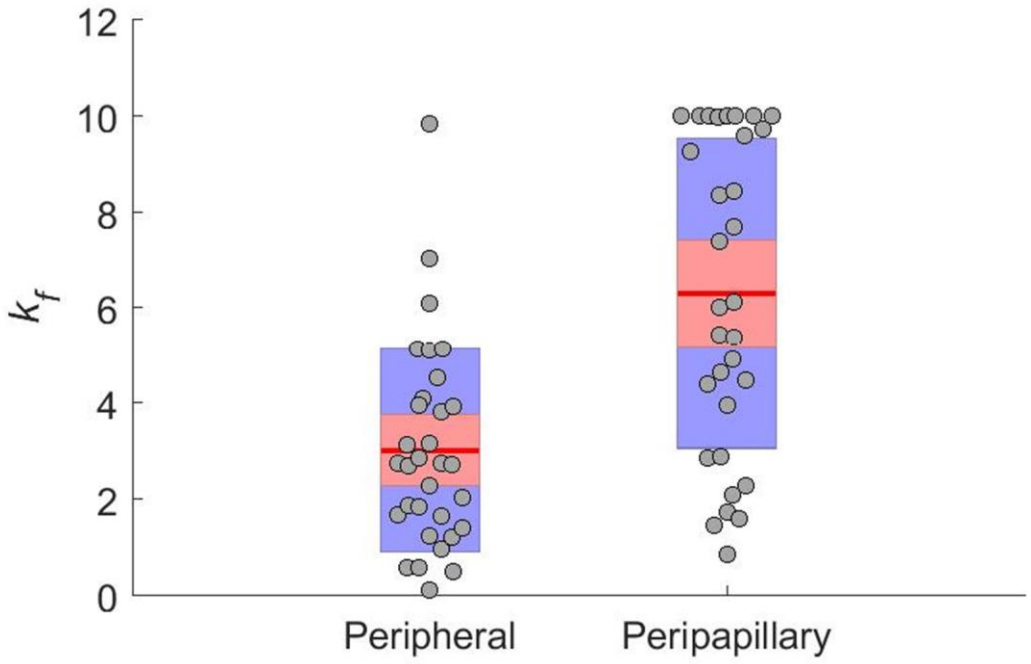


**Figure 22. Peripheral and peripapillary scleral fiber concentration factor ($k_f$) values as determined by inverse FEM. Circles indicate raw values, the red line indicates the mean, the red box indicates the 95% confidence interval, and the blue box indicates the standard deviation. The fiber concentration factor was higher (on average) in the peripapillary region (Wilcoxon; p < 0.0001).**

Several inverse FEM studies have been carried out on human and monkey eyes, but many of these studies used different approaches or material models for the sclera,

which makes comparisons to the present work challenging (Coudrillier et al., 2015, 2015, 2012; Grytz et al., 2014, 2014). However, Girard et al. (2009, 2011, 2009) used a similar inflation approach and the same material model to characterize the material properties of monkey eyes. Compared to these previous inverse FEM studies, the $c_1$ values that we obtained were an order of magnitude lower, while the $c_3$ and the $c_4$ values were comparable (Girard et al., 2011, 2009). In the monkey studies, only two $k_f$ values were assigned per eye (one for the peripapillary region and one for the peripheral region), and they ranged from ~0.5 to ~5.8. The peripheral $k_f$ values from the present study largely lay within that range, but our peripapillary $k_f$ values were higher (Figure 22). These higher values could indicate a greater degree of alignment in the peripapillary rat sclera than in the monkey, or they could be due to the fact that we assigned a separate $k_f$ value to each of the four peripapillary regions. However, as in the monkey study, the peripapillary $k_f$ values were higher than those of the peripheral sclera (on average). This indicates that the fibers in the peripapillary region were more aligned along the preferred axes, making these regions more anisotropic than those in the periphery.

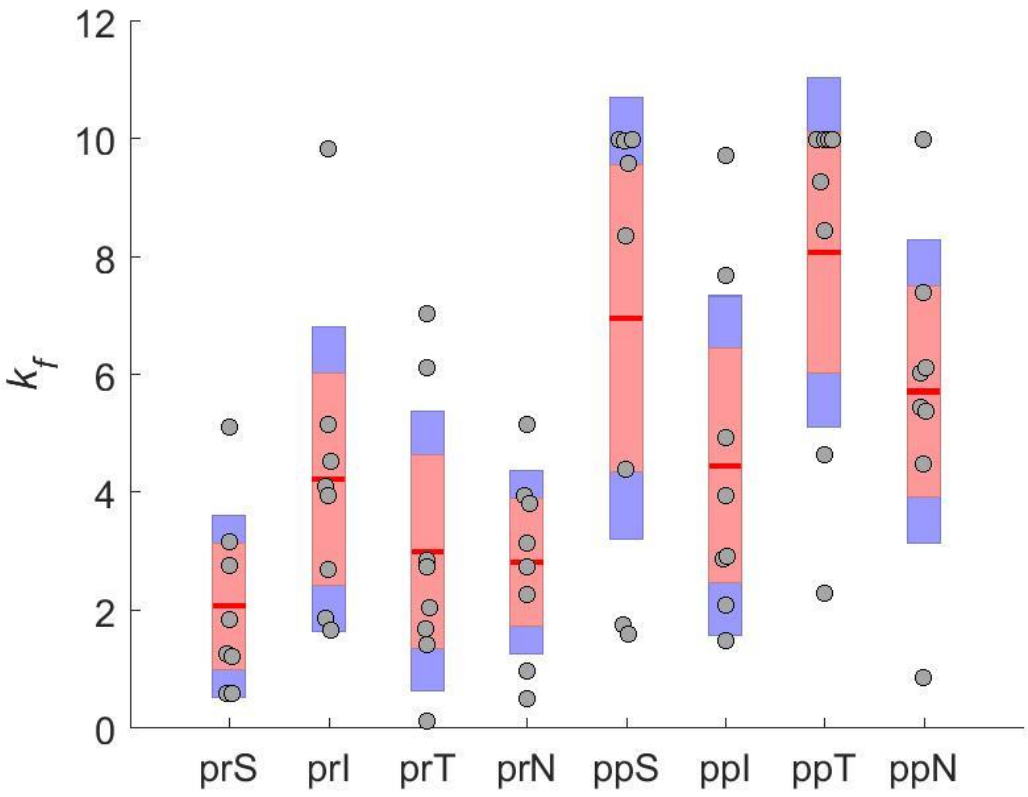


**Figure 23. Scleral fiber concentration factor ($k_f$) values, broken down by scleral region. Symbols indicate the same quantities as in Figure 22. There was a high variability in $k_f$ and no clear trends were apparent across individual regions. Abbreviations as in Figure 18.**

A high fiber alignment in the peripapillary sclera relative to the surrounding posterior sclera has been reported from experimental measurements on several species including the rat (Coudrillier et al., 2015; Girard et al., 2011; Pijanka et al., 2012, 2019). Specifically, the rat eye study by Girard et al., used small angle light scattering (SALS) to measure fiber organization and reported a “degree of fiber alignment” and “degree of circumferentiality” for regions throughout the rat sclera. Although Girard et al. report the same alignment trends that we found, our $k_f$ values generally indicated a much higher degree of alignment than those experimentally determined by SALS. Specifically, near the scleral canal, the area with the highest fiber alignment in the posterior sclera, Girard et al. reported a median

degree of alignment of 0.16, corresponding to a $k_f$ value of approximately 0.26 (see Appendix A), while our inverse FEM predicted a mean $k_f$ value of 6.31. The source of this discrepancy is unclear: it could be due to overestimation of $k_f$ by our inverse FEM method, spatial averaging in the SALS data, or limitations of the von Mises distribution used to describe collagen fiber orientation in the sclera. Indeed, a subsequent publication (Gouget et al., 2012) noted that collagen fiber distributions in sclera were better fit by an extension of the von Mises distribution, albeit at the cost of significant complexity. Future inverse FEM studies should consider a more complex and realistic fiber distribution function.

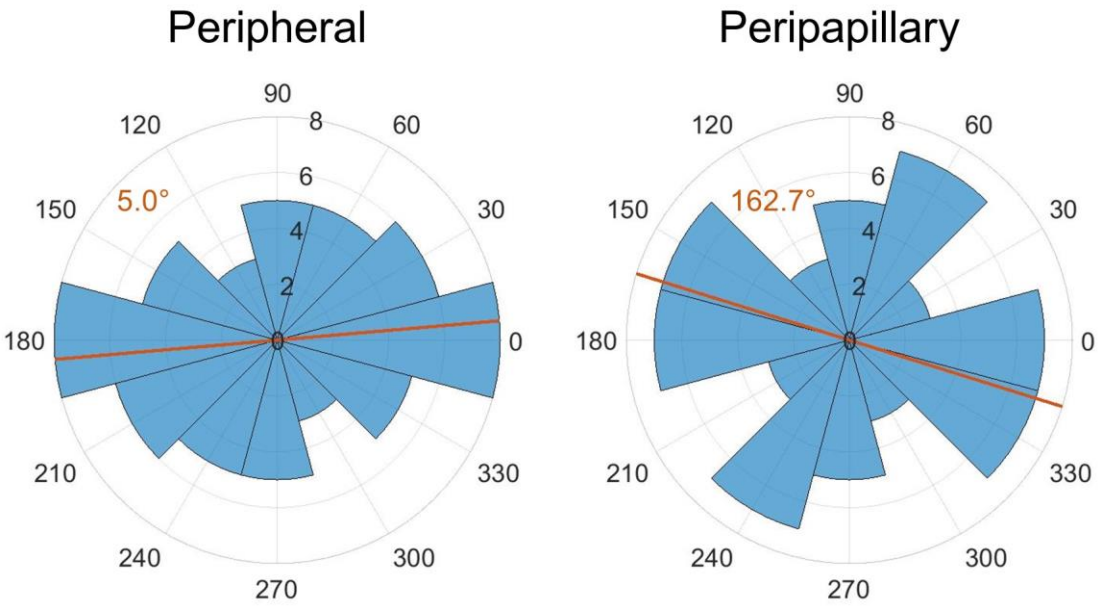


**Figure 24. Symmetric rose plots (circular histograms) of the fiber orientations in the peripheral and peripapillary scleral regions. Each blue wedge represents a bin of width 30°. The radius of each wedge indicates the number of $\theta_p$ values in that bin. Note that since the plot is symmetric, the number of $\theta_p$ values plotted is 64 rather than 32. The orange lines indicate the mean preferred fiber direction which is also given in the orange text. Both mean directions suggest an overall circumferential alignment in the peripheral and peripapillary sclera.**

In the present study, fiber alignment in the peripheral sclera was circumferential on average in both the peripheral and peripapillary sclera, which is the same trend as was

found in the inverse FEM monkey studies (Girard et al., 2011, 2009). At least two studies using experimental measurements of fiber organization have observed this pattern in the rat as well (Baumann et al., 2014; Girard et al., 2011). Note that Girard et al. (the study using SALS) defined a larger peripapillary sclera region than we did here, which is necessary to keep in mind while comparing their results with ours. Girard and colleagues did not report any trends in fiber direction by location around the ONH (i.e. superior, inferior, temporal, or nasal regions) as opposed to the trends we saw in regions prI, prT, and prS (Figure 25).

As is evident from Figure 21, there was a large range of total posterior displacement between eyes, and different eyes displayed different local patterns of displacement. This was expected as the same observation was made in the inverse FEM monkey studies (Girard et al., 2011, 2009). The models closely matched overall levels of displacement for each eye, leading us to conclude that the retrieved values for parameters determining the overall stiffness of the sclera ($c_1$, $c_3$, and $c_4$) were accurate. The low variability exhibited by these parameters supports this conclusion. However, it is possible that these values were overestimated due to the assumption that the eye was at a stress-free state at the reference pressure (see below). This inverse FEM approach also did not perfectly mimic all areas of particularly low or high displacement, indicating that the regionally-specific parameters ($k_f$ and $\theta_p$) may not have accurately described true fiber organization within each region. This is consistent with the large inter-eye variability in $k_f$ and $\theta_p$. Based on the proof-of-concept results, the material parameter values returned for each eye were likely the best set (or close to the best set) of values to match the experimental displacement patterns within the given modeling assumptions; however, those assumptions may have been too limiting to resolve true fiber parameters. This will be discussed further below.

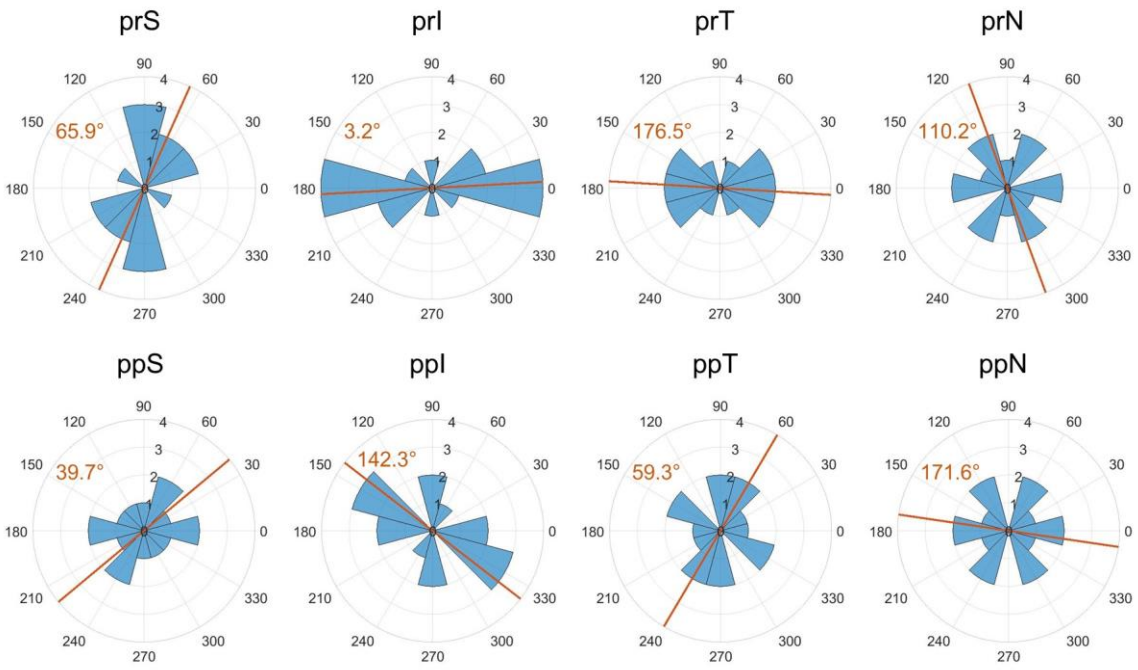


**Figure 25. Symmetric rose plots of the $\theta_p$ values for each scleral region. Symbols and figure interpretation are the same as in Figure 24. Mean fiber directions in the prI and prT regions suggest a trend toward circumferential alignment. The mean direction in prS was near meridional. Although the mean direction is plotted for all other regions, clear trends did not arise due to high variability. Abbreviations as in Figure 18.**

### 4.5.1 Limitations

#### 4.5.1.1 Modeling Assumptions

Several modeling assumptions may have affected the results of this study. One major assumption made in the models was that the sclera only has one layer of collagen fibers. Studies in other species have shown quite clearly that there are several layers of collagen fibers through the thickness of the sclera and that they often have different preferred fiber directions and degrees of alignment (Gogola et al., 2018; Pijanka et al., 2015). In some cases, such as the scenario where a layer of isotropic fiber orientation underlies that of a highly aligned layer, a Von Mises distribution does not accurately describe the true probability density function of fiber orientations (Gouget et al., 2012).

Thus, the values for $k_f$ and $\theta_p$ that we extracted should be interpreted as through-thickness average values for each scleral region. We also assumed that the size and arrangement of the eight scleral model regions were suitable for extracting fiber organization, but this may not have been the case. The patterns of fiber organization in the rat sclera may occur at a smaller scale than the size of the regions we chose. Both of these assumptions decreased the sensitivity of the sclera models, and probably contributed to their inability to recreate highly localized patterns of displacement seen in the experimental data. Further, we assumed a single Young's modulus value for the ONH region in all models and represented this region as an isotropic solid, even though it contained some scleral tissue. This may have affected the resulting retrieved parameters, particularly in the peripapillary region, although our sensitivity study indicated that this effect was likely small. The chosen search limits for optimized parameters may also have affected results. In three eyes, the $k_f$ values in one or two regions reached the specified upper boundary limit of 10, and in three eyes, the $c_3$ values reached the specified lower boundary limit of 0.0001 MPa, meaning that these seven $k_f$ values may have been underestimated and these three $c_3$ values may have been overestimated. Alternatively, reaching the specified limits for these parameters may reflect the overall difficulty/complexity of the inverse FEM procedure.

Finally, we used a simplistic method, "the relative pressure approach", to account for the effects of prestress. Inflation tests require a non-zero reference pressure to prevent buckling of the ocular to shell from affecting results. We assumed that the sclera was in a stress-free state at the reference pressure for each eye and applied loads in the sclera models that were relative to each eye's reference pressure. This is a common approach taken in the field (Coudrillier et al., 2012; Girard et al., 2009) but it is associated with error. Grytz et al. (2013) previously estimated that the error associated with this method could

overestimate the ground substance and fiber stiffness by 54% and 15%, respectively, although the error in fiber orientation was less than 1°. They presented two alternative methods that lowered this error. The first is a complex approach that involves computing the prestress using an iterative method and is not feasible for use in inverse FEM due to the additional computation time it would require. The second is called the "relative displacement approach" and is much simpler to implement. Briefly, it involves adding an extra pressure step (equal to the experimental reference pressure) to the beginning of the FE simulation. The resulting deformed geometry is taken as the reference state for all displacement and strain calculations but has a non-zero stress state. Unfortunately, this second approach was incompatible with our models because of the prescribed displacement boundary conditions that we applied. Grytz et al. had the advantage of using a 3D digitizer to extract scleral surface geometry that included the edge clamped by the testing rig, which allowed them to apply fixed and spring boundary conditions to the model edges. However, it should also be noted Grytz et al. estimated the error for a preload of 5 mmHg, whereas the preload pressures in our study were lower (2.2 mmHg to 2.9 mmHg). Therefore, the error associated with prestress in the current study would be less than Grytz et al. previously reported. Future iterations of the method presented here should include a better way to account for prestress if possible.

#### 4.5.1.2 Methodological Limitations

There were other limitations with the method that may have affected our results. First, the DIC method can produce artifacts due to optical issues such as glare or poor speckling. Although we made efforts to minimize these artifacts, it is possible that some remained and affected the results. Such artifacts probably did not significantly affect overall trends but could have introduced error into the $k_f$ and $\theta_p$ values, especially in the small peripapillary regions. Further, there were several sources of error associated with

SD-OCT thickness measurement location, although not with the thickness measurements themselves. First, there was error associated with projecting the thickness map to the posterior surface of the sclera model, since the SD-OCT images are artificially “flattened” but cannot easily be warped back to the actual shape of the sclera. We estimate that this location error was nearly 0 for locations close to the ONH, and on the order of 150 μm near the edges of the SD-OCT scans. However, we note that the largest variation in scleral thickness occurred near the ONH (Figure 21), so thickness measurement location accuracy in this region was most important. Second, there is error in the horizontal distance within b-scans reported by the SD-OCT system. The horizontal distance is an indirect measure derived from the angle of the rays, the optical power of the rat eye, and the size of the rat eye. Thus, error is introduced if differences between eyes are not accounted for. We can gain an estimate of the horizontal scaling error by comparing the axial length of an imaged eye with that of the standard eye used to calibrate the SD-OCT system by Leica, which was 6.29 mm (information provided by Leica). Assuming a variation in axial length of 6 to 7.5 mm for brown Norway rats around 14 months of age (Lozano & Twa, 2013), the scaling error ranges from 4.6% to -19.2%. Note that again, the absolute error in horizontal distance will be smaller near the ONH in the central SD-OCT scan compared to the edges, and thus this error likely did not significantly affect the most critical regions of our models. Lastly, the steps of delineating the sclera in SD-OCT scans and manually registering SD-OCT delineations with DIC data both had a certain level of subjectivity.

A few other limitations and assumptions are worth mentioning but likely did not significantly affect results. First, the actual IOP at each pressure step varied between eyes. This occurred because the flow rate entering each eye can differ, making the pressure drop across the flow sensor eye-specific. However, we accounted for this by directly

recording IOP throughout the inflation test and including eye-specific IOP data in the inverse FEM framework. Second, we assumed that the choroid did not have a significant effect on scleral deformation. As these were enucleated eyes without blood flow this is a reasonable assumption. Lastly, since only displacements at the posterior scleral surface were recorded, it was assumed that nodes on the model boundary surface shared displacements with the nearest node on the outer boundary edge of the posterior scleral surface.

### 4.5.2 Future Work

In the future, we plan to implement the results from this study in forward FE models of the rat posterior eye. Although it is not clear how accurately the fiber organization parameters describe true fiber directions, the experimental displacements were matched well by the inverse FEM, meaning that the retrieved material parameter sets can be used to inform improved models of the sclera. The FE models that implement the parameter values found in this study will be used to investigate the link between biomechanical insult to the ONH and glaucoma.

In future studies using this method, a combined imaging and inverse modeling approach, similar to that in (Coudrillier et al., 2015), is recommended. Recent studies using polarized light microscopy have provided invaluable information about scleral collagen organization in several species (Gogola et al., 2018). Since the posterior rat eye has the advantage of containing LPCAs that are visible from the outer surface, DIC data could be registered with fiber organization data obtained from polarized light microscopy. This would provide excellent fiber organization information that could be fed into the model at a much higher resolution than in the current study, and a more complex and realistic fiber distribution function could be implemented without adding unknown parameters. In

addition, including experimentally determined fiber orientation data would greatly reduce computation time because the DE algorithm would only have to optimize stiffness parameters. If possible, it would also be helpful to perform non-invasive thickness measurements on the eye while it is mounted in the inflation setup. SD-OCT with a telecentric lens may be able to accomplish this, but we were unable to do so with our existing SD-OCT machine. As mentioned, a better approach for including the effects of prestress should be utilized in future work. The relative displacement approach developed by Grytz et al. (2013) could be used if the geometry of the fixed (glued) scleral edges is recorded during testing. It may be possible obtain this data from an SD-OCT scan as mentioned above.

### 4.5.3 Conclusion

This study is the first to quantify rat scleral biomechanical properties. We implemented an inverse modeling approach that optimized material parameters in subject-specific sclera models to match displacement data acquired from whole globe inflation testing paired with DIC. The chosen material model accounted for the nonlinear and anisotropic properties of the sclera due to collagen fibers. Stiffness parameters for the entire posterior sclera and fiber organization parameters for several regions throughout the posterior sclera were calculated. There was extremely high variability in the regional fiber organization parameters, indicating that the method was likely not sensitive enough to resolve detailed fiber orientation data from specific regions within the sclera, especially within the peripapillary sclera. However, modelled displacements matched experimental displacements well, indicating that the method successfully retrieved scleral stiffness parameters, and the overall trends in the fiber data were consistent with what has been previously reported. Namely, fiber directions in the peripheral and peripapillary sclera were circumferential on average, and the degree of fiber alignment in the peripapillary sclera

was higher than in the peripheral sclera. These stiffness parameters and trends in fiber organization data can be used to inform modeling efforts of the rat ONH, particularly in the context of glaucoma biomechanics research.

# CHAPTER 5. FACTORS AFFECTING OPTIC NERVE HEAD BIOMECHANICS IN A RAT MODEL OF GLAUCOMA

## 5.1 Submission Details

Authors: Stephen A. Schwaner, Andrew J. Feola, C. Ross Ethier

Status: In preparation for submission to *J Royal Society Interface*

### Abstract

Glaucoma is the leading cause of irreversible blindness and is characterized by the death of retinal ganglion cells (RGC), the cells that carry vision information from the retina to the brain. Although it is well-accepted that biomechanics is an important part of the disease process, the mechanisms by which biomechanical insult, usually due to elevated intraocular pressure (IOP), leads to RGC death is not understood. Rat models of glaucoma afford an opportunity for learning more about these mechanisms, but the biomechanics of the rat optic nerve head (ONH), the primary region of damage in glaucoma, are only just beginning to be characterized. In a previous study, we built finite element (FE) models with individual-specific rat ONH geometries. Here, we developed a parameterized model of the rat ONH and used it to perform a sensitivity study to determine the influence that 6 geometric parameters and 14 tissue material properties have on rat optic nerve strains due to IOP elevation. Strain magnitudes and patterns in the parameterized model generally matched those from individual-specific models, suggesting that the parameterized model sufficiently approximated rat ONH anatomy. The five parameters with highest influence on optic nerve strains were optic nerve stiffness, IOP, sclera $c_4$ (collagen fiber uncrimping coefficient), sclera thickness, and the

degree of alignment of scleral collagen fibers. We conclude that efforts should be made to better characterize rat scleral collagen fiber organization and that a parameterized modelling strategy could eventually replace individual-specific models in the study of ONH biomechanics in the rat.

## 5.2 Introduction

Glaucoma is the leading cause of irreversible blindness, with an estimated 76 million cases worldwide (Tham et al., 2014). Blindness in glaucoma is due to the dysfunction and loss of retinal ganglion cell (RGC) axons, the conduits by which vision information is sent from the retina to the brain. Current therapies for glaucoma are all focused on lowering intraocular pressure (IOP), as elevated IOP is a causative risk factor for glaucomatous optic neuropathy. Unfortunately, these therapies are not always effective (Anderson, 2003; Okeke et al., 2009), and the development of novel therapies is made difficult by the current lack of understanding of glaucoma pathophysiology. In particular, it is not known how biomechanical insult to the ONH, widely-accepted as a key aspect of glaucoma pathophysiology (Burgoyne, 2011; Yang et al., 2017), affects the apoptosis of RGCs. Research to-date indicates that the answer is highly complex; remodeling, alteration of cell behavior, decrease in ONH blood flow, and blockage of RGC axonal transport may all result from increased mechanical stress and strain in the ONH (Alqawlaq et al., 2018; Morrison et al., 2011; Yang et al., 2017).

Rodent glaucoma models provide an opportunity to learn more about the role of biomechanics in glaucoma pathophysiology because of their low cost, ease of animal husbandry, and low genetic variability between individuals as compared to primate models (Morrison et al., 2011). These characteristics make them appropriate for use in mechanistic studies requiring high numbers of subjects. Further, the rat has benefits for

biomechanics studies over the mouse due to its larger eye size, which makes its tissues easier to handle for biomechanical testing. In addition, rat ocular hypertensive models present with important characteristics of human glaucoma, and rat models of both acute and chronic IOP elevation exist, allowing early and late events in the disease process to be studied.

However, there are differences in anatomy between the rat and human ONH that result in different ONH biomechanical environments (Schwaner et al., 2018, Schwaner et al. Submitted-b). Specifically, there are five key anatomic differences of note (Figure 26) (Morrison et al., 2011; Pazos et al., 2015): (1) There is not a connective tissue lamina cribrosa within the rat scleral canal. (2) Rather than passing through the center of the nerve at the level of the scleral canal, the central retinal artery (CRA) and vein (CRV) pass through the sclera on the inferior side of the nerve. (3) Between the optic nerve and scleral canal wall (primarily on the superior side of the nerve), there exists a vascular plexus, referred to as the perineural vascular plexus (PNVP). Thus, the scleral canal in the rat is sometimes referred to as the neurovascular scleral canal (Pazos et al., 2015). (4) An additional canal, the inferior arterial canal (IAC), inferior to the neurovascular scleral canal, exists in the rat sclera. The so-called scleral sling separates the IAC from the neurovascular scleral canal, and the CRA (along with other vessels) passes through the IAC. (5) Bruch's membrane (BM) extends toward the nerve axis from the superior side of the nerve, creating a superior BM "overhang" around which RGC axons are forced to pass.

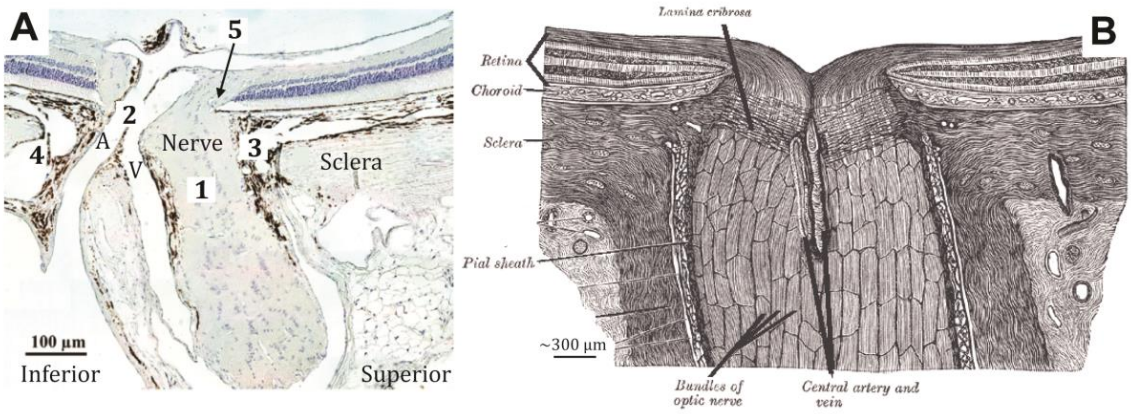


**Figure 26. Histologic section of the rat (A) and schematic drawing of the human (B) ONH. The anatomical differences between the two species are displayed, including 5 key differences of note (numbered 1-5) as described in the text. Abbreviations: central retinal artery (A) and central retinal vein (V). From (Schwaner et al., 2018).**

Our previous studies are the only three to-date that have focused on characterizing rat ONH biomechanics (Schwaner et al., 2018, Submitted-a, Submitted-b). These studies aimed to model stress and strain in individual-specific rat ONH geometries. However, individual-specific modeling is a time-intensive process, and thus, it cannot be used effectively to fully explore how anatomical variation affects the ONH response to elevated IOP.

Therefore, the purpose of this study was to conduct a sensitivity analysis to determine how variation in tissue material properties and anatomical features affect rat ONH biomechanics. To do so, we developed a rat ONH finite element model with parameterized geometry. Using Latin Hypercube Sampling, we varied six geometric parameters and 14 tissue material properties to create 800 rat ONH model variants. A partial rank correlation coefficient approach was used to rank the sensitivity of two outcome measures, namely 95$^{th}$ percentile first principal strain and 5$^{th}$ percentile third principal strain in the anterior optic nerve, to changes in the studied parameters. The

results from this study will guide future rat ONH modeling studies and provide biomechanical context for interpreting results from rat glaucoma studies with the ultimate goal of understanding the role of biomechanical insult in RGC pathophysiology.

## 5.3 Methods

### 5.3.1 Model Geometry

#### 5.3.1.1 Approach

Sensitivity studies in which geometric parameters are varied are especially difficult because they require the generation and meshing of hundreds of different model geometries. Thus, they are infeasible to carry out unless the process is automated. We therefore developed a custom Python script to build and mesh rat ONH geometries in Trelis (v16.5, Computational Simulation Software LLC, American Fork, UT), given a set of geometric input parameters. Model geometry variants were generated by varying input parameters about a baseline model, which was informed from measurements made on seven individual-specific rat ONH geometries used in a previous modeling study (Schwaner et al., Submitted-b). Unlike previous studies on the human ONH, we could not take advantage of axisymmetric anatomy. Thus, to capture complex ONH tissue anatomy, we lofted volumes through tissue cross sections represented by geometric primitives such as ellipses. Finally, a series of Boolean operations were used to produce the finalized geometry for each model.

#### 5.3.1.2 Measurements

To obtain information needed for parameterized geometry development, we measured key tissues within seven previously developed rat ONH model geometries (Schwaner et al., Submitted-b) using Rhino (v5 SR 14, Robert Mcneel and Associates,

Seattle, WA) and custom Matlab (2017a; Mathworks, Natick, MA) scripts. In the following, all surfaces are nonuniform-rational basis spline surfaces and all curves are Bezier curves.

The cross-sectional shapes of key tissues in the ONH were assessed at three reference surfaces: Bruch's membrane, the anterior scleral surface, and the posterior scleral surface. Measured tissues included the optic nerve, the CRA, and the CRV. Rhino was used to fit a curve to the intersection of a tissue boundary and a given reference surface. A group of 72 points were placed on the resulting curve, equally spaced along the curve length. A plane was fit through these points, and the intersection curve and the points were projected to the plane (Figure 27). Using a script from the Matlab file exchange (Gal, 2003), an ellipse was fit to the projected points. The centroid of the projected intersection curve, and the major and minor axes of the ellipse were recorded. The same process was repeated to assess several tissue "openings": BM opening (BMO), the anterior scleral canal opening (ASCO), and the posterior scleral canal opening (PSCO).

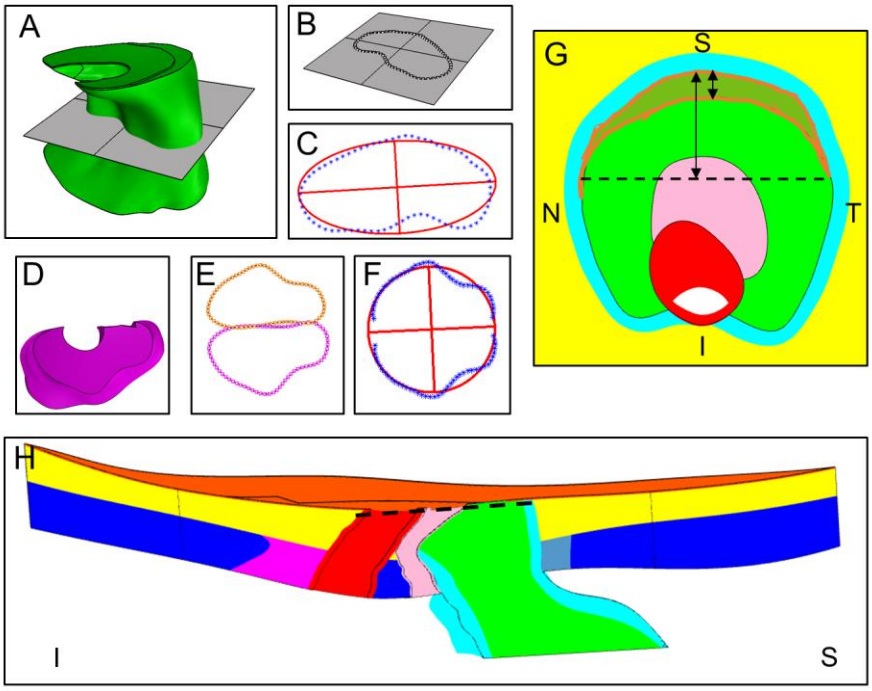


**Figure 27. Examples of measurements made on an individual-specific rat ONH geometry. A-C. Ellipse fitting of the optic nerve cross section at the PSCO plane. A. PSCO plane passing through the optic nerve. B. Intersection curve with points overlaid. C. Ellipse (red) fit through the points (blue). D.-E. Ellipse fitting of the IAC cross section at the anterior scleral surface. D. Top down (looking from anterior to posterior) view of the IAC. E. Cross section points of the IAC at the anterior scleral surface (magenta) and mirrored points (orange). F. Ellipse fit through subsets of the IAC cross section points and mirrored points. G. En face view of the optic nerve with BM hidden. The BM overhang region is outlined in orange. Arrows indicate measurements made to characterize the BM overhang. H. Superior-Inferior cut plane view of the entire individual-specific model for reference. The dashed line indicates the cut plane being viewed in G. Abbreviations: superior (S), inferior (I), nasal (N), temporal (T). Tissue colors: optic nerve (green), BM (orange), choroid (yellow), sclera (blue), pia mater (cyan), CRV (pink), CRA (red), PNVP (gray), IAC (magenta).**

The measurement method described above was slightly modified in several instances. Specifically, the IAC openings have shapes similar to a semi-ellipse. Therefore, the projected points representing an IAC opening shape were first mirrored about an axis coincident with the superior side of the projected IAC opening curve, and then an ellipse was fit to this set of points (Figure 27). Half of the resulting ellipse was taken as the shape of the given IAC opening. Additionally, since the optic nerve boundary is not directly

intersected by the sclera, the optic nerve cross section was assessed by finding the intersection between the nerve boundary and a plane fit through each scleral canal opening (SCO) boundary.

The CRV has two branches that emanate from the main lumen and travel in the inferior direction toward the IAC across the anterior scleral surface. The CRV cross-section near the anterior scleral surface was always measured just posterior to these branches. To obtain information about the optic nerve posterior to the scleral surface, the PSCO plane was offset approximately 75 μm posterior to the PSCO, and this offset plane was then intersected with the nerve boundary. Finally, although the BMO centroid was recorded as described above, we found that representing BMO as an ellipse was problematic for meshing the resulting models because such models often had very thin regions ("sliver geometries") on the temporal and nasal sides of the nerve, where the BMO cross-sectional boundary intersected the nerve cross-sectional boundary at a very shallow angle. Therefore, we instead took measurements of the BM overhang, measuring the distance between the superior edge of the nerve cross section and the inferior edge of the BM overhang along the superior-inferior axis (Figure 27). We also found the locations of the points at the nasal and temporal sides of the nerve-BM cross section at which the BM overhang ended.

#### 5.3.1.3 Generating the model geometry

We developed a custom Python script to generate and mesh rat ONH geometries using Trelis. The parameterized model consisted of the posterior eye, represented by a semi-spherical shell split into a peripheral region and a peripapillary (near the ONH) region that contained the ONH and surrounding tissues. To be comparable with our previous modeling, the peripapillary region was a disc of 1.5 mm diameter. The peripheral region

consisted of two layers, namely the choroid and the sclera, with the following dimensions derived from the literature: outer radius = 3.375 mm (Lozano & Twa, 2013), sclera thickness = 0.105 mm, and choroidal thicknesses = 0.055 mm (Pazos et al., 2015). The axis of the shell was aligned with the BMO centroid and the z-axis, where the z-axis pointed in the posterior direction, the y-axis pointed in the superior direction, and the x-axis pointed in the temporal direction. Although the model was fully three-dimensional, we built it such that it was symmetric about the y-z plane (i.e. the superior-posterior plane). The following tissues were included in the peripapillary region of the model: BM, the choroid, the sclera, the optic nerve, the pia mater, the CRV, the CRA, the PNVP, and the IAC.

To generate the model geometry, the following strategy was used (Figure 28). First, a hemispherical shell was generated and split into layers. Specifically, the peripheral region was split into two layers (the sclera and the choroid), while the peripapillary region was split into three layers: the sclera, the choroid, and BM. Note that the choroidal thickness in the peripapillary region was equal to the peripheral choroid thickness minus the BM thickness (0.052 mm in the baseline model). For all other tissues, a series of cross-sectional shapes were generated based on average values from tissue cross section measurements. Each tissue cross section was placed such that its centroid lay on the y-z (superior-posterior) plane and the z location was approximately concurrent with the appropriate tissue surface. The y location was defined based on the measured x-y distance from the BMO centroid. Once the entire set of cross sections for a given tissue was correctly positioned, a loft operation was performed, resulting in an initial tissue volume. A series of Boolean operations between the volumes was then performed to produce the final model geometry. For example, the CRA volume was subtracted from the CRV volume and then the lumen was subtracted from the CRV volume to produce the

CRV wall. The thicknesses of the CRA wall, the CRV wall, the BM, and the pia mater posterior to the sclera were set at 10 µm, 3 µm, and 3 µm, and 10 µm, respectively (Schwaner et al., 2018). Lastly, the PNVP filled the space between the pia mater and the scleral canal wall.

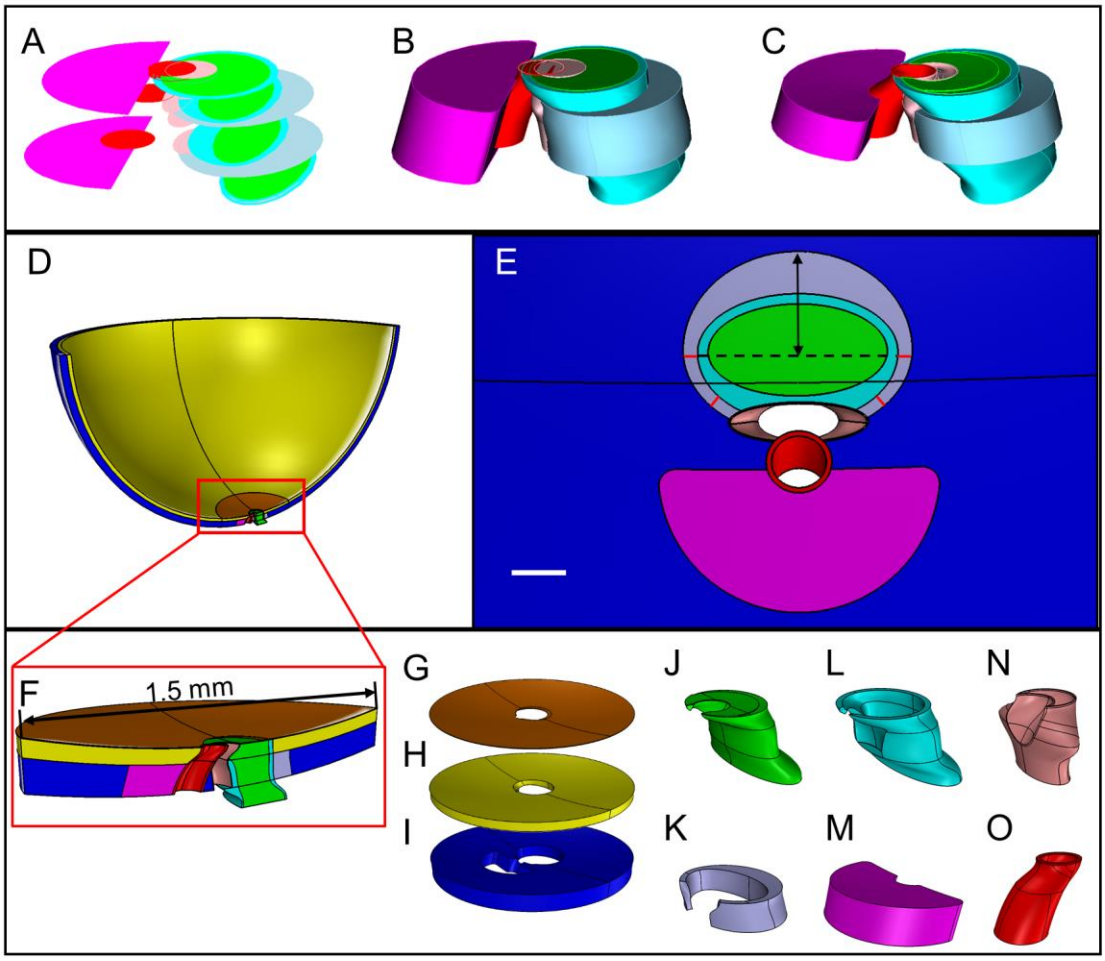


**Figure 28. Baseline model geometry. A Generating cross section shapes for the optic nerve, pia mater, PNVP (SCO), CRV, CRA, and IAC. B. Initial lofts through the cross sections. C. Final volumes after Boolean operations. Minor differences in color between A-C are due to limitations of the display software. D. Superior-inferior cut view of the entire model. E. En face view of tissues with all sections anterior and posterior to the sclera hidden. Red lines indicate where the PNVP thickness was held constant. Double-headed arrow indicates the dimension of the PNVP (SCO) that was varied in the sensitivity analysis. Scale bar is 100 μm. F. Superior-inferior cut view of the peripapillary region of the model. G-O. Final geometries of tissues within the peripapillary region: BM (G), the choroid (H), the sclera (I), the optic nerve (J), the PNVP (K), the pia mater (L), the IAC (M), the CRV(N), the CRA (O). Tissues shown in panels G-O are not precisely to scale. All tissue colors are the same as in Figure 27.**

Several other modeling decisions are worth mentioning. First, we ensured that the space between the optic nerve and CRV was always filled with pia mater tissue. This was accomplished by editing the inferior half of the pia mater cross section within the choroid

and sclera to intersect with the CRV central axis. In addition, allowing the shape of the SCOs to vary often resulted in a poor quality mesh. Therefore, we assumed that the thickness of the PNVP tissue surrounding the inferior pia mater was always 25 μm, based on measurements we made (Figure 28). However, the distance between the optic nerve centroid and superior scleral canal apex was still allowed to vary in the sensitivity analysis. In addition, as opposed to our individual-specific models (Schwaner et al., 2018), the CRV branches were not included in the CRV geometry. Finally, the shapes and sizes of the anterior (at the anterior sclera) and posterior (at the posterior sclera) IAC openings were assumed to be equivalent, and the same assumption was made for the ASCO and PSCO.

### 5.3.2 Finite Element Modeling Details

#### 5.3.2.1 Mesh

The model was meshed with a combination of 4-node tetrahedral, 6-node prism, and 8-node hexahedral elements. Prism elements were used to mesh BM and tetrahedral elements were used to mesh other tissues in the peripapillary region due to their complex shapes. The peripheral region was meshed with hexahedral elements. The peripheral region of the baseline model (see below) was meshed at approximately the same density (156,723 nodes) as our previous individual-specific models (175,000 nodes). Slightly fewer nodes were required because the parameterized model did not contain as much “sliver” geometry as the individual-specific models, and because we did not include as much of the posterior nerve and pia mater in order to save computational resources. The peripheral shell was meshed with the same density (57,344 nodes) as the comparable region of the generic posterior eye model used in our previous study (Schwaner et al., Submitted-b).

#### 5.3.2.2 Loads and Boundary Conditions

We used the “relative displacement” method to account for the effects of prestress in our models (Grytz & Downs, 2013), since the measurements of ONH geometry were all made from ONHs that had been perfusion-fixed at a non-zero IOP. As previously described (Schwaner et al., 2018, Submitted-b), the pressures applied in the model (IOP, CRA blood pressure (BP), and CRV BP) were ramped up in two steps. The first step brought the model to the stress state it would have experienced at perfusion fixation, i.e. IOP was increased from 0 to 10 mmHg, CRV BP was increased from 0 to 10 mmHg, and CRA BP was increased from 0 to 40 mmHg. The resulting state of the model was taken as the reference for all strain calculations. In the second loading step, CRA BP was increased from 40 to 110 mmHg, CRV BP was increased from 10 to 30 mmHg, and the magnitude of IOP increase was varied in the sensitivity analysis.

Boundary conditions were applied to the farthest anterior surface of the peripheral model region (at the eye equator). All nodes on this surface were fixed in the $z$ direction, nodes lying on the $x$-$z$ plane were fixed in the $y$ direction, and nodes lying on the $y$-$z$ plane were fixed in the $x$ direction. This had the effect of allowing nodes on this surface to move in the $r$ direction but not in the $z$ or $\theta$ directions, i.e. to allow radial expansion of the equator, but no twisting or axial translation.

#### 5.3.2.3 Constraints

Due to the nonconforming mesh between the peripheral region and the peripapillary region, tied constraints were applied to join these meshes at their interface. In our previous individual-specific models, the inferior and superior surfaces within the CRV would contact each other due to bending of the CRA around the scleral sling. In case this happened in the current study, we applied a general contact condition without friction to these surfaces.

We note that we manually examined a subset of ten models, picking those especially likely to incur contact due to a thin choroidal thickness. We only observed contact in one of these cases, and conclude that contact was not a common problem.

### 5.3.3 Tissue Material Models

The material models for all tissues were the same as in our previous individual-specific modeling study (Schwaner et al., Submitted-b). Briefly, all tissues except for the sclera were represented as isotropic neo-Hookean solids. All were considered nearly incompressible ($\nu = 0.49$) except for the PNVP, IAC, and choroid, whose $\nu$ values were included as parameters in the sensitivity study (see below). All of their elastic moduli values, $E$, were also varied in the sensitivity study.

The sclera was represented as an isotropic matrix (Mooney-Rivlin solid) reinforced by collagen fibers (Girard et al., 2009). The collagen fibers all lay within a defined material plane, and their directions varied about a defined preferred axis. Briefly, the stiffness of the matrix was defined by the first and second Mooney-Rivlin constants, $c_1$ and $c_2$, and its compressibility was defined by the bulk modulus, $K$. The nonlinear stiffening behavior of the collagen fibers was defined by the exponential fiber stress coefficient, $c_3$, and the fiber uncrimping coefficient $c_4$. in all models, we set $c_2 = 0$ MPa and $K = 1$ GPa (Girard et al., 2009, Schwaner et al., Submitted-a).

The fiber organization was defined by the preferred fiber direction, $\theta_p$, and fiber concentration factor, $k_f$, where $k_f = 0$ resulted in isotropic fiber orientation within the material plane and $k_f = \infty$ resulted in all fibers being oriented along the preferred direction. The material axes of the sclera were defined element by element such that all fibers lay tangent to the scleral surface, a value of $\theta_p = 0°$ resulted in a circumferential

preferred fiber direction, and a value of $\theta_p = 90°$ resulted in a meridional preferred fiber direction. Although all scleral tissue shared the same values of $c_1$ through $c_4$, the peripapillary sclera was subdivided into two regions: a peripapillary sclera region proper, and a scleral sling region. This approach allowed us to specify fiber organization in a region-specific manner. In all model iterations, we set $k_f = 0$ in the peripheral sclera, and varied the common $k_f$ value for the peripapillary sclera and scleral sling. Within the peripapillary sclera proper, we set $\theta_p = 0°$, since our previous inverse modeling study had found that fibers in the peripapillary sclera were oriented circumferentially on average (Schwaner et al., Submitted-a). Within the scleral sling, all fibers were oriented in the *x* direction (along the sling axis) based on a polarized light microscopy image kindly provided by Dr. Ian Sigal as well as images from the literature (Baumann et al., 2014).

### 5.3.4 Sensitivity Study

#### 5.3.4.1 Parameters

We selected a combination of parameters dictating model geometry, tissue material properties, and IOP to vary in our sensitivity study (Table 6). The baseline values for all parameters were selected either from our own data, or to be consistent with values used in our previous individual-specific modeling studies, which in turn were taken from the literature (Schwaner et al., 2018, Submitted-b). The ranges of values were chosen to be consistent with previous sensitivity studies on human ONH biomechanics (Feola et al., 2016; Sigal et al., 2005). In more detail, the baseline values of all geometry parameters were derived from our own measurements except for eye radius (Lozano & Twa, 2013) and the thickness of the sclera and choroid (Pazos et al., 2015), which were taken from the literature. All geometry parameters were varied by ± 20% from their baseline value (Feola et al., 2016; Sigal et al., 2005), except for IAC opening area which was varied by ±

40%,corresponding approximately to a ± 20% variation in IAC opening radius. All material properties were varied ± 60% from baseline values (Feola et al., 2016) with the exception of values for $c_4$ and Poisson's ratio, $\nu$. The range for $c_4$ was chosen as ± 20% because it appears in the exponent of the strain energy density function that dictates fiber behavior, so that changes in this parameter had a proportionately larger effect than changes in other parameters (Feola et al., 2016; Girard et al., 2009). We varied $\nu$ in tissues that are highly vascularized, i.e. contain a relatively large amount of blood compared to other tissues, and which thus may not adhere to the typical incompressibility assumption for soft tissues. Specifically, we varied the Poisson ration for the PNVP, IAC, and choroid (Feola et al., 2018). To be consistent with previous studies (Feola et al., 2016; Sigal et al., 2005), $\nu$ in these tissues was varied by ± 10% about a baseline value of 0.445. The baseline values for sclera $c_1$, $c_3$, $c_4$, were near the average values retrieved in our previous inverse finite element modeling study (Schwaner et al., Submitted-a). However, we chose to set the baseline $k_f$ value to be lower than the average for the peripapillary sclera obtained in that study. The peripapillary $k_f$ values spanned a wide range, and we were interested in how $k_f$ affected the ONH when varied from low alignment to moderate or high alignment. In addition, as discussed in more detail elsewhere (Schwaner et al., Submitted-a), a previous study that measured fiber alignment in rat eyes using small angle light scattering reported much lower levels of alignment than was found by our inverse method. Therefore, we picked a baseline $k_f$ value such that the range of $k_f$ would encompass values on the lower end of what was found by our inverse method. Lastly, IOP was varied from 20 to 30 mmHg because in our experience, this range spans the range of IOP levels in Brown Norway rats, considering both normal physiology and chronic experimentally-induced ocular hypertension (glaucoma).

#### 5.3.4.2 Latin Hypercube Sampling

Latin Hypercube Sampling (LHS) was chosen to explore the parameter space of the ONH model (van Noort et al., 1981; Raspanti et al., 1992). LHS is similar to the Monte Carlo sampling method, but is designed to be more efficient by ensuring that the entire range of each parameter is sampled with every LHS iteration. This is accomplished by dividing parameter ranges into a user-defined number of bins, and randomly assigning parameter values within each bin. The user is also given the option to define the shape of the sampled probability distribution for each parameter. We specified that all parameters be sampled from uniform distributions (Feola et al., 2016), and divided parameter ranges into 50 bins. LHS iterations were completed until the standard deviation of both outcome measures (see below) converged. A small and unchanging value of each standard deviation implied that our outcome measure was stable (Figure 29). All simulations were run using the solver FEBio (v2.9.0) (Maas et al., 2012).

#### 5.3.4.3 Outcome Measures and Parameter Ranking

We assessed the $95^{th}$ percentile first principal strain (95_1P) and $5^{th}$ percentile third principal (05_3P) strain in the anterior optic nerve, defined as the nerve tissue anterior to the PSCO. We focused on these extreme values of strain because they are most likely to induce mechanobiological response. However, the $95^{th}$ and $5^{th}$ percentile values were chosen rather than the $100^{th}$ and $0^{th}$ values in order to avoid artifactual extreme strain values due to poorly shaped elements. These values were obtained from computed strain distributions weighted by element volume to prevent regions with a high number of small elements from biasing results.

**Table 6. Sensitivity study parameter ranges**

| Name | Units | Baseline | Low | High |
|---|---|---|---|---|
| Choroid Thickness | mm | 0.055 | 0.044 | 0.066 |
| Sclera Thickness | mm | 0.105 | 0.084 | 0.126 |
| SCO Superior Radius | mm | 0.33 | 0.264 | 0.396 |
| Anterior Pia Thickness | mm | 0.02 | 0.016 | 0.024 |
| IAC Opening Area | $mm^2$ | 0.107 | 0.064 | 0.150 |
| Eye Radius | mm | 3.375 | 2.7 | 4.05 |
| IOP | mmHg | 25 | 20 | 30 |
| Sclera $\boldsymbol{c_1}$ | MPa | 0.035 | 0.014 | 0.056 |
| Sclera $\boldsymbol{c_3}$ | MPa | 0.0015 | 0.0006 | 0.0024 |
| Sclera $\boldsymbol{c_4}$ | | 330 | 264 | 396 |
| Sclera $\boldsymbol{k_f}$ | | 3.75 | 1.5 | 6 |
| BM $\boldsymbol{E}$ | MPa | 7 | 2.8 | 11.2 |
| Pia $\boldsymbol{E}$ | MPa | 3 | 1.2 | 4.8 |
| Choroid $\boldsymbol{E}$ | MPa | 0.1 | 0.04 | 0.16 |
| PNVP $\boldsymbol{E}$ | MPa | 0.1 | 0.04 | 0.16 |
| IAC $\boldsymbol{E}$ | MPa | 0.1 | 0.04 | 0.16 |
| Nerve $\boldsymbol{E}$ | MPa | 0.03 | 0.012 | 0.048 |
| PNVP $\boldsymbol{\nu}$ | MPa | 0.445 | 0.4005 | 0.4895 |
| Choroid $\boldsymbol{\nu}$ | MPa | 0.445 | 0.4005 | 0.4895 |
| IAC $\boldsymbol{\nu}$ | MPa | 0.445 | 0.4005 | 0.4895 |

To determine outcome measure sensitivity to parameter variation, a partial rank correlation coefficient (PRCC) approach was utilized (Feola et al., 2016). Briefly, a correlation coefficient in the range -1 (strong inverse correlation) to 1 (strong positive correlation) was calculated for each outcome measure with respect to each parameter. The correlation magnitudes for each parameter were then ranked within each outcome measure. In other words, each parameter was assigned a rank from 1 (weakest correlation) to 20 (strongest correlation) with respect to each outcome measure. The ranks were summed across outcome measure and normalized by the highest possible value, i.e. by 40. The resulting "cumulative influence factor" value represented the relative influence of each parameter on both outcome measures. The analysis also produces a *p*-value that gives the significance of correlation between each parameter and each output factor Table 7. We used Bonferonni correction to account for multiple comparisons with 20 input parameters. Thus, the Bonferonni corrected significance level was $\alpha = 0.05\ /20 = 0.0025$.

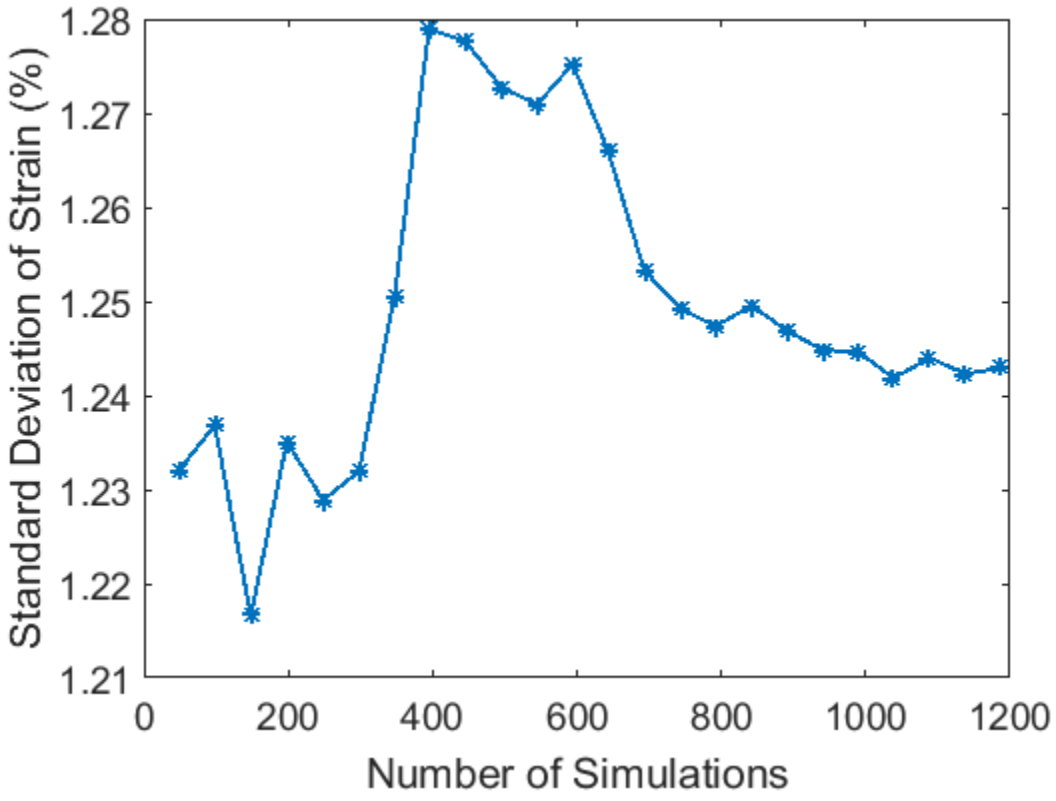


**Figure 29. Standard deviation of 05_3P strain showing convergence after 1188 model simulations. 95_1P strain converged similarly.**

### 5.4 Results

To ensure that the parameter space was sampled sufficiently, we examined the standard deviation of each outcome measure as a function of the number of LHS iterations. The standard deviations converged after 24 LHS iterations and 1188 model simulations (Figure 29), indicating that the outcome measures had stabilized. We note that 12 model variants failed to solve due to FEBio crashes of unknown origin, but this is not expected to affect the results since the number of failed models was very small compared to the total number of simulations in the study. Across all models, 95_1P strains ranged from 1.7% to 7.6%, with a median of 2.5%, while 05_3P strains ranged from -1.5% to -8.2%, with a median of -2.9%. Within the baseline model, in which IOP was raised to

25 mmHg, 95_1P strain was 2.4% and 05_3P strain was -2.8% (Figure 30). In order to provide a better comparison with values from our individual-specific modeling study (Schwaner et al. Submitted-b), we also solved the baseline model after applying an IOP of 30 mmHg, resulting in a 95_1P strain of 3.0% and a 05_3P strain of -3.6%. The ranges observed in the individual-specific modeling study were 3.1% to 3.7% for 95_1P strain and -3.5% to -4.2% for 05_3P strain, and thus our parameterized models were generally consistent with individual-specific modeling results. Within the baseline model, areas of high strain were observed along the inferior and superior sides of the nerve, with slightly higher strains in the inferior nerve (Figure 30). The six parameters demonstrating the largest influence on optic nerve strains were, in ranked order: optic nerve stiffness, IOP, scleral thickness, sclera $k_f$, sclera $c_1$ and sclera $c_4$ (Figure 31). These parameters, pia mater stiffness, and eye radius were significantly correlated with both 95_1P and 05_3P. Choroidal thickness, PNVP $\nu$, sclera $c_3$, and PNVP stiffness were significantly correlated with 05_3P. SCO superior radius was significantly correlated with 95_1P. The least influential parameters were SCO superior radius, anterior pia mater thickness, PNVP stiffness, BM stiffness, IAC stiffness, and IAC $\nu$.

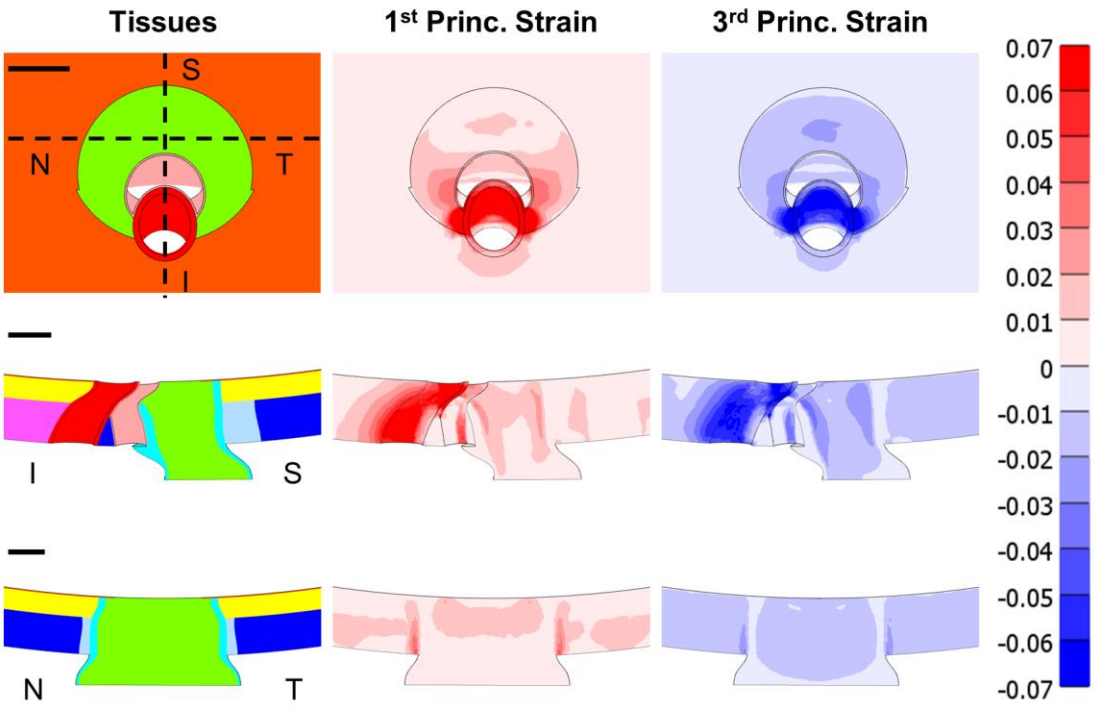


**Figure 30. First and third principal strains in the baseline model at an IOP of 25 mmHg. The en face view (top row), superior (S)-inferior (I) slice (middle row), and nasal (N)-temporal (T) slice (bottom row) are shown. Scale bars shown in the left column are all 100 µm. The superior-inferior and nasal-temporal slices are indicated by the dashed lines in the en face view displaying the model tissues. Tissue colors are the same as in Figure 27. The undeformed configuration is shown in all images to ensure that a consistent slice through the model is shown across columns.**

## 5.5 Discussion

We developed a parameterized rat ONH model and utilized it to investigate the influence of 20 different parameters on rat optic nerve strains. Although sensitivity studies have been performed on the human ONH using parameterized models (Feola et al., 2016; Hua et al., 2018; Sigal et al., 2005), the authors of those studies were able to take advantage of the near axisymmetric anatomy of the human ONH and build axisymmetric models. We overcame the difficulties introduced by the less-symmetric geometry of the rat ONH by automating a series of lofting and Boolean operations to construct our models.

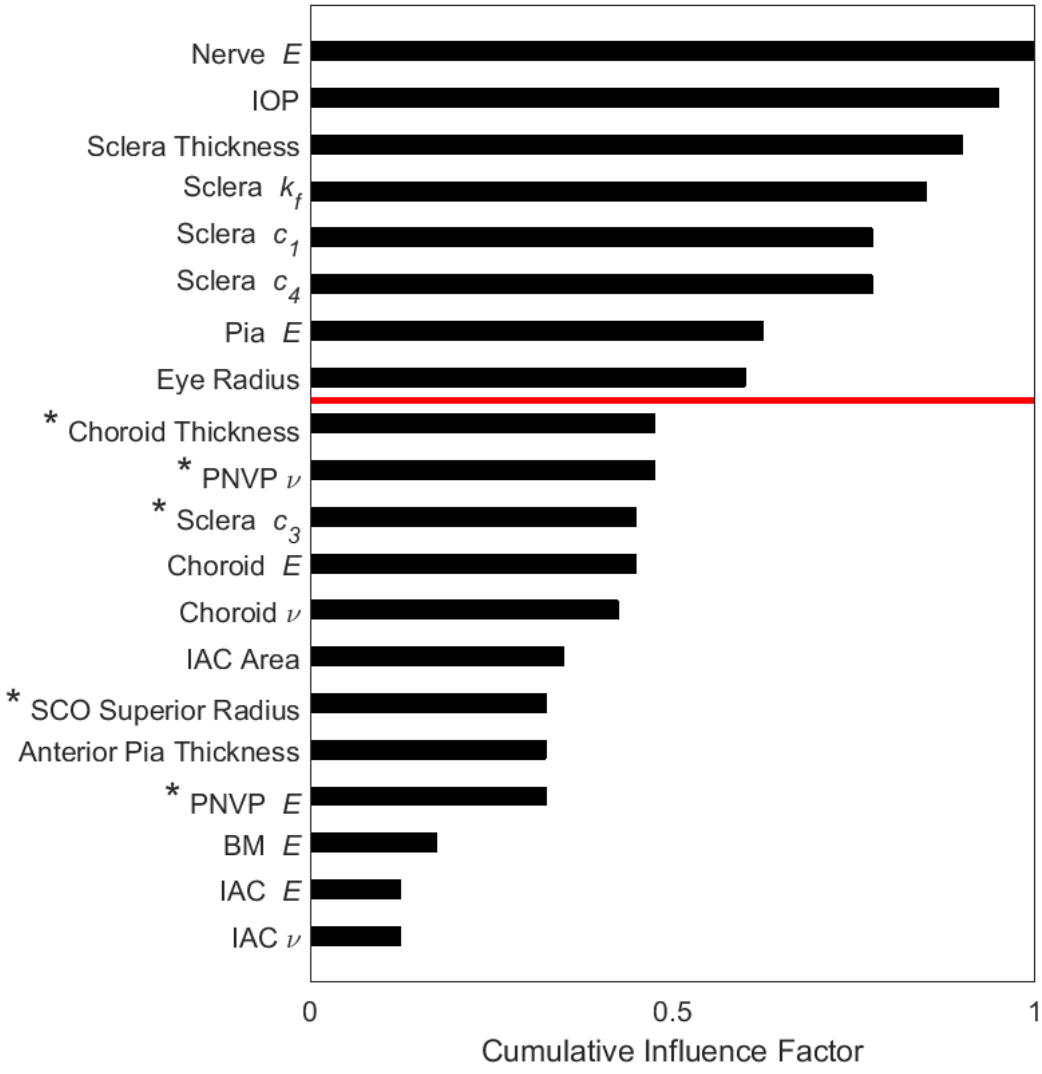


**Figure 31. Tornado plot showing the cumulative influence factor for each parameter included in the sensitivity study. The cumulative influence factor represents the relative influence that each parameter had on the strain outcome measures. Parameters above the red line were significantly correlated with both output factors. Parameters with a (*) were significantly correlated with only one output factor. Abbreviations: intraocular pressure (IOP), Bruch's membrane (BM), perineural vascular plexus (PNVP), scleral canal opening (SCO), inferior arterial canal (IAC).**

The strain patterns viewed in the baseline model were very similar to those seen in the individual-specific models of our previous study that were assigned circumferential

peripapillary collagen fibers (Schwaner et al., Submitted-b). In the baseline model, strain concentrations along the inferior and superior sides of the nerve were more pronounced than along the temporal and nasal sides, and the highest strains occurred in the inferior nerve. In addition, as with the individual-specific models, the optic nerve experienced more compressive strain than tensile strain. Strain magnitudes were also similar, with the range of values in this study containing those observed in the individual-specific modeling study. In addition, the baseline model strain magnitudes at 30 mmHg for 95_1P and 05_3P were just below and within the individual specific ranges, respectively. All of these similarities suggest that we effectively represented the rat ONH geometry with the parameterized model. This could be more rigorously confirmed by quantifying regional strains in the individual-specific and parameterized models, however, this would be difficult due to the way the rat optic nerve cross-sectional shape changes as it passes posteriorly through the BM, choroid, and sclera.

The data from the current study indicates that strain patterns in the rat ONH can be effectively represented using the parameterized model (or possibly an improved version as discussed below). The implication of this is that use of parameterized models will decrease or potentially even eliminate the need for highly labor-intensive individual-specific modeling. Instead, “near”-individual-specific modeling based on measurements of histology or non-invasive ONH imaging could be carried out within rat glaucoma studies with high numbers of animal subjects. By this, we mean that each model would be informed by measurements from a given eye as described above, even though the resulting models would not be exact replicas of the in vivo anatomy; hence the term “near”-individual-specific. Such an approach would allow ONH damage or cell response patterns from a rat eye to be directly compared with strain patterns from matching finite element models. This type of study would be extremely powerful for determining how specific forms

of biomechanical insult result lead to specific types of damage or cellular responses in the ONH.

**Table 7. Significance (p-values) for correlations between input parameters and the two outcome measures, 95_1P and 05_3P. The threshold for significance was taken as 2.50E-03 after Bonferroni correction (see text), with significant correlations being indicated by an asterisk (*).**

| Parameter | 95_1P | 05_3P | Parameter | 95_1P | 05_3P |
|---|---|---|---|---|---|
| Nerve $\boldsymbol{E}$ | 0.00E+00* | 0.00E+00* | Sclera $c_3$ | 3.60E-02 | 1.64E-03* |
| IOP | 0.00E+00* | 0.00E+00* | Choroid $E$ | 3.51E-02 | 5.24E-03 |
| Sclera Thickness | 5.24E-147* | 2.07E-138* | Choroid $\nu$ | 1.30E-02 | 1.45E-01 |
| Sclera $\boldsymbol{k_f}$ | 1.26E-17* | 1.01E-22* | IAC Opening Area | 7.75E-02 | 5.17E-02 |
| Sclera $\boldsymbol{c_1}$ | 1.38E-10* | 9.97E-14* | SCO Superior Radius | 1.21E-03* | 4.80E-01 |
| Sclera $\boldsymbol{c_4}$ | 2.42E-15* | 7.38E-13* | Anterior Pia Thickness | 3.77E-02 | 1.53E-01 |
| Pia $\boldsymbol{E}$ | 5.11E-04* | 1.55E-05* | PNVP $E$ | 6.71E-01 | 6.28E-05* |
| Eye Radius | 3.59E-08* | 2.09E-04* | BM $E$ | 5.06E-01 | 4.37E-01 |
| Choroid Thickness | 2.57E-01 | 3.77E-06* | IAC $E$ | 6.89E-01 | 3.94E-01 |
| PNVP $\boldsymbol{\nu}$ | 1.78E-01 | 7.79E-06* | IAC $\nu$ | 6.43E-01 | 4.68E-01 |

As expected, scleral properties were highly influential on rat optic nerve strain. Indeed, other than IOP and optic nerve stiffness, four of the six most influential parameters were features of the sclera: thickness, $k_f$, $c_1$, and $c_4$ (Figure 31). Previous sensitivity studies on the human eye also found that scleral properties were some of the most influential parameters on ONH biomechanics (Hua et al., 2018; Sigal, 2009; Sigal et al., 2005). However, it is interesting to note that the sclera parameter $c_3$ was much less

influential. Since $c_1$ is the only term that affects scleral compressive stiffness and since $c_4$ appears in the exponent term of the strain energy density function, it is not surprising that they are highly influential. Furthermore, previous studies have found that removing s-glycosaminoglycans from the sclera ground substance, which would likely correlate most with changes in $c_1$, had a substantial effect on scleral biomechanical behavior (Murienne et al., 2016, 2015). This is consistent with our findings. However, what was surprising was that sclera $c_1$ and $c_4$ were so much more influential than sclera $c_3$. This result is probably due to the fact that we accounted for preload, i.e. we evaluated strains occurring due to increases in IOP from a reference state in which IOP was 10 mmHg. The parameter $c_4$ becomes more dominant in the strain energy density function as stress increases and collagen fibers experience greater stretch. In other words, by focusing on strains referenced to an IOP of 10 mmHg, we did not include IOP levels in which $c_3$ might have dominated scleral tensile stiffness, and therefore likely would have had higher influence on optic nerve strains. To acquire accurate anatomical measurements and prevent buckling artifacts in eye specimens, researchers are forced to perfusion fix eyes or to apply a preload before mechanical testing. However, the data from this study brings up the question: is it adequate to only assess strains that occur at levels of pressure higher than those required for perfusion fixation or those used as preload before mechanical testing? Is it necessary to have information on deformation at low pressure levels in order to predict how cells will respond at glaucomatous pressure? In addition, is this knowledge needed to determine which aspects of the ONH biomechanical environment are most important to an ONH's susceptibility to glaucomatous damage and remodeling? These are important questions that should be considered in future modeling and experimental studies.

The high influence of the scleral $k_f$ parameter is not unexpected, but nonetheless is important to note. Highly detailed information about scleral fiber organization is starting to

become available (Gogola et al., 2018; Pijanka et al., 2019), but data for the rat is still inadequate for precise modeling. A previous study using small angle light scattering provided an important first step for quantifying regional rat scleral fiber direction and degree of alignment, but the results were highly variable from rat to rat (Girard et al., 2011). Our previous inverse modeling study on the rat sclera also returned highly variable fiber directions and alignment values (Schwaner et al, Submitted-a). The results shown here indicate the importance of applying new technologies to quantify fiber organization in the rat sclera to inform future modeling attempts. In addition, as $c_4$ is meant to model the uncrimping rate of collagen fibers, fiber crimp data should also be gathered.

The relatively high influence of the choroidal and pia mater stiffnesses make these tissues good targets for future studies aimed at determining rat ONH material properties. However, the geometry of the parameterized model from this study may need to be refined to confirm the importance of the choroidal stiffness. For simplicity, the choroid was modelled as having a constant thickness throughout the entire posterior eye, which likely resulted in overestimating its average thickness. Unlike scleral and pia mater stiffnesses, increased choroid stiffness resulted in increased optic nerve strains. Like the sclera, the pia mater is reinforced with collagen fibers (van Noort et al., 1981; Raspanti et al., 1992), so efforts should be made to quantify their organization and stiffness in the rat. Such stiffness properties will be quite challenging to assess since the rat pia mater is very difficult to isolate.

Of the parameters at the bottom of the influence rankings, only anterior pia mater thickness was surprising. We had hypothesized that pia mater properties would be highly influential in the rat because the rat optic nerve is surrounded by pia mater tissue as far anterior as BM, whereas the pia mater in the human terminates at the posterior sclera. On the other hand, it is helpful to know that PNVP stiffness, stiffness of tissue within the IAC,

and BM stiffness are not highly influential, as they would be extremely difficult to access in order to measure their material properties. Of course, as discussed in the Limitations section, this conclusion assumes that we chose good ranges within which to vary these parameters.

### 5.5.1 Limitations

As in our individual-specific modeling work, a major limitation of this study is our lack of knowledge about the material properties in the rat ONH. In one sense, this lack of knowledge made the current study highly worthwhile because it allowed us to identify first priorities for future tissue characterization studies. Nevertheless, this lack of knowledge may have affected the results. For example, incorrect material property baseline values or ranges can bias sensitivity study results, e.g. specifying unrealistically wide ranges for a parameter can artificially increase its cumulative influence factor. In addition, although our model was definitely an improvement from one in which the sclera was represented as a neo-Hookean material, the sclera was here represented as having only a single layer of collagen fibers, and as only having three sub-regions with unique fiber directions: peripheral sclera, peripapillary sclera proper, and the scleral sling. In reality, the sclera likely has multiple layers of fibers, and differing fiber organization by layer and location (Gogola et al., 2018; Pijanka et al., 2015). Lastly, as tissues that were ranked as being highly and moderately influential, the pia mater and choroid should be modelled differently. Specifically, we recommend that the pia mater be represented with a fiber-reinforced material model; unfortunately, the best way to represent choroidal properties is unclear.

Even though the parameterized models successfully recreated general strain patterns that were seen in the individual-specific modeling study, there were also limitations with the parameterized geometries. Although parameterized models such as

ours can never perfectly represent true anatomy, there are some aspects of the current model that could be improved while maintaining the ability to automatically generate ONH geometries. The most important of these is the assumption of constant thickness for the sclera. In addition, we informed the scleral thickness in this model with measurements that were taken in and near the peripapillary sclera (Pazos et al., 2015). Future work should include a sclera that, at the very least, varies in thickness with distance from the ONH and incorporates measurements of thickness from the peripheral sclera. As mentioned, the same improvements should be made to the choroid.

We chose to quantify strains within the anterior optic nerve, defined as the nerve tissue between the BM surface and the posterior scleral surface. This meant that the region within which we quantified strains varied with choroidal and scleral thicknesses, which may have artificially increased the influence of these parameters. However, a similar situation would have occurred had we picked an absolute distance from BM within which to quantify strains. Therefore, we chose to use the current analysis method since we were most interested in strain values within and anterior to the scleral canal, the region where glaucomatous damage occurs (Morrison et al., 2011; Tehrani et al., 2016).

Constraints should be added to the anterior faces of the CRA and CRV. In most models, the CRA (and adjacent CRV wall) “bends” around the scleral sling toward the superior CRV wall. This causes high strains in the small areas of the anterior-inferior nerve (not the main strain concentration seen in the superior-inferior slice view) that are adjacent to the CRA, as can be seen in the en face view (Figure 30). It was for this reason that we chose not to consider CRA stiffness, CRV stiffness, or blood pressure in this study, since we were concerned that varying these properties may have resulted in numerical convergence issues. These factors could be considered in future studies after constraints

are added to the anterior vessels' surfaces to prevent unrealistic deformations from happening.

Finally, the results from these models have not been validated. It may be possible to do so as non-invasive imaging, such as optical coherence tomography, improves, but even still will be extremely challenging.

## 5.6 Conclusion

We developed a parameterized finite element model of the rat ONH and used it to carry out a sensitivity study evaluating the influence of six geometric parameters and 14 material properties on optic nerve strains. Strain patterns and magnitudes coincided well with those observed in our previous study using individual-specific geometries, including the pattern that the highest strains occurred in the inferior optic nerve. After optic nerve stiffness and IOP, the most influential parameters were those that specified scleral thickness, scleral fiber degree of alignment, scleral fiber stiffness, and scleral ground substance stiffness. Thus, effort should be made to determine more accurate values for these properties. The results from this study can be used to inform future modeling studies, as well as studies aimed at determining rat ONH tissue material properties. In addition, an improved version of this parameterized model could potentially be used to generate near-individual-specific rat ONH finite element models in rat glaucoma studies in order to learn more about how patterns of biomechanical insult result in damage and influence cell behavior in glaucoma.

# CHAPTER 6. INDIVIDUAL-SPECIFIC MODELING OF RAT OPTIC NERVE HEAD BIOMECHANICS IN GLAUCOMA

## 6.1 Submission Details

Authors: Stephen A. Schwaner, Robert N. Perry, Alison M. Kight, Emily R. Winder, Hongli Yang, John C. Morrison, Claude F. Burgoyne, C. Ross Ethier

Status: In preparation for *J. Biomechanical Engineering*

### Abstract

Glaucoma is the second leading cause of blindness worldwide and is characterized by the death of retinal ganglion cells (RGC), the cells that send vision information to the brain. Their axons exit the eye at the optic nerve head (ONH), the main site of damage in glaucoma. The importance of biomechanics in glaucoma is indicated by the fact that elevated intraocular pressure (IOP) is a causative risk factor for the disease. However, exactly how biomechanical insult leads to RGC death is not understood. Although rat models are widely used to study glaucoma, their ONH biomechanics have not been characterized in depth. Therefore, we aimed to do so through finite element (FE) modeling. Utilizing our previously described method, we constructed and analyzed ONH models with individual-specific geometry in which the sclera was modeled as a matrix reinforced with collagen fibers. We developed eight sets of scleral material parameters based on results from our previous inverse FE study, and used them to simulate the effects of elevated IOP in eight model variants of each of seven rat ONHs. Within the optic nerve, highest strains were seen inferiorly, a pattern that was consistent across model geometries and model variants. In addition, changing the collagen fiber direction to be circumferential within the

peripapillary sclera resulted in greater decreases in strain than changing scleral stiffness. The results from this study can be used to interpret data from rat glaucoma studies to learn more about how biomechanics affects RGC pathogenesis in glaucoma.

## 6.2 Introduction

Glaucoma is the most prevalent cause of irreversible blindness, but current therapies are not always effective. The disease is characterized by the dysfunction of retinal ganglion cells (RGC), which send vision information from the retina to the brain via axons that form the optic nerve. Blindness in glaucoma results from RGC apoptosis, but it is not well understood what triggers this process. A large body of evidence indicates that biomechanical insult is an important driver in glaucoma pathophysiology, including the fact that elevated intraocular pressure (IOP) is a key risk factor for the disease (Campbell et al., 2014). Further, previous modeling studies have shown that elevated IOP results in increased stress and strain in the optic nerve head (ONH), the region in the posterior eye where RGC axons exit the globe (Hua et al., 2018; Sigal et al., 2004, 2009); in fact, the ONH is also a main and early site of glaucomatous damage (Burgoyne, 2011; Yang et al., 2017). However, the links between biomechanical insult and RGC apoptosis have not been elucidated.

This incomplete understanding is due in part to the complexity of the relationship between biomechanics and cell dysfunction. Biomechanical insult to the ONH leads to tissue damage/remodeling (Yang et al., 2017), as well as alteration of the behavior of several different cell types within the ONH, and thus, disruption of RGC homeostasis (Alqawlaq et al., 2018). In addition, different ONHs appear to have different levels of susceptibility to damage, as some people with higher-than-normal IOP never experience glaucomatous neuropathy, while others get glaucoma even at normal IOP levels.

However, the characteristics that predispose an ONH for damage are not known. Therefore, detailed study of the biomechanical environment of the ONH and cell phenotypic changes occurring in glaucoma are necessary.

More precise knowledge of the sequence and interaction of events leading to RGC death would provide information for much-needed novel therapies. To better understand the role that biomechanics plays in RGC apoptosis, a model is needed which allows both precise characterization of ONH biomechanics as well as the ability to observe cellular responses at all stages of the disease. The rat ocular hypertensive models of glaucoma are good candidates because they present with important characteristics of human glaucoma when IOP is elevated, and because both chronic and acute models of IOP elevation are available (Morrison et al., 2016, 2011). In addition, rat models have advantages over primate models for mechanistic studies because of their lower cost, ease of care, and low genetic variability between individuals.

However, the rat ONH has substantial differences in anatomy from that of the human and the primate (Pazos et al., 2015), and preliminary modeling studies on the rat ONH predicted that such differences result in patterns of mechanical stress and strain that differ from those in the human ONH (Schwaner et al., 2018). Of note are five key anatomic differences (Figure 32): (1) The rat does not have a connective tissue lamina cribrosa within its scleral canal. (2) Instead of passing through the center of the nerve, the central retinal vein (CRV) and artery (CRA) pass through the sclera on the inferior side of the nerve. (3) A vascular plexus, referred to as the perineural vascular plexus (PNVP), exists between the optic nerve and the neurovascular scleral canal wall. (4) An additional canal, the inferior arterial canal (IAC), exists in the rat sclera and is separated from the neurovascular canal by a so-called scleral sling. The CRA passes through the IAC. (5) On

the superior side of the nerve, Bruch's membrane (BM) extends toward the nerve axis, creating a BM "overhang" around which RGC axons are forced to pass.

Thus, an in-depth characterization of rat ONH biomechanics is needed, but, so far, our two previous studies are the only existing attempts (Schwaner et al., 2018, Schwaner et al. Submitted-a). In the first, we presented a method for building finite element models of rat ONHs with individual-specific geometries and showed the strain patterns computed in three such models. We assumed tissue material properties similar to those used in previous human modeling studies. In the second paper, we performed inverse finite element modeling to extract material properties of the rat sclera, as scleral stiffness has been previously shown to be highly important in rat ONH biomechanics (Hua et al., 2018; Sigal et al., 2005).

Our goal here was to build on these two efforts by creating rat ONH finite element (FE) models incorporating individual-specific geometries and scleral material properties extracted from our previous inverse FE modeling study. We built seven ONH model geometries and analyzed eight variants of each model by varying scleral material properties, resulting in a total of 56 simulations. We analyzed strain magnitudes and patterns within the rat ONH due to elevated IOP as well as the expansion of the optic nerve and neurovascular scleral canal openings. The results from this study can be compared with patterns of damage and cell behavior in rat glaucoma studies to learn more about the role of biomechanical insult in RGC pathophysiology.

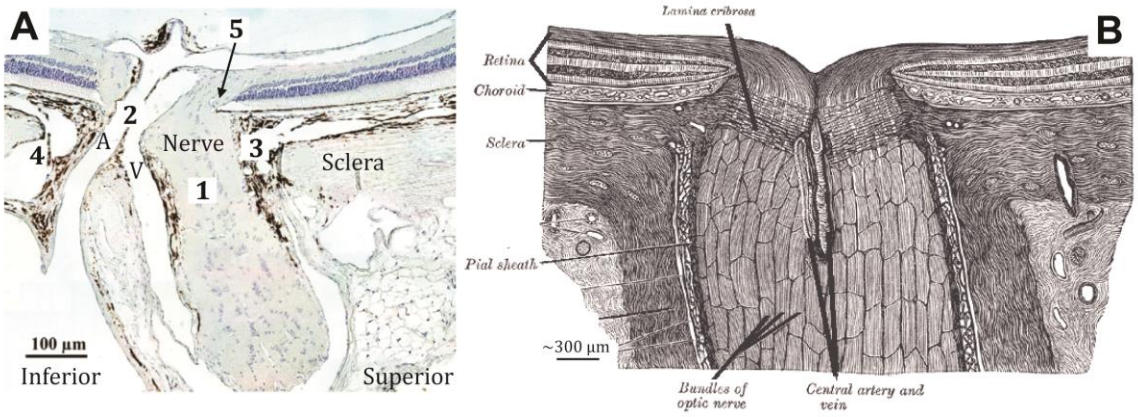


**Figure 32. Histologic section of the rat (A) and schematic drawing of the human (B) ONH illustrating their anatomical differences, including 5 key differences of particular interest (numbered 1-5) as described in the text. Abbreviations: central retinal artery (A) and central retinal vein (V). From (Schwaner et al., 2018).**

## 6.3 Methods

We have previously presented a detailed methodology for building FEM models of rat ONHs incorporating individual-specific geometry. That same method was used here, with the exception of steps to assign material properties to the sclera.

### 6.3.1 Model Geometry

Three dimensional (3D) digital reconstructions of eight normotensive male Brown Norway rat ONHs (ages 9.5 to 10.5 months) were built using a previously described method (Pazos et al., 2015). One of these reconstructions did not provide enough information for modelling, so it was excluded from the present study. Using custom software (Multiview, (Downs et al., 2007)), tissue boundaries were manually delineated within radial and transverse sections through the ONH. Bruch's membrane (BM), BM opening (BMO), the anterior scleral surface, the posterior scleral surface, the anterior

scleral canal opening (ASCO), the posterior scleral canal opening (PSCO), the optic nerve boundary, the posterior pia mater outer surface, and the side branches of the central retinal vein (CRV) were delineated within radial sections that shared an axis of rotation passing through the center of the optic nerve. The central retinal artery, main CRV lumen, and inferior arterial canal (IAC) (also referred to as the inferior arterial opening (Pazos et al., 2015)) were delineated by viewing transverse sections (perpendicular to the optic nerve axis). The resulting 3D point clouds were exported to Rhino (v5 SR 14, Robert Mcneel and Associates, Seattle, WA).

A more detailed description of the geometry building methodology can be found in (Schwaner et al., 2018). In brief, nonuniform rational basis spline surfaces were fit to the point clouds using several different Rhino tools. Next, through a series of Boolean operations and several other tools available in Rhino and the Rhino T-Splines plugin (Autodesk, Inc., San Rafael, CA), 3D volumes were built for the following tissues: BM, the choroid, the sclera, the PNVP, the IAC, the optic nerve, the CRA, and the CRV. We chose to exclude the dura mater but plan to include it in future studies that consider the effects of changes in intracranial pressure. Due to artifacts such as deformation of the sclera during tissue processing, only tissue contained within a cylinder of diameter 1.5 mm centered at BM opening were included in the model. To ensure that the resulting geometries accurately represented the true anatomy of the tissues, we used custom Rhino.Python and Matlab (2017a; Mathworks, Natick, MA) scripts to project the boundaries of tissue volumes onto the original digital sections through the ONH reconstructions. Lastly, the sclera was subdivided into several regions for assigning regional material properties. Specifically, the scleral sling (the scleral tissue between the IAC and scleral canal) was first divided from the rest of the sclera, after which the

remaining scleral volume was divided into superior, inferior, temporal, and nasal quadrants (Figure 33).

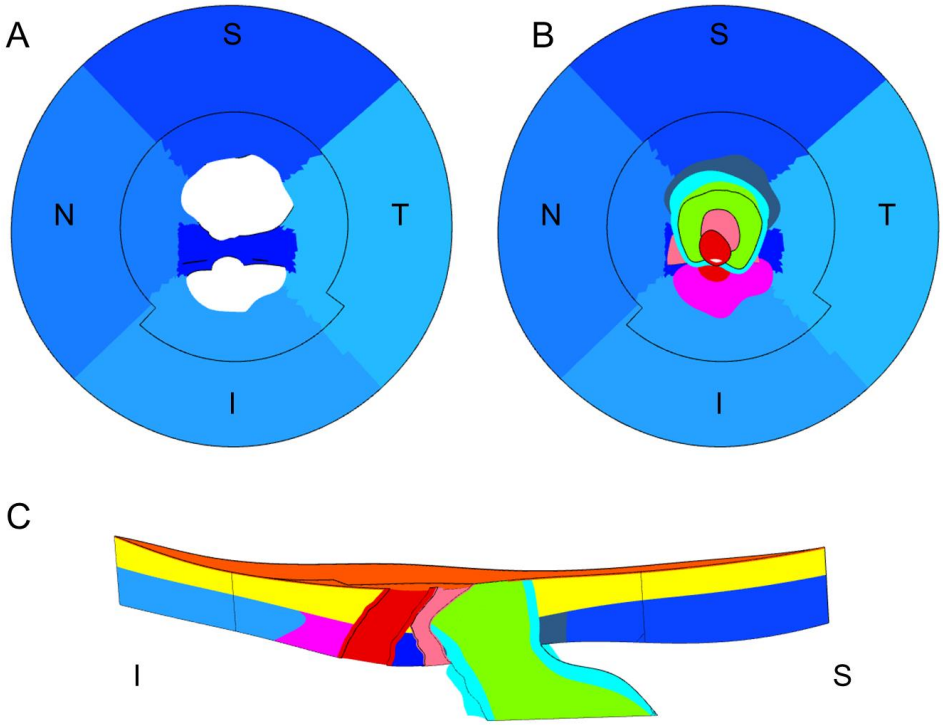


**Figure 33. MR11OS model geometry. A. En face view of the sclera. The scleral sling as well as the superior (S), nasal (N), inferior (I), and temporal (T) scleral quadrants are shown in different shades of blue. The neurovascular scleral canal is just superior to the sling, and the IAC is inferior to the sling. The black line indicates the division between the central region that was meshed with tetrahedral elements and the outer region that was meshed with hexahedral elements. B. En face view of the model with only the choroid and BM hidden. The optic nerve (green), pia mater (cyan), CRV (pink), CRA (red), IAC (magenta), and PNVP (gray) are visible. C. Superior-Inferior cut plane view of the model with all tissues visible. The choroid (yellow) and BM (orange) have been added to the view.**

### 6.3.2 Meshing and Constraints

Model geometries were imported into Trelis (16.5; Computational Simulation Software LLC, American Fork, UT) for meshing using a combination of 4-node tetrahedral,

6-node prism, and 8-node hexahedral elements. The tetrahedral elements were used in the central region of each model where the complex geometry could not be meshed with hexahedral elements, with the exception of BM, which was meshed with prism elements. The peripheral region of each model containing only BM, choroid, and sclera tissue was meshed with hex elements. Each model was meshed with approximately the same mesh density of 175,000 nodes or more (Schwaner et al., 2018). Tied constraints were applied at the interface of the outer (hex elements) and inner (tet and prism elements) model regions. Due to the CRV geometry in two models, MR05_OD and MR08_OD, contact occurred between the inner surfaces of the CRV vessel wall, so a general contact condition without friction was applied in those models.

### 6.3.3 Material Properties

All tissues other than the sclera were treated as isotropic, nearly-incompressible ($\nu$ = 0.49) neo-Hookean solids with the same elastic modulus values as in our previous publication (BM: 7MPa; pia mater: 3 MPa; CRA wall: 0.3 MPa; CRV wall: 0.3 MPa; choroid: 0.1 MPa; PNVP: 0.1 MPa; IAC: 0.1 MPa; optic nerve: 0.03MPa) (Schwaner et al., 2018).

The material model chosen to represent the sclera was an isotropic matrix reinforced by collagen fibers. The fibers lay within the plane locally tangent to the scleral surface, and their orientations followed a Von Mises distribution centered about a preferred direction (Girard et al., 2009). The stiffness of the ground substance (all tissue components other than collagen fibers) was dictated by the first Mooney-Rivlin coefficient, $c_1$, and its compressibility was dictated by the bulk modulus $K$. In all simulations, we assumed that the sclera was nearly incompressible and thus set $K = 1$ GPa (Girard et al., 2009, Schwaner et al. Submitted-a). The nonlinear stiffening behavior of the collagen fibers was dictated by the exponential fiber stress coefficient, $c_3$, and the fiber uncrimping

coefficient, $c_4$. The fiber directions were specified by the preferred fiber direction, $\theta_p$, measured relative to a local material coordinate system, and the degree of fiber alignment was specified by the fiber concentration factor, $k_f$. A value of $k_f = 0$ resulted in fibers being spread uniformly in all directions within the material plane (transverse isotropy), while a value of $k_f = \infty$ resulted in all fibers being aligned in the preferred direction, $\theta_p$. The material coordinate system of each element in the sclera was defined so that all fibers lay within a plane locally tangent to the scleral surface, with a value of $\theta_p = 0°$ representing a fiber axis in the circumferential direction, and a value of $\theta_p = 90°$ representing a fiber axis in the meridional direction.

We utilized scleral material parameter values determined by our previous inverse FEM study. However, we reasoned that it would have been inappropriate to combine them into a single set of "average" parameter values for modeling studies. Specifically, several parameters are used to describe the behavior of the sclera material model, and these parameters interact nonlinearly with each other to influence model behavior. Thus, an "average" set of parameters could potentially result in scleral biomechanical behavior that was physiologically unrealistic. Therefore, we instead selected four material parameter sets from eyes in the inverse FEM study, as described below, and created two groups of four parameter sets ("model variants").

How did we choose scleral material parameters? Since fiber stiffness likely dominates scleral mechanical behavior at high IOP, we chose four parameter sets based on their fiber stiffnesses. Specifically, using the $c_3$ and $c_4$ values from each eye, we generated stress-stretch curves for a single fiber from the following (Maas et al., 2012):

$$\sigma = c_3\left(e^{c_4(\lambda-1)} - 1\right) \tag{10}$$

where $\sigma$ is the fiber stress and $\lambda$ is the fiber stretch. We chose one eye with high fiber stiffness, two eyes with midrange fiber stiffnesses, and one eye with low fiber stiffness (Figure 34).

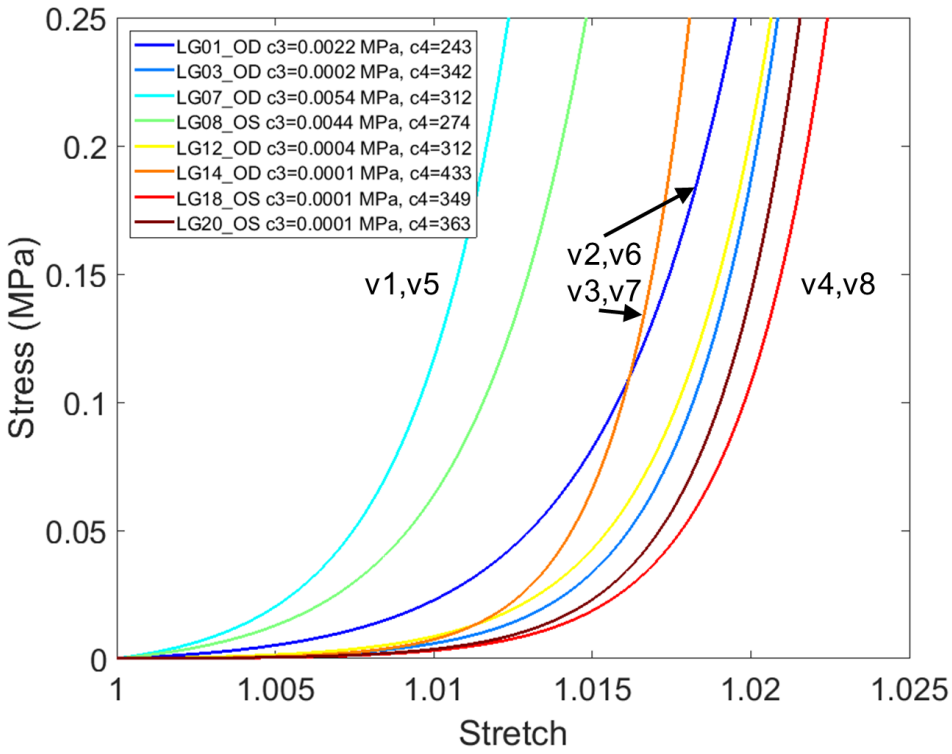


**Figure 34. Stress-stretch curves for a single collagen fiber generated from the $c_3$ and $c_4$ values obtained in (Schwaner et al., Submitted-a). We chose to use the four parameter sets associated with the curves indicated in the figure for the current study. Model variants (v) that utilized parameters from each set are also listed.**

Using these parameter sets, we then created 8 model variants, grouped into two sets of four. In variants 1-4, we used $c_1$, $c_3$, and $c_4$ values, determined as descried above and specified uniformly throughout the sclera. We also specified eye-specific fiber orientation parameter values for the sclera, taken from the same four eyes used to specify $c_1$, $c_3$, and $c_4$ values. In variants 5-8, we used the same set of $c_1$, $c_3$, and $c_4$ values, but

combined these with fiber orientation parameters averaged over several eyes (see below and Table 8). Note that the individual-specific geometries in the current study did not extend past the defined peripapillary scleral region in our previous inverse FEM study (outer diameter of 1.5 mm), so only the peripapillary $\theta_p$ and $k_f$ values were utilized here.

**Table 8. Scleral material properties applied in each of eight model variants (v).**

| | ***v1*** | ***v2*** | ***v3*** | ***v4*** | ***v5*** | ***v6*** | ***v7*** | ***v8*** |
|---|---|---|---|---|---|---|---|---|
| $c_1$ ***(MPa)*** | 0.043 | 0.04 | 0.045 | 0.031 | 0.043 | 0.04 | 0.045 | 0.031 |
| $c_3$ ***(MPa)*** | 0.0054 | 0.0022 | 0.0001 | 0.0001 | 0.0054 | 0.0022 | 0.0001 | 0.0001 |
| $c_4$ | 312 | 243 | 433 | 349 | 312 | 243 | 433 | 349 |
| $\theta_{p\_T}$ **(°)** | 142 | 54 | 79 | 17 | 0 | 0 | 0 | 0 |
| $\theta_{p\_S}$ **(°)** | 137 | 2 | 19 | 89 | 0 | 0 | 0 | 0 |
| $\theta_{p\_I}$ **(°)** | 104 | 63 | 149 | 138 | 0 | 0 | 0 | 0 |
| $\theta_{p\_N}$ **(°)** | 51 | 173 | 8 | 129 | 0 | 0 | 0 | 0 |
| $\theta_{p\_sling}$ **(°)** | sling axis | sling axis | sling axis | sling axis | sling axis | sling axis | sling axis | sling axis |
| $k_{f\_T}$ | 10 | 10 | 8.45 | 2.3 | 6.31 | 6.31 | 6.31 | 6.31 |
| $k_{f\_S}$ | 10 | 4.4 | 1.61 | 9.6 | 6.31 | 6.31 | 6.31 | 6.31 |
| $k_{f\_I}$ | 3.96 | 2.88 | 4.94 | 7.7 | 6.31 | 6.31 | 6.31 | 6.31 |
| $k_{f\_N}$ | 7.41 | 5.45 | 4.48 | 0.86 | 6.31 | 6.31 | 6.31 | 6.31 |
| $k_{f\_sling}$ | 6.31 | 6.31 | 6.31 | 6.31 | 6.31 | 6.31 | 6.31 | 6.31 |

In more detail**,** in variants 1-4, each of the scleral quadrants received its own $\theta_p$ ($\theta_{p\_S}, \theta_{p\_I}, \theta_{p\_T}, \theta_{p\_N}$,) and $k_f$ ($k_{f\_S}$, $k_{f\_I}$, $k_{f\_T}$, $k_{f\_N}$) values. In variants 5-8, we utilized fiber stiffness properties from the four selected eyes but assumed that $\theta_p = 0°$ and $k_f = 6.31$

for all scleral quadrants. This approach was motivated by observations of high variability in regional $\theta_p$ and $k_f$ values from the iFEM study (Schwaner et al., Submitted-a), which led to concerns about noisiness in the $\theta_p$ and $k_f$ values for individual scleral regions. Since the overall data trends indicated that fibers were oriented circumferentially, on average, we considered it to be useful to create models that reflected this average fiber orientation.

The scleral sling was not included as a specific region in our previous iFEM study, and thus we did not have material parameters for this region. Based on a polarized light microscopy image kindly provided by Dr. Ian Sigal and other images from the literature (Baumann et al., 2014), in all variants 1-8 we set the fiber direction within the scleral sling, $\theta_{p\_sling}$, to be parallel to the sling axis (i.e. angled slightly from the Nasal-Temporal direction). We also set the fiber concentration factor, $k_{f\_sling}$ to be 6.31, which was the average value for peripapillary scleral regions in the iFEM study.

In summary, we ran eight simulations (one for each model variant) within each of the seven rat ONH geometries, for a total of 56 simulations.

### 6.3.4 Loading Conditions

Since the ONH geometries were perfusion-fixed at a non-zero IOP, we used the "relative displacement" method to account for the effects of prestress (Grytz & Downs, 2013). Therefore, the pressures in the model (IOP, CRA blood pressure (BP), and CRV BP) were ramped up in two steps, as previously described (Schwaner et al., 2018). In the first step the ONH was loaded until it reached the stress state experienced at perfusion fixation. Thus, IOP was increased from 0 to 10 mmHg, CRV BP was increased from 0 to 10 mmHg, and CRA BP was increased from 0 to 40 mmHg. In the second step, IOP was increased from 10 to 30 mmHg, CRV BP was increased from 10 to 30 mmHg, and CRA

BP was increased from 40 to 110 mmHg. The resulting model configuration after the first loading step was used as the reference configuration for all displacement and strain calculations. Thus, all displacement and strain values reported reflect the change due to an IOP increase from 10 to 30 mmHg. Reported stress values reflect the change due to IOP increase from 0 to 30 mmHg (i.e. they include prestress).

### 6.3.5 Boundary Conditions

To apply boundary conditions to the ONH models, we used a submodeling boundary approach, as previously described in detail (Schwaner et al., 2018). However, we here solved four posterior eye model versions instead of the one model that was used previously. In more detail, to match the scleral stiffness properties of the ONH models, we generated four posterior eye model versions, one for each set of $c_1$, $c_3$, and $c_4$ values. Further, since the purpose of the posterior eye model was to provide suitable boundary conditions for the ONH model, rather than to determine strain patterns near the ONH, we assumed $k_f = 0$ throughout the sclera in all four versions, eliminating the need to specify a $\theta_p$ value. IOP was applied in two steps from 0 to 10 mmHg and 10 to 30 mmHg as in the ONH models. Nodes on the farthest anterior surface of the model (at the eye equator location) were not allowed to move in the $z$ or $\theta$ directions but were allowed to displace radially, where the $z$ axis was aligned with the central axis of the half sphere. To apply boundary conditions to the ONH models, each ONH model was semi-automatically registered with the posterior eye model and displacements from nearby nodes in the posterior eye model were interpolated to nodes on the peripheral (farthest from the optic nerve) surface of the ONH model.

### 6.3.6 Outcome Measures

All simulations were run using FEBio (v2.9; (Maas et al., 2012)). To assess the effect of elevated IOP on the ONH, we calculated the $50^{th}$ (median) and $95^{th}$ percentile first principal strain and the $50^{th}$ and $5^{th}$ percentile third principal strain, in the anterior nerve. The anterior nerve was defined as the nerve tissue from BM opening to approximately 150 µm posterior to the opening. The $95^{th}$ and $5^{th}$ percentiles were selected rather than the $100^{th}$ and $0^{th}$ in order to exclude the extreme values often produced by a few elements of poor shape quality. In addition, all percentiles were weighted by element volume to prevent areas of the nerve that contained large numbers of relatively small elements from biasing the results.

We also calculated the change in area of the ASCO, of the PSCO, of the nerve opening at the ASCO (nerve-ASCO), and of the nerve opening at the PSCO (nerve-PSCO). To find ASCO area, we fit a plane through the nodes lying on the ASCO edge, projected those nodes to the plane, and found the area enclosed in the resulting curve. This was repeated for the PSCO. Next, the planes fit through the ASCO and PSCO were used to select nodes outlining the nerve boundary at the level of each opening. Nodes on the nerve boundary surface within 5 µm of each plane were selected, and the areas of the nerve-ASCO and nerve-PSCO were then calculated using the same method as for the ASCO and PSCO.

As detailed by Pazos et al. (Pazos et al., 2016), the eyes used in this study were obtained from rats in which one eye of each rat was normotensive (the eyes we modeled) while the contralateral eyes were hypertensive. The axonal damage within the optic nerve of each hypertensive eye was assessed using a grading system (Jia et al., 2000), which assigned scores from 1 (no damage) to 5 (degeneration involving the entire nerve area).

We tested each of our biomechanical modeling outcome measures for association with the damage score in the contralateral eye using Pearson correlation to determine whether there were animal-specific anatomic features that would lead to an association between biomechanical factors and nerve damage. Note that this approach assumes a high degree of contralateral concordance in anatomy and other physiological properties of the rat ONH.

## 6.4 Results

As shown in Figure 35, within model variants 1-4, anterior nerve principal strains depended on both geometry and scleral material properties. Within variant 1, there was especially large differences in strain between geometries, with the range in 50$^{th}$ percentile third principal strain being -2.4% to -4.1%. Also within variants 1-4, the ordering of geometries with respect to strain level was not consistent. For example, MR11OD had one of the highest 95$^{th}$ percentile 3$^{rd}$ principal strain values in variant 1, yet also had the lowest value among models in variant 2. In variants 5-8, within which only fiber stiffness values were changed, the variation in strain between geometries and between variants was much smaller. For example, the maximum difference in 50$^{th}$ percentile 3$^{rd}$ principal strain between geometries was only 0.58% and the maximum difference produced by changes in material properties was only 0.26%. In addition, the ordering of geometry with respect to strain value was consistent across variants 5-8. Lastly, all strain values within variants 5-8 were smaller in magnitude than those in variants 1-4.

Like the principal strain values, principal stress values had smaller magnitude in variants 5-8 compared to variants 1-4 (Figure 36). However, changes in stress due to geometry were on the same order as those due to differences in material properties. Overall, the models demonstrated more compressive stress in the nerve than tensile

stress, with some models even having negative values for the 50th percentile first principal stress.

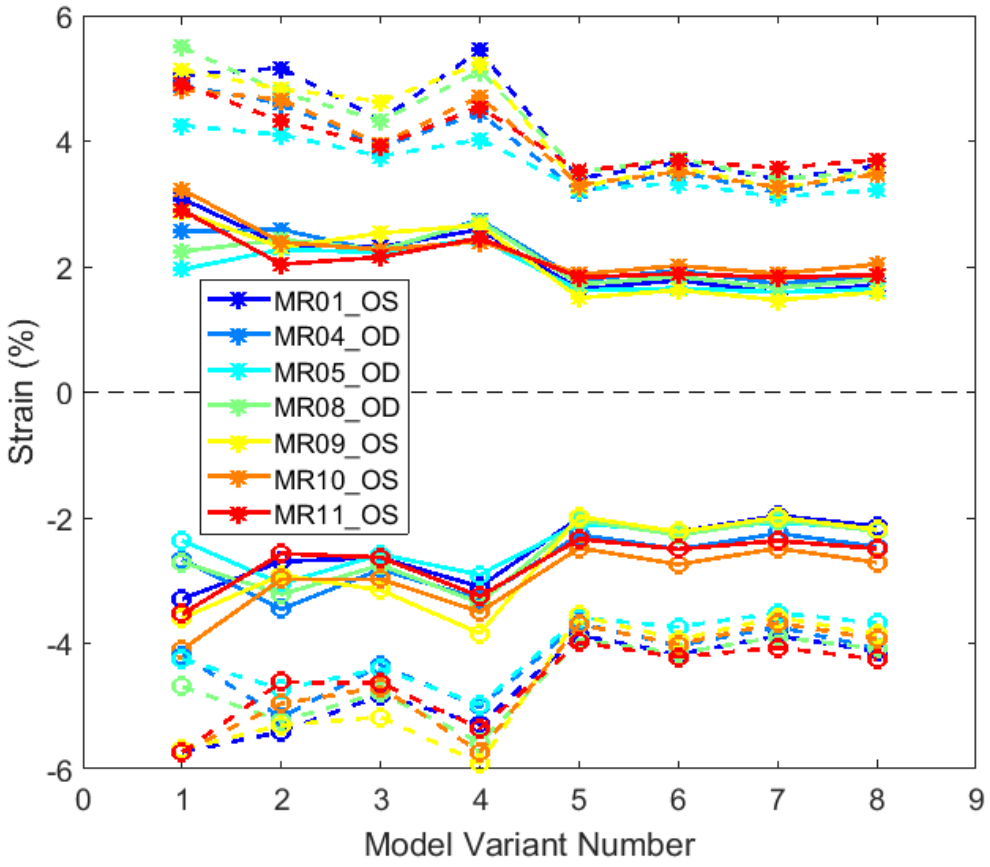


**Figure 35. Principal strains in the anterior nerve from all model simulations. The groupings of lines from top to bottom are the 95th percentile 1st principal strain, 50th percentile 1st principal strain, 50th percentile 3rd principal strain, and 5th percentile third principal strain. The different colors indicate different ONH model geometries.**

The magnitudes of ASCO, PSCO, nerve-ASCO, and nerve-PSCO expansion were all low, with values ranging from approximately 0.5% to 3.1% increases in area (Figure 37). Trends in the data were similar to those seen in the strains. More variation occurred within variants 1-4 compared to 5-8, and variants 5-8 had lower change in area than variants 1-4, in general.

All outcome measures were tested for possible association with contralateral eye optic nerve damage grade. The $r^2$ values and *p* values of the resulting linear regressions were highly variable between model variants for all outcome measures, and there were no significant correlations between any outcome measure and damage grade. We plotted 95$^{th}$ percentile strain versus damage grade from model variants 1, 4, 5, and 8 as an example (Figure 38).

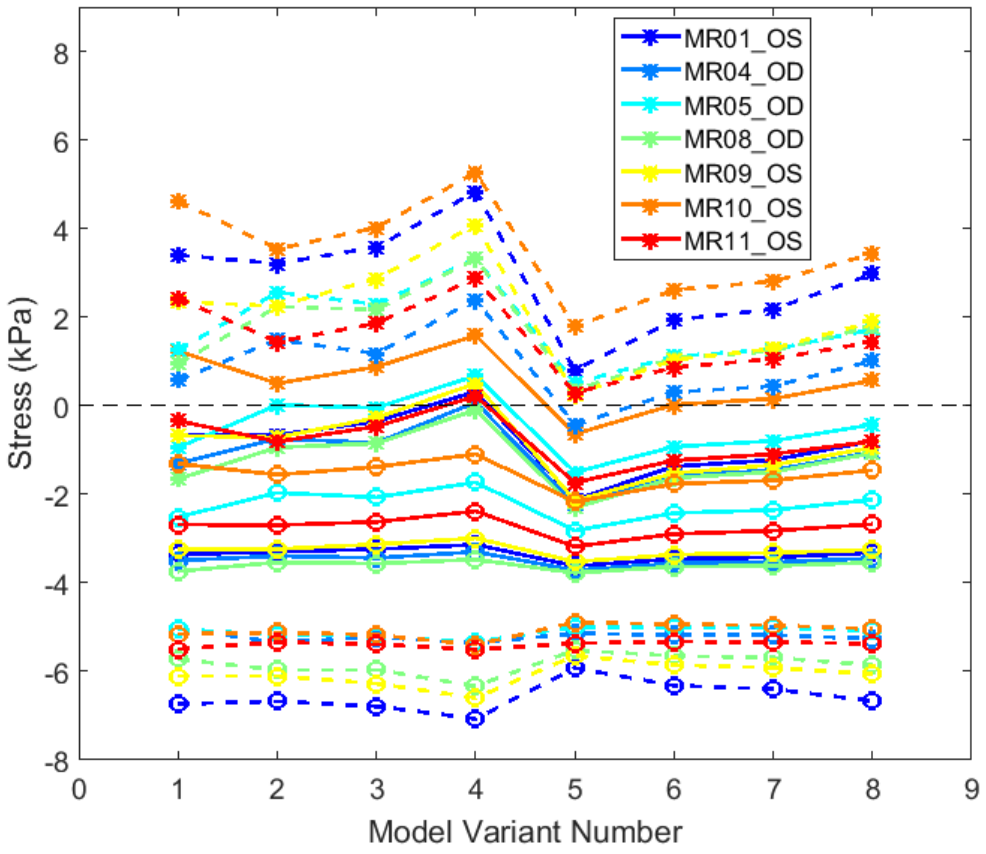


**Figure 36. First and third principal stresses in the anterior nerve for all models. Asterisks indicate first principal stress and open circles indicate third principal stress. Solid lines indicate 50$^{th}$ percentile values and dashed lines indicate either 95$^{th}$ percentile first principal stress or 5$^{th}$ percentile third principal stress.**

To examine patterns of strain within the nerve due to changes in material properties, we plotted heat maps showing first and third principal strain in all model variants of

MR11_OS (Figure 39). As seen in the en face views and superior-inferior cut views, first and third principal strain concentrations occurred primarily in the inferior nerve. This effect was less pronounced in variants 5-8 compared to variants 1-4, but the regions of highest strain were still found in the inferior nerve. As seen in the nasal-temporal cut, it appears that there was a slight tendency for higher strains to occur toward the nasal side of the nerve, but this was not as pronounced as the difference between the inferior and superior nerve.

To examine how patterns of strain varied between geometries, we plotted heat maps showing first and third principal strain in four eyes for variant 1 (Figure 40). Again, the highest strains and largest regions of high strain were consistently found in the inferior nerve. This effect was seen in all four eyes but was most pronounced in MR08_OD. Compared to MR10OS and MR09OS, MR05OD and MR08OD had lower strains in the superior nerve, particularly near the BM overhang on the superior side of the anterior nerve.

## 6.5 Discussion

This study is the first to perform individual-specific computational modeling of rat ONH biomechanics while incorporating a fiber-reinforced model for the sclera, an improvement on past models that modelled the sclera as a simple neo-Hookean solid. We built seven rat ONH models with individual-specific geometries and incorporated material properties that were informed by our previous inverse FEM study. To assess the effects of elevated IOP on the rat ONH, eight variants of each ONH model were solved, each with a different set of material properties for the sclera. Outcome measures included $50^{th}$ and $95^{th}$ percentile first principal stress and strain, $50^{th}$ and $5^{th}$ percentile third principal stress

and strain, ASCO expansion, PSCO expansion, nerve-ASCO expansion, and nerve-PSCO expansion.

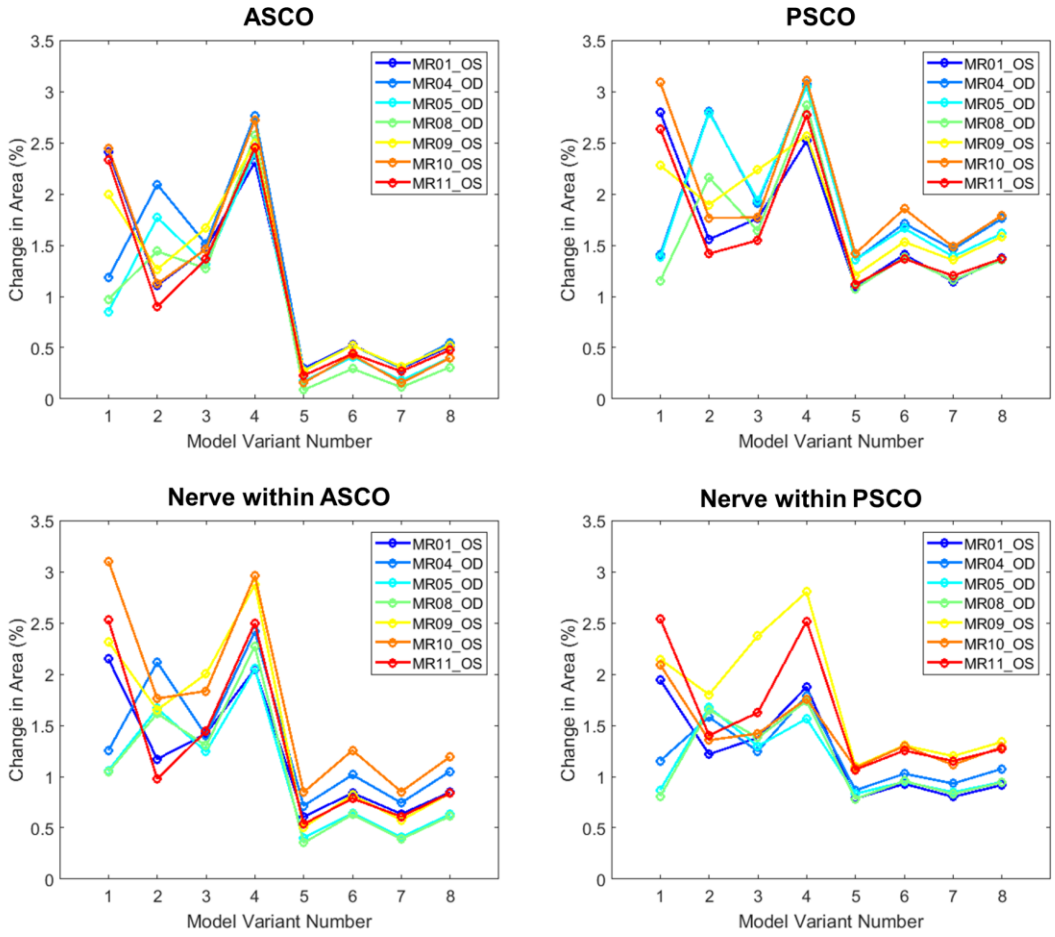


**Figure 37. Changes in area of the ASCO, PSCO, nerve-ASCO, and nerve-PSCO for different ONH models and variants. Different ONH models are indicated by color.**

In our previous publication, we presented strain magnitudes and patterns for three ONH models (MR05OD, MR04OD, and MR10OS) in which neo-Hookean behavior was assumed for the sclera. In the present study, the strain magnitudes of these ONH models were lower in all variants (Figure 35). However, as in the previous study, highest strains occurred primarily in the inferior nerve, in spite of the different scleral material model used here. In addition, this trend was present across all model variants in MR11OS. We

hypothesize that this pattern is due to the presence of the blood vessels and the IAC directly inferior to the rat optic nerve, creating a weak point in the sclera. This sets the rat apart from the human ONH, which experiences strain patterns that are largely axisymmetric (Sigal et al., 2009). Interestingly, there are two published patterns of glaucomatous damage that involve the superior and inferior regions of the rat nerve. Namely, RGC axonal degeneration occurs preferentially in the superior nerve (Morrison et al., 2011), while astrocytes (known to be mechanosensitive) are activated and reorient their processes in the inferior nerve before those in the superior nerve (Tehrani et al., 2016). Although it is confusing why RGC axons would preferentially degenerate in the superior nerve, Tehrani and colleagues postulated that the inferior astrocytes withdraw processes extending into the superior nerve, leaving the superior axons more vulnerable to apoptosis. Our data supports this possibility, but further study will have to be carried out to determine its validity.

Comparing the strain magnitudes across model variants emphasizes the importance of scleral collagen fiber direction on optic nerve strains. In variants 5-8, the circumferentially-aligned fibers resulted in decreased strain in every ONH model and resulted in low variability between models. In addition to the high variability seen in variants 1-4, some interesting patterns involving the relative strains between ONH models emerged. Note that strain magnitudes of the OD (right) and OS (left) eyes tended to be grouped together in variants 1 and 2. For example, in variant 1, the OS eyes were the four eyes with highest third principal strain magnitude and the OD eyes were the three eyes with lowest third principal strain magnitude. In addition, from variant 1 to 2, the third principal strains in the OS eyes decreased, while the third principal strains in the OD eyes increased. These observations indicate that there was interaction between the regional fiber alignment (scleral anisotropic properties) and geometry, but perhaps not between

scleral stiffness and geometry. In other words, the changes in material properties between variants 1 and 2 produced different effects on strain in different ONH geometries, but the same effect did not occur between variants 5 and 6, where only scleral stiffness was changed. The similar patterns seen in canal and nerve expansion are consistent with this point. However, the apparent lack of interaction between geometry and scleral stiffness may be due to the fact that scleral stiffness did not actually vary between models as much as Figure 34 would initially seem to suggest (see below).

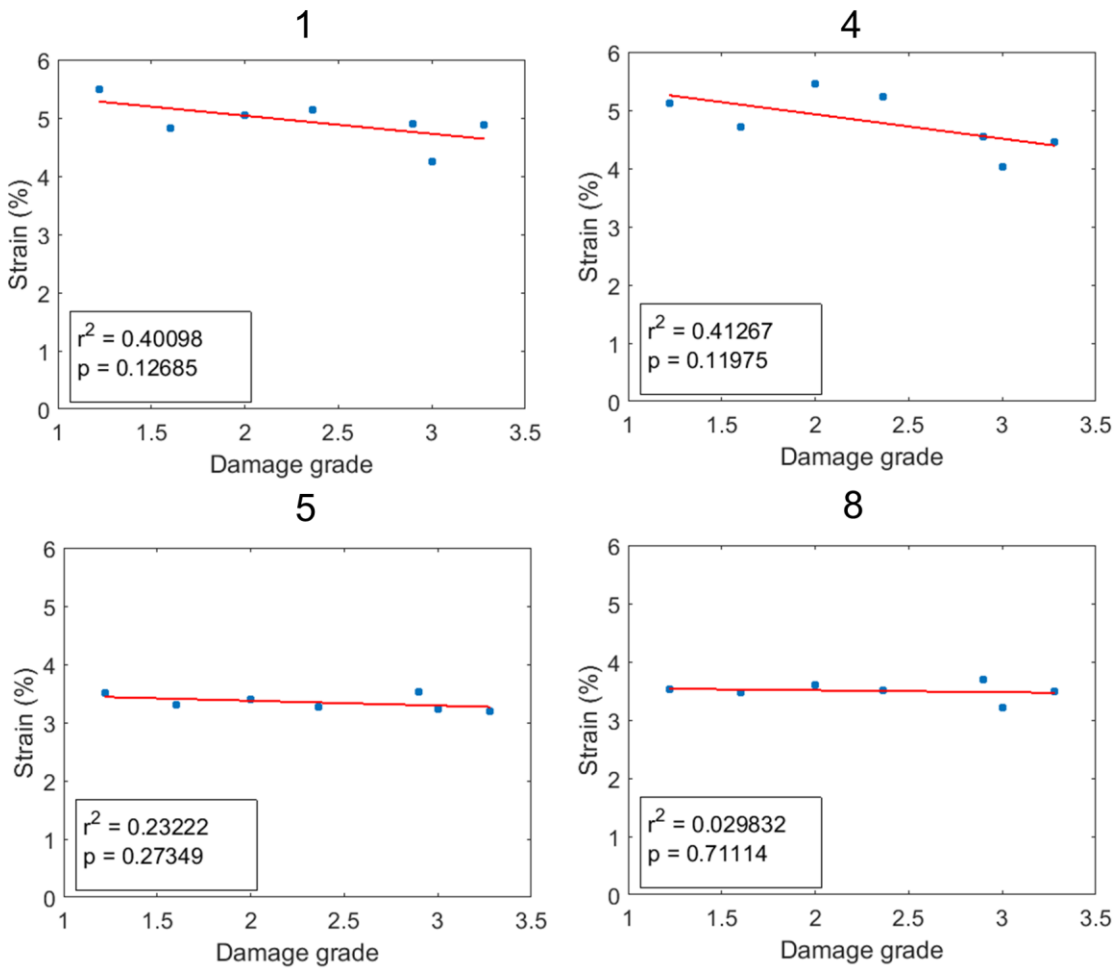


**Figure 38. First principal 95th percentile strain versus contralateral eye damage for model variants 1, 4, 5, and 8. Similar to the situation with all other outcome measures and for all model variants, $r^2$ and *p* values were highly variable. No correlations achieved significance.**

This observation also brings to light an important point for future fiber-reinforced models of the sclera. In our previous inverse FEM study and in the present study, we defined the material axes at each element such that the **i** vector (along which $\theta_p = 0°$) pointed in the counterclockwise direction (when looking at the posterior sclera surface), and the **j** vector (along which $\theta_p = 90°$) pointed at the optic nerve. This convention was used for both OD and OS eyes. In the future, it would be better to switch the direction of the **i** component for OS eyes to be clockwise, so that a $\theta_p$ angle of 45º or 135° would result

in fiber orientations that had the same effect on both OS eyes and OD eyes. In other words, this change would result in the **i** vector always pointing from inferior to temporal, temporal to superior, superior to nasal, and nasal to inferior quadrants.

One might ask why there seemed to be so little change in strain with different fiber stiffnesses, and why decreasing the fiber stiffness did not always result in decreased strain, as seen when comparing variants 5 and 7 (Figure 35). This is likely due to the way in which we calculated strain. Recall that the model was prestressed by raising IOP from 0 mmHg to 10 mmHg and that all strains were calculated with respect to the resulting state. By comparing the curves in Figure 34, one can see that even though there was a wide range of stretch values between curves at a given stress, the slopes of the curves were fairly similar once a certain stress threshold was reached. For example, at a stress of 0.05 MPa, the slopes of the fiber stress-stretch curves for model variants 5-8 were approximately 17.4, 12.7, 21.8, and 17.6 MPa, respectively. The stiffness of the fibers in each model will depend on their stress level at 10 mmHg and higher, and the overall scleral stiffness will also depend on $c_1$. Therefore, the changes in strain observed between model variants are unintuitive, but not unreasonable.

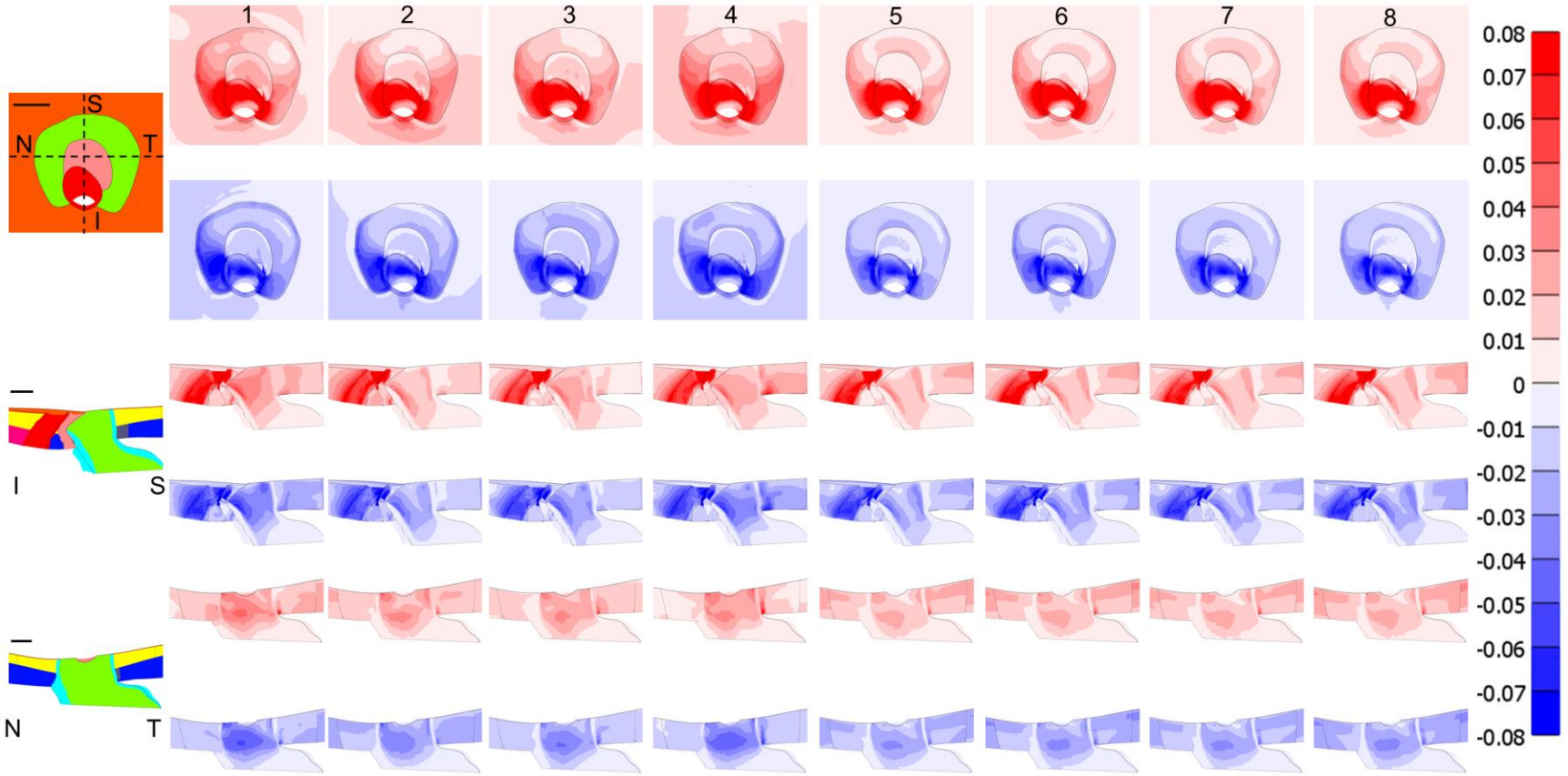


**Figure 39. First (top sub-rows) and third (bottom sub-rows) principal strains for different model variants (columns) of MR11_OS. The highest strains are concentrated in the inferior nerve regardless of model variant, although the pattern is less pronounced in variants 5-8. Tensile strain is shown in red and compressive strain is shown in blue. The en face view (top), superior (S)-inferior (I) cut plane view (middle) and nasal (N)-temporal (T) cut plane view (bottom) are shown. Scale bars shown in the far left column are 100 µm. Dashed lines in the en face view indicate S-I and N-T cut planes. Tissue colors are: nerve (green), CRV (pink), CRA (red), BM (orange), choroid (yellow), sclera (blue), pia mater (cyan). The undeformed configuration is shown in all images to ensure viewing of a consistent cut plane across columns.**

Finally, there were no significant correlations between any outcome measures and contralateral eye optic nerve damage grade. This was disappointing, but not entirely unexpected. Although the models incorporate individual-specific geometry, they do not incorporate individual-specific material properties, nor do they account for the highly variable IOP burden in the ocular hypertensive eye. As discussed above, there was obvious interaction between model geometry and material properties, and both are likely essential for computing deformation at the accuracy needed to predict damage levels of a given eye. Other limitations also prevented our models from computing the true strain values experienced by a given eye, and they are discussed below.

### 6.5.1 Limitations

The largest limitations of this study have to do with material properties. Although we made significant improvements from our previous rat ONH modeling study by treating the sclera as a fiber-reinforced matrix and by incorporating parameter values that were derived from experiments on rat sclera, even these improvements had drawbacks. First, the material model that we selected is still only an approximation of scleral structure. It is likely that the rat sclera contains multiple layers of fibers through its thickness, each with unique organization (Gogola et al., 2018). Von Mises distributions cannot always accurately describe the fiber directions of multiple fiber layers (Gouget et al., 2012). In addition, the organization of fibers changes gradually with distance from the nerve and location around the nerve (Girard et al., 2011), as opposed to being organized in quadrants. Next, as discussed in detail elsewhere (Schwaner et al., Submitted-a), there were limitations with our inverse FEM study that affected the accuracy of retrieved parameter values. Unfortunately, we were unable to effectively account for preload which likely resulted in an overestimation of scleral stiffness (Grytz & Downs, 2013). Also, as

mentioned above, we were concerned about noisiness of the $k_f$ and $\theta_p$ estimates for individual regions.

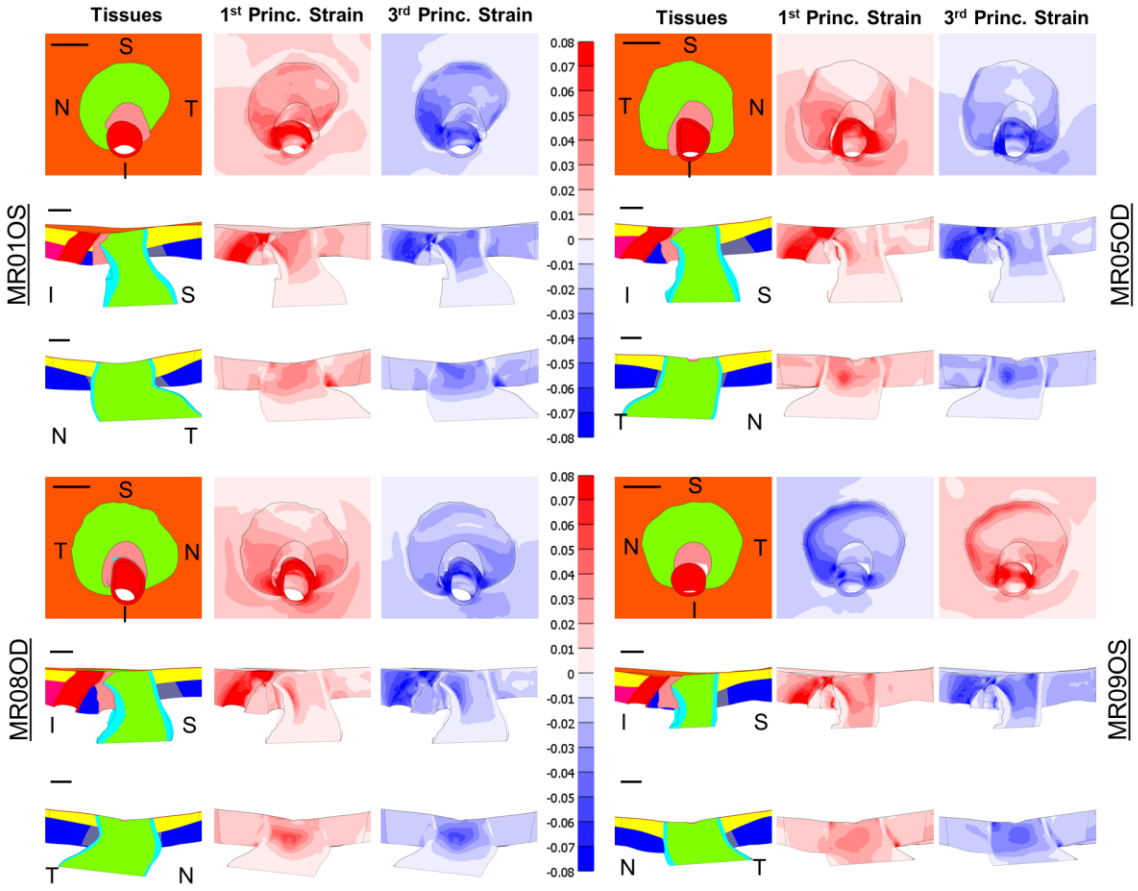


**Figure 40. First (middle sub-columns) and third (right sub-columns) principal strain in variant 1 of ONH models MR01OS (top left), MR05OD (top right), MR08OD (bottom left), and MR09OS (bottom right). The en face (top sub-rows), superior-inferior (middle sub-rows) cut plane, and nasal-temporal (bottom sub-rows) cut plane views are shown. Scale bars are 100 μm. All colors and abbreviations are as in Figure 39. The undeformed configuration is shown in all images to ensure viewing of consistent cut planes.**

The choice of material properties for all other tissues was an additional limitation. All other tissues were modelled as neo-Hookean solids, even though they probably are anisotropic. The pia mater in particular is more likely to behave like a transversely isotropic solid due to the collagen fibers in its structure. We also do not have experimental measurements of the stiffnesses of the other tissues in the rat ONH. These tissues are

difficult to access and extremely small, making them difficult to mechanically test. However, advances in inverse methods paired with non-invasive imaging may provide solutions to this problem in the future (Zhang et al., 2017).

Constraints should be added to the anterior faces of the CRA and CRV. In most models, the CRA (and adjacent CRV wall) “bent” around the scleral sling toward the superior CRV wall. In some model variants, this resulted in contact between the inferior and superior CRV walls that was likely not physiologic. The bending of the CRV also resulted in small areas of high strain in the anterior-inferior nerve (not the main strain concentration seen in the superior-inferior cut plane view) that surround the CRA on either side that can be seen in the en face view (Figure 35, Figure 36). Constraints to enforce more realistic deformation should be added.

Although the histomorphometric method used to build the rat ONH digital reconstructions accurately preserves important anatomic and morphological relationships, there is a known issue with shrinkage associated with the embedding and fixation steps (Pazos et al., 2015). Unfortunately, the extent of shrinkage is not well characterized and may vary from tissue to tissue, so we could not correct for it.

Finally, the computed results from these models have not been validated. This would be extremely difficult and would require highly accurate, non-invasive imaging of the rat ONH to be carried out while controlling IOP. It may be possible to do this in the future using optical coherence tomography (Fortune et al., 2011). However, complex corrections would have to be made for differences in optical properties and sizes between rat eyes in order to obtain accurate measurements of deformation (Kuo et al., 2013; Lozano & Twa, 2013).

## 6.6 Conclusion

We built seven FE models with individual-specific rat ONH geometries to evaluate the effects of elevating IOP from 10 mmHg to 30 mmHg on the ONH. Improving on a previous study, we modelled the sclera as a fiber-reinforced matrix to account for its nonlinear and anisotropic behavior. We solved eight variants of each model by incorporating different sets of experimentally-derived scleral material properties for a total of 56 simulations. Regardless of scleral property differences, strains were highest in the inferior optic nerve. In model variants with highly aligned circumferential fibers in the sclera, optic nerve strains were substantially reduced. No significant correlations were found between contralateral eye optic nerve damage grade and any of the outcome measures, which included strain, stress, scleral canal expansion, and optic nerve expansion. The strain patterns and effects of material property changes reported here can be used to inform future modeling studies on the rat ONH and interpret results from rat glaucoma studies to better understand how biomechanical insult affects RGC pathogenesis in glaucoma.

# CHAPTER 7. CONCLUSIONS AND FUTURE DIRECTIONS

Rat models of ocular hypertension have the potential to help researchers make concrete connections between degenerative events in glaucoma and specific forms and magnitudes of biomechanical insult to the ONH. However, a deep understanding of rat ONH biomechanics is necessary in order to utilize rat glaucoma models as tools to accomplish this goal. Therefore, the purpose of this thesis was to provide the first characterization of rat ONH biomechanics. We defined three specific aims towards this objective, and the conclusions, limitations, and future directions for each are described below.

**Specific Aim1:** Determine the biomechanical properties of the rat sclera using inverse finite element modeling

To provide meaningful information, FE models must be informed by accurate tissue mechanical properties. We developed an inverse modeling method, based on previous work done on the monkey eye, that combined inverse FE modeling with whole-globe inflation testing and DIC to extract material properties from the rat sclera, based on experiments we conducted in eight rat eyes. Specifically, the stiffness of the scleral ground substance ($c_1$), stiffness of scleral collagen fibers ($c_3$, $c_4$), regional fiber preferred direction ($\theta_p$), and regional fiber concentration factor ($k_f$) were extracted. The inverse models were unable to recreate highly localized patterns of measured scleral deformation but matched general patterns well. Although, the regional $\theta_p$ and $k_f$ values were highly variable, $c_1$ and $c_4$ values were relatively consistent between eyes, and $c_3$ values congregated into two groups that differed by an order of magnitude. Further, on average, fibers were more highly

aligned (higher $k_f$) in the peripapillary sclera than in the peripheral sclera, and fibers were aligned circumferentially, on average, throughout the sclera.

The inverse method appeared to perform well in obtaining overall stiffness properties of the sclera, but likely failed to retrieve the true fiber directions and concentration factors from individual scleral regions. The possible reasons for this limitation could include local artifacts in the digital image correlation data, errors associated with the locations of scleral thickness measurements, defining scleral regions in the model that were too large, defining an improper boundary for the peripapillary sclera (i.e. one that did not align with the transition in collagen organization between peripapillary and peripheral sclera), and/or using an oversimplified material model for the sclera. Because this list is long and varied, we suggest that future inverse studies must include experimentally determined fiber organization data. Fiber crimp data should also be gathered, if possible. In theory, experimental measurements of fiber crimp should correlate with sclera $c_4$. Therefore, this data could be used to help validate the fiber-reinforced model used in this thesis, or it could be used to generate $c_4$ input values.

It is also worth noting that we failed to adjust the material axes specified in the sclera models when switching between OD (right) and OS (left) eyes. This was of no consequence in Aim 1 because the fiber directions were so variable, and this oversight was obviously not the source of this variation, as evident from heat maps showing how many degrees each fiber direction was from 0°. However, this is not always explicitly mentioned in other studies that performed inverse FE modeling on eyes, and thus we think it is important to call attention to it.

Two other limitations that must be addressed are the errors associated with thickness measurement locations obtained via OCT and the suboptimal handling of

prestress. The OCT error could be resolved by performing corrections on in vivo OCT scans, using a telecentric OCT lens, or by using a different imaging method. Correcting the OCT data is not advised as it is difficult to do and would require researchers to collect additional data in order to perform the correction. Using a telecentric OCT lens would be a better solution if the scans could be effectively interpreted. We were unable to distinguish between the sclera and other tissue layers in the posterior eye when using the telecentric lens. However, if possible, the best solution would be to acquire scleral thickness from the same data set used to measure fiber organization.

Regarding the handling of prestress, we were forced to use the relative pressure approach as opposed to the relative displacement approach to account for preload due to the way in which we applied boundary conditions to the models. As a result, we likely overestimated scleral stiffness values. The DIC system was unable to provide information describing the geometry of the posterior eye near where it was fixed in place by glue, so we prescribed displacement boundary conditions within the confines of the DIC facet map. The location of this fixed region of the sclera could potentially be determined using a telecentric OCT scan or a 3D digitizer, allowing fixed boundary conditions to be applied. Regardless of how it is accomplished, future studies using this method must include a better accounting for preload.

Incorporating these changes into a new inverse FE modeling study would provide a significant improvement from the data presented here. Hopefully, the changes would lead to shorter computational time, lower error, and lower variability in the extracted fiber organization properties. The improved data set would be invaluable for future parameterized or individual-specific modeling studies on the rat ONH. Nonetheless, the data we have provided here is an improvement over what was previously available and is useful, with several caveats, for future modeling studies.

**Specific Aim 2:** Determine the factors that most influence rat optic nerve head biomechanics in a sensitivity analysis using a parameterized finite element model

Parameterized models can be powerful tools for characterizing a biomechanical system because they allow one to effectively sample a parameter space that includes both geometry and material properties. We developed a parameterized model of the rat ONH and used it to investigate the sensitivity of optic nerve strains to six geometric parameters and 14 material parameters. Magnitudes and patterns of strain corresponded well with individual-specific models from Aim 3, indicating that our parameterized model effectively approximated individual-specific geometry After optic nerve stiffness and IOP, scleral thickness, sclera $k_f$, sclera $c_1$, and sclera $c_4$ were the most influential parameters, which was consistent with the points made above for Aim 1. Namely, the most important next step in characterizing rat ONH biomechanics is to quantify fiber organization and to perform additional scleral stiffness characterization with the changes suggested above. In addition, PNVP stiffness, BM stiffness, and IAC stiffness were all ranked low in influence ($17^{th}$, $18^{th}$, and $19^{th}$), and thus are relatively unimportant in understanding ONH biomechanics; this is a welcome result, since quantifying the stiffness of these tissues would be extremely difficult.

We suggest several specific improvements that should be made to the parameterized model for future work. As indicated by the results of the sensitivity study, the most important is to include more realistic scleral thickness distributions. Specifically, scleral thickness should change with distance from the optic nerve, rather than assuming a constant value over the entire posterior eye. The same improvement should be made to choroidal thickness.

Pia mater stiffness was ranked relatively high (seventh out of 20) in parameter influence. Therefore, its material model should be changed from an isotropic neo-Hookean solid to a fiber-reinforced matrix. The current representation likely overestimates its compressive stiffness, which could have implications for the strain patterns observed in the optic nerve. Note that the thickest part of the pia mater occurs between the nerve and CRV, directly adjacent to where the high strains in the inferior nerve are observed in our models. As with the sclera, this change would require quantification of pia mater fiber organization and stiffness parameters. The organization could presumably be determined at the same time scleral fibers are evaluated, but the matrix and fiber stiffness would be more difficult to assess. As a start, the pia mater could be given similar stiffness properties to those of the sclera, which would, in our opinion, be an improvement over its current representation as an isotropic solid.

Other improvements should also be made. As in the individual-specific models, constraints should be added to the anterior vessel surfaces to prevent the unrealistic deformation that they experienced in this study. In addition, a method for quantifying regional strains in the optic nerve should be developed. Further, we did not investigate interaction effects between parameters, but this would be a useful information to gather in future work. Lastly, a longer list of parameters that include items such as SCO horizontal radius, optic nerve cross-sectional area, blood pressure, and CRA and CRV stiffness could be considered for future sensitivity studies.

A particularly important limitation is the fact that the results of the parameterized model have not been validated. This would be extremely difficult, and it may require advances in non-invasive imaging technology before it is feasible. In addition, model predictions are unlikely to have high agreement with experimental data without improved

fiber organization data. Therefore, priority in the meantime should be given to making the other improvements suggested above.

The most exciting possibility of future work arising from this method is its potential to replace the need for modeling individual-specific geometries using the method in Aim 3. Instead, near-individual-specific geometries using the parameterized model would be used. By this, we mean that each model would be informed by measurements from a given eye, but slight inaccuracies would be introduced into the geometry due to the approximations (idealized geometry) necessary for automated model building. Since automated geometry building and meshing reduce the model building time from approximately one week (by an expert) to about three minutes (by a non-expert), near-individual specific models would be feasible to build for every single eye included in a rat glaucoma study. However, a solution for obtaining material properties from each eye would need to be developed. Even so, the investigational power afforded by building computational models for comparison with every eye in a rat glaucoma study more than justifies continued work on this approach. Specifically, the improvements suggested above should be incorporated, and effort should be made to further validate the parameterized model's ability to predict the same strain patterns and magnitudes seen in models with individual-specific geometry.

**Specific Aim 3:** Determine strain patterns in rat ONHs under elevated IOP using individual-specific finite element modeling

In order to learn more about how biomechanics leads to RGC death in glaucoma using the rat model, detailed characterization of strain patterns within the rat ONH is required. Therefore, we developed a methodology for building rat ONH models with individual-specific geometries. In Chapter 3, we presented this method and the initial

results from three models that incorporated material property values similar to those used in previous human modeling studies. Strain magnitudes in the optic nerve were lower than those seen in the human ONH and strain patterns were not axisymmetric. Specifically, the region of highest strain occurred in the inferior nerve. This is particularly interesting when considering data from recent studies on the behavior of astrocytes in a rat model of ocular hypertension. They showed that astrocytes in the inferior optic nerve activate and reorient their processes before those in the superior nerve after the eye is exposed to acute IOP elevation.

In Chapter 6, we built an additional four models and changed the sclera material model from being a neo-Hookean solid to an isotropic matrix reinforced by collagen fibers. Informed by data from Aim 1, we developed eight sets of material parameters for the sclera and incorporated them into model geometries to solve eight variants of each model. We found that changes in scleral material properties resulted in larger strain magnitude variations than did different model geometries. Setting all scleral collagen fibers to be circumferentially oriented resulted in lower optic nerve strain magnitudes and lower variation between geometries, suggesting that interactions between geometry and fiber organization occurred when both were varied at the same time. Although less pronounced when fibers were circumferential, the highest strains occurred in the inferior optic nerve across all model geometries and variants. We also noticed that OD versus OS eyes reacted to changes in fiber organization differently, making it clear that care should be taken to adjust material axes when switching between OD and OS eyes. No correlations were found between contralateral eye damage grade and any outcome measure, including first and third principal strains, first and third principal stresses, ASCO and PSCO expansions, and nerve-ASCO and nerve-PSCO expansions. This last result was not

surprising, since we did not incorporate individual-specific material properties into the ONH models.

The results from Aim 3 reinforce the need for accurate and precise fiber organization information for the rat sclera. The greatest changes in model strains were seen when fiber organization was changed, not when scleral stiffness was changed. Other potential model improvements include, as for the parameterized models, the following: the pia mater should be modelled as a fiber-reinforced matrix; constraints should be added to the anterior vessel surfaces; the material model for the choroid should be improved, if possible; and a method should be developed to quantify regional strains in the optic nerve. As with the parameterized models, the lack of validation for the individual-specific models is a large limitation, and needs to be addressed when possible, in the future.

The low variability in strain between model geometries with circumferential fibers is encouraging, and it adds support to the idea that parameterized models may be sufficient to capture individual-to-individual variation in strains brought on by anatomical differences. In the future, after the suggested improvements are made, a head-to-head comparison between individual-specific models and parameterized model iterations informed by measurements made from the individual-specific geometries should be made. Comparing quantitative regional strain magnitudes will confirm whether the parameterized model is sufficient or if more refinements need to be made.

## 7.1 Final Thoughts

This dissertation provides the first characterization of rat ONH biomechanics to the glaucoma field. We have extracted scleral material properties using inverse modeling, identified important parameters to rat ONH biomechanics using a sensitivity study, and identified initial patterns and magnitudes of strain in the rat optic nerve using individual-

specific FE modeling. We do not claim that the models presented here were able to calculate the exact strain patterns and magnitudes experienced by the ONHs that we modelled, but we do feel that they describe overall biomechanical patterns in the rat ONH. Further, the sum of this work forms the basis for future modeling and experimental studies in glaucoma biomechanics utilizing the rat model. If the suggestions that we made above are implemented, it could be feasible to perform powerful mechanistic studies of glaucoma pathogenesis in rats, in which an FE model of each rat eye is built to directly compare patterns of stress and strain with patterns of damage and cellular behavior. Such a study could be an important development, allowing glaucoma researchers to identify which events in the glaucomatous process occur as a direct result of specific modes and magnitudes of stress or strain. Thus, the glaucoma field may finally understand the link between biomechanical insult and RGC pathophysiology in glaucoma.

# APPENDIX A. RELATIONSHIP BETWEEN FIBER CONCENTRATION FACTOR ($k_f$) AND DEGREE OF ALIGNMENT

We wished to compare our extracted $k_f$ values with the experimental data on degree of fiber alignment ($DA$) reported by Girard et al. (2011) in the rat sclera, for which it was necessary to relate $k_f$ and $DA$. The $DA$ parameter reported by Girard et al. (2011) is defined by (note typographic error in that publication)

$$DA = 1 - \frac{OI}{\pi/4} \tag{11}$$

where the orientation index (Sacks et al., 1997), $OI$, is defined as

$$\int_{\theta_p - OI}^{\theta_p + OI} P(\theta) d\theta = \frac{1}{2} \tag{12}$$

where $P(\theta)$ is the probability density function of fiber directions and satisfies

$$\int_{-\pi/2}^{\pi/2} P(\theta) d\theta = 1 \tag{13}$$

In other words, half of all fiber directions lie within $-OI$ to $+OI$ about a preferred direction, $\theta_p$. For $DA$, a value of 0 means that fiber direction is isotropic within a plane, and

a value of 1 means that all fibers have an orientation of $\theta_p$. The von Mises distribution is defined as

$$P(\theta) = \frac{1}{\pi I_0(k_f)} \exp\left[k_f \cos 2(\theta - \theta_p)\right] \tag{14}$$

where $I_0$ is the modified Bessel function of the first kind of order zero and $k_f$ is the fiber concentration factor. By substituting Equation 14 into Equation 12, and substituting $\varphi = \theta_p - \theta$, we obtain

$$\frac{-1}{\pi I_0(k_f)} = \int_{OI}^{-OI} \exp(k_f \cos 2\varphi) d\varphi = \frac{1}{2} \tag{15}$$

which can be rearranged to obtain an implicit relationship between $k_f$ and $OI$

$$\int_0^{OI} \exp(k_f \cos 2\varphi) d\varphi = \frac{\pi}{4} I_0(k_f) \tag{16}$$

Although obtaining an analytical solution to equation (15) is difficult, one can iteratively find the value of $OI$ that satisfies Equation 16 for a given $k_f$ by plugging a value for $k_f$ into the term on the right and numerically evaluating the integral on the left with different values for $OI$ until the equation is satisfied.

# REFERENCES


Agapova, O. A., Kaufman, P. L., Lucarelli, M. J., Gabelt, B. T., and Hernandez, M. R., 2003, "Differential Expression of Matrix Metalloproteinases in Monkey Eyes with Experimental Glaucoma or Optic Nerve Transection," Brain Res, **967**(1–2), pp. 132–143.

AGIS7, 2010, "The Advanced Glaucoma Intervention Study (AGIS): 7. the Relationship between Control of Intraocular Pressure and Visual Field Deterioration," Am. J. Ophthalmol., **130**, pp. 429–440.

Agoumi, Y., Sharpe, G. P., Hutchison, D. M., Nicolela, M. T., Artes, P. H., and Chauhan, B. C., 2011, "Laminar and Prelaminar Tissue Displacement during Intraocular Pressure Elevation in Glaucoma Patients and Healthy Controls," Ophthalmology, **118**(1), pp. 52–59.

Akagi, T., Hangai, M., Takayama, K., Nonaka, A., Ooto, S., and Yoshimura, N., 2012, "In Vivo Imaging of Lamina Cribrosa Pores by Adaptive Optics Scanning Laser Ophthalmoscopy," Investig. Opthalmology Vis. Sci., **53**(7), p. 4111.

Albon, J., Karwatowski, W. S., Avery, N., Easty, D. L., and Duance, V. C., 1995, "Changes in the Collagenous Matrix of the Aging Human Lamina Cribrosa.," Br. J. Ophthalmol., **79**(4), pp. 368–75.

Alqawlaq, S., Flanagan, J. G., and Sivak, J. M., 2018, "All Roads Lead to Glaucoma: Induced Retinal Injury Cascades Contribute to a Common Neurodegenerative Outcome," Exp. Eye Res., (November), pp. 0–1.

Anderson, D. R., 2003, "Collaborative Normal Tension Glaucoma Study.," Curr. Opin. Ophthalmol., **14**(2), pp. 86–90.

Anderson, D. R., 1969, "Ultrastructure of Human and Monkey Lamina Cribrosa and Optic Nerve Head," Arch Ophthalmol, **82**(6), pp. 800–814.

Ashpole, N. E., Overby, D. R., Ethier, C. R., and Stamer, W. D., 2014, "Shear Stress-Triggered Nitric Oxide Release From Schlemm's Canal Cells," Invest. Ophthalmol. Vis. Sci., **55**(12), pp. 8067–8076.

Avetisov, E. S., Savitskaya, N. F., Vinetskaya, M. I., and Iomdina, E. N., 1983, "A Study of Biochemical and Biomechanical Qualities of Normal and Myopic Eye Sclera in Humans of Different Age Groups.," Metab. Pediatr. Syst. Ophthalmol., **7**(4), pp. 183–8.

Bailey, T. A., Alexander, R. A., Dubovy, S. R., Luthert, P. J., and Chong, N. H., 2001, "Measurement of TIMP-3 Expression and Bruch's Membrane Thickness in Human Macula," Exp. Eye Res., **73**(6), pp. 851–858.

Balaratnasingam, C., Morgan, W. H., Bass, L., Cringle, S. J., and Yu, D.-Y. Y., 2008, "Time-Dependent Effects of Elevated Intraocular Pressure on Optic Nerve Head Axonal Transport and Cytoskeleton Proteins," Investig. Opthalmology Vis. Sci., **49**(3),

p. 986.

Band, L. R., Hall, C. L., Richardson, G., Jensen, O. E., Siggers, J. H., and Foss, A. J. E., 2009, “Intracellular Flow in Optic Nerve Axons: A Mechanism for Cell Death in Glaucoma,” Investig. Ophthalmol. Vis. Sci., **50**(8), pp. 3750–3758.

Baumann, B., Rauscher, S., Gl, M., Erich, G., Pircher, M., Fialov, S., Gr, M., and Hitzenberger, C. K., 2014, “Peripapillary Rat Sclera Investigated In Vivo With Polarization-Sensitive Optical Coherence Tomography,” Invest. Ophthalmol. Vis. Sci., **55**, pp. 7686–7696.

Bellezza, a. J., Hart, R. T., and Burgoyne, C. F., 2000, “The Optic Nerve Head as a Biomechanical Structure: Initial Finite Element Modeling,” Investig. Ophthalmol. Vis. Sci., **41**(10), pp. 2991–3000.

Bellezza, A. J., Rintalan, C. J., Thompson, H. W., Downs, J. C., Hart, R. T., and Burgoyne, C. F., 2003, “Deformation of the Lamina Cribrosa and Anterior Scleral Canal Wall in Early Experimental Glaucoma,” Investig. Opthalmology Vis. Sci., **44**(2), p. 623.

Bello, S. A., and Passaglia, C. L., 2017, “A Wireless Pressure Sensor for Continuous Monitoring of Intraocular Pressure in Conscious Animals,” Ann. Biomed. Eng., **45**(11), pp. 2592–2604.

Beotra, M. R., Wang, X., Tun, T. A., Zhang, L., Baskaran, M., Aung, T., Strouthidis, N. G., and Girard, M. J. A., 2018, “In Vivo Three-Dimensional Lamina Cribrosa Strains in Healthy, Ocular Hypertensive, and Glaucoma Eyes Following Acute Intraocular Pressure Elevation,” Investig. Ophthalmol. Vis. Sci., **59**(1), pp. 260–272.

Berdahl, J. P., Allingham, R. R., and Johnson, D. H., 2008, “Cerebrospinal Fluid Pressure Is Decreased in Primary Open-Angle Glaucoma,” Ophthalmology, **115**(5), pp. 763–768.

Berdahl, J. P., Fautsch, M. P., Stinnett, S. S., and Allingham, R., 2008, “Intracranial Pressure in Primary Open Angle Glaucoma, Normal Tension Glaucoma, and Ocular Hypertension: A Case-Control Study,” Investig. Ophthalmol. Vis. Sci., **49**(12), pp. 5412–5418.

Berens, P., 2009, “CircStat : A MATLAB Toolbox for Circular Statistics,” J. Stat. Softw., **31**(10).

Bihlmeyer, N. A., Kinebuchi, M., Kim, K.-Y., Phan, S., Zhou, Y., Shih, T., Jin, Y., Nguyen, J. V., Ellisman, M. H., Mills, E. A., Davis, C. O., Boassa, D., Marsh-Armstrong, N., and Bushong, E. A., 2014, “Transcellular Degradation of Axonal Mitochondria,” Proc. Natl. Acad. Sci., **111**(26), pp. 9633–9638.

Bosco, A., Romero, C. O., Breen, K. T., Chagovetz, A. A., Steele, M. R., Ambati, B. K., and Vetter, M. L., 2015, “Neurodegeneration Severity Can Be Predicted from Early Microglia Alterations Monitored in Vivo in a Mouse Model of Chronic Glaucoma,” Dis. Model. Mech., **8**(5), pp. 443–455.

Brazile, B. L., Hua, Y., Jan, N. J., Wallace, J., Gogola, A., and Sigal, I. A., 2018, “Thin Lamina Cribrosa Beams Have Different Collagen Microstructure than Thick Beams,”

Investig. Ophthalmol. Vis. Sci., **59**(11), pp. 4653–4661.

Buehren, M., 2017, “Differential Evolution,” Matlab Cent. File Exch. [Online]. Available: http://www.mathworks.com/matlabcentral/fileexchange/authors/12286. [Accessed: 05-Jan-2018].

Burgoyne, C. F., Quigley, H. A., Thompson, H. W., Vitale, S., and Varma, R., 1995, “Early Changes in Optic Disc Compliance and Surface Position in Experimental Glaucoma.,” Ophthalmology, **102**(12), pp. 1800–1809.

Burgoyne, C., 2015, “The Morphological Difference between Glaucoma and Other Optic Neuropathies,” J. Neuro-Ophthalmology, **35**(0 1), pp. S8–S21.

Burgoyne, C. F., 2011, “A Biomechanical Paradigm for Axonal Insult within the Optic Nerve Head in Aging and Glaucoma.,” Exp. Eye Res., **93**(2), pp. 120–32.

Burgoyne, C. F., Downs, J. C., Bellezza, A. J., and Hart, R. T., 2004, “Three-Dimensional Reconstruction of Normal and Early Glaucoma Monkey Optic Nerve Head Connective Tissues,” Investig. Opthalmology Vis. Sci., **45**(12), p. 4388.

Campbell, I. C., Hannon, B. G., Read, A. T., Sherwood, J. M., Schwaner, S. A., and Ethier, C. R., 2017, “Quantification of the Efficacy of Collagen Cross-Linking Agents to Induce Stiffening of Rat Sclera,” J. R. Soc. Interface, **14**(129), pp. 1–9.

Campbell, I. C., Coudrillier, B., and Ross Ethier, C., 2014, “Biomechanics of the Posterior Eye: A Critical Role in Health and Disease,” J. Biomech. Eng., **136**(2), p. 021005.

Candiello, J., Balasubramani, M., Schreiber, E. M., Cole, G. J., Mayer, U., Halfter, W., and Lin, H., 2007, “Biomechanical Properties of Native Basement Membranes,” FEBS J., **274**(11), pp. 2897–2908.

Chan, W. H., Hussain, A. A., and Marshall, J., 2007, “Youngs Modulus of Bruchs Membrane: Implications for AMD,” Invest. Ophthalmol. Vis. Sci., **48**(13), pp. 2187–2187.

Chauhan, B. C., O’Leary, N., AlMobarak, F. A., Reis, A. S. C., Yang, H., Sharpe, G. P., Hutchison, D. M., Nicolela, M. T., and Burgoyne, C. F., 2013, “Enhanced Detection of Open-Angle Glaucoma with an Anatomically Accurate Optical Coherence Tomography-Derived Neuroretinal Rim Parameter.,” Ophthalmology, **120**(3), pp. 535–543.

Chen, K., Rowley, A. P., and Weiland, J. D., 2010, “Elastic Properties of Porcine Ocular Posterior Soft Tissues,” J. Biomed. Mater. Res. - Part A, **93**(2), pp. 635–645.

Chen, K., Rowley, A. P., Weiland, J. D., and Humayun, M. S., 2014, “Elastic Properties of Human Posterior Eye.,” J. Biomed. Mater. Res. A, **102**(6), pp. 2001–7.

Chung, H. S., Sung, K. R., Lee, J. Y., and Na, J. H., 2016, “Lamina Cribrosa-Related Parameters Assessed by Optical Coherence Tomography for Prediction of Future Glaucoma Progression,” Curr. Eye Res., **41**(6), pp. 806–813.

Coleman, D. J., and Trokel, S., 1969, “Direct-Recorded Intraocular Pressure Variations in a Human Subject,” Arch. Ophthalmol., **82**(5), pp. 637–640.

Coudrillier, B., Boote, C., Quigley, H. A., and Nguyen, T. D., 2013, “Scleral Anisotropy and Its Effects on the Mechanical Response of the Optic Nerve Head,” Biomech. Model. Mechanobiol., **12**(5), pp. 941–963.

Coudrillier, B., Campbell, I. C., Read, A. T., Geraldes, D. M., Vo, N. T., Feola, A., Mulvihill, J., Albon, J., Abel, R. L., and Ethier, C. R., 2016, “Effects of Peripapillary Scleral Stiffening on the Deformation of the Lamina Cribrosa,” Investig. Opthalmology Vis. Sci., **57**(6), p. 2666.

Coudrillier, B., Geraldes, D. M., Vo, N. T., Atwood, R., Reinhard, C., Campbell, I. C., Raji, Y., Albon, J., Abel, R. L., and Ethier, C. R., 2016, “Phase-Contrast Micro-Computed Tomography Measurements of the Intraocular Pressure-Induced Deformation of the Porcine Lamina Cribrosa,” IEEE Trans. Med. Imaging, **35**(4), pp. 988–999.

Coudrillier, B., Pijanka, J., Jefferys, J., Sorensen, T., Quigley, H. a., Boote, C., and Nguyen, T. D., 2015, “Collagen Structure and Mechanical Properties of the Human Sclera: Analysis for the Effects of Age,” J. Biomech. Eng., **137**(4), p. 041006.

Coudrillier, B., Pijanka, J., Jefferys, J., Sorensen, T., Quigley, H. A., Boote, C., and Nguyen, T. D., 2015, “Effects of Age and Diabetes on Scleral Stiffness,” J. Biomech. Eng., **137**(7), p. 071007.

Coudrillier, B., Pijanka, J. K., Jefferys, J. L., Goel, A., Quigley, H. a., Boote, C., and Nguyen, T. D., 2015, “Glaucoma-Related Changes in the Mechanical Properties and Collagen Micro-Architecture of the Human Sclera,” PLoS One, **10**(7), p. e0131396.

Coudrillier, B., Tian, J., Alexander, S., Myers, K. M., Quigley, H. a, and Nguyen, T. D., 2012, “Biomechanics of the Human Posterior Sclera: Age- and Glaucoma-Related Changes Measured Using Inflation Testing.,” Invest. Ophthalmol. Vis. Sci., **53**(4), pp. 1714–28.

Crawford Downs, J., Burgoyne, C. F., Seigfreid, W. P., Reynaud, J. F., Strouthidis, N. G., and Sallee, V., 2011, “24-Hour IOP Telemetry in the Nonhuman Primate: Implant System Performance and Initial Characterization of IOP at Multiple Timescales,” Investig. Ophthalmol. Vis. Sci., **52**(10), pp. 7365–7375.

Cull, G. A., Reynaud, J., Wang, L., Cioffi, G. A., Burgoyne, C. F., and Fortune, B., 2012, “Relationship between Orbital Optic Nerve Axon Counts and Retinal Nerve Fiber Layer Thickness Measured by Spectral Domain Optical Coherence Tomography,” Investig. Opthalmology Vis. Sci., **53**(12), p. 7766.

Cull, G., Burgoyne, C. F., Fortune, B., and Wang, L., 2013, “Longitudinal Hemodynamic Changes within the Optic Nerve Head in Experimental Glaucoma,” Investig. Ophthalmol. Vis. Sci., **54**(6), pp. 4271–4277.

Curcio, C. A., and Johnson, M., 2012, “Structure, Function, and Pathology of Bruch’s Membrane,” Retin. Fifth Ed., **1**, pp. 465–481.

Dai, C., Khaw, P. T., Yin, Z. Q., Li, D., Raisman, G., and Li, Y., 2012, “Structural Basis of Glaucoma: The Fortified Astrocytes of the Optic Nerve Head Are the Target of Raised Intraocular Pressure,” Glia, **60**(May 2011), pp. 13–28.

Dandona, L., 1990, “Quantitative Regional Structure of the Normal Human Lamina Cribrosa,” Arch. Ophthalmol., **108**(3), p. 393.

Danford, F. L., Yan, D., Dreier, R. A., Cahir, T. M., Girkin, C. A., and Vande Geest, J. P., 2013, “Differences in the Region- and Depth-Dependent Microstructural Organization in Normal Versus Glaucomatous Human Posterior Sclerae,” Investig. Opthalmology Vis. Sci., **54**(13), p. 7922.

Dastiridou, A. I., Ginis, H. S., De Brouwere, D., Tsilimbaris, M. K., and Pallikaris, I. G., 2009, “Ocular Rigidity, Ocular Pulse Amplitude, and Pulsatile Ocular Blood Flow: The Effect of Intraocular Pressure,” Investig. Opthalmology Vis. Sci., **50**(12), p. 5718.

Downs, J. C., Yang, H., Girkin, C., Sakata, L., Bellezza, A., Thompson, H., and Burgoyne, C. F., 2007, “Three-Dimensional Histomorphometry of the Normal and Early Glaucomatous Monkey Optic Nerve Head: Neural Canal and Subarachnoid Space Architecture,” Investig. Ophthalmol. Vis. Sci., **48**(7), pp. 3195–3208.

Downs, J. C., Roberts, M. D., Burgoyne, C. F., and Hart, R. T., 2009, “Multiscale Finite Element Modeling of the Lamina Cribrosa Microarchitecture in the Eye,” *2009 Annual International Conference of the IEEE Engineering in Medicine and Biology Society*, IEEE, pp. 4277–4280.

Downs, J. C., Roberts, M. D., and Burgoyne, C. F., 2008, “Mechanical Environment of the Optic Nerve Head in Glaucoma,” Optom. Vis. Sci., **85**(6), pp. E425–E435.

Downs, J. C., Suh, J. K. F., Thomas, K. a, Bellezza, A. J., Burgoyne, C. F., and Hart, R. T., 2003, “Viscoelastic Characterization of Peripapillary Sclera: Material Properties by Quadrant in Rabbit and Monkey Eyes.,” J. Biomech. Eng., **125**(1), pp. 124–131.

Eilaghi, A., Flanagan, J. G., Simmons, C. a., and Ethier, C. R., 2010, “Effects of Scleral Stiffness Properties on Optic Nerve Head Biomechanics,” Ann. Biomed. Eng., **38**(4), pp. 1586–1592.

Eilaghi, A., Flanagan, J. G., Tertinegg, I., Simmons, C. a., Wayne Brodland, G., and Ross Ethier, C., 2010, “Biaxial Mechanical Testing of Human Sclera,” J. Biomech., **43**(9), pp. 1696–1701.

Elsheikh, A., Geraghty, B., Alhasso, D., Knappett, J., Campanelli, M., and Rama, P., 2010, “Regional Variation in the Biomechanical Properties of the Human Sclera,” Exp. Eye Res., **90**(5), pp. 624–633.

Ethier, C. R., and Simmons, C. a., 2007, *Introductory Biomechanics*, Cambridge University Press, Cambridge.

Feola, A. J., Coudrillier, B., Mulvihill, J., Geraldes, D. M., Vo, N. T., Albon, J., Abel, R. L., Samuels, B. C., and Ethier, C. R., 2017, “Deformation of the Lamina Cribrosa and Optic Nerve Due to Changes in Cerebrospinal Fluid Pressure,” Investig. Ophthalmol. Vis. Sci., **58**(4), pp. 2070–2078.

Feola, A. J., Myers, J. G., Raykin, J., Mulugeta, L., Nelson, E. S., Samuels, B. C., and Ethier, C. R., 2016, “Finite Element Modeling of Factors Influencing Optic Nerve Head Deformation Due to Intracranial Pressure,” Investig. Opthalmology Vis. Sci., **57**(4), p.

1901.

Feola, A. J., Nelson, E. S., Myers, J., Ethier, C. R., and Samuels, B. C., 2018, “The Impact of Choroidal Swelling on Optic Nerve Head Deformation,” Investig. Opthalmology Vis. Sci., **59**(10), p. 4172.

Flammer, J., and Konieczka, K., 2015, “Retinal Venous Pressure: The Role of Endothelin,” EPMA J., **6**(1), p. 21.

Fortune, B., Choe, T. E., Reynaud, J., Hardin, C., Cull, G. a, Burgoyne, C. F., and Wang, L., 2011, “Deformation of the Rodent Optic Nerve Head and Peripapillary Structures during Acute Intraocular Pressure Elevation.,” Invest. Ophthalmol. Vis. Sci., **52**(9), pp. 6651–61.

Fortune, B., Hardin, C., Reynaud, J., Cull, G., Yang, H., Wang, L., and Burgoyne, C. F., 2016, “Comparing Optic Nerve Head Rim Width, Rim Area, and Peripapillary Retinal Nerve Fiber Layer Thickness to Axon Count in Experimental Glaucoma,” Investig. Opthalmology Vis. Sci., **57**(9), p. OCT404.

Fortune, B., Reynaud, J., Hardin, C., Wang, L., Sigal, I. A., and Burgoyne, C. F., 2016, “Experimental Glaucoma Causes Optic Nerve Head Neural Rim Tissue Compression: A Potentially Important Mechanism of Axon Injury,” Investig. Ophthalmol. Vis. Sci., **57**(10), pp. 4403–4411.

Friberg, T. R., and Lace, J. W., 1988, “A Comparison of the Elastic Properties of Human Choroid and Sclera.,” Exp. Eye Res., **47**(3), pp. 429–36.

Friedman, D. S., 2004, “Prevalence of Open-Angle Glaucoma among Adults in the United States,” Arch. Ophthalmol., **122**(4), pp. 532–538.

Gaasterland, D., Tanishima, T., and Kuwabara, T., 1978, “Axoplasmic Flow during Chronic Experimental Glaucoma. 1. Light and Electron Microscopic Studies of the Monkey Optic Nervehead during Development of Glaucomatous Cupping.,” Invest. Ophthalmol. Vis. Sci., **17**(9), pp. 838–46.

Gal, O., 2003, “Fit_ellipse” [Online]. Available: https://www.mathworks.com/matlabcentral/fileexchange/3215-fit_ellipse. [Accessed: 10-Jul-2017].

García-Montesinos, J., Muñoz-Negrete, F. J., de Juan, V., and Rebolleda, G., 2017, “Relationship between Lamina Cribrosa Displacement and Trans-Laminar Pressure Difference in Papilledema,” Graefe’s Arch. Clin. Exp. Ophthalmol., **255**(6), pp. 1237–1243.

Gardiner, S. K., Fortune, B., Wang, L., Downs, J. C., and Burgoyne, C. F., 2012, “Intraocular Pressure Magnitude and Variability as Predictors of Rates of Structural Change in Non-Human Primate Experimental Glaucoma,” Exp. Eye Res., **103**, pp. 1–8.

Geraghty, B., Jones, S. W., Rama, P., Akhtar, R., and Elsheikh, A., 2012, “Age-Related Variations in the Biomechanical Properties of Human Sclera,” J. Mech. Behav. Biomed. Mater., **16**(1), pp. 181–191.

Girard, M. J. A., Dahlmann-Noor, A., Rayapureddi, S., Bechara, J. A., Bertin, B. M. E., Jones, H., Albon, J., Khaw, P. T., and Ethier, C. R., 2011, “Quantitative Mapping of Scleral Fiber Orientation in Normal Rat Eyes.,” Invest. Ophthalmol. Vis. Sci., **52**(13), pp. 9684–93.

Girard, M. J. A., Downs, J. C., Bottlang, M., Burgoyne, C. F., and Suh, J.-K. F., 2009, “Peripapillary and Posterior Scleral Mechanics—Part II: Experimental and Inverse Finite Element Characterization,” J. Biomech. Eng., **131**(5), p. 051012.

Girard, M. J. A., Downs, J. C., Burgoyne, C. F., and Suh, J.-K. F., 2009, “Peripapillary and Posterior Scleral Mechanics—Part I: Development of an Anisotropic Hyperelastic Constitutive Model,” J. Biomech. Eng., **131**(5), p. 051011.

Girard, M. J. A., Francis Suh, J. K., Bottlang, M., Burgoyne, C. F., and Crawford Downs, J., 2011, “Biomechanical Changes in the Sclera of Monkey Eyes Exposed to Chronic IOP Elevations,” Investig. Ophthalmol. Vis. Sci., **52**(8), pp. 5656–5669.

Girard, M. J. A., Suh, J. K. F., Bottlang, M., Burgoyne, C. F., and Downs, J. C., 2009, “Scleral Biomechanics in the Aging Monkey Eye,” Investig. Ophthalmol. Vis. Sci., **50**(11), pp. 5226–5237.

Girkin, C. A., Fazio, M. A., Yang, H., Reynaud, J., Burgoyne, C. F., Smith, B., Wang, L., and Downs, J. C., 2017, “Variation in the Three-Dimensional Histomorphometry of the Normal Human Optic Nerve Head with Age and Race: Lamina Cribrosa and Peripapillary Scleral Thickness and Position,” Investig. Ophthalmol. Vis. Sci., **58**(9), pp. 3759–3769.

Gogola, A., Jan, N., Lathrop, K. L., and Sigal, I. A., 2018, “Radial and Circumferential Collagen Fibers Are a Feature of the Peripapillary Sclera of Human, Monkey, Pig, Cow, Goat, and Sheep,” Investig. Opthalmology Vis. Sci., **59**(12), p. 4763.

Goldbaum, M. H., 1989, “The Extracellular Matrix of the Human Optic Nerve,” Arch. Ophthalmol., **107**(8), p. 1225.

Gouget, C. L. M., Girard, M. J., and Ethier, C. R., 2012, “A Constrained von Mises Distribution to Describe Fiber Organization in Thin Soft Tissues,” Biomech. Model. Mechanobiol., **11**(3–4), pp. 475–482.

Grytz, R., Fazio, M. a., Libertiaux, V., Bruno, L., Gardiner, S., Girkin, C. a., and Downs, J. C., 2014, “Age- and Race-Related Differences in Human Scleral Material Properties,” Invest. Ophthalmol. Vis. Sci., **55**(12), pp. 8163–8172.

Grytz, R., and Downs, J. C., 2013, “A Forward Incremental Prestressing Method with Application to Inverse Parameter Estimations and Eye-Specific Simulations of Posterior Scleral Shells,” Comput. Methods Biomech. Biomed. Engin., **16**(7), pp. 768–780.

Grytz, R., Fazio, M. A., Girard, M. J. A., Libertiaux, V., Bruno, L., Gardiner, S., Girkin, C. A., and Crawford Downs, J., 2014, “Material Properties of the Posterior Human Sclera,” J. Mech. Behav. Biomed. Mater., **29**, pp. 602–617.

Grytz, R., and Meschke, G., 2010, “A Computational Remodeling Approach to Predict the

Physiological Architecture of the Collagen Fibril Network in Corneo-Scleral Shells," Biomech. Model. Mechanobiol., **9**(2), pp. 225–235.

Grytz, R., Meschke, G., and Jonas, J. B., 2011, "The Collagen Fibril Architecture in the Lamina Cribrosa and Peripapillary Sclera Predicted by a Computational Remodeling Approach," Biomech. Model. Mechanobiol., **10**(3), pp. 371–382.

Grytz, R., and Siegwart, J. T., 2015, "Changing Material Properties of the Tree Shrew Sclera During Minus Lens Compensation and Recovery," Investig. Opthalmology Vis. Sci., **56**(3), p. 2065.

Guo, L., Moss, S. E., Alexander, R. A., Ali, R. R., Fitzke, F. W., and Cordeiro, M. F., 2005, "Retinal Ganglion Cell Apoptosis in Glaucoma Is Related to Intraocular Pressure and IOP-Induced Effects on Extracellular Matrix.," Invest. Ophthalmol. Vis. Sci., **46**(1), pp. 175–82.

Hanninen, V. A., Pantcheva, M. B., Freeman, E. E., Poulin, N. R., and Grosskretuz, C. L., 2002, "Activation of Caspase 9 in a Rat Model of Experimental Glaucoma.," Curr Eye Res, **25**(6), pp. 389–395.

Hao, L., Xiao, H., Gao, X., Xu, X., and Liu, X., 2019, "Measurement of Structural Parameters of the Lamina Cribrosa in Primary Open-Angle Glaucoma and Chronic Primary Angle-Closure Glaucoma by Optical Coherence Tomography and Its Correlations with Ocular Parameters," Ophthalmic Res., pp. 1–10.

Hasenfratz, G., 1987, "Experimental Studies on the Display of the Optic Nerve," pp. 587–602.

Hayreh, S. S., 2001, "The Blood Supply of the Optic Nerve Head and the Evaluation of It — Myth and Reality," Prog. Retin. Eye Res., **20**(5), pp. 563–593.

Henry Vandyke Carter, 1918, *Anatomy of the Human Body*, Lea and Febiger, Philadelphia and New York.

Hernandez, M. R., 2000, "The Optic Nerve Head in Glaucoma: Role of Astrocytes in Tissue Remodeling," Prog. Retin. Eye Res., **19**(3), pp. 297–321.

Hernandez, M. R., Andrzejewska, W. M., and Neufeld, A. H., 1990, "Changes in the Extracellular Matrix of the Human Optic Nerve Head in Primary Open-Angle Glaucoma," Am. J. Opthalmol., **109**(2), pp. 180–188.

Hernandez, M. R., Luo, X. X., Igoe, F., and Neufeld, A. H., 1987, "Extracellular Matrix of the Human Lamina Cribrosa," Am. J. Ophthalmol., **104**(6), pp. 567–576.

Hernandez, M. R., Miao, H., and Lukas, T., 2008, "Astrocytes in Glaucomatous Optic Neuropathy," Prog Brain Res, **173**, pp. 353–373.

Heuven, W. A. J. Van, and Kiel, J. W., 2009, "Arterial Pressure at the Entrance to the Retinal and Choroidal Circulations in the Rat," Invest. Ophthalmol. Vis. Sci, **50**(13), p. 406.

Hirata, M., Tsujikawa, A., Matsumoto, A., Hangai, M., Ooto, S., Yamashiro, K., Akiba, M., and Yoshimura, N., 2011, "Macular Choroidal Thickness and Volume in Normal

Subjects Measured by Swept-Source Optical Coherence Tomography," Investig. Ophthalmol. Vis. Sci., **52**(8), pp. 4971–4978.

Howell, G. R., Soto, I., Zhu, X., Ryan, M., Macalinao, D. G., Sousa, G. L., Caddle, L. B., MacNicoll, K. H., Barbay, J. M., Porciatti, V., Anderson, M. G., Smith, R. S., Clark, A. F., Libby, R. T., and John, S. W. M., 2012, "Radiation Treatment Inhibits Monocyte Entry into the Optic Nerve Head and Prevents Neuronal Damage in a Mouse Model of Glaucoma," J. Clin. Invest., **122**(4), pp. 1246–1261.

Hua, Y., Voorhees, A. P., and Sigal, I. A., 2018, "Cerebrospinal Fluid Pressure: Revisiting Factors Influencing Optic Nerve Head Biomechanics," Investig. Ophthalmol. Vis. Sci., **59**(1), pp. 154–165.

Ing, E., Ivers, K. M., Yang, H., Gardiner, S. K., Reynaud, J., Cull, G., Wang, L., and Burgoyne, C. F., 2016, "Cupping in the Monkey Optic Nerve Transection Model Consists of Prelaminar Tissue Thinning in the Absence of Posterior Laminar Deformation," Investig. Opthalmology Vis. Sci., **57**(6), p. 2914.

Ivers, K. M., Yang, H., Gardiner, S. K., Qin, L., Reyes, L., Fortune, B., and Burgoyne, C. F., 2016, "In Vivo Detection of Laminar and Peripapillary Scleral Hypercompliance in Early Monkey Experimental Glaucoma," Investig. Opthalmology Vis. Sci., **57**(9), p. OCT388.

Jan, N.-J., Grimm, J. L., Tran, H., Lathrop, K. L., Wollstein, G., Bilonick, R. A., Ishikawa, H., Kagemann, L., Schuman, J. S., and Sigal, I. A., 2015, "Polarization Microscopy for Characterizing Fiber Orientation of Ocular Tissues," Biomed. Opt. Express, **6**(12), p. 4705.

Jan, N.-J., Lathrop, K. L., and Sigal, I. A., 2017, "Collagen Architecture of the Posterior Pole: High-Resolution Wide Field of View Visualization and Analysis Using Polarized Light Microscopy," Invest. Ophthalmol. Vis. Sci., **58**, pp. 735–744.

Jan, N. J., Gomez, C., Moed, S., Voorhees, A. P., Schuman, J. S., Bilonick, R. A., and Sigal, I. A., 2017, "Microstructural Crimp of the Lamina Cribrosa and Peripapillary Sclera Collagen Fibers," Investig. Ophthalmol. Vis. Sci., **58**(9), pp. 3378–3388.

Jan, N. J., and Sigal, I. A., 2018, "Collagen Fiber Recruitment: A Microstructural Basis for the Nonlinear Response of the Posterior Pole of the Eye to Increases in Intraocular Pressure," Acta Biomater., **72**, pp. 295–305.

Jia, L., Cepurna, W. O., Johnson, E. C., and Morrison, J. C., 2000, "Effect of General Anesthetics on IOP in Rats with Experimental Aqueous Outflow Obstruction.," Invest. Ophthalmol. Vis. Sci., **41**(11), pp. 3415–9.

Jia, L., Cepurna, W. O., Johnson, E. C., and Morrison, J. C., 2000, "Patterns of Intraocular Pressure Elevation after Aqueous Humor Outflow Obstruction in Rats," Investig. Ophthalmol. Vis. Sci., **41**(6), pp. 1380–5.

Jiang, X., Johnson, E., Cepurna, W., Lozano, D., Men, S., Wang, R. K., and Morrison, J., 2018, "The Effect of Age on the Response of Retinal Capillary Filling to Changes in Intraocular Pressure Measured by Optical Coherence Tomography Angiography," Microvasc. Res., **115**(July 2017), pp. 12–19.

Jin, X., Mao, H., Yang, K. H., and King, A. I., 2014, “Constitutive Modeling of Pia-Arachnoid Complex,” Ann. Biomed. Eng., **42**(4), pp. 812–821.

Jin, Y., Wang, X., Zhang, L., Jonas, J. B., Aung, T., Schmetterer, L., and Girard, M. J. A., 2018, “Modeling the Origin of the Ocular Pulse and Its Impact on the Optic Nerve Head,” Investig. Ophthalmol. Vis. Sci., **59**(10), pp. 3997–4010.

Johnson, D. H., Richardson, T. M., and Epstein, D. L., 1989, “Trabecular Meshwork Recovery after Phagocytic Challenge,” Curr. Eye Res., **8**(11), pp. 1121–1130.

Johnson, E. C., Morrison, J. C., Farrell, S., Deppmeier, L., Moore, C. G., and McGinty, M. R., 1996, “The Effect of Chronically Elevated Intraocular Pressure on the Rat Optic Nerve Head Extracellular Matrix.,” Exp. Eye Res., **62**(6), pp. 663–74.

Johnson, E. C., Cepurna, W. O., Choi, D., Choe, T. E., and Morrison, J. C., 2014, “Radiation Pretreatment Does Not Protect the Rat Optic Nerve from Elevated Intraocular Pressure–Induced Injury,” Investig. Ophthalmol. Vis. Sci., **56**(1), pp. 412–419.

Johnson, E. C., Doser, T. A., Cepurna, W. O., Dyck, J. A., Jia, L., Guo, Y., Lambert, W. S., and Morrison, J. C., 2011, “Cell Proliferation and Interleukin-6-Type Cytokine Signaling Are Implicated by Gene Expression Responses in Early Optic Nerve Head Injury in Rat Glaucoma,” Investig. Ophthalmol. Vis. Sci., **52**(1), pp. 504–518.

Johnson, E. C., Deppmeier, L. M. H., Wentzien, S. K. F., Hsu, I., and Morrison, J. C., 2000, “Chronology of Optic Nerve Head and Retinal Responses to Elevated Intraocular Pressure,” IOVS, **41**(2).

Jonas, J. B., 2003, “Anatomic Relationship between Lamina Cribrosa, Intraocular Space, and Cerebrospinal Fluid Space,” Invest. Ophthalmol. Vis. Sci., **44**(12), pp. 5189–5195.

Jonas, J. B., Mardin, C. Y., Schlotzer-Schrehardt, U., and Naumann, G. O. H., 1991, “Morphometry of the Human Lamina Cribrosa Surface,” Investig. Ophthalmol. Vis. Sci., **32**(2), pp. 401–405.

Jonas, J. B., Holbach, L., and Panda-Jonas, S., 2014, “Peripapillary Ring: Histology and Correlations,” Acta Ophthalmol., **92**(4), pp. e273–e279.

Kang, M., and Yu, D.-Y., 2015, “Distribution Pattern of Axonal Cytoskeleton Proteins in the Human Optic Nerve Head,” Neural Regen. Res., **10**(8), p. 1198.

Keeley, F. W., Morin, J. D., and Vesely, S., 1984, “Characterization of Collagen from Normal Human Sclera,” Exp. Eye Res., **39**(5), pp. 533–542.

Kim, J. A., Kim, T. W., Weinreb, R. N., Lee, E. J., Girard, M. J. A., and Mari, J. M., 2018, “Lamina Cribrosa Morphology Predicts Progressive Retinal Nerve Fiber Layer Loss in Eyes with Suspected Glaucoma,” Sci. Rep., **8**(1), pp. 1–10.

Kim, M., Bojikian, K., Slabaugh, M., Ding, L., and Chen, P., 2016, “Lamina Depth and Thickness Correlate with Glaucoma Severity,” Indian J. Ophthalmol., **64**(5), p. 358.

Kim, Y. W., Kim, D. W., Jeoung, J. W., Kim, D. M., and Park, K. H., 2015, “Peripheral

Lamina Cribrosa Depth in Primary Open-Angle Glaucoma: A Swept-Source Optical Coherence Tomography Study of Lamina Cribrosa," Eye, **29**(10), pp. 1368–1374.

Kim, Y. W., Jeoung, J. W., Girard, M. J. A., Mari, J. M., and Park, K. H., 2016, "Positional and Curvature Difference of Lamina Cribrosa According to the Baseline Intraocular Pressure in Primary Open-Angle Glaucoma: A Swept-Source Optical Coherence Tomography (SS-OCT) Study," PLoS One, **11**(9), p. e0162182.

Kimball, E. C., Nguyen, C., Steinhart, M. R., Nguyen, T. D., Pease, M. E., Oglesby, E. N., Oveson, B. C., and Quigley, H. a, 2014, "Experimental Scleral Cross-Linking Increases Glaucoma Damage in a Mouse Model.," Exp. Eye Res., **128**, pp. 129–140.

Komai, Y., and Ushiki, T., 1991, "The Three-Dimensional Organization of Collagen Fibrils in the Human Cornea and Sclera," Investig. Ophthalmol. Vis. Sci., **32**(8), pp. 2244–2258.

Kotecha, A., Izadi, S., and Jeffery, G., 2006, "Age-Related Changes in the Thickness of the Human Lamina Cribrosa," Br. J. Ophthalmol., **90**(12), pp. 1531–1534.

Kuo, A. N., McNabb, R. P., Chiu, S. J., El-Dairi, M. A., Farsiu, S., Toth, C. A., and Izatt, J. A., 2013, "Correction of Ocular Shape in Retinal Optical Coherence Tomography and Effect on Current Clinical Measures," Am. J. Ophthalmol., **156**(2), pp. 304–311.

Langham, M., 1980, "The Temporal Relation between Intraocular Pressure and Loss of Vision in Chronic Simpe Glaucoma.," Glaucoma, **2**, pp. 427–435.

Lee, K. M., Lee, E. J., and Kim, T. W., 2016, "Juxtapapillary Choroid Is Thinner in Normal-Tension Glaucoma than in Healthy Eyes," Acta Ophthalmol., **94**(8), pp. e697–e708.

Lee, S. H., Kim, T. W., Lee, E. J., Girard, M. J. A., and Mari, J. M., 2017, "Diagnostic Power of Lamina Cribrosa Depth and Curvature in Glaucoma," Investig. Ophthalmol. Vis. Sci., **58**(2), pp. 755–762.

Leske, M. C., 2009, "Ocular Perfusion Pressure and Glaucoma: Clinical Trial and Epidemiologic Findings," Curr. Opin. Ophthalmol., **20**(2), pp. 73–78.

Li, L., Bian, A., Cheng, G., and Zhou, Q., 2016, "Posterior Displacement of the Lamina Cribrosa in Normal-Tension and High-Tension Glaucoma," Acta Ophthalmol., **94**(6), pp. e492–e500.

Li, Y., Li, D., Ying, X., Khaw, P. T., and Raisman, G., 2015, "An Energy Theory of Glaucoma," Glia, p. n/a-n/a.

Liang, Y., Downs, J. C., Fortune, B., Cull, G., Cioffi, G. A., and Wang, L., 2009, "Impact of Systemic Blood Pressure on the Relationship between Intraocular Pressure and Blood Flow in the Optic Nerve Head of Nonhuman Primates," Investig. Ophthalmol. Vis. Sci., **50**(5), pp. 2154–2160.

Lockwood, H., Reynaud, J., Gardiner, S., Grimm, J., Libertiaux, V., Downs, J. C., Yang, H., and Burgoyne, C. F., 2015, "Lamina Cribrosa Microarchitecture in Normal Monkey Eyes Part 1: Methods and Initial Results," Investig. Ophthalmol. Vis. Sci., **56**(3), pp. 1618–1637.

Lozano, D. C., and Twa, M. D., 2013, “Development of a Rat Schematic Eye from in Vivo Biometry and the Correction of Lateral Magnification in SD-OCT Imaging,” Investig. Ophthalmol. Vis. Sci., **54**(9), pp. 6446–6455.

Maas, S. A., Ellis, B. J., Ateshian, G. A., and Weiss, J. A., 2012, “FEBio: Finite Elements for Biomechanics,” J. Biomech. Eng., **134**(1), p. 011005.

Meek, S., Mashimo, T., and Burdon, T., 2017, “From Engineering to Editing the Rat Genome,” Mamm. Genome, **28**(7–8), pp. 302–314.

Midgett, D. E., Pease, M. E., Jefferys, J. L., Patel, M., Franck, C., Quigley, H. A., and Nguyen, T. D., 2017, “The Pressure-Induced Deformation Response of the Human Lamina Cribrosa: Analysis of Regional Variations,” Acta Biomater., **53**, pp. 123–139.

Minckler, D. S., Bunt, A. H., and Johanson, G. W., 1977, “Orthograde and Retrograde Axoplasmic Transport during Acute Ocular Hypertension in the Monkey,” Invest Ophthalmol Vis Sci, **16**(5), pp. 426–441.

Moons, L., Salinas-Navarro, M., Geeraerts, E., Dekeyster, E., De Groef, L., Baekelandt, V., Van den Haute, C., and Buyens, T., 2015, “Tackling Glaucoma from within the Brain: An Unfortunate Interplay of BDNF and TrkB,” PLoS One, **10**(11), p. e0142067.

Morgan, J. E., 2000, “Optic Nerve Head Structure in Glaucoma: Astrocytes as Mediators of Axonal Damage.,” Eye (Lond)., **14 ( Pt 3B**, pp. 437–444.

Morgan, J. E., 2004, “Circulation and Axonal Transport in the Optic Nerve.,” Eye (Lond)., **18**(11), pp. 1089–95.

Morgan, J. E., and Tribble, J. R., 2015, “Microbead Models in Glaucoma,” Exp. Eye Res., **141**, pp. 9–14.

Morgan, W. H., Yu, D. Y., Alder, V. A., Cringle, S. J., Cooper, R. L., House, P. H., and Constable, I. J., 1998, “The Correlation between Cerebrospinal Fluid Pressure and Retrolaminar Tissue Pressure,” Investig. Ophthalmol. Vis. Sci., **39**(8), pp. 1419–1428.

Morrison, J. C., Moore, C. G., Deppmeier, L. M., Gold, B. G., Meshul, C. K., and Johnson, E. C., 1997, “A Rat Model of Chronic Pressure-Induced Optic Nerve Damage.,” Exp. Eye Res., **64**(1), pp. 85–96.

Morrison, J. C., Cepurna, W. O., and Johnson, E. C., 2015, “Modeling Glaucoma in Rats by Sclerosing Aqueous Outflow Pathways to Elevate Intraocular Pressure,” Exp. Eye Res., **141**, pp. 23–32.

Morrison, J. C., Cepurna, W. O., Tehrani, S., Choe, T. E., Jayaram, H., Lozano, D. C., Fortune, B., and Johnson, E. C., 2016, “A Period of Controlled Elevation of IOP (CEI) Produces the Specific Gene Expression Responses and Focal Injury Pattern of Experimental Rat Glaucoma,” Investig. Opthalmology Vis. Sci., **57**(15), p. 6700.

Morrison, J. C., Cepurna Ying Guo, W. O., and Johnson, E. C., 2011, “Pathophysiology of Human Glaucomatous Optic Nerve Damage: Insights from Rodent Models of Glaucoma,” Exp. Eye Res., **93**(2), pp. 156–164.

Morrison, J. C., Dorman-Pease, M. E., Dunkelberger, G. R., and Quigley, H. A., 1990, “Optic Nerve Head Extracellular Matrix in Primary Optic Atrophy and Experimental Glaucoma,” Arch Ophthalmol, **108**(7), pp. 1020–1024.

Morrison, J. C., Johnson, E., and Cepurna, W. O., 2008, “Rat Models for Glaucoma Research,” *Progress in Brain Research*, pp. 285–301.

Morrison, J. C., Johnson, E. C., Cepurna, W., and Jia, L., 2005, “Understanding Mechanisms of Pressure-Induced Optic Nerve Damage.,” Prog. Retin. Eye Res., **24**(2), pp. 217–40.

Mosaed, S., Liu, J. H. K., and Weinreb, R. N., 2005, “Correlation between Office and Peak Nocturnal Intraocular Pressures in Healthy Subjects and Glaucoma Patients,” Am. J. Ophthalmol., **139**(2), pp. 320–324.

Mulvihill, J. J. E., Raykin, J., Snider, E. J., Schildmeyer, L. A., Zaman, I., Platt, M. O., Kelly, D. J., and Ethier, C. R., 2018, “Development of a Platform for Studying 3D Astrocyte Mechanobiology: Compression of Astrocytes in Collagen Gels,” Ann. Biomed. Eng., **46**(2), pp. 365–374.

Murienne, B. J., Chen, M. L., Quigley, H. A., and Nguyen, T. D., 2016, “The Contribution of Glycosaminoglycans to the Mechanical Behaviour of the Posterior Human Sclera,” J. R. Soc. Interface, **13**(119).

Murienne, B. J., Jefferys, J. L., Quigley, H. a., and Nguyen, T. D., 2015, “The Effects of Glycosaminoglycan Degradation on the Mechanical Behavior of the Posterior Porcine Sclera,” Acta Biomater., **12**, pp. 195–206.

Myers, K. M., Cone, F. E., Quigley, H. a., Gelman, S., Pease, M. E., and Nguyen, T. D., 2010, “The in Vitro Inflation Response of Mouse Sclera,” Exp. Eye Res., **91**(6), pp. 866–875.

Nadler, Z., Wang, B. B., Schuman, J. S., Daniel Ferguson, R., Patel, A., Hammer, D. X., Bilonick, R. A., Ishikawa, H., Kagemann, L., Sigal, I. A., Wollstein, G., Ferguson, R. D., Patel, A., Hammer, D. X., Bilonick, R. A., Ishikawa, H., Kagemann, L., Sigal, I. A., Wollstein, G., Daniel Ferguson, R., Patel, A., Hammer, D. X., Bilonick, R. A., Ishikawa, H., Kagemann, L., Sigal, I. A., and Wollstein, G., 2014, “In Vivo Three-Dimensional Characterization of the Healthy Human Lamina Cribrosa with Adaptive Optics Spectral-Domain Optical Coherence Tomography,” Investig. Ophthalmol. Vis. Sci., **55**(10), pp. 6459–6466.

Nguyen, C., Midgett, D. E., Kimball, E. C., Steinhart, M. R., Nguyen, T. D., Pease, M. E., Ogelsby, E. N., and Quigley, H. A., 2017, “Measuring Deformation in the Mouse Optic Nerve Head and Peripapillary Sclera,” Invest. Ophthalmol. Vis. Sci.

Nguyen, C., Cone, F. E., Nguyen, T. D., Coudrillier, B., Pease, M. E., Steinhart, M. R., Oglesby, E. N., Jefferys, J. L., and Quigley, H. a., 2013, “Studies of Scleral Biomechanical Behavior Related to Susceptibility for Retinal Ganglion Cell Loss in Experimental Mouse Glaucoma,” Investig. Ophthalmol. Vis. Sci., **54**(3), pp. 1767–1780.

Nguyen, J. V., Soto, I., Kim, K.-Y., Bushong, E. A., Oglesby, E., Valiente-Soriano, F. J.,

Yang, Z., Davis, C. -h. O., Bedont, J. L., Son, J. L., Wei, J. O., Buchman, V. L., Zack, D. J., Vidal-Sanz, M., Ellisman, M. H., and Marsh-Armstrong, N., 2011, “Myelination Transition Zone Astrocytes Are Constitutively Phagocytic and Have Synuclein Dependent Reactivity in Glaucoma,” Proc. Natl. Acad. Sci., **108**(3), pp. 1176–1181.

Nissirios, N., Chanis, R., Johnson, E., Morrison, J., Cepurna, W. O., Jia, L., Mittag, T., and Danias, J., 2008, “Comparison of Anterior Segment Structures in Two Rat Glaucoma Models: An Ultrasound Biomicroscopic Study,” Investig. Opthalmology Vis. Sci., **49**(6), p. 2478.

van Noort, R., Black, M. M., Martin, T. R. P., and Meanley, S., 1981, “A Study of the Uniaxial Mechanical Properties of Human Dura Mater Preserved in Glycerol,” Biomaterials, **2**(1), pp. 41–45.

Norman, R. E., Flanagan, J. G., Rausch, S. M. K., Sigal, I. A., Tertinegg, I., Eilaghi, A., Portnoy, S., Sled, J. G., and Ethier, C. R., 2010, “Dimensions of the Human Sclera: Thickness Measurement and Regional Changes with Axial Length,” Exp. Eye Res., **90**(2), pp. 277–284.

Norman, R. E., Flanagan, J. G., Sigal, I. a., Rausch, S. M. K., Tertinegg, I., and Ethier, C. R., 2011, “Finite Element Modeling of the Human Sclera: Influence on Optic Nerve Head Biomechanics and Connections with Glaucoma,” Exp. Eye Res., **93**(1), pp. 4–12.

Okeke, C. O., Quigley, H. A., Jampel, H. D., Ying, G., Plyler, R. J., Jiang, Y., and Friedman, D. S., 2009, “Adherence with Topical Glaucoma Medication Monitored Electronically,” Ophthalmology, **116**(2), pp. 191–199.

Oxlund, H., and Andreassen, T. T., 1980, “The Roles of Hyaluronic Acid, Collagen and Elastin in the Mechanical Properties of Connective Tissues.,” J. Anat., **131**(Pt 4), pp. 611–20.

Papazafeiropoulos, G., Muñiz-Calvente, M., and Martínez-Pañeda, E., 2017, “Abaqus2Matlab: A Suitable Tool for Finite Element Post-Processing,” Adv. Eng. Softw., **105**, pp. 9–16.

Pazos, M., Yang, H., Gardiner, S. K., Cepurna, W. O., Johnson, E. C., Morrison, J. C., and Burgoyne, C. F., 2015, “Rat Optic Nerve Head Anatomy within 3D Histomorphometric Reconstructions of Normal Control Eyes,” Exp. Eye Res., **139**, pp. 1–12.

Pazos, M., Yang, H., Gardiner, S. K., Cepurna, W. O., Johnson, E. C., Morrison, J. C., and Burgoyne, C. F., 2016, “Expansions of the Neurovascular Scleral Canal and Contained Optic Nerve Occur Early in the Hypertonic Saline Rat Experimental Glaucoma Model,” Exp. Eye Res., **145**, pp. 173–186.

Pease, M. E., McKinnon, S. J., Quigley, H. a., Kerrigan-Baumrind, L. a., and Zack, D. J., 2000, “Obstructed Axonal Transport of BDNF and Its Receptor TrkB in Experimental Glaucoma,” Invest. Ophthalmol. Vis. Sci., **41**(3), pp. 764–774.

Pena, J. D. O., Agapova, O., Gabelt, B. T., Levin, L. A., Lucarelli, M. J., Kaufman, P. L., and Hernandez, M. R., 2001, “Increased Elastin Expression in Astrocytes of the

Lamina Cribrosa in Response to Elevated Intraocular Pressure," Investig. Ophthalmol. Vis. Sci., **42**(10), pp. 2303–2314.

Pijanka, J. K., Coudrillier, B., Ziegler, K., Sorensen, T., Meek, K. M., Nguyen, T. D., Quigley, H. A., and Boote, C., 2012, "Quantitative Mapping of Collagen Fiber Orientation in Non-Glaucoma and Glaucoma Posterior Human Sclerae," Investig. Opthalmology Vis. Sci., **53**(9), p. 5258.

Pijanka, J. K., Kimball, E. C., Pease, M. E., Abass, A., Sorensen, T., Nguyen, T. D., Quigley, H. A., and Boote, C., 2014, "Changes in Scleral Collagen Organization in Murine Chronic Experimental Glaucoma," Invest. Ophthalmol. Vis. Sci., **55**(10), pp. 6554–6564.

Pijanka, J. K., Markov, P. P., Midgett, D., Paterson, N. G., White, N., Blain, E. J., Nguyen, T. D., Quigley, H. A., and Boote, C., 2019, "Quantification of Collagen Fiber Structure Using Second Harmonic Generation Imaging and Two-Dimensional Discrete Fourier Transform Analysis: Application to the Human Optic Nerve Head," J. Biophotonics, (December 2018), p. e201800376.

Pijanka, J. K., Spang, M. T., Sorensen, T., Liu, J., Nguyen, T. D., Quigley, H. A., and Boote, C., 2015, "Depth-Dependent Changes in Collagen Organization in the Human Peripapillary Sclera," PLoS One, **10**(2), pp. 1–17.

Price, K. V, Storn, R. M., and Lampinen, J. A., 2005, *Differential Evolution: A Practical Approach to Global Optimization*, Springer, Berlin.

Quigley, H. a, 1999, "Neuronal Death in Glaucoma.," Prog. Retin. Eye Res., **18**(1), pp. 39–57.

Quigley, H. A., and Addicks, E. M., 1981, "Regional Differences in the Structure of the Lamina Cribrosa and Their Relation to Glaucomatous Optic Nerve Damage," Arch Ophthalmol, **99**(1), pp. 137–143.

Quigley, H. A., Dorman-Pease, M. E., and Brown, A. E., 1991, "Quantitative Study of Collagen and Elastin of the Optic Nerve Head and Sclera in Human and Experimental Monkey Glaucoma," Curr Eye Res, **10**(9), pp. 877–888.

Quigley, H. a, McKinnon, S. J., Zack, D. J., Pease, M. E., Kerrigan-Baumrind, L. a, Kerrigan, D. F., and Mitchell, R. S., 2000, "Retrograde Axonal Transport of BDNF in Retinal Ganglion Cells Is Blocked by Acute IOP Elevation in Rats.," Invest. Ophthalmol. Vis. Sci., **41**(11), pp. 3460–6.

Quigley, H., and Anderson, D. R., 1976, "The Dynamics and Location of Axonal Transport Blockade by Acute Intraocular Pressure Elevation in Primate Optic Nerve.," Invest. Ophthalmol., **15**(8), pp. 606–16.

Quigley, H. A., 2005, "Glaucoma: Macrocosm to Microcosm The Friedenwald Lecture," Investig. Opthalmology Vis. Sci., **46**(8), p. 2663.

Quigley, H. A., Addicks, E. M., and Green, W. R., 1982, "Optic Nerve Damage in Human Glaucoma: Iii. Quantitative Correlation of Nerve Fiber Loss and Visual Field Defect in Glaucoma, Ischemic Neuropathy, Papilledema, and Toxic Neuropathy," Arch.

Ophthalmol., **100**(1), pp. 135–146.

Quigley, H. A., Brown, A., and Dorman-Pease, M. E., 1991, “Alterations in Elastin of the Optic Nerve Head in Human and Experimental Glaucoma,” Br. J. Ophthalmol., **75**(9), pp. 552–557.

Quigley, H. A., Hohman, R. M., Addicks, E. M., Massof, R. W., and Green, W. R., 1983, “Morphologic Changes in the Lamina Cribrosa Correlated with Neural Loss in Open-Angle Glaucoma,” Am. J. Ophthalmol., **95**(5), pp. 673–691.

Quigley, H. a, and Addicks, E. M., 1980, “Chronic Experimental Glaucoma in Primates. II. Effect of Extended Intraocular Pressure Elevation on Optic Nerve Head and Axonal Transport.,” Invest. Ophthalmol. Vis. Sci., **19**(2), pp. 137–52.

Quigley, H. A., Addicks, E. M., Green, W. R., and Maumenee, A. E., 1981, “Optic Nerve Damage in Human Glaucoma. II. The Site of Injury and Susceptibility to Damage,” Arch Ophthalmol, **99**(4), pp. 635–49.

Quigley, H. a, Nickells, R. W., Kerrigan, L. a, Pease, M. E., Thibault, D. J., and Zack, D. J., 1995, “Retinal Ganglion Cell Death in Experimental Glaucoma and after Axotomy Occurs by Apoptosis,” Invest. Ophthalmol., **36**(April), pp. 774–86.

Quigley, H., Arora, K., Idrees, S., Solano, F., Bedrood, S., Lee, C., Jefferys, J., and Nguyen, T. D., 2017, “Biomechanical Responses of Lamina Cribrosa to Intraocular Pressure Change Assessed by Optical Coherence Tomography in Glaucoma Eyes,” Investig. Ophthalmol. Vis. Sci., **58**(5), pp. 2566–2577.

Raspanti, M., Marchini, M., Della Pasqua, V., Strocchi, R., and Ruggeri, A., 1992, “Ultrastructure of the Extracellular Matrix of Bovine Dura Mater, Optic Nerve Sheath and Sclera,” J. Anat., **181**(2), pp. 181–187.

Raykin, J., Forte, T. E., Wang, R., Feola, A., Samuels, B. C., Myers, J. G., Mulugeta, L., Nelson, E. S., Gleason, R. L., and Ethier, C. R., 2017, “Characterization of the Mechanical Behavior of the Optic Nerve Sheath and Its Role in Spaceflight-Induced Ophthalmic Changes,” Biomech. Model. Mechanobiol., **16**(1), pp. 33–43.

Ren, R., Jonas, J. B., Tian, G., Zhen, Y., Ma, K., Li, S., Wang, H., Li, B., Zhang, X., and Wang, N., 2010, “Cerebrospinal Fluid Pressure in Glaucoma,” Ophthalmology, **117**(2), pp. 259–266.

Reynaud, J., Lockwood, H., Gardiner, S. K., Williams, G., Yang, H., and Burgoyne, C. F., 2016, “Lamina Cribrosa Microarchitecture in Monkey Early Experimental Glaucoma: Global Change,” Investig. Ophthalmol. Vis. Sci., **57**(7), pp. 3451–3469.

Roberts, M. D., Grau, V., Grimm, J., Reynaud, J., Bellezza, A. J., Burgoyne, C. F., and Downs, J. C., 2009, “Remodeling of the Connective Tissue Microarchitecture of the Lamina Cribrosa in Early Experimental Glaucoma,” Investig. Opthalmology Vis. Sci., **50**(2), p. 681.

Roberts, M. D., Liang, Y., Sigal, I. a., Grimm, J., Reynaud, J., Bellezza, A., Burgoyne, C. F., and Downs, J. C., 2010, “Correlation between Local Stress and Strain and Lamina Cribrosa Connective Tissue Volume Fraction in Normal Monkey Eyes,” Investig.

Ophthalmol. Vis. Sci., **51**(1), pp. 295–307.

Roberts, M. D., Sigal, I. A., Liang, Y., Burgoyne, C. F., and Downs, J. C., 2010, “Changes in the Biomechanical Response of the Optic Nerve Head in Early Experimental Glaucoma,” Investig. Opthalmology Vis. Sci., **51**(11), p. 5675.

Sacks, M. S., Smith, D. B., and Hiester, E. D., 1997, “A Small Angle Light Scattering Device for Planar Connective Tissue Microstructural Analysis,” Ann. Biomed. Eng., **25**(4), pp. 678–689.

Schlamp, C. L., Li, Y., Dietz, J. A., Janssen, K. T., and Nickells, R. W., 2006, “Progressive Ganglion Cell Loss and Optic Nerve Degeneration in DBA/2J Mice Is Variable and Asymmetric,” BMC Neurosci., **7**(1), p. 66.

Schmidl, D., Garhofer, G., and Schmetterer, L., 2011, “The Complex Interaction between Ocular Perfusion Pressure and Ocular Blood Flow - Relevance for Glaucoma,” Exp. Eye Res., **93**(2), pp. 141–155.

Schwaner, S. A., Kight, A. M., Perry, R. N., Pazos, M., Yang, H., Johnson, E. C., Morrison, J. C., Burgoyne, C. F., and Ross Ethier, C., 2018, “A Methodology for Individual-Specific Modeling of Rat Optic Nerve Head Biomechanics in Glaucoma,” J. Biomech. Eng., **140**(8), pp. 084501-1-084501–10.

Scott, A., 2015, “Attitudinal Survey of Americans on Eye and Vision Health,” Investig. Ophthalmol. Vis. Sci., **56**(7), p. 1672.

Sherwood, J. M., Reina-Torres, E., Bertrand, J. A., Rowe, B., and Overby, D. R., 2016, “Measurement of Outflow Facility Using IPerfusion,” PLoS One, **11**(3), p. e0150694.

Shetye, S. S., Deault, M. M., and Puttlitz, C. M., 2014, “Biaxial Response of Ovine Spinal Cord Dura Mater,” J. Mech. Behav. Biomed. Mater., **34**, pp. 146–153.

Sigal, I. A., 2009, “Interactions between Geometry and Mechanical Properties on the Optic Nerve Head,” Investig. Ophthalmol. Vis. Sci., **50**(6), pp. 2785–2795.

Sigal, I. A., Bilonick, R. A., Kagemann, L., Wollstein, G., Ishikawa, H., Schuman, J. S., and Grimm, J. L., 2012, “The Optic Nerve Head as a Robust Biomechanical System,” Investig. Ophthalmol. Vis. Sci., **53**(6), pp. 2658–2667.

Sigal, I. A., Brazile, B., Wei, J., Hua, Y., Jan, N.-J., and Yang, B., 2018, “Structured Polarized Light Microscopy for Collagen Fiber Structure and Orientation Quantification in Thick Ocular Tissues,” J. Biomed. Opt., **23**(10), p. 1.

Sigal, I. a., Flanagan, J. G., Tertinegg, I., and Ethier, C. R., 2009, “Modeling Individual-Specific Human Optic Nerve Head Biomechanics. Part II: Influence of Material Properties,” Biomech. Model. Mechanobiol., **8**(2), pp. 99–109.

Sigal, I. A., Flanagan, J. G., Tertinegg, I., and Ethier, C. R., 2007, “Predicted Extension, Compression and Shearing of Optic Nerve Head Tissues,” Exp. Eye Res., **85**(3), pp. 312–322.

Sigal, I. A., Grimm, J. L., Jan, N.-J., Reid, K., Minckler, D. S., and Brown, D. J., 2014, “Eye-Specific IOP-Induced Displacements and Deformations of Human Lamina

Cribrosa," Invest. Ophthalmol. Vis. Sci., **55**(1), pp. 6834–6940.

Sigal, I. A., Yang, H., Roberts, M. D., Burgoyne, C. F., and Crawford Downs, J., 2011, "IOP-Induced Lamina Cribrosa Displacement and Scleral Canal Expansion: An Analysis of Factor Interactions Using Parameterized Eye-Specific Models," Investig. Ophthalmol. Vis. Sci., **52**(3), pp. 1896–1907.

Sigal, I. A., Yang, H., Roberts, M. D., and Downs, J. C., 2010, "Morphing Methods to Parameterize Specimen-Specific Finite Element Model Geometries," J Biomech, **43**(2), pp. 254–262.

Sigal, I. A., Yang, H., Roberts, M. D., Grimm, J. L., Burgoyne, C. F., Demirel, S., and Downs, J. C., 2011, "IOP-Induced Lamina Cribrosa Deformation and Scleral Canal Expansion: Independent or Related?," Investig. Ophthalmol. Vis. Sci., **52**(12), pp. 9023–9032.

Sigal, I. a, Flanagan, J. G., and Ethier, C. R., 2005, "Factors Influencing Optic Nerve Head Biomechanics.," Invest. Ophthalmol. Vis. Sci., **46**(11), pp. 4189–99.

Sigal, I. a, Flanagan, J. G., Tertinegg, I., and Ethier, C. R., 2004, "Finite Element Modeling of Optic Nerve Head Biomechanics.," Invest. Ophthalmol. Vis. Sci., **45**(12), pp. 4378–87.

Sigal, I. a, Flanagan, J. G., Tertinegg, I., and Ethier, C. R., 2009, "Modeling Individual-Specific Human Optic Nerve Head Biomechanics. Part I: IOP-Induced Deformations and Influence of Geometry.," Biomech. Model. Mechanobiol., **8**(2), pp. 85–98.

Sigal, I. a, Flanagan, J. G., Tertinegg, I., and Ethier, C. R., 2005, "Reconstruction of Human Optic Nerve Heads for Finite Element Modeling.," Technol. Health Care, **13**(4), pp. 313–29.

Spoerl, E., Boehm, A. G., and Pillunat, L. E., 2005, "The Influence of Various Substances on the Biomechanical Behavior of Lamina Cribrosa and Peripapillary Sclera," Investig. Ophthalmol. Vis. Sci., **46**(4), pp. 1286–1290.

Stowell, C., Burgoyne, C. F., Tamm, E. R., Ethier, C. R., Dowling, J. E., Downs, C., Ellisman, M. H., Fisher, S., Fortune, B., Fruttiger, M., Jakobs, T., Lewis, G., Masland, R. H., Mitchell, C. H., Morrison, J., Sharma, S. C., Sigal, I., Sofroniew, M., Wang, L., Wiggs, J., and Wu, S., 2017, "Biomechanical Aspects of Axonal Damage in Glaucoma: A Brief Review," Exp. Eye Res., **157**, pp. 13–19.

Strouthidis, N. G., Fortune, B., Yang, H., Sigal, I. A., and Burgoyne, C. F., 2011, "Effect of Acute Intraocular Pressure Elevation on the Monkey Optic Nerve Head as Detected by Spectral Domain Optical Coherence Tomography," Investig. Ophthalmol. Vis. Sci., **52**(13), pp. 9431–9437.

Strouthidis, N. G., Fortune, B., Yang, H., Sigal, I. A., and Burgoyne, C. F., 2011, "Longitudinal Change Detected by Spectral Domain Optical Coherence Tomography in the Optic Nerve Head and Peripapillary Retina in Experimental Glaucoma," Investig. Opthalmology Vis. Sci., **52**(3), p. 1206.

Strouthidis, N. G., Grimm, J., Williams, G. A., Cull, G. A., Wilson, D. J., and Burgoyne, C.

F., 2010, “A Comparison of Optic Nerve Head Morphology Viewed by Spectral Domain Optical Coherence Tomography and by Serial Histology,” Investig. Opthalmology Vis. Sci., **51**(3), p. 1464.

Stumpff, F., and Wiederholt, M., 2000, “Regulation of Trabecular Meshwork Contractility,” Ophthalmologica, **214**(1), pp. 33–53.

Summers Rada, J. A., Shelton, S., and Norton, T. T., 2006, “The Sclera and Myopia,” Exp. Eye Res., **82**(2), pp. 185–200.

Sun, D., Qu, J., and Jakobs, T. C., 2013, “Reversible Reactivity by Optic Nerve Astrocytes,” Glia, **61**(8), pp. 1218–1235.

Taban, M., Spoor, T. C., McHenry, J. G., and Sadun, A. A., 2001, “Histopathology and Ultrastructural Examination of Optic Nerve Sheath Biopsies After Optic Nerve Sheath Decompression With and Without Mitomycin,” Ophthal. Plast. Reconstr. Surg., **17**(5), pp. 332–337.

Tan, N. Y. Q., Koh, V., Girard, M. J. A., and Cheng, C. Y., 2018, “Imaging of the Lamina Cribrosa and Its Role in Glaucoma: A Review,” Clin. Exp. Ophthalmol., **46**(2), pp. 177–188.

Tehrani, S., Davis, L., Cepurna, W. O., Choe, T. E., Lozano, D. C., Monfared, A., Cooper, L., Cheng, J., Johnson, E. C., and Morrison, J. C., 2016, “Astrocyte Structural and Molecular Response to Elevated Intraocular Pressure Occurs Rapidly and Precedes Axonal Tubulin Rearrangement within the Optic Nerve Head in a Rat Model,” PLoS One, **11**(11), p. e0167364.

Tehrani, S., Johnson, E. C., Cepurna, W. O., and Morrison, J. C., 2014, “Astrocyte Processes Label for Filamentous Actin and Reorient Early within the Optic Nerve Head in a Rat Glaucoma Model.,” Invest. Ophthalmol. Vis. Sci., **55**(10), pp. 6945–52.

Thakku, S. G., Tham, Y.-C., Baskaran, M., Mari, J.-M., Strouthidis, N. G., Aung, T., Cheng, C.-Y., and Girard, M. J. A., 2015, “A Global Shape Index to Characterize Anterior Lamina Cribrosa Morphology and Its Determinants in Healthy Indian Eyes,” Investig. Opthalmology Vis. Sci., **56**(6), p. 3604.

Tham, Y. C., Li, X., Wong, T. Y., Quigley, H. A., Aung, T., and Cheng, C. Y., 2014, “Global Prevalence of Glaucoma and Projections of Glaucoma Burden through 2040: A Systematic Review and Meta-Analysis,” Ophthalmology, **121**(11), pp. 2081–2090.

Ugarte, M., Hussain, A. A., and Marshall, J., 2006, “An Experimental Study of the Elastic Properties of the Human Bruch’s Membrane-Choroid Complex: Relevance to Ageing.,” Br. J. Ophthalmol., **90**(5), pp. 621–626.

Varma, R., Lee, P. P., Goldberg, I., and Kotak, S., 2011, “An Assessment of the Health and Economic Burdens of Glaucoma,” Am. J. Ophthalmol., **152**(4), pp. 515–522.

Voorhees, A. P., Grimm, J. L., Bilonick, R. A., Kagemann, L., Ishikawa, H., Schuman, J. S., Wollstein, G., and Sigal, I. A., 2016, “What Is a Typical Optic Nerve Head?,” Exp. Eye Res., **149**, pp. 40–47.

Voorhees, A. P., Jan, N.-J., and Sigal, I. A., 2017, “Effects of Collagen Microstructure and Material Properties on the Deformation of the Neural Tissues of the Lamina Cribrosa,” Acta Biomater., **58**, pp. 278–290.

Voorhees, A. P., Jan, N. J., Austin, M. E., Flanagan, J. G., Sivak, J. M., Bilonick, R. A., and Sigal, I. A., 2017, “Lamina Cribrosa Pore Shape and Size as Predictors of Neural Tissue Mechanical Insult,” Investig. Ophthalmol. Vis. Sci., **58**(12), pp. 5336–5346.

Voorhees, A. P., Jan, N. J., Hua, Y., Yang, B., and Sigal, I. A., 2018, “Peripapillary Sclera Architecture Revisited: A Tangential Fiber Model and Its Biomechanical Implications,” Acta Biomater., **79**, pp. 113–122.

Vulsteke, C., Stalmans, I., Fieuws, S., and Zeyen, T., 2008, “Correlation between Ocular Pulse Amplitude Measured by Dynamic Contour Tonometer and Visual Field Defects,” Graefe’s Arch. Clin. Exp. Ophthalmol., **246**(4), pp. 559–565.

Vurgese, S., Panda-Jonas, S., and Jonas, J. B., 2012, “Scleral Thickness in Human Eyes,” PLoS One, **7**(1), p. e29692.

Wang, B., Lucy, K. A., Schuman, J. S., Sigal, I. A., Bilonick, R. A., Kagemann, L., Kostanyan, T., Lu, C., Liu, J., Grulkowski, I., Fujimoto, J. G., Ishikawa, H., and Wollstein, G., 2016, “Decreased Lamina Cribrosa Beam Thickness and Pore Diameter Relative to Distance From the Central Retinal Vessel Trunk,” Investig. Opthalmology Vis. Sci., **57**(7), p. 3088.

Wang, B., Lucy, K. A., Schuman, J. S., Sigal, I. A., Bilonick, R. A., Lu, C., Liu, J., Grulkowski, I., Nadler, Z., Ishikawa, H., Kagemann, L., Fujimoto, J. G., and Wollstein, G., 2018, “Tortuous Pore Path Through the Glaucomatous Lamina Cribrosa,” Sci. Rep., **8**(1), pp. 1–7.

Wang, B., Nevins, J. E., Nadler, Z., Wollstein, G., Ishikawa, H., Bilonick, R. A., Kagemann, L., Sigal, I. A., Grulkowski, I., Liu, J. J., Kraus, M., Lu, C. D., Hornegger, J., Fujimoto, J. G., and Schuman, J. S., 2013, “In Vivo Lamina Cribrosa Micro-Architecture in Healthy and Glaucomatous Eyes as Assessed by Optical Coherence Tomography,” Invest. Ophthalmol. Vis. Sci., **54**(13), pp. 8270–8274.

Wang, L., Burgoyne, C. F., Cull, G., Thompson, S., and Fortune, B., 2014, “Static Blood Flow Autoregulation in the Optic Nerve Head in Normal and Experimental Glaucoma,” Investig. Ophthalmol. Vis. Sci., **55**(2), pp. 873–880.

Wang, X., Fisher, L. K., Milea, D., Jonas, J. B., and Girard, M. J. A., 2017, “Predictions of Optic Nerve Traction Forces and Peripapillary Tissue Stresses Following Horizontal Eye Movements,” Investig. Ophthalmol. Vis. Sci., **58**(4), pp. 2044–2053.

Wang, X., Rumpe, H., Lim, W. E. H., Baskaran, M., Perera, S. A., Nongpiur, M. E., Aung, T., Milea, D., and Girard, M. J. A., 2016, “Finite Element Analysis Predicts Large Optic Nerve Head Strains during Horizontal Eye Movements,” Investig. Ophthalmol. Vis. Sci., **57**(6), pp. 2452–2462.

Wang, X., Teoh, C. K. G., Chan, A. S. Y., Thangarajoo, S., Jonas, J. B., and Girard, M. J. A., 2018, “Biomechanical Properties of Bruch’s Membrane-Choroid Complex and Their Influence on Optic Nerve Head Biomechanics,” Investig. Ophthalmol. Vis. Sci.,

**59**(7), pp. 2808–2817.

Watson, P. G., and Young, R. D., 2004, “Scleral Structure, Organisation and Disease. A Review,” Exp. Eye Res., **78**(3), pp. 609–623.

Weinreb, R. N., Aung, T., and Medeiros, F. A., 2014, “The Pathophysiology and Treatment of Glaucoma,” JAMA, **311**(18), p. 1901.

Werkmeister, R., Schmetterer, L., Garhofer, G., Cherecheanu, A. P., and Schmidl, D., 2012, “Ocular Perfusion Pressure and Ocular Blood Flow in Glaucoma,” Curr. Opin. Pharmacol., **13**(1), pp. 36–42.

Yan, D. B., Coloma, F. M., Metheetrairut, A., Trope, G. E., Heathcote, J. G., and Ethier, C. R., 1994, “Deformation of the Lamina Cribrosa by Elevated Intraocular Pressure.,” Br. J. Ophthalmol., **78**(8), pp. 643–8.

Yang, D., Fu, J., Hou, R., Liu, K., Jonas, J. B., Wang, H., Chen, W., Li, Z., Sang, J., Zhang, Z., Liu, S., Cao, Y., Xie, X., Ren, R., Lu, Q., Weinreb, R. N., and Wang, N., 2014, “Optic Neuropathy Induced by Experimentally Reduced Cerebrospinal Fluid Pressure in Monkeys,” Investig. Opthalmology Vis. Sci., **55**(5), p. 3067.

Yang, H., Downs, J. C., Bellezza, A., Thompson, H., and Burgoyne, C. F., 2007, “3-D Histomorphometry of the Normal and Early Glaucomatous Monkey Optic Nerve Head: Prelaminar Neural Tissues and Cupping,” Investig. Opthalmology Vis. Sci., **48**(11), p. 5068.

Yang, H., Downs, J. C., and Burgoyne, C. F., 2009, “Physiologic Intereye Differences in Monkey Optic Nerve Head Architecture and Their Relation to Changes in Early Experimental Glaucoma,” Investig. Ophthalmol. Vis. Sci., **50**(1), pp. 224–234.

Yang, H., Downs, J. C., Girkin, C., Sakata, L., Bellezza, A., Thompson, H., and Burgoyne, C. F., 2007, “3-D Histomorphometry of the Normal and Early Glaucomatous Monkey Optic Nerve Head: Lamina Cribrosa and Peripapillary Scleral Position and Thickness,” Investig. Opthalmology Vis. Sci., **48**(10), p. 4597.

Yang, H., Downs, J. C., Sigal, I. A., Roberts, M. D., Thompson, H., and Burgoyne, C. F., 2009, “Deformation of the Normal Monkey Optic Nerve Head Connective Tissue after Acute IOP Elevation within 3-D Histomorphometric Reconstructions,” Investig. Opthalmology Vis. Sci., **50**(12), p. 5785.

Yang, H., Reynaud, J., Lockwood, H., Williams, G., Hardin, C., Reyes, L., Stowell, C., Gardiner, S. K., and Burgoyne, C. F., 2017, “The Connective Tissue Phenotype of Glaucomatous Cupping in the Monkey Eye - Clinical and Research Implications,” Prog. Retin. Eye Res., **59**, pp. 1–52.

Yang, H., Thompson, H., Roberts, M. D., Sigal, I. A., Downs, J. C., and Burgoyne, C. F., 2011, “Deformation of the Early Glaucomatous Monkey Optic Nerve Head Connective Tissue after Acute IOP Elevation in 3-D Histomorphometric Reconstructions,” Investig. Ophthalmol. Vis. Sci., **52**(1), pp. 345–363.

Yang, H., Williams, G., Downs, J. C., Sigal, I. A., Roberts, M. D., Thompson, H., and Burgoyne, C. F., 2011, “Posterior (Outward) Migration of the Lamina Cribrosa and

Early Cupping in Monkey Experimental Glaucoma," Investig. Opthalmology Vis. Sci., **52**(10), p. 7109.

Young, R. D., 1985, "The Ultrastructural Organization of Proteoglycans and Collagen in Human and Rabbit Scleral Matrix.," J. Cell Sci., **74**, pp. 95–104.

Yu, D. Y., Cringle, S. J., Yu, P. K., Balaratnasingam, C., Mehnert, A., Sarunic, M. V., An, D., and Su, E. N., 2019, "Retinal Capillary Perfusion: Spatial and Temporal Heterogeneity," Prog. Retin. Eye Res., (September 2018), pp. 0–1.

Yuan, L., and Neufeld, A. H., 2000, "Tumor Necrosis Factor-α: A Potentially Neurodestructive Cytokine Produced by Glia in the Human Glaucomatous Optic Nerve Head," Glia, **32**(1), pp. 42–50.

Zhang, L., Thakku, S. G., Beotra, M. R., Baskaran, M., Aung, T., Goh, J. C. H., Strouthidis, N. G., and Girard, M. J. A., 2017, "Verification of a Virtual Fields Method to Extract the Mechanical Properties of Human Optic Nerve Head Tissues in Vivo," Biomech. Model. Mechanobiol., **16**(3), pp. 871–887.

Zhang, Z., Liu, D., Jonas, J. B., Wu, S., Kwong, J. M. K., Zhang, J., Liu, Q., Li, L., Lu, Q., Yang, D., Wang, J., and Wang, N., 2015, "Axonal Transport in the Rat Optic Nerve Following Short-Term Reduction in Cerebrospinal Fluid Pressure or Elevation in Intraocular Pressure," Investig. Opthalmology Vis. Sci., **56**(8), p. 4257.

Zhang, Z., 1994, "Iterative Point Matching for Registration of Free Form Curves and Surfaces," Int. J. Comput. Vis., **13**(2), pp. 119–152.